Joint experimental and theoretical approaches in coordination chemistry : from the trans effects to Single Molecule Magnets

Frédéric Guégan

To cite this version:

Frédéric Guégan. Joint experimental and theoretical approaches in coordination chemistry : from the trans effects to Single Molecule Magnets. Coordination chemistry. Université de Lyon, 2016. English. ⟨NNT : 2016LYSE1267⟩. ⟨tel-01475448⟩

HAL Id: tel-01475448
https://theses.hal.science/tel-01475448v1

Submitted on 23 Feb 2017

N° d'ordre NNT : 2016LYSE1267

THÈSE DE DOCTORAT DE L'UNIVERSITÉ DE LYON
opérée au sein de
l'Université Claude Bernard Lyon 1

École Doctorale de Chimie de Lyon ED206
Chimie, Procédés, Environnement

Spécialité de doctorat : chimie

Thèse soutenue le 14/12/2016, par :

Frédéric Guégan

JOINT EXPERIMENTAL AND THEORETICAL APPROACHES IN COORDINATION CHEMISTRY:

"from the *trans* effects to Single Molecule Magnets"

Devant le jury composé de :

De Proft Frank, Professeur, Vrije Universiteite Brussel	Rapporteur
Winpenny Richard, Professeur, University of Manchester	Rapporteur
Albela Belen, Maître de conférences HDR, ENS de Lyon	Examinatrice
Costuas Karine, Directrice de Recherches, Université Rennes 1	Examinatrice
Joubert Laurent, Professeur, Université de Rouen	Examinateur
Larionova Joulia, Professeure, Université de Montpellier	Présidente de jury
Luneau Dominique, Professeur, Université de Lyon	Directeur de thèse
Morell Christophe, Professeur, Université de Lyon	Co-directeur de thèse

UNIVERSITE CLAUDE BERNARD-LYON 1

Président de l'Université	**M. le Professeur Frédéric FLEURY**
Président du Conseil Académique	M. Le Professeur Hamda BEN HADID
Vice-président du Conseil d'Administration	M. le Professeur Didier REVEL
Vice-président du Conseil Formation et Vie Universitaire	M. le Professeur Philippe CHEVALIER
Vice-président de la Commission Recherche	M. Fabrice VALLEE
Directrice Générale des Services	Mme Dominique MARCHAND

COMPOSANTES SANTE

Faculté de Médecine Lyon Est – Claude Bernard	Directeur : M. le Professeur G. RODE
Faculté de Médecine et de Maïeutique Lyon Sud – Charles Mérieux	Directeur : Mme la Professeure C. BURILLON
Faculté d'Odontologie	Directeur : M. le Professeur D. BOURGEOIS
Institut des Sciences Pharmaceutiques et Biologiques	Directeur : Mme la Professeure C. VINCIGUERRA
Institut des Sciences et Techniques de la Réadaptation	Directeur : M. X. PERROT
Département de formation et Centre de Recherche en Biologie Humaine	Directeur : Mme la Professeure A-M. SCHOTT

COMPOSANTES ET DEPARTEMENTS DE SCIENCES ET TECHNOLOGIE

Faculté des Sciences et Technologie	Directeur : M. F. DE MARCHI
Département Biologie	Directeur : M. le Professeur F. THEVENARD
Département Chimie Biochimie	Directeur : Mme C. FELIX
Département GEP	Directeur : M. Hassan HAMMOURI
Département Informatique	Directeur : M. le Professeur S. AKKOUCHE
Département Mathématiques	Directeur : M. le Professeur G. TOMANOV
Département Mécanique	Directeur : M. le Professeur H. BEN HADID
Département Physique	Directeur : M. le Professeur J-C PLENET
UFR Sciences et Techniques des Activités Physiques et Sportives	Directeur : M. Y.VANPOULLE
Observatoire des Sciences de l'Univers de Lyon	Directeur : M. B. GUIDERDONI
Polytech Lyon	Directeur : M. le Professeur E.PERRIN
Ecole Supérieure de Chimie Physique Electronique	Directeur : M. G. PIGNAULT
Institut Universitaire de Technologie de Lyon 1	Directeur : M. le Professeur C. VITON
Ecole Supérieure du Professorat et de l'Education	Directeur : M. le Professeur A. MOUGNIOTTE
Institut de Science Financière et d'Assurances	Directeur : M. N. LEBOISNE

Dans la vie, rien n'est à craindre, tout est à comprendre.

Marie Curie

On ne fait jamais attention à ce qui a été fait ; on ne voit que ce qu'il reste à faire.

Idem

Remerciements

Certains chapitres sont plus compliqués à rédiger que d'autres, et les remerciements sont indéniablement une partie ardue dans une rédaction de thèse. Il s'agit en effet de remercier toutes les personnes qui ont rendu cette thèse possible, donc de n'oublier personne, et de manière relativement personnalisée et originale, c'est à dire si possible sans répétition. Enfonçons des portes ouvertes : la tâche est complexe, d'autant plus qu'il n'existe à ma connaissance (et à celle des rédacteurs du Petit Larousse) pas de synonyme pour le verbe "remercier". Je vais donc commencer ces remerciements en m'excusant par avance pour les éventuels oublis, forcément involontaires, et pour les répétitions, hélas nécessaires.

Je souhaite tout d'abord exprimer ma plus profonde reconnaissance(i) à mes directeurs de thèse, Dominique et Christophe, pour leur présence et leur aide au cours de ces trois années de thèse, mais aussi au cours des différents stages que j'ai pu effectuer avec l'un ou l'autre. Vous avez toujours su vous rendre disponibles pour mes questions, et votre curiosité a été un moteur important dans ma thèse. Je pense que je n'arriverais jamais à vous remercier suffisamment pour la liberté que vous m'avez donné dans le choix des orientations de ma thèse, me permettant d'expérimenter librement (et n'intervenant que pour me rappeler de ne pas me disperser). J'ai énormément appris au cours de ces trois années à vos côtés.

Je tiens aussi à adresser mes remerciements les plus sincères à Frank de Proft et Richard Winpenny, pour avoir accepté de rapporter mon manuscrit de thèse, ainsi qu'à Belen Albela, Karine Costuas, Joulia Larionova et Laurent Joubert d'avoir bien voulu faire partie de mon jury de thèse.

Cette thèse s'est effectuée entre deux laboratoires, le LMI et l'ISA. Je tiens donc à adresser ma gratitude à leurs directeurs respectifs, Arnaud Brioude et Nathalie Schildknecht, pour m'avoir accueilli dans leurs services. J'aimerais au passage étendre ces remerciements à ceux qui sont trop souvent oubliés mais qui font que les laboratoires tiennent debout d'un jour sur l'autre, à savoir toutes les secrétaires, gestionnaires et personnels techniques, qui ont pendant ces trois années fait preuve de beaucoup de patience face à mes questions éplorées (en particulier face au monstre administratif qu'est l'Université).

Poussant l'analyse un peu plus loin, on est en droit de se dire que, dans un laboratoire, on peut y trouver des collègues. Cette propriété est effectivement vraie, et ils ont joué un rôle de premier plan dans ces trois années. Je ne sais pas comment les remercier pour leur présence au quotidien, leur patience sans borne face à mes jeux de mots vaseux ou mon humeur en montagnes russes, ainsi que pour la bonne ambiance qu'ils ont su installer.

(i) Notez le contournement de la difficulté sus-mentionnée !

J'ai une pensée presque émue quand je pense à la quantité de café[ii] qu'on a du descendre en trois ans.

Même si la frontière entre collègues et amis est plus que poreuse, j'aimerais faire une mention spéciale à ceux-ci. Mille mercis pour votre soutien au jour le jour, et pour tout ce qu'on a pu traverser ensemble (et vous êtes toujours là !). Je vais aussi éviter de faire une liste ici, qui serait longue et très probablement incomplète, mais sachez que je pense à vous tous en écrivant cela, et ce même si on ne se voit pas forcément autant qu'avant (pensée particulière pour les amis bretons, hélas éloignés suite à mon exil lyonnais). Je voudrais au passage en profiter pour remercier aussi mes colocs successifs de m'avoir supporté pendant un certain nombre d'années successives, et d'avoir rendu la vie en dehors du boulot plus agréable. Un grand merci donc à Julien, Anh Thy, Aisling, Alexis, François et Vincent.[iii]

J'aimerais aussi profiter de cette partie pour remercier ma famille, et tout particulièrement mes parents d'avoir toujours cru en moi et de m'avoir toujours poussé, non pas à aller plus loin ou viser plus haut, mais à faire ce que j'aime et à essayer de bien le faire. Si j'en suis là aujourd'hui c'est grâce à vous, et je ne l'oublierai jamais.

Enfin, je voudrais profiter de ces quelques dernières lignes pour remercier celui qui me supporte depuis tant d'années (5 ans, déjà ?), et dont la présence ensoleille mes journées. Mathias, cette thèse est un peu la tienne.

[ii] Et aussi de bières, mais il faut sans doute moins le mentionner dans une thèse...

[iii] Ne sois pas impatient Mathias, ton tour vient après !

Contents

Introduction

La chimie de coordination est un domaine de recherche diversifié et fertile. De nombreuses et originales propriétés (magnétisme, luminescence, réactivité) peuvent en effet naître de l'interaction entre cations métalliques et ligands, et peuvent en outre être finement contrôlées par une ingéniérie chimique appropriée. Plusieurs modèles ont été successivement étudiés et appliqués avec succès pour décrire les propriétés des composés de coordination; par exemple, la théorie du champ cristallin et son successeur, la théorie du champ des ligands.

Ces modèles sont très précieux pour le chimiste, dans la mesure où ils offrent un cadre théorique robuste pour comprendre, interpréter et rationaliser les observations expérimentales, comme par exemple les variations dans les propriétés optiques d'une série de complexes. En général, ils possèdent une solide base théorique et ont dans le même temps l'avantage d'être relativement généraux et souples dans leur formulation.

Néanmoins, ces modèles sont tous intrinsèquement limités et peuvent être trop simplifiés pour pouvoir réellement s'appliquer à des cas concrets. Par exemple, la théorie du champ cristallin est bien formulée pour des complexes présentant de hautes symétries, tandis que les composés étudiés peuvent être assez peu – voire pas du tout – symétriques.

Dans de tels cas, il est utile de revenir aux bases théoriques de ces modèles. Grâce à l'intense développement informatique de ces dernières années, les domaines d'application de la chimie quantique se sont considérablement élargis. De plus en plus de systèmes peuvent être étudiés par des calculs de haut niveau, les limites de taille étant sans cesse repoussées. En parallèle de ce développement technique, le développement d'interfaces plus ergonomiques de nombreux programmes de chimie quantique permet un élargissement de leur public vers les non-spécialistes (pour peu qu'ils soient tout de même familiers avec la chimie quantique). Il est donc de plus en plus aisé de vérifier et de compléter nos modèles.

De fait, il nous apparait fort probable que la pratique expérimentale s'appuie de plus en plus sur la théorie au cours des années à venir. Un dialogue toujours plus fourni entre les deux domaines ne saurait être que fructueux, laissant envisager la possibilité à terme que les expérimentateurs eux-mêmes effectuent des calculs de chimie quantique sur les systèmes qui les intéressent, et vice-versa.

Le présent travail s'insère dans cette idée de "construire des ponts" entre expérience et modélisation. La partie expérimentale de cette thèse a été effectuée dans l'équipe de Chimie Inorganique Moléculaire et Précurseurs du Laboratoire des Multimatériaux et Interfaces (LMI), et la partie théorique au sein de l'équipe Chimiométrie et Chimie Théorique de l'Institut des Sciences Analytiques de Lyon (ISA).

Au cours de cette thèse, nous nous sommes principalement intéressés à la description et la compréhension de propriétés magnétiques, de luminescence et de réactivité de complexes de coordination. Le chapitre 1 présente les fondamentaux de la chimie quantique et computationnelle. Y sont développés les outils utilisés dans le reste du manuscrit, à savoir les théories de Hartree-Fock, post Hartree-Fock et de la Fonctionnelle de la Densité. Une mention toute particulière est réservée à la DFT conceptuelle, qui a été intensivement utilisée au cours de ce travail.

Dans le chapitre 2, nous donnons un certain nombre d'éléments de théorie relatifs à la chimie de coordination et ses modèles. Une part importante de ce chapitre est dédiée au magnétisme moléculaire qui, s'il ne se résume pas à la chimie de coordination, a une importance majeure dans le développement de cette dernière et aussi dans le présent travail.

Le chapitre 3 revisite les interactions métal-ligands en chimie de coordination par la DFT conceptuelle. Le travail est triple : dans un premier temps, nous proposons une nouvelle approche computationnelle du Descripteur Dual, basée sur un formalisme de théorie des perturbations indépendantes du temps. Dans un second temps, à travers une courte étude des propriétés de coordination des ligands nous illustrons la puissance prédictive de ce descripteur. Enfin, il est utilisé dans un dernier temps pour caractériser et rationaliser l'effet *trans* dans les complexes de coordination octaédriques. Pour la première fois, nous proposons une échelle purement théorique des ligands *trans*-orienteurs. Ces deux études ont été réalisés en collaboration avec Vincent Tognetti et Laurent Joubert (Université de Rouen).

Dans le chapitre 4, nous nous intéressons aux propriétés physico-chimiques de complexes de cuivre(II) et de bases de Schiff dérivant d'acides aminés chiraux, en particulier au magnétisme. L'un des but de cette étude est en effet de déterminer si la chiralité de nos ligands a un impact sur les propriétés magnétiques des complexes formés. Dans ce chapitre, nous présenterons donc les synthèses et les propriétés magnétiques et de réactivité de ces derniers, que nous rationaliserons par des études DFT et post Hartree-Fock (DDCI, NEVPT2). Les calculs DDCI ont été réalisés en collaboration avec Marie-Bernadette Lepetit (Institut Néel, Grenoble).

Enfin, le chapitre 5 présente les synthèses et caractérisations magnétiques de deux familles de complexes de coordination mononucléaires de lanthanide. Pour la plupart, ces composés présentent un comportement de molécule-aimant induit par le champ. La dynamique de l'aimantation de ces complexes a pu être rationalisée grâce à une étude de leurs propriétés de luminescence et des calculs *ab initio*, les résultats demeurant cependant préliminaires dans le cas de la seconde famille de composés. Les mesures de luminescence ont été réalisés en collaboration avec Olivier Maury et François Riobé (ENS Lyon), et les calculs *ab initio* en collaboration avec Julie Jung et Boris le Guennic (Université de Rennes 1).

Chapter 1

Elements of quantum chemistry

The aim of quantum chemistry is to describe chemical systems, *i.e.* molecules or solids, through the equations of quantum mechanics. To this extent, many different formulations and methods were developed. The goal of this chapter is to present them. Here, we decided to focus on the concepts, rather than going deep into the algebraic details. The main idea is to provide, for the non-specialist, the flavour of these methods, leaving the mathematical details to the dedicated textbooks. With this idea in mind, it seemed rather logical for us to leave aside all the methods that were not employed in this thesis. Presenting them all would indeed be quite a Promethean task, and we may refer the curious reader to the hereafter cited textbooks.

1.1 Solving the Schrödinger equation

First of all, let us restrict the scope to molecular systems, in which we will consider nuclei as classical particles. The central problem in quantum chemistry is thus to solve the stationary Schrödinger equation:

$$\mathcal{H}|\Psi\rangle = E|\Psi\rangle \tag{1.1}$$

for a given molecule with M nuclei **A** and N electrons **i**.[1,2] The wavefunction Ψ contains all the information on the the system. Here, we will be considering the chemical properties only at a fixed geometry, and we will assume the motions of electrons and nuclei can be separated (Born-Oppenheimer approximation).[3] In such a case, the total energy is distributed into two components, one related to the nuclei exclusively, and one related to the electrons. We will only focus on the latter, which is expressed as:

$$\begin{aligned}\mathcal{H}_{el} &= \sum_{A=1}^{M}\sum_{i=1}^{N} -\frac{Z_A}{|\mathbf{R_A}-\mathbf{r_i}|} + \sum_{i=1}^{N} -\frac{1}{2}\nabla_r^2 + \sum_{i=1}^{N}\sum_{j>i}^{N}\frac{1}{|\mathbf{r_i}-\mathbf{r_j}|} && (1.2)\\ &= \mathcal{V}_{en} + \mathcal{T}_e + \mathcal{V}_{ee} && (1.3)\end{aligned}$$

with $\mathcal{V}_{en}$ the electron-nuclei attraction, $\mathcal{T}_e$ the kinetic energy of the electrons and $\mathcal{V}_{ee}$ the electron-electron repulsion energy.[4]

Obviously, the two first operators are monoelectronic, *i.e.* the contribution from each electron can be treated separately from that of the others. Considering only these two terms, the Schrödinger equation could be analytical solved. Often, they are gathered into a monoelectronic operator $h(i)$. $\mathcal{V}_{ee}$ on the other hand is a two-electrons operator, and the contribution of a specific electron **i** cannot be decorrelated from the contribution of

the other electrons $\mathbf{j}^{(i)}$.[5,6] Because of this latter term, in the general case the Schrödinger equation cannot be analytical solved.
In order to describe correctly molecules, we thus need to devise efficient approximations. They can be developed in two different frameworks, which are presented in the following. The first one is based on a wavefunction formalism: the Hartree-Fock approximation and its corrections, the so-called post Hartree-Fock methods. The second one is based on the electron density: the Density Functional Theory. Noteworthy, this approach is formally exact if applied to a non-degenerate ground state. However, as we will show its exact formulation is inapplicable, and approximations are also called.

1.2 Wavefunction based theories

1.2.1 Hartree-Fock method

The Slater determinant

Before getting into the details of the Hartree-Fock formalism, we may say a few words about the wavefunction itself. The electrons are indiscernible particles, which furthermore obey the Pauli principle of exclusion, due to their fermionic nature.[1,7] These two properties imply that the wavefunction must change its sign upon the exchange of two electrons: Ψ is said to be antisymmetric. If we assume we can develop the wavefunction over a basis of monoelectronic orbitals ϕ_i, a convenient form of Ψ is given by the Slater determinant:

$$\Psi = \frac{1}{\sqrt{N!}} \begin{vmatrix} \phi_1(\mathbf{x}_1) & \phi_2(\mathbf{x}_1) & \dots & \phi_N(\mathbf{x}_1) \\ \phi_1(\mathbf{x}_2) & \phi_2(\mathbf{x}_2) & \dots & \phi_N(\mathbf{x}_2) \\ \vdots & \vdots & \vdots & \vdots \\ \phi_1(\mathbf{x}_N) & \phi_2(\mathbf{x}_N) & \dots & \phi_N(\mathbf{x}_N) \end{vmatrix}, \tag{1.4}$$

where $\mathbf{x}_i$ represents the position $\mathbf{r}_i$ and spin (γ=α or β) of electron i. For the sake of simplicity, in the following we will use the common and simplified notation $\Psi = |\phi_1\phi_2 \dots \phi_N\rangle$.

The Hartree-Fock approximation

The Hartree-Fock approximation states that the wavefunction Ψ can indeed be written as a single Slater determinant.[6,8] Fundamentally, this implies that the fully coupled problem in equation (1.3) has been simplified to a mean field approach. The electron-electron repulsion can thus be explicited for each electron, feeling the influence of the N-1 remaining electrons. The energy of the system can then be written as:

$$\begin{aligned} E = \langle\Psi|\mathcal{H}_{el}|\Psi\rangle &= \sum_{i=1}^{N} \langle\phi_1 \dots \phi_i \dots \phi_N|h(i)|\phi_1 \dots \phi_i \dots \phi_N\rangle \\ &+ \sum_{i=1}^{N}\sum_{j>i}^{N} \langle\phi_1 \dots \phi_i \dots \phi_j \dots \phi_N|\frac{1}{|\mathbf{r_i}-\mathbf{r_j}|}|\phi_1 \dots \phi_i \dots \phi_j \dots \phi_N\rangle \\ &- \sum_{i=1}^{N}\sum_{j>i}^{N} \langle\phi_1 \dots \phi_i \dots \phi_j \dots \phi_N|\frac{1}{|\mathbf{r_i}-\mathbf{r_j}|}|\phi_1 \dots \phi_j \dots \phi_i \dots \phi_N\rangle \end{aligned} \tag{1.5}$$

[(i)] Actually, we retrieve a N-body in interaction scheme.

$$= \sum_{i=1}^{N} \langle \phi_i | h(i) | \phi_i \rangle + \sum_{i=1}^{N} \sum_{j>i}^{N} \langle \phi_i \phi_j | \frac{1}{|\mathbf{r_i} - \mathbf{r_j}|} | \phi_i \phi_j \rangle - \langle \phi_i \phi_j | \frac{1}{|\mathbf{r_i} - \mathbf{r_j}|} | \phi_j \phi_i \rangle \tag{1.6}$$

$$= \sum_{i=1}^{N} h_i + \sum_{i=1}^{N} \sum_{j>i}^{N} \langle \phi_i | J_j(i) | \phi_i \rangle - \langle \phi_i | K_j(i) | \phi_i \rangle \tag{1.7}$$

In equation (1.7), the first term in the double sum is called the Coulomb term. It translates the repulsion between one electron in the orbital ϕ_i and another electron in ϕ_j. The second term has no classical counterpart. It translate the energetic stabilisation when the electrons in orbitals ϕ_i and ϕ_j are exchanged, hence its name exchange energy.

To solve the Schrödinger equation within this scheme, one thus needs to minimise E (variational principle). An additional condition to this minimisation is the fact that the orbitals ϕ_i must be orthonormal.[5] This leads to the minimisation of the following Lagrangian:

$$\mathcal{L} = \langle \Psi | \mathcal{H}_{el} | \Psi \rangle - \sum_{i=1}^{N} \sum_{j=1}^{N} \epsilon_{ij} (\langle \phi_i | \phi_j \rangle - \delta_{ij}). \tag{1.8}$$

Each ϵ_{ij} has the dimension of an energy, and their sum over j yield the energy of the orbital ϕ_i. Practically, the Lagrangian is minimised using a Self-Consistent Field (SCF) procedure: from a set of guess orbitals, the value of $\mathcal{L}$ is computed. The orbitals are then modified in order to diminish $\mathcal{L}$, and the calculation develops until convergence is detected.

Restricted and Unrestricted Hartree-Fock

The Hartree-Fock formalism thus permits the calculation of the ground state wavefunction and energy, under the approximation that the former can be written as a single Slater determinant. Actually, two formulations are found: Restricted (RHF) and Unrestricted (UHF) Hartree-Fock calculations.

In the former case, the orbitals occupation can only be 2 or 0. If we separate the spin and spatial component of the orbitals $\phi = \zeta(\mathbf{r})\chi(\gamma)$, this implies that the spatial parts $\zeta(\mathbf{r})$ are set to be equal for two electrons with spin α and β. Note this is what one usually assumes when drawing a molecular orbital diagram (two electrons per orbital at most).

In the UHF description on the other hand, one allows the spatial parts for spin α and β to be different, and orbitals occupations can only be 1 or 0. Such a formalism is needed if one wants to describe open-shell structures (radicals, transition metal ions). It is also necessary in order to describe correctly homolytic bond cleavage.[7] Yet, as underlined in the latter reference, even though UHF yields in that case an improvement over RHF, it may still be quite inaccurate. This is the consequence of the underlying simplifications in the Hartree-Fock formulations: the mean-field and mono-determinental approximations.

We will show in the following section how the descriptions can be improved, starting from a RHF or UHF calculation.

1.2.2 Post-Hartree Fock methods

The correlation energy

In the previous section, we mentioned that the Hartree-Fock formalism implicitly describes the electron-electron repulsion by a mean-field approach. Hence, in such calculations the actual correlation – which we will precisely define later – between the electrons is mistreated. Usually, one defines the correlation energy[7] as

$$E_{corr} = E_{exact} - E_{HF}. \tag{1.9}$$

The goal of the post Hartree-Fock approaches reduces more or less to the computation of an accurate enough E_{corr}.

Working on the wavefunction: the full CI development

Formally, the mean-field approximation that is used throughout the Hartree-Fock model is not coming from a simplification of the Hamiltonian, but rather from the arbitrary form of the wavefunction. The Slater determinant of equation (1.4) is indeed an antisymmetric function, but any linear combination of such determinants would also be an antisymmetric function.

Actually, provided that there exists an infinite basis of orbitals ϕ_i, the exact wavefunction Ψ should be a linear combination of all the possible Slater determinants constructed on this basis.[5,9] Let's consider the following Slater determinant, solution of the Hartree-Fock equations:

$$|\Psi_{HF}\rangle = |\phi_1\phi_2\ldots\phi_a\phi_b\phi_c\ldots\phi_N\ldots\phi_r\phi_s\phi_t\ldots\rangle \tag{1.10}$$

with an infinite number of orbitals. ϕ_a, ϕ_b and ϕ_c represent occupied orbitals, and ϕ_r, ϕ_s, ϕ_t virtual (unoccupied) ones. We can construct an infinity of orthogonal determinants by promoting L ($L \leq N$) electrons from the occupied orbitals to the virtual ones:

$$|\Psi_a^r\rangle = |\phi_1\phi_2\ldots\phi_r\phi_b\phi_c\ldots\phi_N\ldots\phi_a\phi_s\phi_t\ldots\rangle \tag{1.11}$$

$$|\Psi_{ab}^{rs}\rangle = |\phi_1\phi_2\ldots\phi_r\phi_s\phi_c\ldots\phi_N\ldots\phi_a\phi_b\phi_t\ldots\rangle \tag{1.12}$$

$$|\Psi_{abc}^{rst}\rangle = |\phi_1\phi_2\ldots\phi_r\phi_s\phi_t\ldots\phi_N\ldots\phi_a\phi_b\phi_c\ldots\rangle \text{ ...} \tag{1.13}$$

Doing so, we actually build all the possible determinants with the given orbital basis. They are called n-excited determinants. Hence, we can write the wavefunction as

$$|\Psi\rangle = c_0|\Psi_{HF}\rangle + \sum_{a=1}^{N}\sum_{r=N+1}^{\infty} c_a^r|\Psi_a^r\rangle + \sum_{\substack{a=1\\ b>a}}^{N}\sum_{\substack{r=N+1\\ s>r}}^{\infty} c_{ab}^{rs}|\Psi_{ab}^{rs}\rangle + \ldots \tag{1.14}$$

Conceptually, equation (1.14) develops the wavefunction upon all the possible electronic configurations. Though these determinants are mutually orthogonal, they are going to be coupled by the Hamiltonian, and as such each determinant is likely to interact with the others, directly or not. This development is called "Full Configuration Interaction" (full-CI).(ii)

(ii) Actually, the Brillouin's theorem states that the interaction of $|\Psi_{HF}\rangle$ with the mono-excited $|\Psi_a^r\rangle$ is null. Furthermore, the Slater rules imply that there is no interaction through $\mathcal{H}$ between determinants differing by more than 2 orbitals. Thus, the CI matrix can be written as the block matrix:

$$\begin{pmatrix}
\langle\Psi_{HF}|\mathcal{H}|\Psi_{HF}\rangle & 0 & \langle\Psi_{HF}|\mathcal{H}|D\rangle & 0 & 0 & \ldots \\
 & \langle S|\mathcal{H}|S\rangle & \langle S|\mathcal{H}|D\rangle & \langle S|\mathcal{H}|T\rangle & 0 & \ldots \\
 & & \langle D|\mathcal{H}|D\rangle & \langle D|\mathcal{H}|T\rangle & \langle D|\mathcal{H}|Q\rangle & \ldots \\
 & & & \langle T|\mathcal{H}|T\rangle & \langle T|\mathcal{H}|Q\rangle & \ldots \\
 & & & & \langle Q|\mathcal{H}|Q\rangle & \ldots \\
 & & & & & \ldots
\end{pmatrix} \tag{1.15}$$

where $|S\rangle$, $|D\rangle$, $|T\rangle$, $|Q\rangle$ represent the subsets of simple, double, triple and quadruple excitations, respectively.

Stating the obvious, it is rather cumbersome to deal with an infinite number of basis functions. In a full-CI calculation, one will often restrict to a finite number of orbitals $N' \gg N$. The calculated energy will thus be an upper bond of the exact energy, and one can arbitrarily set the precision of the calculation by adjusting N'. Yet, the cost of the calculation becomes quickly prohibitive, since the number of Slater determinants increases quickly with N', and thus with N:

$$\binom{N'}{N} = \frac{N'!}{N!(N'-N)!}. \tag{1.16}$$

Full-CI calculations are said to scale exponentially with the number of orbitals, and will thus be limited to very simple systems, with a low number of atoms. These may not be the most interesting systems to study. Further levels of simplifications are still needed if one wants to take the effects of correlation into account.

Truncating the CI development

A first simplification that comes to mind is simply to truncate the development of equation (1.14). There are indeed physical arguments for this simplification. First of all, the more electrons are promoted to virtual orbitals, the higher in energy will be the resulting configuration. Furthermore, from the form of the full-CI matrix (cf. equation (1.15)) it appears that only the doubly excited determinants couple directly with the Hartree-Fock determinants. Truncating at the second order would then give:

$$|\Psi\rangle = c_0|\Psi_{HF}\rangle + \sum_{a=1}^{N}\sum_{r=N+1}^{N'} c_a^r|\Psi_a^r\rangle + \sum_{\substack{a=1\\b>a}}^{N}\sum_{\substack{r=N+1\\s>r}}^{N'} c_{ab}^{rs}|\Psi_{ab}^{rs}\rangle \tag{1.17}$$

$$E_{corr} = c_0\sum_{\substack{a=1\\b>a}}^{N}\sum_{\substack{r=N+1\\s>r}}^{N'} c_{ab}^{rs}\langle\Psi_{HF}|\mathcal{H}|\Psi_{ab}^{rs}\rangle. \tag{1.18}$$

This approach is called CISD[10]: Configuration Interaction of Single and Double excitations. In a similar way, one can define a CIS and CID development.

The truncation alleviates a large part of the computational effort, but this simplification has a down side. First of all, even though only the doubly excited determinants are directly coupled to the Hartree-Fock one, they are all interacting indirectly. Neglecting this interaction will change the coefficients c_a^r and c_{ab}^{rs}, and as such the calculated correlation energy.[7]

More importantly, the truncated CI development is not size-extensive. This means the energy of N independent molecules will indeed be different to N times the energy of an isolated one. This is due to the truncation to a given order, which does not necessarily allow excitations on all the molecules at the same time.[8] For instance, for a system of two identical molecules, at the second order the only possible determinants are the following:

- $|0,0\rangle$ for the ground configuration (0 indicating the non-excited determinant for one molecule)
- $|0,S\rangle$ and $|S,0\rangle$ for the mono-excitation (S indicating singly excited determinants)
- $|S,S\rangle$, $|0,D\rangle$ and $|D,0\rangle$ for the di-excitations (D representing the doubly excited determinants).

No cross-double excitations $|D, D\rangle$ are possible since they correspond formally to a quadruple excitation (four electrons in four orbitals).
A possible solution comes from an alternative formulation in the framework of the second quantization theory: the coupled cluster formulation.[11] Let's define two operators:

$$\mathcal{T}_1|\Psi_{HF}\rangle = \sum_{a=1}^{N} \sum_{r=N+1}^{N'} c_a^r |\Psi_a^r\rangle \tag{1.19}$$

$$\mathcal{T}_2|\Psi_{HF}\rangle = \sum_{\substack{a=1\\ b>a}}^{N} \sum_{\substack{r=N+1\\ s>r}}^{N'} c_{ab}^{rs} |\Psi_{ab}^{rs}\rangle. \tag{1.20}$$

$\mathcal{T}_1$ is a creation/annihilation operator: it annihilates an electron in Ψ_{HF}, in the orbital a, and creates an electron in the orbital r. Similarly $\mathcal{T}_2$ annihilates two electrons in Ψ_{HF}, in the orbitals a and b, and creates two electrons in the orbitals r and s. The CISD wavefunction can thus be written as

$$|\Psi_{CISD}\rangle = (1 + \mathcal{T}_1 + \mathcal{T}_2)\,|\Psi_{HF}\rangle. \tag{1.21}$$

Basing on these two operators only, we can define another wavefunction: the CCSD (Coupled Cluster restricted to the Single and Double excitations) wavefunction

$$|\Psi_{CCSD}\rangle = e^{(\mathcal{T}_1+\mathcal{T}_2)}|\Psi_{HF}\rangle. \tag{1.22}$$

The interest of this formulation is more obvious if we expand the exponential as a series:

$$\begin{aligned}|\Psi_{CCSD}\rangle &= \left(1 + (\mathcal{T}_1 + \mathcal{T}_2) + \frac{1}{2}(\mathcal{T}_1 + \mathcal{T}_2)^2 + \dots\right)|\Psi_{HF}\rangle & (1.23)\\ &= \left(1 + (\mathcal{T}_1 + \mathcal{T}_2) + \frac{1}{2}(\mathcal{T}_1^2 + 2\mathcal{T}_2\mathcal{T}_1 + \mathcal{T}_2^2) + \dots\right)|\Psi_{HF}\rangle & (1.24)\end{aligned}$$

using the commutation properties of the two operators $\mathcal{T}_1$ and $\mathcal{T}_2$.
Indeed, from this development it appears that we are able to access the single and double excitations, but also some of the triples and quadruples, from the $\mathcal{T}_2\mathcal{T}_1$ and $\mathcal{T}_2^2$ terms. Furthermore, CCSD is size-extensive. Yet, it is still a very expensive and heavy formalism, with a N'^6 scaling,[12] hence restricted to small-size systems. For instance, on a small complex of 17 heavy atoms and 21 hydrogens, the initialisation step of a CCSD calculation in Gaussian 09 (with triple-zeta quality bases) is requiring more than 16 Go of disk space! Very likely, this approach will not be accessible for the kind of molecules we will be interested in in this thesis.

Perturbative approach: Møller-Plesset approach

The aim of Møller-Plesset (MP) approach[8,13] is to correct the Hartree-Fock wavefunction and energy basing on the framework of Rayleigh-Schrödinger perturbations. The ingenious idea is to treat the r_{ij}^{-1} potential as a perturbation of the Hartree-Fock mean field one. Let's start from the so-called Fock operator

$$\mathcal{H}_0 = \sum_{i=0}^{N} \mathcal{F}(i) = \sum_{i=1}^{N} \left(h(i) + \sum_{j=1}^{N} J_j(i) - K_j(i)\right). \tag{1.25}$$

As one must note, the eigenvalues E_0^k of this operator are **not** the Hartree-Fock energies, but rather the sum of the orbitals energies (for the given state k). This is due to the second sum (over the bielectronic operators), whose indices are not limited to $j > i$.
The genuine Hamiltonian of the system, as defined in equation (1.3), can be written as

$$\mathcal{H}_{el} = \mathcal{H}_0 + \mathcal{V} \tag{1.26}$$

with

$$\mathcal{V} = \sum_{i=1}^{N} \sum_{j>i}^{N} \frac{1}{\mathbf{r}_{ij}} - \sum_{i=1}^{N} \sum_{j=1}^{N} J_j(i) - K_j(i). \tag{1.27}$$

Assuming the correction on energies due to the application of $\mathcal{V}$ will be small, we can indeed apply the time-independent perturbation theory. We will call $E_k^{(i)}$ the ith correction of the energy of state k, $\Psi_k^{(i)}$ the corresponding wavefunctions correction, and E^0 and Ψ^0 the ground eigenvalue and eigenvector. At the first order, we have:

$$\begin{aligned}
E_0^{(1)} &= \langle\Psi^0|\mathcal{V}|\Psi^0\rangle && (1.28)\\
&= \langle\Psi^0|\sum_{i=1}^{N}\sum_{j>i}^{N}\frac{1}{\mathbf{r}_{ij}}|\Psi^0\rangle - \langle\Psi^0|\sum_{i=1}^{N}\sum_{j=1}^{N} J_j(i) - K_j(i)|\Psi^0\rangle && (1.29)\\
&= \frac{1}{2}\langle\Psi^0|\sum_{i=1}^{N}\sum_{j>i}^{N} J_j(i) - K_j(i)|\Psi^0\rangle - \langle\Psi^0|\sum_{i=1}^{N}\sum_{j=1}^{N} J_j(i) - K_j(i)|\Psi^0\rangle && (1.30)\\
E_0^{(1)} &= -\frac{1}{2}\langle\Psi^0|\sum_{i=1}^{N}\sum_{j>i}^{N} J_j(i) - K_j(i)|\Psi^0\rangle && (1.31)
\end{aligned}$$

and:

$$\Psi_0^{(1)} = \sum_{k}^{N'} \frac{\langle\Psi^0|\mathcal{V}|\Psi_k^{(0)}\rangle}{E^0 - E_k^{(0)}}|\Psi_k^{(0)}\rangle. \tag{1.32}$$

The first order correction thus allows to retrieve the Hartree-Fock energy. At the second order in energy, the result is more interesting:

$$E_0^{(2)} = \sum_{\substack{k\\ l\neq k}}^{N'} \frac{\langle\Psi^0|\mathcal{V}|\Psi_k^{(0)}\rangle\langle\Psi_k^{(0)}|\mathcal{V}|\Psi^0\rangle}{E^0 - E_k^{(0)}}. \tag{1.33}$$

Indeed, we may identify the $|\Psi_k^{(0)}\rangle$ determinants to the n-excited determinants in equations (2.11) to (2.13). Furthermore, because of the Brillouin's theorem we know only the doubly excited determinants will couple with the ground state wavefunction. As such, we may write:

$$E_0^{(2)} = \sum_{\substack{a,b>a\\ r,s>r}}^{N,N'} \frac{\langle\Psi^0|\mathcal{V}|\Psi_{ab}^{rs}\rangle\langle\Psi_{ab}^{rs}|\mathcal{V}|\Psi^0\rangle}{\epsilon_a + \epsilon_b - \epsilon_r - \epsilon_s}. \tag{1.34}$$

At the second order of perturbation, the correlation energy will thus simply be:

$$E_{corr} \approx E^0 + E_0^{(1)} + E_0^{(2)} - E_{HF} = E_0^{(2)}. \tag{1.35}$$

A major interest of the MP2 (second order Møller-Plesset) approach is its relatively low complexity: it evolves as N'^5,[12] along with a fairly good representation in energy. The higher order formulations (MP3, MP4...) are rarely used, since they do not bring a marked improvement with respect to their cost (N'^6 and N'^7, respectively). Actually, MP2 itself presents a quite marked drawback: it does not comply with the Ritz (variational) principle, hence the computed energy has no lower bound. This can likely be problematic during a calculation...

Multi-Reference methods

Static correlation. So far, we have presented the improvements that can be brought to the Hartree-Fock description, starting from a single Slater determinant. The different approximations we presented allow to retrieve a part of the correlation energy that stems from the dynamic interaction of electrons, hence its name *dynamical correlation*. Another kind of correlation can also be encountered, called *static correlation*.

For an easy grasp of the concept, let's consider the case of a d^1 metal ion in an octahedral ligand field, for instance $[V(NH_3)_6]^{4+}$. As we will see in the next chapter, the ligand field induces a splitting of the d metal atomic orbitals (AO), such that the three non-bonding d_{xz}, d_{xy} and d_{yz} metal AO are degenerate. The unpaired electron of V^{4+} could thus be placed in any of the three d_{xz}, d_{xy} and d_{yz} orbitals, as represented on Figure 1.2.1.

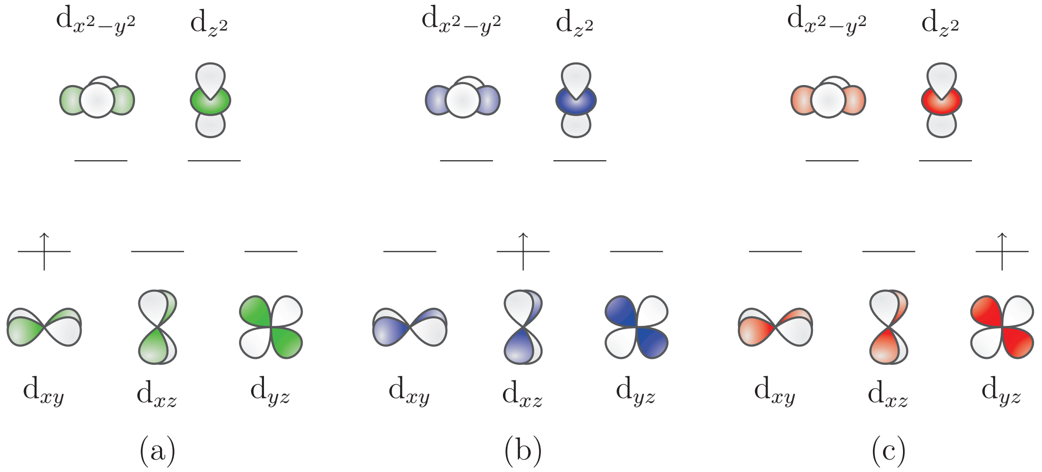

FIGURE 1.2.1: Ground electronic configurations associated to the localisation of a single electron in a d metal AO, in the case of an octahedral field.

In such cases, quantum mechanics suggests the actual wavefunction will be a linear combination of each "limit" configuration (a), (b) and (c) (with coefficients that should roughly be of the same order of magnitude).[7,8] In the Hartree-Fock formulation on the other hand, we would expect to converge to one of the three determinants. We would thus miss a correlation effect that is not linked to the dynamic interaction of electrons, but rather to the fact that some systems may be described by several "limit forms". This is the effect of static correlation, which will be encountered for any system that cannot be properly described by a single determinant.

As one may infer already, this correlation effect is likely to be significant in the case of coordination complexes. In order to retrieve it, we should optimise not only the coefficients of each orbital in the Hartree-Fock determinant, but also all the orbitals themselves (through the coefficients of the atomic orbitals that compose them). This is what one achieves with the multi-reference methods. Obviously, the double optimisation of both the determinants and the orbital is a complex problem, and simplifications can be made.

Complete Active Space SCF (CASSCF). A first simplification can be achieved using physical arguments. If the chemical and physical properties of molecules are essentially due to the electrons, one can furthermore state they are primarily related to the valence electrons, with a very small impact of the fine structure of core electrons(iii). This suggests that corrections due to the multi-reference nature of the wavefunction are going to be predominant only on the valence electrons, *i.e.* those located near the Fermi level in the Hartree-Fock reference determinant. In the same spirit, the correction due to the virtual orbitals is likely to be relevant only for the few ones located near the HOMO - LUMO gap. Actually, chemists often use this approximation - as we did in Figure 1.2.1.
In a CASSCF calculation,[8,14,15] we thus restrict the construction of the CI determinants to a subset of M orbitals near the Fermi level, populated by N electrons. This subset is called the active space, in opposition to the remaining orbitals that are called inactive(iv). Such a calculation is generally called a CAS(N,M). Starting from a reference Hartree-Fock determinants, all the possible electronic configurations of N electrons in M orbitals are build, and then optimised. For instance, the case of Figure 1.2.1 corresponds to a CAS(1,3): the unpaired electron can be located in any of the three metal AO.

As one can see, the main degree of freedom in the CAS formulation is the choice of the active space. For instance, in the previous CAS(1,3) example, no ligand to metal charge transfer can be reproduced, since the ligands electrons and orbitals are not introduced in the active space. In order to take this effect into account, one would need to incorporate the latter in the active space. Nevertheless, one cannot extend the active space to all the orbitals, because of the factorial scaling of the method. As a result, one often has to go through a trial and error approach. Among the possible criteria, one may follow the final occupation of the orbitals. As a rule of thumb, all the orbitals with an occupation above 1.98 or below 0.02 can be removed from the active space - they even *should* be removed to avoid instabilities.[16]

State Averaged CASSCF (SA-CASSCF). With the CASSCF methodology, it is then possible to compute the wavefunction for any state, ground or excited, associated to a given spin multiplicity. If we consider the case of the d^1 ion of Figure 1.2.1, obviously all states are going to be spin doublets. If, on the other hand, we consider a Dy^{3+} ion ($4f^9$ electronic configuration), then several spin multiplicities are possible: sextet, quartet and doublet.

In a state-averaged calculation, the wavefunction is not optimised to describe a unique state, but rather to reproduce a set of states, usually with the same multiplicities. This is a quite powerful formulation, since a large number of electronic states can be described with a reduced number of orbitals.

In a SA-CASSCF calculation, one obtains what are called "spin-free" wavefunctions. The expression is rather plain: the considered configurations are irrespective of the actual spin projection. For instance, in the case of a Dy^{3+} ion, 9 electrons are to be placed in 14 different spin-orbitals. This leads to evaluate 2002 different determinants, but they can be gathered in doublets, quartets and sextets. In the end, there are only 735 different

---

(iii) Note that this is completely wrong for Mossbauer shifts, for instance.

(iv) Sometimes a distinction is made between the occupied inactive orbitals and the empty ones, which are then called "virtual".

configurations to compute: 21 sextets, 224 quadruplets and 490 doublets(v).[17] As can be infered from the choice of the example, these kind of calculations are going to be very useful to reproduce the properties of lanthanide complexes, whose wavefunctions are going to be highly non-monodeterminantal and thus will present a large static correlation.

Adding the dynamic correlation As we said, in a (SA-)CASSCF calculation the static correlation is taken into account, but not the dynamic correlation. It could be desirable to also take those effects into account; for instance, in Chapter 4 we will deal with Cu(II) complexes, for which both dynamical and static correlations are important. They can be incorporated in a perturbative manner, retrieving a formulation that is similar to the Møller-Plesset one, but based on a CASSCF (or SA-CASSCF) wavefunction. Usually, the perturbation development is truncated at the second order: this is the so-called (SA-)CASPT2 approach.[18,19] Experience shows that, for most of the lanthanide ions, the correction due to dynamic correlation is very small and can safely be neglected. Actually, only Yb(III) and Ce(III) ions seem to need the PT2 correction in order to reproduce correctly experimental trends.[20] These two lanthanide ions are also known to have a singular redox behaviour: the $4f$ and $6s$,$5d$ orbitals are close in energy, and they may also be close to the ligands orbitals.[21] As such, electronic configurations with electron transfers from (or to) the $4f$ shell to the $6s$, $5p$ or ligands orbitals may have a large weight in the wavefunction for Yb(III) and Ce(III) than for the other lanthanides. Since these orbitals have a larger extent in space than the $4f$, the electron-electron interaction may to be stronger in these "excited" configurations. Hence, this may explain why Ce(III) and Yb(III) call for the inclusion of dynamical correlation, more than any other lanthanide.
Another second-order formulation exists, called N-Electron Valence Perturbation Theory (NEVPT2). It is very close to CASPT2, but is based on a different zeroth order Hamiltonian: the so-called Dyall Hamiltonian.[22] This Hamiltonian is constructed in such a way that it is equal to the CASSCF Hamiltonian in the active space, and to the zeroth order Møller-Plesset one in the inactive and virtual spaces. Without going into much details, this formulation offers several advantages over CASPT2, noticeably a strict size-consistency and the absence of the so-called intruder states(vi).

Dynamic correlation can also be incorporated by the means of a CI development on the basis of the CASSCF wavefunctions. As one may infer, the complexity of such calculations is higher than that of a Hartree-Fock based CI. Yet, many approximations have been proposed that allow a practical implementation of such methods. Noticeably, it can be shown that most of the excitations included in the CI development are irrespective of the spin state.[24,25] Said otherwise, if one is interested only in the energy difference between, let's say, the singlets and the triplets states - for instance while evaluating a magnetic coupling between two copper(II) ions -, most of the matrix elements of equation (1.15) do not need to be evaluated, because they will be shared by all the states. The only excitations that actually need to be calculated are the $1h$, $1p$, $1h1p$, $2h$, $2p$, $2h1p$ and $1h2p$, following the usual terminology, as shown in Figure 1.2.2.
This leads to a tremendous alleviation of the computation task, and such calculation become feasible for relatively large systems. This approach is called "Difference Dedicated CI", DDCI, also called DDCI-3 (3 refers to the number of degree of freedom, *i.e.* the maximum order of the allowed excitations).[26] Further simplifications are also implemented,

---

(v) And one can verify that $21 \times 6 + 224 \times 4 + 490 \times 2 = 2002$.

(vi) Which are singly and doubly excited states that display a quasidegenerate energy with the reference states.[23]

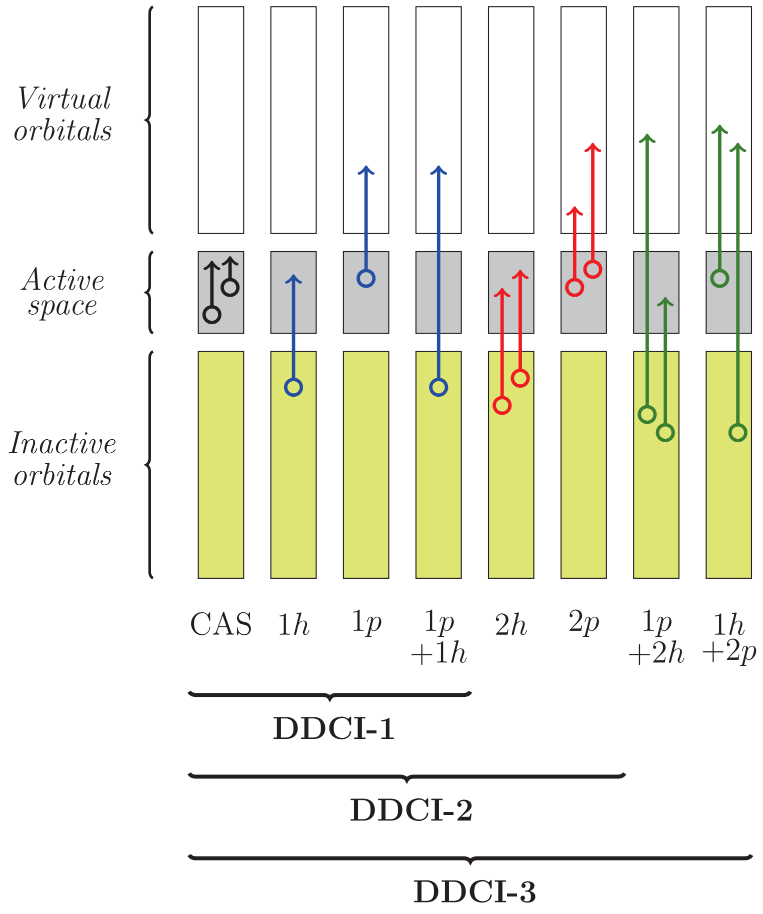

FIGURE 1.2.2: Schematic representation of the different excitations included in the DDCI-n calculations.

named DDCI-2 (only single and double excitations) and DDCI-1 (only single excitations).

1.3 Density Functional theory

1.3.1 Why resorting to density?

In the previous section, we were interested in solving the Schrödinger equation in terms of wavefunctions and energy. For the ground state, the problem reduces to the minimisation of $E[\Psi]$ with respect to Ψ, *i.e.* the minimisation of a functional of Ψ. The solution E is uniquely determined by the form of the functional, which is itself uniquely determined by the Hamiltonian.[27]
In Density Functional Theory (DFT), the energy is expressed as a functional of the electron density, which can be written as

$$\rho(\mathbf{r}) = N \int \dots \int |\Psi(\mathbf{r_1}, \mathbf{s_1}, \mathbf{r_2}, \mathbf{s_2} \dots \mathbf{r_N}, \mathbf{s_N})|^2 d\mathbf{s}_1 d\mathbf{r}_2 d\mathbf{s}_2 \dots d\mathbf{r}_N d\mathbf{s}_N \tag{1.36}$$

rather than the wavefunctions.[1] The goal is multiple: first, the electron density is a quantum observable, and direct comparisons can be made with experiments - for instance using X-Ray diffraction or Polarised Neutron Diffraction.[28] Furthermore, the wavefunction is a complicated function of $4N$ variables for a molecule of N electrons (3 spatial coordinates per electron, plus the spin momentum), in general complex. On the other hand, the electron density is a real function of 3 coordinates only (4 with the inclusion of spin). Direct interpretations based on the electron density may thus be considered, while they remain rather unlikely basing on wavefunctions.

In the following, we will present the two founding theorems of DFT, which prove it is possible to express the energy as a functional of electron density. We will also show how DFT is implemented in practice, and the associated limitations with each formulation.

1.3.2 The Hohenberg-Kohn theorems

The first Hohenberg-Kohn theorem[29–31] provides the proof that energy can be written as a unique functional of the electron density, which is a necessary condition to be fulfilled if we want to reformulate the Schrödinger equation in a framework of electron density. More precisely, it states:

HK-Theorem 1. *The external potential $v(\mathbf{r})$ is determined, within a trivial additive constant, by the electron density $\rho(\mathbf{r})$.*

Since in equation (1.3) the only system-dependant term is the external (nuclei-electrons) potential, as a consequence from this theorem we find that the Hamiltonian is uniquely determined by the electron density. The energy of the system is then directly determined by $\rho(\mathbf{r})$. The proof of this theorem is very simple and elegant, and we thus felt it could be presented here.

Proof. Let's consider two chemical systems $\mathcal{S}_1$ and $\mathcal{S}_2$, which only differ by their external potential (hence their structure), $v_1(\mathbf{r})$ and $v_2(\mathbf{r})$. They are thus described by two different Hamiltonians $\mathcal{H}_1$ and $\mathcal{H}_2$. The ground state (non-degenerate) solutions of the Schrödinger equations for these two systems are (E_1, Ψ_1) and (E_2, Ψ_2). We will assume $\mathcal{S}_1$ and $\mathcal{S}_2$ are described by the same electron density. If we use Ψ_1 as a trial function for $\mathcal{H}_2$, by the variational principle it comes that

$$E_2 < \langle \Psi_1 | \mathcal{H}_2 | \Psi_1 \rangle \tag{1.37}$$

and similarly

$$E_1 < \langle \Psi_2 | \mathcal{H}_1 | \Psi_2 \rangle. \tag{1.38}$$

We can re-write equations (1.37):

$$E_2 < \langle \Psi_1 | \mathcal{H}_1 | \Psi_1 \rangle + \langle \Psi_1 | \mathcal{H}_2 - \mathcal{H}_1 | \Psi_1 \rangle \tag{1.39}$$

$$E_2 < E_1 + \int \rho(\mathbf{r}) \left(V_2(\mathbf{r}) - V_1(\mathbf{r}) \right) d\mathbf{r} \tag{1.40}$$

and (1.38):

$$E_1 < E_2 - \int \rho(\mathbf{r}) \left(V_2(\mathbf{r}) - V_1(\mathbf{r}) \right) d\mathbf{r} \tag{1.41}$$

which directly lead to:

$$E_1 + E_2 < E_2 + E_1. \tag{1.42}$$

This is clearly impossible, hence $\mathcal{S}_1$ and $\mathcal{S}_2$ cannot be described by the same electron density if $v_1(\mathbf{r}) \neq v_2(\mathbf{r})$ (up to a trivial additive constant). □

The electron density is thus uniquely determined by the external potential, *i.e.* by the structure of the molecule and the eventual external fields. In practice, the first Hohenberg-Kohn theorem is not sufficient because of its non constructive form: it proves E is a unique functional of $\rho(\mathbf{r})$, but we do not know how to compute it. The second theorem provides a variational principle for DFT:

HK-Theorem 2. *For any trial electron density* $\tilde{\rho}(\mathbf{r})$ *that verifies*

$$\tilde{\rho}(\mathbf{r}) \geq 0 \qquad \int \tilde{\rho}(\mathbf{r}) d\mathbf{r} = N$$

we have

$$E_0 \leq E\left[\tilde{\rho}(\mathbf{r})\right] \tag{1.43}$$

where E_0 *is the ground state energy and* $E\left[\tilde{\rho}(\mathbf{r})\right]$ *is the energy density functional, applied to* $\tilde{\rho}(\mathbf{r})$*.*

This implies that DFT is rigorously formulated only for a non degenerate ground state, and that SCF procedures can be applied in order to determine the true ground state density and energy, starting from any well-conditioned guess.

1.3.3 The Kohn-Sham ansatz

Yet, a strong *caveat* exists: DFT is formally an exact theory, provided that we know the *exact form of the energy functional.* In the same way that we can separate the kinetic, electron-electron and electron-nuclei contribution to the Hamiltonian, we can write

$$E[\rho] = T[\rho] + V_{ee}[\rho] + \int \rho(\mathbf{r}) v(\mathbf{r}) d\mathbf{r} \tag{1.44}$$

$$= F_{HK}[\rho] + \int \rho(\mathbf{r}) v(\mathbf{r}) d\mathbf{r} \tag{1.45}$$

with $T[\rho]$ the kinetic energy functional, $V_{ee}[\rho]$ the electron-electron repulsion functional and $F_{HK}[\rho]$ the Hohenberg Kohn functional. Since only the external potential is system dependant, $F_{HK}[\rho]$ is also called universal functional.
In order to solve the Schrödinger equation in that case, we thus need to determine the analytical form of the universal functional. The problem is two-fold: we do not know the form of the kinetic part in an electron density representation, and the electron-electron term is also unknown. This last term can be rewritten:

$$V_{ee}[\rho(\mathbf{r})] = \frac{1}{2} \iint \frac{\rho(\mathbf{r_1})\rho(\mathbf{r_2})}{|\mathbf{r_1} - \mathbf{r_2}|} d\mathbf{r_1} d\mathbf{r_2} + E_{nc}[\rho(\mathbf{r})] = J[\rho] + E_{nc}[\rho] \tag{1.46}$$

where $J[\rho]$ represents a classical Coulomb interaction, and $E_{nc}[\rho]$ all the non-classical contributions to V_{ee} (exchange and dynamic correlation).

There are, overall, two terms whose analytical forms are not known. The brilliant idea of Kohn and Sham[32] was to express them as corrections applied to a much simpler system. In their so-called ansatz(vii), they considered a fictitious system of N non-interacting

---

(vii) German word that can be approximately translated as "start, initialisation". It consists of an educated guess to solve a given problem, often being the solution of a simplified equation.

electrons, evolving in an external potential $\mathcal{V}_S$ such that $E_S = E$ and $\rho_S(\mathbf{r}) = \rho(\mathbf{r})$. The system is also such that its electron density can be decomposed over a set of spin-orbitals:

$$\rho(\mathbf{r}) = \sum_{i=1}^{2N} |\phi_i(\mathbf{r})|^2. \tag{1.47}$$

The expression of the kinetic energy of such a system is fairly simple:

$$T_S\left[\rho\right] = -\frac{1}{2}\sum_{i=1}^{2N} \langle\phi_i|\nabla^2|\phi_i\rangle \tag{1.48}$$

and the energy of the fictitious system is simply

$$E_S\left[\rho_S\right] = E\left[\rho\right] = T_S\left[\rho\right] + \int \rho(\mathbf{r})\mathcal{V}_S(\mathbf{r})d\mathbf{r}. \tag{1.49}$$

We may then rewrite equations (2.44) and (2.49) as

$$E\left[\rho\right] = T_S\left[\rho\right] + T\left[\rho\right] - T_S\left[\rho\right] + J\left[\rho\right] + E_{nc}\left[\rho\right] + \int \rho(\mathbf{r})v(\mathbf{r})d\mathbf{r} \tag{1.50}$$

$$= T_S\left[\rho\right] + J\left[\rho\right] + \int \rho(\mathbf{r})v(\mathbf{r})d\mathbf{r} + E_{xc}\left[\rho\right]. \tag{1.51}$$

Every terms in equation (1.51) are known but $E_{xc}\left[\rho\right]$, which is called the exchange-correlation functional. This term, generally small compared to the other contributions, translates the deviation from the fictitious systems, *i.e.* it conveys informations about the correlation and the exchange between the electrons.

The Kohn Sham ansatz might seem to be a simple trick on the equations, but it actually permits the numerical calculation of most contributions to the energy, transforming the problem of solving the Schrödinger equation into finding an appropriate exchange-correlation functional. An important part of research in computational chemistry is dedicated to this task. The next section summarises briefly the different kind of functionals that were proposed, and their relative efficiencies.

1.3.4 The Jacob's ladder and the limits of the model

As we said, thanks to the Kohn-Sham ansatz the resolution of the Schrödinger equation is reduced to the determination of an accurate exchange-correlation functional. Several different forms of functionals were proposed over time, and are usually classified along what Perdew called the "*Jabob's ladder of DFT*", represented on Figure 1.3.1.[33]

The lowest rung of the ladder corresponds to the Local Density Approximation functionals, which are well formulated for a uniform (or slowly varying) electron gaz. They are more efficient for describing solids with a rather high delocalisation of the electron density (conductors), rather than molecules which may present strong local variations of the density - noticeably around the nuclei. As a result, they are more or less unused in the modelisation of molecular systems.

The second rung corresponds to the Generalised Gradient Approximation functionals. Their analytical form involve the electron density and its first derivative, or rather a reduced gradient $\nabla\rho(\mathbf{r})/\rho(\mathbf{r})$ (which prevents any risk of divergence in a gradient expansion). These functionals can yield a very efficient description of molecular systems, noticeably they permit a fairly efficient reproduction of vibrational spectra.

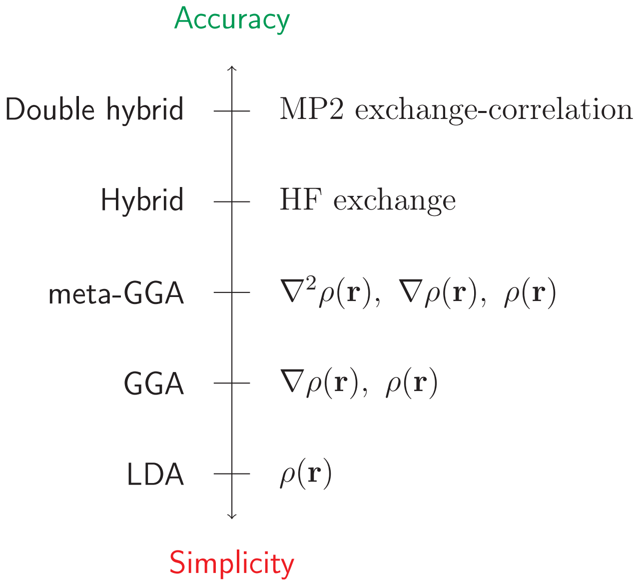

FIGURE 1.3.1: Schematic representation of the Jacob's ladder of DFT.

On the third rung, one finds the meta-GGA, which are based on the electron density, its gradient and its Laplacian. Though in principle more efficient than the GGA, they are not as much employed as the latter. This may be due to the small improvement over computational effort ratio these functional give, as compared to the GGA.[34]

Hybrid functionals, on the fourth rung of the ladder, are on the contrary very popular functionals. They incorporate a certain percentage of Hartree-Fock exchange, along with a GGA exchange/correlation. They tend to be very efficient to describe reaction mechanisms and optical spectra.

Finally, the last rung corresponds to the double hybrids, which incorporate Hartree-Fock exchange and MP2 correlation. They are not much used for the moment, mostly because of the rather prohibitive cost of the calculations.

Nevertheless, we must say that the picture is not as rigid as suggested by the Jacob's ladder, and really depends on the studied systems. Most of functionals are indeed benchmarked to reproduce the properties of some molecular sets (for instance small copper coordination complexes), and there may be cases where GGA work generally better than hybrid functionals.

As a closing remark, DFT is a very efficient theoretical framework, provided that the studied system can be represented efficiently with a single determinant, *i.e.* if static correlation is negligible. Its algorithmic complexity is close to that of a Hartree-Fock calculation (N'^3 to N'^4), with much better results. Actually, DFT calculations yield comparable results to post-Hartree Fock calculations, even very close to CCSD(T). It will be intensively used in this manuscript, noticeably for reactivity studies.

1.3.5 A few words on TDDFT

So far, we discussed the possibility to solve the Schrödinger equation for the ground state only. This is the consequence of the variational principle employed in the first Hohenberg-Kohn theorem. Actually, it also possible to access the low excited states in a density-based formalism, called Time Dependent DFT. As suggested by the name, the excited states are evaluated in a framework of time-dependent perturbations of the ground density. We will not discussed it into details, but rather provide a qualitative framework of understanding,

highly inspired by C. J. Cramer.[8]
Let us consider a molecule whose ground-state density and energy are known. It is placed in an oscillating electrical field

$$\mathbf{E} = \mathbf{r}\cos(\omega t) \tag{1.52}$$

with $\mathbf{r}$ the position operator(viii) and ω the frequency of the field. As underlined by Cramer, the polarisability of the molecule is well approximated by

$$\langle\alpha\rangle = \sum_{i\neq 0}^{P} \frac{|\langle\Psi_0|\mathbf{r}|\Psi_i\rangle|^2}{\omega - (E_i - E_0)} \tag{1.53}$$

where the indices $i = \{1, \ldots, P\}$ are attributed to the different excited states.
It is rather plain from this formula that the polarisability diverges when ω equals any excitation energy. Using a Green's function approach, it is then possible to determine directly the poles of $\langle\alpha\rangle$ without having to compute all the excited states energies and densities, hence it is possible to determine the excitation energies.
It is furthermore possible to access the excited electron densities, thanks to the Runge-Gross theorem.[35] It can be seen as an extension of the first Hohenberg-Kohn theorem, and proves that at any time t during a time-dependent perturbation there is a unique mapping between the external potential and the electron density. Said otherwise, provided we know the form of the perturbation, we can access the electron density at any time, and it will be linked - *via* perturbation theory - to the ground and excited states densities.

1.4 Conceptual DFT, or DFT for Chemical Reactivity

Thanks to Hohenberg-Kohn and Runge-Gross theorems, we know that there is a unique mapping between the electron density at a given time and the wavefunction. This has a direct implication which we did not develop much up to now: the electron density contains as much information on the system as the wavefunction does. In the following, we will restrict ourselves to the ground state. By construction, $\rho(\mathbf{r})$ contains all the measurable information on it, thus implying that the ground state properties can be entirely described using electron density.[30]
This is the cornerstone of Conceptual DFT.[36,37] In CDFT, one is indeed interested in describing the properties of a given system using electron density-based descriptors, defined in first principles. The first reported one is the chemical potential μ. Already present in Hohenberg and Kohn original paper,[29] it is defined as the first derivative of energy with respect to the number of electrons in the system:

$$\mu = \left(\frac{\partial E}{\partial N}\right)_{v(\mathbf{r})}. \tag{1.54}$$

Physically, this descriptor translates the stabilisation or destabilisation a molecule endures when the number of electrons is varying at a constant geometry, *i.e.* the tendency to give away or hold back electron density. μ is then closely related to the concept of electronegativity, and using a very simple line of argument Parr showed that μ is actually the opposite of χ.[30,38]

(viii)Note this form of $\mathbf{E}$ seems less arbitrary once it is recognised that an electrical field has the same symmetry properties as the position operator.

The consequences were enormous: for the first time since the concept was introduced in chemistry, it was possible to unequivocally define electronegativity, noteworthy for molecules or fragments of molecules, and not only for atoms and ions. Furthermore, it appears μ is negative for stable systems, and as such E is a decreasing function of N.

If we take the second order derivative with respect to N, we introduce another descriptor η that is linked to the concavity of the energy. η translates the variations of the energy stabilisation consequent to a change in the number of electrons: the bigger η, the more quickly μ varies with N. This descriptor is actually defining hardness in the sense of Pearson's Hards and Soft Acids and Bases theory.[39] Indeed, high values of η are going to be associated to systems unlikely to vary much their number of electrons (sharp evolution of μ with N), thus species that will not interact in a covalent but rather ionic way (no sharing of electron density), as hard species do. Low η values on the other hand will characterise systems that may accept a rather large variation of their number of electrons, thus soft species.

These two descriptors (and all the successive N-derivatives of E) are global descriptors, in the sense that they apply to the whole molecule. Taking derivatives with respect to the other natural variable, $v(\mathbf{r})$, allows to introduce locality - and even non-locality at high orders. The first derivative is simply the electron density,

$$\left(\frac{\delta E\left[\rho\right]}{\delta v(\mathbf{r})}\right)_N = \rho(\mathbf{r}) \tag{1.55}$$

where δ indicate functional derivatives. Taking then the N derivative of $\rho(\mathbf{r})$ introduces

$$f(\mathbf{r}) = \left(\frac{\partial\rho(\mathbf{r})}{\partial N}\right)_{v(\mathbf{r})} = \left(\frac{\delta\mu}{\delta v(\mathbf{r})}\right)_N \tag{1.56}$$

which translates the variations of electron density upon an electron uptake or release. In a frontier orbital framework (FMO), this descriptor will thus be related to the HOMO and LUMO orbitals densities, hence explaining the name of Fukui fonction.[40] The second-order N derivative of $\rho(\mathbf{r})$ is even more interesting:

$$\Delta f(\mathbf{r}) = \left(\frac{\partial^2\rho(\mathbf{r})}{\partial N^2}\right)_{v(\mathbf{r})} \tag{1.57}$$

called the Dual Descriptor (DD), conveys similar information on the reactivity as the Fukui function, without presenting its principal flaw.[41] It is indeed well-defined, while the left $f^-(\mathbf{r})$ and right $f^+(\mathbf{r})$ derivatives associated to $f(\mathbf{r})$ are not identical. Actually, it can be shown that the DD approximates to the difference of both Fukui functions, and in a FMO framework

$$\Delta f(\mathbf{r}) \approx f^+(\mathbf{r}) - f^-(\mathbf{r}) \approx \rho_{LUMO}(\mathbf{r}) - \rho_{HOMO}(\mathbf{r}). \tag{1.58}$$

From this last expression, it becomes rather plain that the DD is a reactivity and selectivity descriptor: regions associated to a negative value of the DD are prone to cede electron density, *i.e.* are nucleophilic, while positive values are associated to electrophilicity.

In Chapter 4, we will propose a new formulation for this descriptor, and extensively use it to rationalise the chemical properties of ligands and complexes.

1.5 Basis sets and relativistic corrections

1.5.1 Basis sets

In the previous sections, we detailed the theoretical formulation of different methods of quantum chemistry, setting aside the practical details of the calculations.

As we have seen, bases of orbitals are used in the computations, and they are generally devised to reproduce atomic orbitals, whose combination will yield molecular orbitals. They usually consist in sets of functions, which are called basis sets. There are of two types: the Slater-type orbitals (STO), and Gaussian-type orbitals (GTO).[8,9]

The STO decay exponentially with the distance to the nucleus, and yield a very efficient representation of the electron density behaviour in the vicinity of nuclei (cusp). GTO, on the other hand, do not present this cusp because of their Gaussian form. However, linear combination of Gaussian functions can approximate efficiently this cusp. They also offer the advantage that products and convolution products of Gaussian functions are Gaussian functions, hence they permit a strong speed-up in computations compared to STO.

In this work, we used either STO – calculations with the Amsterdam Density Functional program – and GTO basis sets – calculations with Gaussian09 and ORCA –. These basis sets were split-valence ones, which means the valence electrons are modelled with more functions than the core ones. 6-311++G(2d) is an example of such basis sets: the core electrons are represented by 6 primitive Gaussian functions, while the valence electrons are represented by 3 different bases of functions. The first one is a linear combination of 3 primitive Gaussian functions, while the second and third are unique primitive. The "++" label indicates that additional functions are incorporated to all atoms to model more efficiently the density far away from the nucleus, and are called diffuse functions. The suffix "(2d)" indicates that two *d*-type polarisation functions are also added to non-H atoms, in order to allow the atomic orbitals to distort, in a way that recalls the hybridisation theory.

A further step in the previous idea can be taken: for elements with a large N, core electrons are not going to have a large influence on most of the physical properties, and they may be modelled at a relatively low level without impacting the accuracy. Eventually, they may not be treated explicitly and be replaced by a local potential acting on the valence electrons: this is the pseudo-potential approach. In this work, we used principally the Stuttgart-Dresden (SDD) pseudopotential for heavy atoms (metal cations).[9]

1.5.2 Relativistic corrections

Scalar relativistic corrections. We will end this chapter by underlining an implicit hypothesis was used throughout these sections. Here, we assumed the electrons were quasi-classical particles, in the sense that no relativistic effect was explicitly taken into account. When dealing with heavy elements, like late transition metals and lanthanides, this is far from being true.

One thus needs to reformulate the Schrödinger equation in a relativistic frame. Generally, this is achieved using the Dirac equation

$$\mathcal{H}_D \Psi = E_D \Psi \tag{1.59}$$

with

$$\mathcal{H}_D = \begin{pmatrix} \mathcal{E}_{UU} + c^2 & \mathcal{O}_{UL} \\ \mathcal{O}_{UL} & \mathcal{E}_{LL} - c^2 \end{pmatrix} \tag{1.60}$$

where the matrix elements are 2×2 matrices themselves.[42] This approach is not without problems, since the Dirac Hamiltonian presents two continua of states, above $+c^2$ and below $-c^2$. This means that bound states are found only between these two limit values, which are the only states that may interest us.

The solutions of the Dirac equation are 4-dimension vectors, which can be separated in two 2-dimensions vectors ψ and χ, respectively called the large and small components and associated to the 2×2 matrices in $\mathcal{H}_D$. The only solutions that interest us are the large components, being the only solutions related to the bound states. Two formulations were proposed to obtain them only.

The first one is the Zeroth Order Regular Approximation (ZORA).[43] Without going too deep into the algebra, it is based on a series expansion of the large-component terms of $\mathcal{H}_D$, truncated at the zeroth order. It already contains the so-called "scalar relativistic corrections" to the Schrödinger equation, and proved to yield a relatively efficient description of atoms and molecules.

The second correction is the Douglas-Kroll-Hess approximation.[44] In that case, the Hamiltonian is not simplified but block-diagonalised, in order to decouple the large and small components. To do so, a series of unitary transformations are applied on $\mathcal{H}_D$, which progressively remove the non-diagonal terms. Formally, the derivation is exact if the expansion is infinite, but it was shown that the approximation is already efficient at low orders.

In the following, we will mostly be using the second-order DKH approximation for lanthanide ions, and we will not directly evaluate relativistic effects for transition metals. In that latter case, the use of small-core pseudopotential actually provides an already efficient description, thus eluding the need to explicitly compute relativistic corrections.[45]

Spin-orbit coupling Aside from the scalar corrections, relativistic effects also have an impact on the kinetic momenta of atoms and molecules. Noticeably, in general spin and orbit moments are no longer decoupled: this is the so called spin-orbit coupling, which can be represented by the following Hamiltonian:[4,46]

$$\mathcal{H}_{so} = \lambda \hat{L} \cdot \hat{S} \tag{1.61}$$

with $\hat{L}$ and $\hat{S}$ the spin and orbit moment operators.

While it may be safely ignored for light transition elements, this effect becomes very strong for lanthanide ions. For instance, a Dy^{3+} ion with a $4f^9$ valence electronic configuration cannot be simply described as a ground $S = 5/2$ spin state, because S is no longer an appropriate quantum number.[21] The correct quantum number becomes the total momentum $|L - S| \leq J \leq L + S$, and in that case the ground state is finally ${}^6H_{15/2}$, thus with $J = 15/2$.

In order to model correctly the properties of lanthanide ions (and late transition metals), one thus needs to take this effect into account during the calculations. Here, we will principally consider it for the lanthanide ions. It will thus be computed on top of the DKH/SA-CASSCF (PT2) calculations through the Restricted Active Space State Interaction Spin-Orbit (RASSI-SO) procedure, which evaluates the spin-orbit coupling between all the calculated states.[47,48]

1.6 Long story short...

In the following, we will use the different levels of theory according to the studied system, trying to use the most adequate framework whenever possible. More specifically, when we will be dealing with reactivity, we will principally use tools from DFT and conceptual DFT, because of both their simplicity and conceptual strength. Nevertheless, because of the single-determinant nature of DFT methods, whenever ground state degeneracy will be found we will have to use post-Hartree Fock methods. An example will be provided in Chapter 3.

When dealing with magnetic properties, because of the needed accuracy (around the tenth of cm^{-1} in the case of the weakly coupled trinuclear complex of Chapter 4), we will focus solely on post-Hartree Fock methods. In the case of the lanthanide complexes of Chapter 5, as previously said we will principally use SA-CASSCF-based methods, while for the complexes of Chapter 4 DDCI and NEVPT2 methods appear to be the most appropriate.

Chapter 2

Elements of coordination chemistry and molecular magnetism

To the beginner, chemistry is often seen as a world of bright colours. Many of them are due to transition metal complexes, like the well-known royal blue $[Cu(NH_3)_4]^{2+}$ complex. A coordination complex, or coordination compound, is made of one or several metal cations, bonded to inorganic or organic ions or molecules called ligands.[49]
As we will recall in the following sections, properties of coordination compounds are intimately related to their molecular and electronic structures. A special mention will be given to molecular magnetism, whose scope is not restricted to coordination chemistry but which flourished within it.

2.1 From Werner's work to the ligand field theory

2.1.1 First studies of octahedral complexes

The middle and end of the nineteenth century have witnessed the development of what could be called "structural chemistry", whose aim was to describe the molecular structure of compounds. Chemists indeed realised that different compounds could be described by the same total formula, although their properties were completely different. Among them, two classes of compounds were found: organic molecules on one hand, and complexes on the other.
Thanks to the work of, noticeably, Van't Hoff and Le Bel,[50] the problem could be partially solved for organic molecules by supposing saturated carbon atoms tend to be tetrahedral. This permitted noteworthy to understand why some molecules, with the same "scalar" properties - melting point, *et caetera* - could show either a positive or negative deviation of polarised light: at molecular formula, different backbones of atoms in space will be associated to different compounds.
Using the same line of arguments, others tried to solve the problem for coordination compounds – with great difficulty, as suggested by the adjective "complex" –. Alfred Werner studied intensively cobalt(III) complexes. With a fantastic intuition, he supposed the metal cation in these structures had a central role, being used as a scaffold by the ligands.[51] Extending the idea of Le Bel and Van't Hoff, he supposed it would similarly be located on the center of a regular polyhedron – here, an octahedron – and the ligands would be located on the vertices. Isomerism would then be due to differences in the sequence of ligands on the vertices. For this theory, which has been proved afterwards by X-ray diffraction experiments, Alfred Werner received the Nobel Prize for Chemistry in

1913.[52]

2.1.2 Crystal field theory

Werner's theory permitted to link differences in properties to differences in geometry for coordination complexes, but it did not allow to understand why, fundamentally, the properties were different. Neither could it explain why the octahedral(i) symmetry was obtained.

Explanation was provided with the advent of quantum chemistry. The first model to be proposed was the Crystal Field theory, hereafter abbreviated CF.[53,54] The idea is the following: the energy levels of the complex, which will ultimately determine the properties, can be deduced from those of the free ion, undergoing a perturbation due to the ligands. This perturbation was initially described as a Stark effect: ligands act essentially in an electrostatic manner, lifting the degeneracy of the metal energy levels, but also of its d or f AOs.

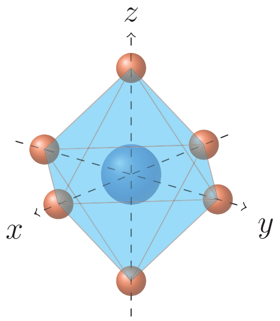

Figure 2.1.1: Schematic representation of an octahedral complex. The metal cation is represented by the blue sphere, while the red spheres represent the ligands.

Let us consider the example of an octahedral complex, pictured on Figure 2.1.1. In the case of a transition metal, the relevant valence orbitals to consider are the d metal AOs: d_{xy}, d_{yz}, d_{xz}, $d_{x^2-y^2}$ and d_{z^2}. These AOs will shift in energy because of the electrostatic field induced by the ligands. On a first crude approximation, the field can be considered isotropic; as a consequence, all AOs are equally destabilised ("spherical field" situation on Scheme 2.1.1). If we now set the ligands on their actual positions in the complex, the $d_{x^2-y^2}$ and d_{z^2} AOs are further destabilised. They indeed point directly towards the ligands, and thus electrons in these AOs will strongly interact with the ligands field. On the other hand, the d_{xy}, d_{yz} and d_{xz} AOs present nodes on the ligands positions. They will not be destabilised, and if the ligands field is set to have the same magnitude as the isotropic one, they will even be slightly stabilised, because of a barycentre rule.

The same construction can be applied to lanthanide (and actinide) ions. In that case, the relevant valence AOs are the $4f$ (and $5f$) orbitals. They are represented on Figure 2.1.2, and the expected energy splitting in an octahedral field is given on Scheme 2.1.2. The peculiar energy splittings obtained in the CF model permit to account for many properties of coordination complexes, depending on their symmetry. Noteworthy, using only symmetry arguments one can already find out that the d orbitals will be splitted in two subsets in an octahedral field: the irreducible representations (RI) of the quadratic

---

(i) Actually, we know now that other symmetries can be obtained, such as tetrahedral, square-based pyramidal...

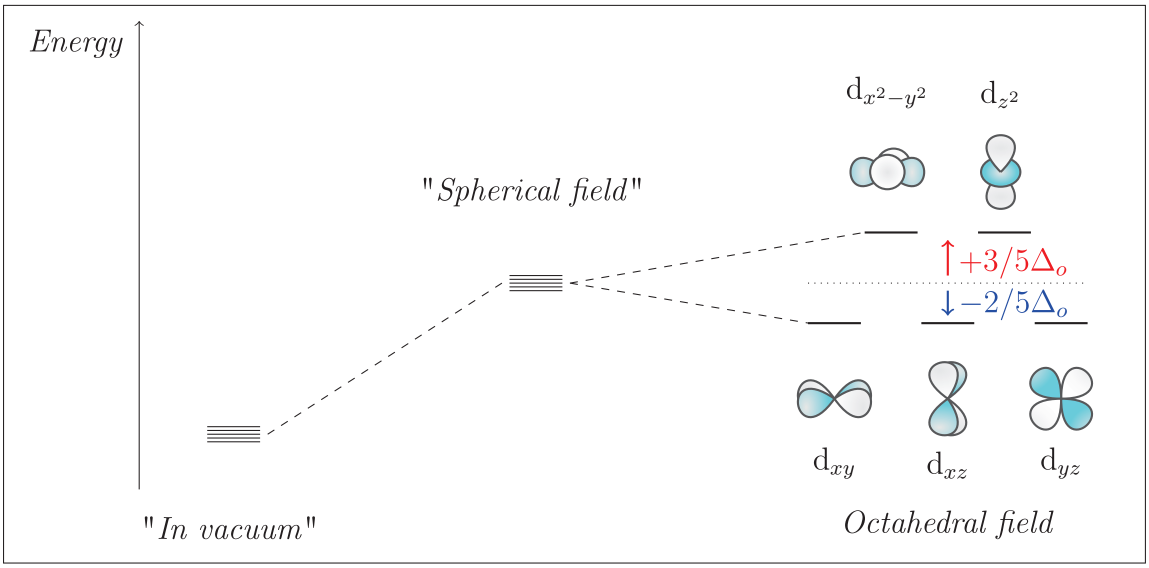

SCHEME 2.1.1: Energy diagram focusing on the d metal AO in an octahedral field. Δ_o represents the total energy splitting between the lowest and highest AOs.

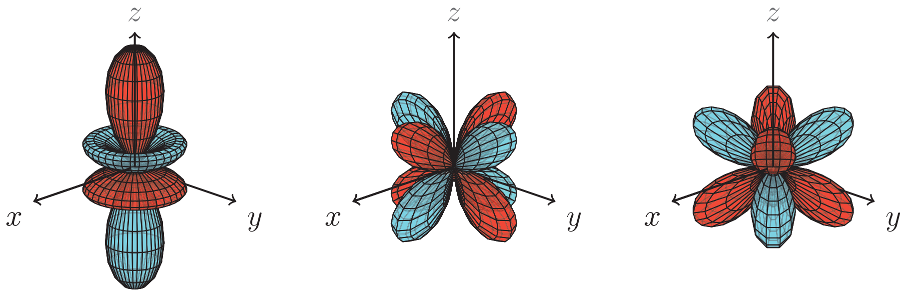

FIGURE 2.1.2: Schematic representation of the f orbitals, from top left to bottom right: f_{z^3}, $f_{z(x^2-y^2)}$ and f_{xyz}. The f_{x^3} and f_{y^3} can be deduced from the f_{z^3} AO by an appropriate rotation of the frame. The same is true for the $f_{y(x^2-z^2)}$ and $f_{x(y^2-z^2)}$, from the $f_{z(x^2-y^2)}$.

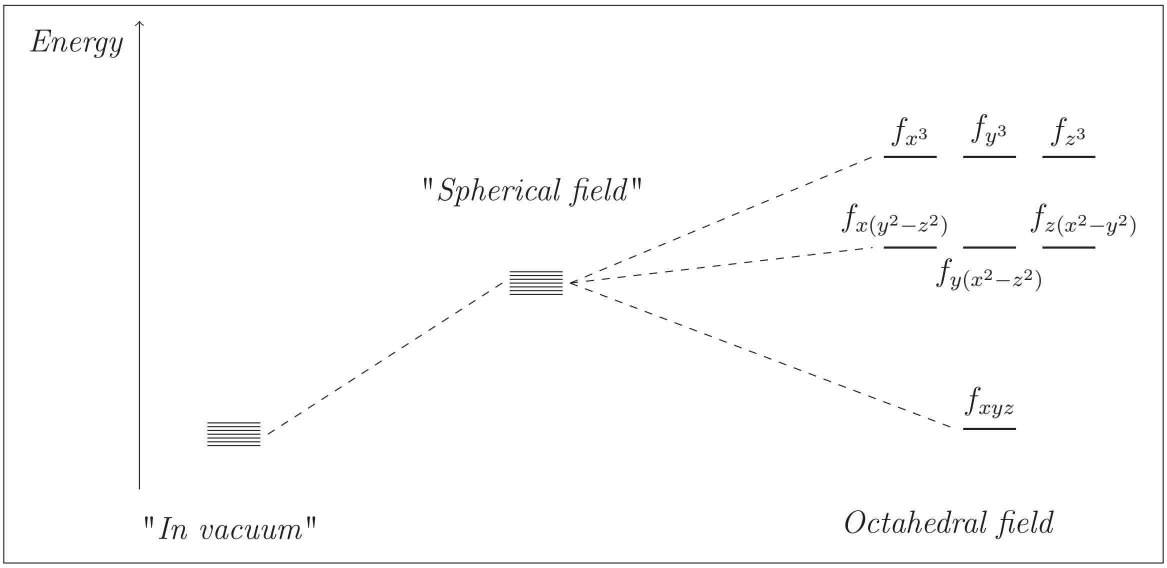

SCHEME 2.1.2: Energy diagram focusing on the f metal AO in an octahedral field.

operators $x^2 - y^2$, z^2, xy, xz and yz operators in the O_h point group are, respectively, E_g (twice-degenerate) and T_{2g} (three-times degenerate).[55] They should thus be found at different energies, even though we may not precise which set of orbitals will be destabilised. Similarly, in the same point group the third-order operators (related to the f orbitals) are represented by the T_{1u} (three-times degenerate), T_{2u} (three-times degenerate) and A_{2u} RI.[56] This point highlights the importance of symmetry. The properties of the complexes will be linked to their energy patterns, which are directly due to the symmetry of the complexes. This is actually Curie's principle: "When some causes induce some effects, the symmetry elements of the causes are necessarily found in the effects." (ii)

One of the great successes of this model is that it explains why many transition metal complexes are coloured: electronic transitions can occur within the d AOs, and fall in the visible range. It also permits to understand why, for instance, some Fe(II) complexes are magnetic and some others not: depending on the splitting between the lowest and highest orbitals, the six d electrons of Fe(II) will tend to pair in the three lowest orbitals (low spin state) or on the contrary to locate in all the accessible AOs (high spin state).

2.1.3 Ligand field theory

Yet, the CF model involves parameters that cannot be derived from a purely theoretical point of view, and as such raises many questions. Noticeably, how can we quantify the energy splitting? And why are some complexes more coloured than others?

These two questions can actually be answered if we now consider covalent effects in the metal-ligand interaction.[58] This is what is achieved by the successor of the crystal field theory, the so-called ligand field theory, which is built in the framework of the Molecular Orbitals (MO) theory. The basic idea in that case is to draw the whole MO diagram of the complexes, thus involving explicitly the ligands in the construction. Interestingly, the splitting pattern of the d orbitals is very similar in the two models. As such, and since it can be found in any advanced inorganic chemistry textbook,[51,54] we will not develop it here, but we may emphasise two points.

First, thanks to this approach it is now possible to quantify the energy splitting but also to understand why some complexes present more intense electronic transitions than others. In the CF model, the only possible transitions are $d \rightarrow d$ electron transitions. Using symmetry argument, we can indeed see that these transitions are forbidden: the representation product corresponding to the dipole transition moment (DTM) does not contain the all-symmetric representation Γ_0,[59,60]

$$(\Gamma_{DTM} = \Gamma_d \otimes \Gamma_{\vec{r}} \otimes \Gamma_d) \not\supset \Gamma_0. \tag{2.1}$$

For instance, if we consider a d^1 ion in an octahedral field, the ground state will have a T_{2g} symmetry. Formally, d-d excitations will consist in the promotion of the electron from a t_{2g} orbital to a e_g orbital, which implies d-d excited states will have a E_g symmetry. The dipole moment, on the other hand, transforms as the translation operators, and in the O_h point group it is thus represented by the T_{1u} irreducible representation. The symmetry representation of the transition dipole moment will thus be the product $\Gamma = T_{2g} \otimes T_{1u} \otimes E_g$. From the character table of the O_h point group:

(ii) "*Lorsque certains causes produisent certains effets, les éléments de symétrie des causes doivent se retrouver dans les effets produits.*"[57].

E	$8C_3$	$6C_2$	$6C_4$	$3C_2$	i	$6S_4$	$8S_6$	$3\sigma_h$	$6\sigma_d$	
3	0	-1	1	-1	-3	-1	0	1	1	T_{1u}
3	0	1	-1	-1	3	-1	0	-1	1	T_{2g}
2	-1	0	0	2	2	0	-1	2	0	E_g
18	0	0	0	2	-18	0	0	-2	0	Γ

it comes rather directly that Γ does not contain the all-symmetric representation (denoted A_{1g} in O_h). The number of occurrence of A_{1g} in Γ is indeed

$$a(A_{1g}) = \frac{1}{48}(1 \times 18 + 0 + 0 + 0 + 2 \times 6 - 18 \times 1 + 0 + 0 - 2 \times 3 + 0) = 0. \tag{2.2}$$

By taking the ligands orbitals explicitly in the ligand field model, we allow a mixing of the d metal AOs and the σ, p or π type ligands orbitals. As such, the representation product in equation (2.1) is modified and may now involve Γ_0: the selection rule is lifted. Furthermore, using the same symmetry arguments, it appears that other transitions are now feasible, from or to ligands orbitals, to or from metal orbitals. One speaks of Ligand to Metal or Metal to Ligand Charge Transfer (LMCT/MLCT). The selection rule in these cases is even less strictly observed, and the corresponding transitions are even more intense (extinction coefficient $\epsilon \sim 10^2 - 10^6$ L.mol^{-1}.cm^{-1}, compared to the $\epsilon \sim 10^0 - 10^2$ L.mol^{-1}.cm^{-1} of d-d transitions).[51]

Second, these charge transfer effects can actually be more generally described as electron density transfers from one part of the complex to another. Through this subtlety, we can generalise the previous concepts in non-MO frameworks.

2.1.4 The metal-ligands interaction and the Klopman-Salem model

Actually, this whole section can be generalised in a non-MO framework. The CF model can indeed be seen as a focus on the electrostatic contribution to the total metal-ligands interactions. The ligand field theory on the other hand retrieves the covalent – or density relaxation – contribution to the interaction. Conceptually, we fall back onto an extended Klopman-Salem model for the coordination complexes.[61,62] (iii)

Generally, transition metals will tend to interact in a covalent way with ligands, *i.e.* they tend to act as soft acids (in the sense of the Parr-Pearson HSAB theory).[39] This of course becomes less true when their oxidation degree is high, high charges leading the electrostatic interaction to prevail. Similarly, lanthanide ions will tend to act as hard acids, interacting principally in an electrostatic manner with the ligands.[21] This is due to the small spatial extent of the $4f$ orbitals, which explains why lanthanide cations present very similar reactivities – they all almost act as 3+ point charges – . In the following chapters, we will principally use these lines of arguments (rather than CF or ligand field analyses). Noticeably, Chapter 4 is dedicated to revisiting coordination chemistry through conceptual DFT.

(iii) We indeed remind that, in this model, the energy of interaction between two molecules is expressed in separated contributions, depending on their electrostatic (charge-charge, solvent shell reorganisation) or covalent (orbital overlap) nature.

2.2 Molecular magnetism

2.2.1 Diamagnetism, paramagnetism and related properties

Every substance reacts to the application of a magnetic field $\vec{H}$ by an induced magnetic moment $\vec{m}$. This reaction can essentially be of two kinds: either the sample repels the magnetic field lines, hence $\vec{m}$ opposes — at least partially — $\vec{H}$, or it concentrates them, hence $\vec{m}$ and $\vec{H}$ point in the same direction.[63] The first situation is referred to as diamagnetism. It is a microscopic analogue of the Lenz' law of electrodynamics, due to the electron motion. The electronic cloud around a nucleus can indeed be seen as a current loop (orbital momentum of the electrons), which will react to the application of the magnetic field through an additional current i that opposes the perturbation. It is a general property of matter, in the sense that the only condition for a sample to present diamagnetism is to bear electrons.

The second situation is referred to as paramagnetism. It is only encountered in open-shell structures such as radicals, transition metals and rare earth ions, and is due to the non zero angular momentum of electrons.

It is possible to define a quantity that links the induced magnetisation to the applied magnetic field:[64]

$$\bar{\bar{\chi}} = \frac{d\vec{m}}{d\vec{H}} = \begin{pmatrix} \chi_{xx} & \chi_{xy} & \chi_{xz} \\ \chi_{xy} & \chi_{yy} & \chi_{yz} \\ \chi_{xz} & \chi_{yz} & \chi_{zz} \end{pmatrix} \tag{2.3}$$

called the magnetic susceptibility. Formally, it is a second-rank tensor, which we assume to be symmetric. It is always possible to diagonalise such tensor[(iv)]

$$\bar{\bar{\chi}} = \begin{pmatrix} \chi_u & 0 & 0 \\ 0 & \chi_v & 0 \\ 0 & 0 & \chi_w \end{pmatrix} \tag{2.4}$$

where the eigenvectors $\vec{u}$, $\vec{v}$ and $\vec{w}$ are called the magnetic axes. If the three components of the diagonal tensor are equal, then the magnetic susceptibility is simply a scalar, and the magnetism is said to be isotropic. In the following, we will assume this is the case, else stated otherwise. We will also assume the magnetic field is small, in which case the magnetisation evolves linearly with field:

$$\vec{m} = \chi\vec{H}. \tag{2.5}$$

Generally, χ is the sum of a diamagnetic ($\chi^D < 0$) and paramagnetic ($\chi^P > 0$) term

$$\chi = \chi^D + \chi^P. \tag{2.6}$$

Often, the paramagnetic susceptibility is much stronger than the diamagnetic one, which furthermore tends to be temperature independent. It can also be quite correctly reproduced from tabulated data, the so-called Pascal tables.[65] Since we are interested in the paramagnetic component of susceptibility, we can simply withdraw from the measured susceptibility the diamagnetic (tabulated) component, $\chi^P = \chi - \chi^D$. For the sake of simplicity, in the following we will use the term "susceptibility" in the sense of paramagnetic susceptibility.

[(iv)] Provided naturally that its determinant is not zero, which will be the case here.

2.2.2 The van Vleck equation

As we said, the paramagnetic susceptibility is the consequence of the interaction of the angular momentum of unpaired electrons with a magnetic field. We also know from quantum mechanics that to each energy level E_i of the system will be associated a specific total angular momentum J_i, hence a specific magnetisation m_i.[1] It can be expressed as

$$m_i = -\frac{\partial E_i}{\partial H} \tag{2.7}$$

with E_i the energy of level i.
Overall, the molar magnetisation will be the resultant of the levels contribution, weighted by their population:[66]

$$M = N_A \frac{\sum_i m_i \exp\left(\frac{-E_i}{k_B T}\right)}{\sum_i \exp\left(\frac{-E_i}{k_B T}\right)}. \tag{2.8}$$

Van Vleck suggested an approximation of this formula, based on a series expansion of the energy with respect to H:(v) [68,69]

$$E_i = \sum_{k=0}^{\infty} E_i^{(k)} H^k = E_i^{(0)} + E_i^{(1)} H + E_i^{(2)} H^2 + \dots \tag{2.9}$$

The levels magnetisation is thus straightforwardly

$$m_i = \sum_{k=1}^{\infty} -k E_i^{(k)} H^{k-1} = -E_i^{(1)} - 2E_i^{(2)} H + \dots \tag{2.10}$$

If the field is small enough, the energy expansion can be safely truncated at the first order. Furthermore, the exponential can be expanded as a Taylor series:

$$\exp\left(\frac{-E_i}{k_B T}\right) \approx \exp\left(\frac{-E_i^{(0)}}{k_B T}\right)\left(1 - \frac{E_i^{(1)} H}{k_B T}\right). \tag{2.11}$$

Hence we have

$$M = N_A \frac{\sum_i -E_i^{(1)} \exp\left(\frac{-E_i^{(0)}}{k_B T}\right)\left(1 - \frac{E_i^{(1)} H}{k_B T}\right)}{\sum_i \exp\left(\frac{-E_i^{(0)}}{k_B T}\right)\left(1 - \frac{E_i^{(1)} H}{k_B T}\right)}. \tag{2.12}$$

If the magnetisation is zero when the field is turned off, we get:

$$\sum_i -E_i^{(1)} \exp\left(\frac{-E_i^{(0)}}{k_B T}\right) = 0 \tag{2.13}$$

thus

$$M = \frac{N_A H}{k_B T} \frac{\sum_i (E_i^{(1)})^2 \exp\left(\frac{-E_i^{(0)}}{k_B T}\right)}{\sum_i \exp\left(\frac{-E_i^{(0)}}{k_B T}\right)}. \tag{2.14}$$

(v) Note that this corresponds to an expansion in Zeeman's kth order effects.[67]

Equation 2.14 is called the Van Vleck equation (truncated at the first order). As one can already infer, it provides a direct link between the measured magnetisation and the quantum levels of the system under study. It is thus possible to deduce an energy diagram from magnetic measurements, or on the contrary to compute magnetisation from an energy diagram.

In the following subsection, we will show how this can be achieved for the transition metals and lanthanide complexes that will be presented in this manuscript. It is largely inspired from Olivier Kahn's (land marking) book, and the reader is referred to it for any further details.[64]

2.2.3 Magnetism of coordination complexes: basic principles

As we briefly evoked in the previous section, the Hamiltonian that describes the interaction of a given system with a magnetic field is the Zeeman Hamiltonian:

$$\mathcal{H}_{ZE} = \mu_B \sum_{i=1}^{N} \left(\vec{L}_i + g_e \vec{S}_i \right) \cdot \vec{H} \tag{2.15}$$

with $\vec{L}_i$ and $\vec{S}_i$ the orbital and spin momenta of electron i, and g_e the gyromagnetic factor of the free electron.

Provided that the zero-energy spectrum is known, one simply needs to compute the Zeeman Hamiltonian energy spectrum in order to determine the magnetic properties of the system.

Isotropic case

Let us first consider the case of molecules with a unique magnetic centre and with $\vec{L}_i = \vec{0}$, and no higher-order anisotropy. The Zeeman Hamiltonian in that case reduces to the projection of the total spin along the magnetic field. This actually will be the case for Cu(II) (isotropic $S = 1/2$ ion) and Gd(III) (isotropic $S = 7/2$ ion). Provided that $\vec{H}$ is constant, the energy spectrum of $\mathcal{H}_{ZE}$ is thus simply the energy spectrum of the $\hat{S}_z$ operator, $E_{ZE} = M_S \mu_B H$. It is quite simple to show that, in such cases,

$$\chi = \frac{N_A g^2 \mu_B^2}{3 k_B T} S(S+1) = \frac{\mathcal{C}}{T}. \tag{2.16}$$

This is the Curie Law (with $\mathcal{C}$ the Curie constant).

Lets us now consider the (more interesting) case of a heterodinuclear complex, involving two species A and B such that $S_A \neq S_B$. We will assume these two magnetic centres are isotropically coupled (Heisenberg coupling). As such, the zero-field energies are now given by the following Hamiltonian:

$$\mathcal{H}_{HDVV} = -J \hat{S}_A \cdot \hat{S}_B \tag{2.17}$$

where J is called the magnetic coupling between A and B. Note that $J > 0$ is associated to a ferromagnetic coupling, and $J < 0$ to an antiferromagnetic coupling.(vi) The determination the energy spectrum of $\mathcal{H}_{HDVV}$ was proposed by Heisenberg, Dirac and Van Vleck. Let us consider the total spin $\hat{S} = \hat{S}_A + \hat{S}_B$. From the law of composition of kinetic momenta and commutation rules, it follows that

$$|S_A - S_B| \leq S \leq S_A + S_B \tag{2.18}$$

(vi) If $S_A \neq S_B$, the antiferromagnetic case can also be described as ferrimagnetic.

$$\hat{S}^2 = \hat{S}_A^2 + \hat{S}_B^2 + 2\hat{S}_A\hat{S}_B. \tag{2.19}$$

From equation (2.19), one easily gets that

$$\mathcal{H}_{HDVV} = -\frac{J}{2}\left(\hat{S}^2 - \hat{S}_A^2 - \hat{S}_B^2\right) \tag{2.20}$$

which involve the quadratic spin operators whose eigenvalues are known. The energies can then simply be written as:

$$E(S) = -\frac{J}{2}\left(S(S+1) - S_A(S_A+1) - S_B(S_B+1)\right) \tag{2.21}$$

$$= -\frac{J}{2}S(S+1) + constant. \tag{2.22}$$

For the sake of simplicity, we will set the constant to zero (shifting the energies). The resulting spectra are displayed on Scheme 2.2.1.

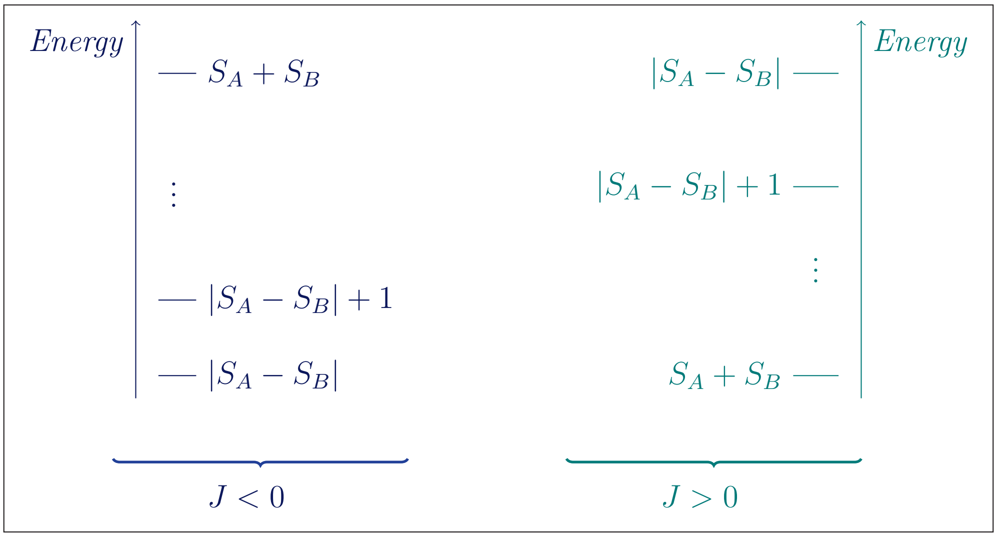

Scheme 2.2.1: Energy spectrum of the Heisenberg-Dirac-Van Vleck Hamiltonian, for the antiferromagnetic (left) and ferromagnetic (right) cases.

The resulting states will be further split by the application of a field, because of the Zeeman effect. If we use the same notation as in equation (2.14), we have

$$E_i = -\frac{J}{2}S_i(S_i+1) + \mu_B g M_{S_i} \tag{2.23}$$

$$E_i^{(0)} = -\frac{J}{2}S_i(S_i+1), \quad E_i^{(1)} = \mu_B g M_{S_i} \tag{2.24}$$

for any state i associated to the spin S_i. For instance, if we set $S_A = S_B = 1/2$, as could be found for instance in a dinuclear Cu(II) complex, two states can be constructed:

- $S = 0$, singlet state, with $E^{(0)}(S=0) = 0$ and $E^{(1)}(S=0) = 0$;
- $S = 1$, triplet state, with $E^{(0)}(S=1) = -J$ and $E^{(1)}(S=1) = -\mu_B g, 0, \mu_B g$.

The Van Vleck formula reduces in that case to

$$\chi = \frac{M}{H} = \frac{N_A}{k_B T}\frac{0 + (-\mu_B g)^2 \exp\left(+J/k_B T\right) + 0 + (\mu_B g)^2 \exp\left(+J/k_B T\right)}{1 + 3\exp\left(+J/k_B T\right)} \tag{2.25}$$

$$= \frac{2N_A g^2 \mu_B^2}{k_B T} \frac{1}{3 + \exp\left(-J/k_B T\right)}. \tag{2.26}$$

Thus, the thermal variation of χ (or even better, χT) provides direct information on J: it is possible to gain information on the coupling between these two spins by the simple measurement of susceptibility versus temperature.

This is unfortunately not always the case. In Chapter 5, we will study an asymmetric trinuclear complex of Cu(II), where all the spins are supposed to be coupled. A schematic representation of such complexes is given on Figure 2.2.1. If we label A, B, and C the three copper centres, the zero-field Hamiltonian now writes

$$\mathcal{H}_{\mathrm{Cu}_3} = -J_{AB}\hat{S}_A \cdot \hat{S}_B - J_{AC}\hat{S}_A \cdot \hat{S}_C - J_{BC}\hat{S}_B \cdot \hat{S}_C. \tag{2.27}$$

The solutions in that case are less straightforward. We are interested here in the coupling of three $S = 1/2$ spins. The solutions are thus going to be quartet ($S = 3/2$) and doublet ($S = 1/2$) states.

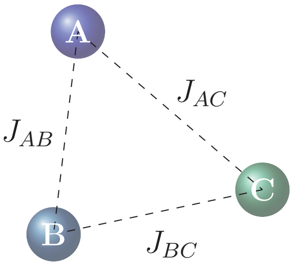

FIGURE 2.2.1: Schematic representation of an asymmetric Cu(II) trinuclear complex.

Only one quartet state can actually be build, by aligning all the spins. We will label that state $|\uparrow\uparrow\uparrow\rangle$, where the direction of the arrows indicates the spin projection (up or down) for, respectively, spin A, B or C. The energy of this state is thus simply given by the expectation value of the Hamiltonian

$$\begin{aligned} E(3/2) = \langle\uparrow\uparrow\uparrow|\mathcal{H}_{\mathrm{Cu}_3}|\uparrow\uparrow\uparrow\rangle = &- J_{AB}\langle\uparrow\uparrow\uparrow|\hat{S}_A \cdot \hat{S}_B|\uparrow\uparrow\uparrow\rangle \\ &- J_{AC}\langle\uparrow\uparrow\uparrow|\hat{S}_A \cdot \hat{S}_C|\uparrow\uparrow\uparrow\rangle \\ &- J_{BC}\langle\uparrow\uparrow\uparrow|\hat{S}_B \cdot \hat{S}_C|\uparrow\uparrow\uparrow\rangle. \end{aligned} \tag{2.28}$$

The Heisenberg-Dirac-Van Vleck approach of equation (3.19) can, as previously, be unfolded and yields:

$$E(3/2) = -\frac{J_{AB} + J_{AC} + J_{BC}}{4}. \tag{2.29}$$

The doublet states may be more difficult to picture. Three doublet configurations can indeed be constructed by flipping one spin in $|\uparrow\uparrow\uparrow\rangle$: $|\downarrow\uparrow\uparrow\rangle$, $|\uparrow\downarrow\uparrow\rangle$ and $|\uparrow\uparrow\downarrow\rangle$, and the expected doublet states are going to be linear combinations of these "limit forms".

They will be eigenvectors of the Hamiltonian, *i.e.* they are such that $\mathcal{H}_{\mathrm{Cu}_3}$ is diagonal in their basis. Overall, the problem reduces then to the diagonalisation of $\mathcal{H}_{\mathrm{Cu}_3}$ in the subspace of doublet configurations. In the $\{|\downarrow\uparrow\uparrow\rangle, |\uparrow\downarrow\uparrow\rangle, |\uparrow\uparrow\downarrow\rangle\}$ basis, the matrix elements of $\mathcal{H}_{\mathrm{Cu}_3}$ are

$$\begin{pmatrix} (J_{AB} + J_{AC} - J_{BC})/4 & -J_{AB}/2 & -J_{AC}/2 \\ -J_{AB}/2 & (J_{AB} + J_{BC} - J_{AC})/4 & -J_{BC}/2 \\ -J_{AC}/2 & -J_{BC}/2 & (J_{AC} + J_{BC} - J_{AB})/4 \end{pmatrix} \tag{2.30}$$

where we used equation (2.19) and[vii]

$$\hat{S}^2 = \hat{S}_A^+\hat{S}_A^- + \hat{S}_A^+\hat{S}_B^- + \hat{S}_A^-\hat{S}_B^+ + \hat{S}_B^+\hat{S}_B^- - \hat{S}_{Az} - \hat{S}_{Bz} + \hat{S}_{Az}^2 + \hat{S}_{Bz}^2 + 2\hat{S}_{Az}\hat{S}_{Bz}. \quad (2.33)$$

The problem is thus to solve $det(\mathcal{H}_{\mathrm{Cu}_3} - E\mathbb{I}_3) = 0$ (where $\mathbb{I}_3$ represents the identity matrix). This leads to a third degree polynomial, which can be factorised once it is recalled that one of the energies (root of the polynomial) is necessarily equal to the energy of the quartet, $E(1/2)_1 = E(3/2)$ ($M_S = \pm 1/2$ component of the quartet). After a bit of calculation, the two other roots are found:

$$\begin{aligned} E(1/2)_{2,3} =& \frac{J_{AB} + J_{AC} + J_{BC}}{4} \\ & \pm \sqrt{\frac{(J_{AB} - J_{BC})^2 + (J_{BC} - J_{AC})^2 + (J_{AC} - J_{AB})^2}{8}}. \end{aligned} \quad (2.34)$$

It is then here also possible to express susceptibility from the coupling constants, but the reciprocal is not true. This is rather logical: in Van Vleck's formula, the relevant parameters are not the absolute energies of each state but rather their relative energies. Here, we want to relate two energy differences (three-state system) to three independent coupling constants, which is not possible.

Anisotropic case

Let us now consider the possibility, for the system, to show some magnetic anisotropy. By magnetic anisotropy, we mean the possibility to display different values of the magnetisation for a same magnitude of the field, depending only on the orientation of the latter.

This is a direct consequence of the spin-orbit coupling. In the simplest case, the orbital momentum is negligible in the ground state, but not in the excited ones. This will generally be the case for transition metal octahedral complexes. Ground and excited states may then be coupled through the spin-orbit Hamiltonian of equation (1.61), with L and S being the total spin and orbital moment. This leads to two phenomena: first, the gyromagnetic factor becomes anisotropic ($g_u \neq g_u \neq g_w$). Furthermore, if the spin is larger than 1/2, one may observe an energy splitting between substates with a different absolute value of M_S: this is the so-called Zero Field Splitting (ZFS). Phenomenologically, the ZFS Hamiltonian can be written as

$$\mathcal{H}_{ZFS} = \hat{S}\bar{\bar{D}}\hat{S} \quad (2.35)$$

where $\bar{\bar{D}}$ is a traceless and symmetric tensor,[viii] called the ZFS or anisotropy tensor. Equation (2.35) can also be found written as

$$\mathcal{H}_{ZFS} = D\left[\hat{S}_z^2 - \frac{S(S+1)}{3}\right] + E\left(S_x^2 + S_y^2\right) \quad (2.36)$$

[vii] We remind that the $\hat{S}^+$ and $\hat{S}^-$ operator verify

$$\hat{S}^+|\uparrow\rangle = |0\rangle, \quad \hat{S}^-|\uparrow\rangle = |\downarrow\rangle \quad (2.31)$$

$$\hat{S}^+|\downarrow\rangle = |\uparrow\rangle, \quad \hat{S}^-|\downarrow\rangle = |0\rangle \quad (2.32)$$

[viii] Traceless since, overall, the sum of the levels energy should remain unchanged.

where the D and E parameters are related to the eigenvalues of $\bar{\bar{D}}$ by the following equations

$$D = \frac{3D_z}{2} \tag{2.37}$$

$$E = \frac{|D_x - D_y|}{2} \tag{2.38}$$

(assuming x, y and z are the principal axes for both $\bar{\bar{D}}$ and $\bar{\bar{g}}$). They are called, respectively, axial and rhombic anisotropy parameter.
This form of anisotropy will principally be encountered for transition metals ions, with spins larger than 1/2. As such, it will not be considered in the following, since we will focus in this thesis on the magnetic properties of Cu(II) ($S = 1/2$) and lanthanide complexes only.
In this latter case, the orbital momentum in the ground state is non negligible, and may thus be coupled by the spin-orbit coupling to the spin momentum.(ix) Furthermore, previously we implicitly assumed that the spin-orbit coupling was only acting as a small perturbation on the eigenstates of the (spin) Hamiltonian. This implied that the spin quantum number S remained an adapted quantum number – in the sense that it still permitted to describe the state of the system –.
This is no longer the case if the spin-orbit interaction is large enough, compared to the other terms in the Hamiltonian. In the case of the lanthanide ions, the magnitude of the spin-orbit interaction becomes comparable to the magnitude of the other terms of the free ion Hamiltonian (10^3 cm^{-1} compared to 10^4 cm^{-1}, respectively)[70]. Spin is thus no longer a relevant quantum number, and since the degeneracy of the ground state is lifted according to the value of the total angular momentum

$$\hat{J} = \hat{L} + \hat{S} \tag{2.39}$$

J will be the new relevant quantum number. We can infer from this formula that magnetic anisotropy will be caused by the orbital momentum $\hat{L}$, provided naturally that it is itself anisotropic. This is likely to happen, thanks to the coordination of ligands around the lanthanide cation. The crystal field splitting (presented in the previous section), lifting the degeneracy of the orbitals depending on their relative orientation with respect to the coordination sphere, may indeed preferentially stabilise orbitals pointing along (a) specific direction(s) in space. As a result, the different orientations in space become non-equivalent – we lose the spherical symmetry of the free ion –, and so do the different components of $\hat{L}$, and thus of $\hat{J}$. As we will see in the following section, this anisotropy can be very large. Actually, it is often much larger than transition metals anisotropy.

In summary, we have seen so far that, introducing more and more term to the Hamiltonian of a metal free ion, we may describe more and more precisely its magnetic properties. Noteworthy, the approach that was unfolded at the beginning of this section remains valid in the anisotropic case – one may still invoke Van Vleck's formula –, even though much more difficult to handle. We also see the tremendous importance of the coordination symmetry and geometry, since they will act on the energy splitting and thus on the exponentials of Van Vleck's formula, but also on the anisotropy itself. In a way, controlling coordination should permit to control anisotropy.

(ix) Note that this may also be true for transition metal complexes, noticeably those of Co(II).

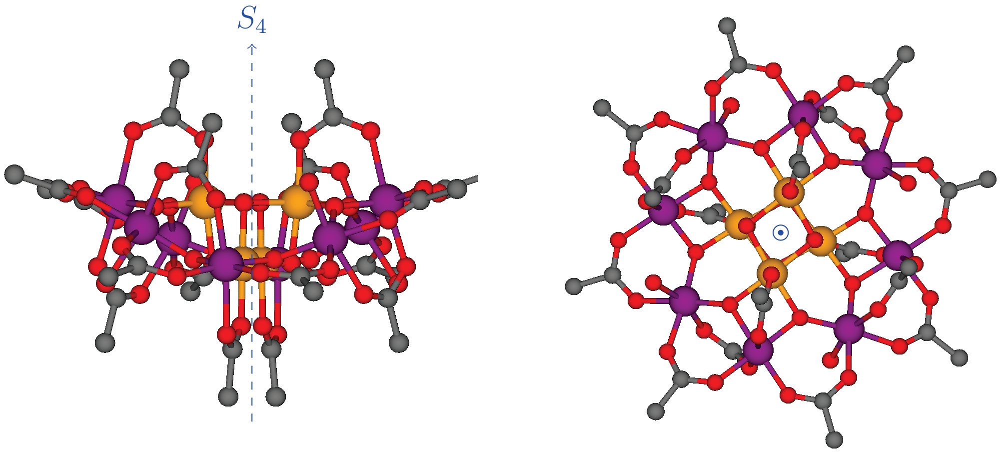

FIGURE 2.2.2: Crystal structure of the Mn_{12} complex, represented as viewed along the $\vec{a}$ (left) and $\vec{c}$ axes. Colour scheme: Mn(III), purple; Mn(IV), orange; O, red; C, gray. H atoms omitted for the sake of clarity. The S_4 axis direction is indicated by the blue arrow.

2.2.4 Single Molecule Magnets

The latter point has actually been a central issue of coordination chemistry in the last twenty five years. Indeed, at the beginning of the 1990s was discovered the first Single Molecule Magnet (SMM), $[Mn_{12}O_{12}(CH_3COO)_{16}(H_2O)_4]$ (simplified as Mn_{12}). This complex was first synthesised in 1980, but its intriguing magnetic properties were characterised and explained only thirteen years later.[71,72] In 1993, it was indeed discovered that this complex could retain its magnetisation in the absence of any external magnetic field, and for very long times at low temperatures – about 2 months at 2 K –.

In other words, this complex acts, at least at low temperatures, as a molecular equivalent of the magnets. The word molecular is very important: the slow relaxation is not due to an extended (solid state) order, but solely to its uniaxial magnetic anisotropy. The picture is actually quite simple: because of this uniaxial anisotropy, the magnetic moment will preferentially orient along the easy axis, and will tend to avoid the hard axes directions (hence their name). They should be found at 90° from the easy axis,(x) which means the continuous reversal of magnetisation – "upside down" – will be quite severely hampered: relaxation of magnetisation will thus be slowed down.

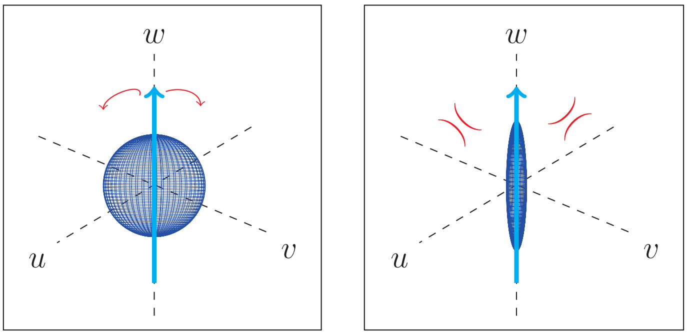

SCHEME 2.2.2: Schematic representation of the reversal of magnetisation in the isotropic (left) and uniaxal anistropic (right) cases. The magnetisation vector is represented by the cyan arrow, and the blue volume represents the susceptibility tensor ellipsoid. w is taken as the easy axis.

Actually, in the case of the Mn_{12} complex it could be shown that the temperature depen-

---

(x)Being the eigenvectors of a symmetrical real tensor, the magnetic axes are necessarily orthogonal.

dence of the magnetisation dynamics obeys an Arrhenius law

$$\nu_{rel} = \nu_0 \ \exp\left(-\frac{\Delta E}{k_B T}\right) \tag{2.40}$$

with

$$\Delta E = |D|S^2 = 66K \tag{2.41}$$

and $S = 10$ (ferrimagnetic coupling of the Mn(IV) and Mn(III) ions).(xi) Physically, this expression means the relaxation from the $M_S = +10$ substate towards the $M_S = -10$ substate proceeds *via* a thermal activation to the $M_S = 0$ substate, as pictured on Scheme 2.2.3.(xii)

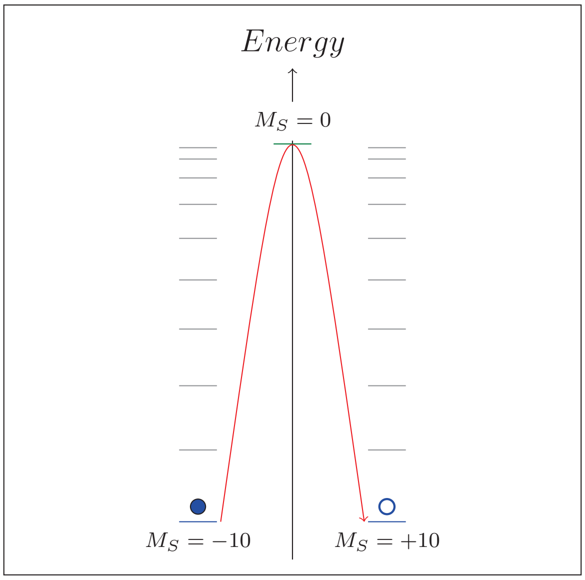

SCHEME 2.2.3: Schematic representation of the relaxation of magnetisation in Mn_{12}.

As one may note, the energy barrier ΔE involves both the uniaxal anisotropy parameter and the total spin. The higher these parameters (in absolute value), the slower the relaxation. In order to obtain more efficient SMMs, because of the apparent quadratic evolution of S chemists tried at first to develop systems with giant spins. Indeed, more efficient SMMs means higher working temperatures, but also higher magnetic moments. Unfortunately, even though very large S values could be obtained – such as S =83/2[73] –, no improvement was observed on the relaxation rates. Actually, it could be shown that the diagonal terms of the ZFS Hamiltonian actually evolve as S^{-2}, thus making ΔE globally independent of S.[74]

Furthermore, the reason for the slow relaxation of Mn_{12} is its high anisotropy, which is itself due to a rather efficient addition of the local anisotropies of the Mn(III) and Mn(IV) ions. The fact that the single ion anisotropies add instead of subtract is due the high symmetry – tetragonal – which force the easy axes of each ion to lie approximately along the S_4 axis. In order to optimise the SMM behaviour, it is thus better to control

---

(xi) One may note the form of the energy term, which is directly linked to the ZFS Hamiltonian of equation (2.35).

(xii) Indeed, relaxation of magnetisation means that the system is able to reverse its magnetic moment, hence to exchange the population of the $M_S = \pm 10$ substates.

strictly the way local anisotropies interact, and this calls for rather small assemblies of very anisotropic ions.[75]

The discovery of the first Single Ion Magnet in the early 2000's can be seen as a wonderful support to this idea. In 2004, Ishikawa indeed showed that two mononuclear lanthanide complexes, $[TbPc_2]^-$ and $[DyPc_2]^-$ (with Pc = phthalocyanate), displayed a slow relaxation of magnetisation at quite high temperatures (between 10 K and 40 K).[76] This was solely due to the magnetic anisotropy of the complexes, which overall contains only a single paramagnetic centre. This discovery lead to a huge research effort on lanthanide-based single molecule magnets, and noteworthy on mononuclear Ln-based SMM.[77,78]

The lanthanide ions appear indeed very promising in the seek for more efficient SMM. As we mentioned earlier, because of the strong spin-orbit coupling they may indeed present strong single-ion anisotropies, and for the last half of them (Tb - Yb) they also present high magnetic moments(xiii). Furthermore, since the crystal field controls the final anisotropy, in turn it should be possible to control anisotropy through an appropriate tuning of the coordination sphere.

This was summarised in 2008 by Rinehart and Long,[79] who offered guidelines to design lanthanide-based SMMs, basing on the mutual adaptation of the $4f$ electron density in the substates with the highest $|M_J|$ value and the ligand field. It appears that lanthanide cations can be separated into two classes, showing either a prolate or oblate deformation of the $4f$ electron density in these substates (as compared to the ideal spherical distribution of the free ion). Ligand fields displaying a marked negative charge density encapsulating these "deformation ellipsoids" are thus expected to stabilise them, hence inducing or reinforcing an energy barrier between the different M_J substates.

Yet, we will see in Chapter 6 that this model, though quite elegant, is too simplified. Relaxation of magnetisation is indeed a very complicated phenomenon, involving mechanisms that are not restricted to the level of the isolated molecule.[80] Let us consider the case of a SMM in its crystalline state, assuming that intermolecular magnetic interactions are negligible. Relaxation of magnetisation in that case can occur through four different mechanisms.(xiv)

First, the two degenerate ground states with opposite magnetisation may not be completely uninteracting. Provided that these two states may "communicate", quantum tunnelling of magnetisation can occur, through the fast inversion between these two substates. "Communication" between the states may be induced for instance by hyperfine coupling between the electronic and nuclear spin, which indirectly couples the two components of the ground doublet. The resulting relaxation rate is independent of temperature, but is on the other hand strongly dependent on the magnetic field magnitude. Indeed, provided that a magnetic field is applied on the system, the degeneracy in the ground state is lifted and thus the quantum tunnelling should be suppressed. Overall, the rate of magnetic relaxation due to quantum tunnelling writes

$$\nu_{QTM} = \frac{1}{a + bH^2} \tag{2.42}$$

with a and b two constants.

Second, the molecule is not suspended in a vacuum, but embedded within a crystal lattice. This implies every molecule feels an electric (Madelung) field created by all the point charges in the crystal. The quantum state of each molecule is thus dependent on this electric field, and because of the spin-orbit coupling this means the magnetic properties

---

(xiii) For a more than half-filled shell, we remind that $J = L + S$, while for a less than half-filled shell one gets $J = |L - S|$.

(xiv) The curious reader is referred to Stevens' publication for more details.[81]

are likely going to be impacted by any variation of the Madelung field. Since we study molecules at a non-zero temperature, vibration modes are expected to be populated, which in turn means all the point charges that contribute to the Madelung field may be moving. The Madelung potential is then expected to be time dependent, and its variations in time induce the so-called spin-phonon coupling, *i.e.* the coupling of magnetic properties and vibrations.

The interplay between the vibration modes and magnetic states thus allows magnetisation to relax, through three different mechanisms. First, the direct relaxation, which consists in the absorption of a vibration quantum $\hbar\omega$ exactly equal to the energy gap between two states. It is a field and temperature dependent mechanism:

$$\nu_{direct} = \left(cH^2 + dH^4\right) T. \tag{2.43}$$

Second, the Orbach relaxation, which can be seen as double direct mechanism: the system absorbs a first quantum $\hbar\omega$ to reach an intermediate state $|\psi_{int}\rangle$, and then releases another quantum $\hbar\omega_2$ in order to reach the final state. It is temperature dependent but field independent:

$$\nu_{Orbach} = \nu_0 \ \exp\left(-\frac{\Delta E}{k_B T}\right) \tag{2.44}$$

with $\Delta E = |\hbar(\omega - \omega_2)|$. One may note the mono-exponential – Arrhenius-like – form, reminiscent of equation (2.40).

Finally, the Raman relaxation, which can be seen as an Orbach mechanism involving a "virtual" intermediate state (excitation energies are much larger than the energy span of the ground configuration). The relaxation rate for this mechanism is strongly temperature dependant:

$$\nu_{Raman} = eT^n \tag{2.45}$$

with n being an integer, and e being possibly field independent.

Overall, the magnetisation dynamics for an isolated yet crystallised SMM is thus expected to be the resultant of these different contributions, being noted furthermore that each mechanism can intervene several times – for instance, two Orbach relaxations with different energy barriers can be found –. In turn, SMM are very complex systems whose properties are still very hard to control, if it is only possible. Indeed, single ion anisotropies seem now quite easy to control, but we still do not know how to ensure the highly anisotropic molecules will behave as SMMs in the solid state. As we will show in Chapter 6, playing solely on the energy barriers in the system may not be the most appropriate way to design SMM, since "under barrier" phenomena (*i.e.*, Raman and direct relaxations) may completely control the relaxation rate.

2.2.5 Characterising magnetic anisotropy locally

So far, we did not mention how magnetic anisotropy can be measured and quantified from the experimental point of view. Many different experimental techniques are available, and the curious reader is referred to the Molecular Magnetism Website[82] (`www.molmag.de`) for more details and informations. In the following paragraphs, we will present two techniques that were used during this thesis: angular-resolved magnetometry and polarised neutron diffraction.

Angular-resolved magnetometry

Scheme 2.2.4 represents a simplified magnetometry experiment: a sample (red rectangle) is placed in the middle of a superconducting circuit, which consists in three successive coils. The coiling orientation is alternating when going from top to bottom. Initially, the cavity is empty and a vertical static magnetic field is applied. Since the magnetic flux is not evolving with time, no voltage appears across the circuit (Lenz' law).
If now we introduce a sample in the cavity, then the magnetic flux is perturbed. Yet, if the sample is static no electric signal will be measured, since the magnetic flux is not varying in time. If on the other hand we move the sample or if we set the magnetic field to be alternating, then a voltage is expected across the circuit, which can be linked to the vertical component of the magnetic moment of the sample. Because of the setup, the voltage versus position is expected to show a "cardinal sine"-like shape, with a maximum in 0 and minima in $\pm L$ (if the sample is paramagnetic).
In "classical" SQUID(xv) magnetometry, one usually measures the magnetic moment of a sample with respect to field magnitude, temperature, AC field frequency or even light irradiation, on a powder sample. This means that the measured magnetic moment is averaged over all possible orientations of the molecules. Direct information on the magnetic anisotropy cannot be obtained at this point.

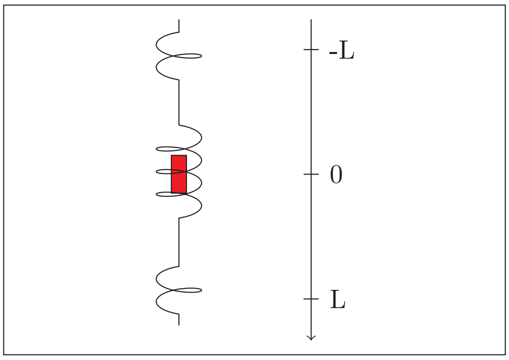

Scheme 2.2.4: Schematic representation of a magnetometer

In angular resolved magnetometry,[83,84] the same kind of measurements are performed but on a single crystal, whose orientation is precisely known and can be controlled (additional parameter). In the apparatus we used, the single crystals were fixed on a rotating sample holder, aligning the rotation axis with a lattice direction. The measurement of the magnetisation against the rotation angle and temperature or magnetic field magnitude thus provides information on the magnetic properties at the level of the crystal lattice. If we write the susceptibility tensor according to equation (2.3), then the measured magnetic moment will be expressed as:[85]

$$m_{meas} = \frac{1}{N} \sum_{i \in Lattice\ positions}^{N} \left(\bar{\bar{\chi}}_i \cdot \vec{H} \right) \cdot \frac{\vec{H}}{||\vec{H}||}. \tag{2.46}$$

If the crystal lattice contains no symmetry equivalent positions, then sum of equation (2.46) reduces to a single term. Hence, measuring the magnetisation as a function of angle for three non collinear rotation axes should, in principle, permit to extract every

---

(xv) SQUID: Superconduction QUantum Interference Device. This device translates the magnetic flux produced by the studied sample into a current – using Lenz' induction law –, which is itself translated into a voltage directly linked to the magnetic moment of the sample.

component of the susceptibility tensor, and thus access experimentally the molecular magnetic anisotropy.

This is also true if only inversion-related positions are found in the lattice: applying an inversion symmetry operation should not lead magnetic moments to oppose the magnetic field (unstable equilibrium). The susceptibility tensor is indeed invariant under space inversion:[28]

$$\begin{aligned} i\left(\bar{\bar{\chi}}\right) &= \begin{pmatrix} -1 & 0 & 0 \\ 0 & -1 & 0 \\ 0 & 0 & -1 \end{pmatrix} \cdot \begin{pmatrix} \chi_{xx} & \chi_{xy} & \chi_{xz} \\ \chi_{xy} & \chi_{yy} & \chi_{yz} \\ \chi_{xz} & \chi_{yz} & \chi_{zz} \end{pmatrix} \cdot \begin{pmatrix} -1 & 0 & 0 \\ 0 & -1 & 0 \\ 0 & 0 & -1 \end{pmatrix} \qquad (2.47) \\ &= (-1)^2\, \mathbb{I}_3 \cdot \bar{\bar{\chi}} \cdot \mathbb{I}_3 = \bar{\bar{\chi}}. \qquad (2.48) \end{aligned}$$

Molecules related by an inversion symmetry are thus expected to yield the same magnetisation, and one can express the magnetic moment of a unit cell as being N times the magnetic moment of a molecule, with N the number of equivalent positions. As such, angular-resolved magnetometry allows the unambiguous determination of the molecular magnetic anisotropy in triclinic crystal cells.

This is unfortunately untrue if other symmetry operations are found in the unit cell. For instance, in a monoclinic $P2/m$ cell there are four symmetry related positions:

- (x,y,z): asymmetric unit position
- (-x,y,-z): equivalent of the former through the 2-fold axis
- (x,-y,z): equivalent of (x,y,z) through the mirror plane
- (-x,-y,-z): equivalent of (x,y,z) through both operations.

It is rather plain to see that the two last positions can be deduced from the two first ones *via* an inversion operation, hence they may safely be discarded. Equation (2.46) in that case reduces to

$$m_{meas} = \frac{2}{4} \times \left[\left(\bar{\bar{\chi}} \cdot \vec{H} \right) + \left(\mathcal{C}_2(\bar{\bar{\chi}}) \cdot \vec{H} \right) \right] \cdot \frac{\vec{H}}{||\vec{H}||} \qquad (2.49)$$

where $\mathcal{C}_2$ is the 2-fold rotation operator. After a bit of calculations, the term within the bracket in equation (2.49) is found to be equal to

$$\left(\bar{\bar{\chi}} \cdot \vec{H} \right) + \left(\mathcal{C}_2(\bar{\bar{\chi}}) \cdot \vec{H} \right) = 2 \begin{pmatrix} \chi_{xx}\, H_x + \chi_{xz}\, H_z \\ \chi_{yy}\, H_y \\ \chi_{xz}\, H_x + \chi_{zz}\, H_z \end{pmatrix} \quad with\ \ \vec{H} = \begin{pmatrix} H_x \\ H_y \\ H_z \end{pmatrix}. \qquad (2.50)$$

It is thus clear that an angular-resolved measurement on a monoclinic single-crystal cannot provide a complete information on the molecular susceptibility tensor: the off-diagonal terms involving y are absent from equation (2.50). The same reasoning can be applied on any higher order symmetry, thus implying that angular-resolved magnetometry itself cannot allow a complete determination of the molecular magnetic anisotropy for crystal cells with at least a monoclinic symmetry.

Still, the diagonal and some off-diagonal terms are still present in equation (2.50). This means that, depending on the orientation of the magnetic field, it should be possible to see through the value of m_{meas} an effect of the anisotropy. For instance, we have plotted on Figure 2.2.3 the angular dependence of m_{meas} for a rotation along the $\vec{b}$ axis, with the $\vec{c}$ axis initially set along the magnetic field, and for different relative values of the χ_{ij} terms (more specifically, for $0 \leq \chi_{zz} \leq 0.75\chi_{xx}$, and also for $\chi_{zz} = 0.2\chi_{xx}$ and $-0.75\chi_{xx} \leq \chi_{xz} \leq 0.75\chi_{xx}$). The effect of anisotropy on these curves is plain, thus showing angular-resolved SQUID measurements may be of interest even in the case of a monoclinic cell. Noteworthy, the effect of the off-diagonal components can be retrieved from the shift of the curve extrema.

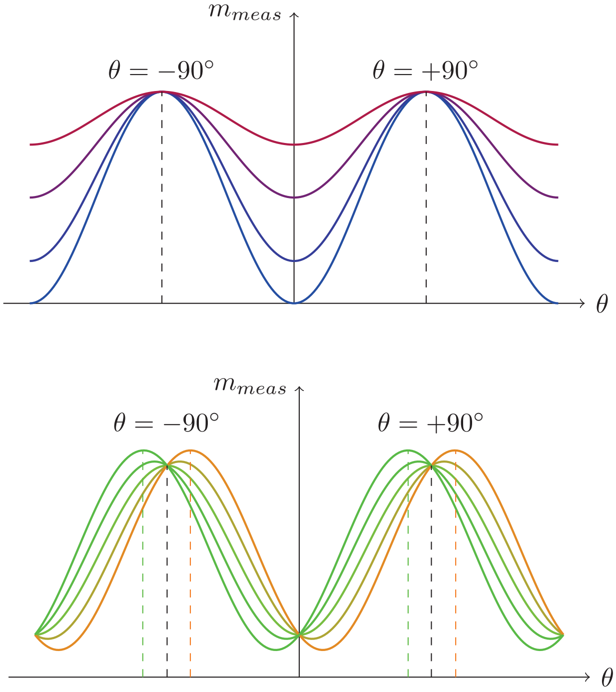

FIGURE 2.2.3: $m_{meas} = f(\theta)$ plots for a rotation along the $\vec{b}$ axis of a monoclinic cell, according to equation (2.50). **Upper part**: evolution of m_{meas} depending on the relative values of χ_{xx} and χ_{zz}, fixing $\chi_{zx} = 0$. Colour scheme: from blue to violet, fixed χ_{xx} and variable χ_{zz} (from $0.2\chi_{xx}$ to $0.75\chi_{xx}$). **Lower part**: evolution of m_{meas} with $\chi_{zz} = 0.2\chi_{xx}$, with χ_{zx} varying from $-0.75\chi_{xx}$ (green) to $+0.75\chi_{xx}$ (orange).

Polarised Neutron Diffraction (PND)

We have seen in the previous paragraphs that angular-resolved magnetometry does not allow to retrieve a complete information on the magnetic anisotropy at the molecular level. This is because SQUID magnetometry is not exactly a local probe, in the sense that it yields information on the unit cell rather than on the isolated complex. Polarised Neutron Diffraction, on the other hand, allows an unambiguous determination of the magnetic susceptibility tensor at the single molecule level.

Neutrons are massive and chargeless fermionic particles, and some of their properties are gathered in Table 2.1.[70] Because of their zero electric charge, they may penetrate deeply into matter without interaction. Their large mass also permits to thermalise them, which thus allows to attribute them a specific wavelength thanks to de Broglie's equation(xvi).

(xvi) If we neglect the gravitational potential energy, we may write the total energy of a neutron as being equal to its kinetic energy, $E = 1/2 m_n p^2$. Placed in a temperature controlled bath (for instance a pool of water), a neutron will tend to equal its energy to $k_B T$. Using de Broglie's equation, we get:

$$\lambda = \frac{h}{p} = \frac{h}{\sqrt{2k_B T m_n}}. \qquad (2.51)$$

Of course, if we consider an ensemble of neutrons we need to consider a more accurate model; neutrons

Table 2.1: Some physical characteristics of the neutron.

Masse	$m_n = 1.675\ 10^{-24}$ g
Charge	$q_n = 0$ C
Spin	$S = 1/2$

This means neutrons can be used, exactly as X-Rays, to perform diffraction experiments on single crystals. Thermal and "hot" neutrons (thermalised at room temperature and around 1000 °C, respectively) indeed present wavelengths in the order of 1 Å, thus are adapted to the study of molecular compounds.

The interaction of neutrons with crystalline matter is two-fold.[86] First, neutrons may interact with nuclei at very short distances, through the strong nuclear interaction. The resulting nuclear structure factor can be written as(xvii)

$$F_N(\mathbf{Q}) = \sum_j^{maille} b_j \exp\left(i\mathbf{Q}\cdot\mathbf{r}_j\right) \tag{2.52}$$

with $\mathbf{Q}$ the scattering vector and b_j the scattering length of atom j, located at $\mathbf{r}_j$. The similarity with the equations of X-Ray diffraction is rather striking.

Being also fermionic particles, neutrons may furthermore interact with the magnetic moments in the lattice. The corresponding magnetic form factor writes

$$\mathbf{F}_M(\mathbf{Q}) = \sum_j^{maille} \bar{\bar{\chi}}_j \cdot \mathbf{H}\ f_{j,M}(\mathbf{Q}) \exp\left(i\mathbf{Q}\cdot\mathbf{r}_j\right) \tag{2.53}$$

where $\bar{\bar{\chi}}_j$ represents the magnetic susceptibility tensor of atom j, and $f_{j,M}(\mathbf{Q})$ its normalised magnetic scattering factor(xviii).

Interestingly, the scattered amplitudes stemming from these two form factors are of the same order of magnitude. Nuclear and magnetic diffusion are thus of a comparable intensity. If we assume the neutron beam is polarised along the z direction, then the diffracted intensity can be written as

$$I^{\pm} \propto |F_N|^2 + |F_M^{\perp}|^2 + P^{\pm}\left(F_N F_{M,z}^{\perp\star} + F_N^{\star} F_{M,Z}^{\perp}\right) \tag{2.54}$$

where $\star$ indicates a complex conjugate, and $P^{\pm}$ the real polarisation of the neutron beam for the up $(+)$ and down (-) orientations. As one can infer from equations (2.54) and (2.53), comparison of the scattered intensities for a upwards and downwards beam polarisation should, in principle, yield information on the atomic susceptibility tensors.[87,88]

In a PND experiment, one measures the diffracted intensities for each Bragg peak, successively with a up and down beam polarisation, under a static magnetic field whose orientation with respect to the lattice axes is known. Practically, the sample is placed at the end of a rod, in a cryostat, and a vertical magnetic field is applied to it. The crystal is then rotated thanks to the rod, and for each angular position "up" and "down" diffracted

---

being fermions, the mean wavelength should be given by a similar formula, involving furthermore a Fermi-Dirac statistics weighing.

(xvii) Assuming the neutron wavelength is much larger than the strong interaction length, which in will be the case here: $\lambda \sim$ Å, compared to 10^{-4} Å for the interaction length.

(xviii) Note that, actually, the magnetic scattering amplitude will be related only to the component of $F_M(\mathbf{Q})$ that will be perpendicular to the scattering vector $\mathbf{Q}$. Furthermore, equation (2.53) is only valid for small magnetic fields, such that magnetisation evolves linearly with field.

intensities are collected using either a bidimensional detector or a single detector placed in the diffracted beam direction. This operation is performed for three different orientations of the crystal (for instance, first $\vec{a}$ vertical, then $\vec{b}$, then $\vec{c}$).

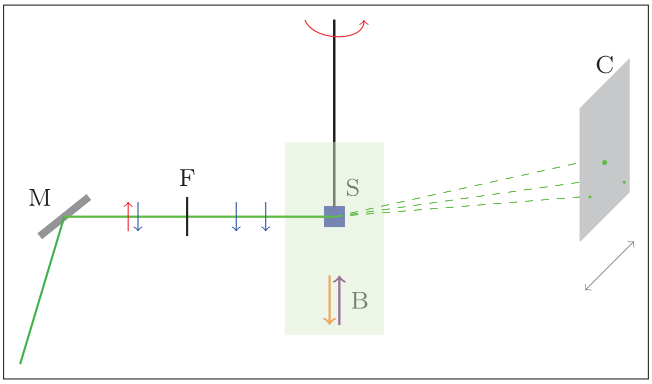

Scheme 2.2.5: Schematic representation of PND diffractometer. Labels: M , monochromator; F, flipper; S, sample; B, magnetic field orientation; C, 2D detector.

In the end, one obtains a set of $\{h, k, l, R_{hkl}\}$ values with

$$R_{hkl} = \frac{I^+}{I^-} = \frac{|F_N|^2 + |F_M^{\perp}|^2 + P^+ \left(F_N F_{M,z}^{\perp\star} + F_N^{\star} F_{M,Z}^{\perp}\right)}{|F_N|^2 + |F_M^{\perp}|^2 + P^- \left(F_N F_{M,z}^{\perp\star} + F_N^{\star} F_{M,Z}^{\perp}\right)} \tag{2.55}$$

being called the flipping ratio. The deviation of this ratio from unity is a marker of magnetic scattering, and its values can be used in a least-square refinement to determine the χ_{ij} terms for each atom of the lattice, basing on equation (2.53). Generally, and it will be the case in Chapter 6, the magnetic moment is due essentially to the central metal cation of a complex. As such, one focuses on the susceptibility tensor of the latter, considering all the other atoms as being magnetically innocent(xix) ($\chi_{ij} = 0$).

2.3 Long story short

In conclusion, we have seen through this Chapter how, by the interplay of ligands and metal cations (either transition metals or lanthanides), coordination may lead to a fine tuning in their electronic structures, eventually giving the resulting complexes original physical and chemical properties.

As we have seen, ligands are more than mere point charges – as they are modelled in the crystal field model –, and depending on their nature the properties of the corresponding complexes may vary significantly. In the following Chapter, we propose to revisit these ligands effects using a conceptual-DFT based approach. More specifically, we will see how the Dual Descriptor and the Molecular Electrostatic Potential permit to retrieve efficiently their coordination properties, *i.e.* binding geometries and charge transfer character. Following this line of argument, we then propose to study and rationalise the *trans* effects of octahedral complexes. This effect, which consists in the differential reactivity or stability of a metal-ligand bond depending on the ligand on the *trans* position, is indeed rather ubiquitous in coordination chemistry and yet remained for a long time misunderstood.

(xix) Note that, when the magnetic properties are isotropic or the field high, one can also use PND to determine spin density maps. In that case, it is possible to determine spin delocalisation or polarisation on ligands.

In Chapter 4, we will consider both the reactivity and magnetic properties of some Cu(II) complexes. As we will show, here also they can be understood in the simple terms of electron density donation, back-donation and electrostatic interactions.

Finally, in Chapter 5 we will be interested in the magnetic properties of some lanthanide complexes showing a SMM behaviour. We will show how, using local and global measurements we were able to understand the physical mechanisms behind the slow relaxation of magnetisation they display.

Chapter 3

Revisiting the metal-ligand interactions through conceptual DFT

In this chapter, we wish to study some coordination complexes from the viewpoint of conceptual DFT. In a first time, we present an original approach of the dual descriptor, based on time independent perturbation theory. Then, through a rather simple study, we show how conceptual DFT can help to understand the chemical properties of ligands. Finally, we show on a rather large set of complexes how conceptual DFT allows to rationalise a phenomenon that remained largely misunderstood for almost a century: the *trans* effect.

3.1 State specific Dual Descriptor

In Chapter 2, we introduced the Dual Descriptor (DD) $\Delta f(\mathbf{r})$ according to its first derivation[41]

$$\Delta f(\mathbf{r}) = \left(\frac{\partial^2 \rho(\mathbf{r})}{\partial N^2}\right)_{v(\mathbf{r})}. \tag{3.1}$$

Evaluation of the derivative in this equation can be cumbersome, and people generally use a finite difference approximation to evaluate it:

$$\Delta f(\mathbf{r}) \approx \frac{\rho_{N+1}(\mathbf{r}) - \rho_N(\mathbf{r})}{(N+1) - N} - \frac{\rho_N(\mathbf{r}) - \rho_{N-1}(\mathbf{r})}{N - (N-1)} = \rho_{N+1}(\mathbf{r}) + \rho_{N-1}(\mathbf{r}) - 2\rho_N(\mathbf{r}) \tag{3.2}$$

with $\rho_{N+i}(\mathbf{r})$ representing the electron density of the molecule with an addition of i electrons(i). Noteworthy, this derivation is formally exact at 0 K.

Though helpful, this formulation has strong limitations. Noticeably, addition of one electron formally changes the spin state of the molecule. In the case of organometallic species, it is not plain which spin state to consider. Furthermore, the anionic state could be unbound, thus hampering the calculation.

An alternative formulation was proposed in 2013 by C. Morell and V. Tognetti, using electron density differences between the ground and the excited states.[89] The key idea

---

(i) If we assume furthermore that addition or subtraction of electrons leave the orbital diagram unchanged (frozen orbital hypothesis), we retrieve equation 1.58:

$$\Delta f(\mathbf{r}) \approx \rho_{LUMO}(\mathbf{r}) - \rho_{HOMO}(\mathbf{r}). \tag{2.58}$$

was to describe the early stages of a chemical event as a perturbation from the state where molecules are infinitely remote from each other, thus involving the ground and excited states of the isolated molecules to built the real electron density. The electron density variation between this situation and the starting point (isolated molecules) should thus be equal to the DD. Therefore, one can write:

$$\Delta f(\mathbf{r}) = \sum_{i=1}^{\infty} \omega_i \left(\rho_i(\mathbf{r}) - \rho_0(\mathbf{r})\right) \tag{3.3}$$

with $\rho_i(\mathbf{r})$ the electron density in the ith excited state, and ω_i being a weighting parameter. Unfortunately, no mathematical formula is accessible for the weighting parameter. In this formulation, $\Delta f(\mathbf{r})$ is coined "generalised Dual Descriptor", and the electron density differences are referred to as "state specific Dual Descriptors". Conceptually, it makes sense that the higher in energy the excited state, the less it contributes to the ground state reactivity. One would then expect a form that involves a strong convergence with the excited state energy, as found for instance in the molecular polarisability formula.[8]
Returning to perturbation theory, we can actually convince ourselves that ω_i indeed converge with the excitation energies. Let us consider two molecules, initially separated by an infinite distance. At time $t = 0$, they are separated by a distance R, large compared to their mean radius. They thus start to interact with one another, as pictured on Figure 3.1.1.

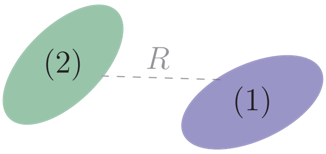

FIGURE 3.1.1: Schematic representation of the two molecules in interaction.

Because of the large distance, the interaction can be considered to be only electrostatic[(ii)]. Molecule (1), acting as a collection of point charges, induces an electric field in space, noticeably on molecule (2). The reverse is also true.
Calling $\mathcal{V}(\mathbf{r})$ the potential from which the field derives, using the same notations as in Chapter 2 we may express the Hamiltonian of the electrostatic interaction of (2) with the field of (1)

$$\mathcal{H}_{int} = -\int_{\mathbb{R}^3} \rho(\mathbf{r})\mathcal{V}(\mathbf{r})d^3\mathbf{r} + \sum_{nuclei} Z_i \mathcal{V}(\mathbf{r}_i) \tag{3.4}$$

in complete analogy with classical electrostatics.[90]
A simple form of perturbation would thus be such that $\mathcal{H}_{int}$ is modulated by a factor λ[(iii)] [4]

$$\mathcal{H}_{pert} = \lambda \mathcal{H}_{int}. \tag{3.5}$$

Let the solutions of the unperturbed Schrödinger equation be:

$$\mathcal{H}|n\rangle = E_n|n\rangle. \tag{3.6}$$

[(ii)] Note that other forms of perturbations could be considered, for instance basing on dispersion effects.

[(iii)] Physically, this factor may represent the magnitude of the potential; $\lambda \ll 1$ means a small perturbation.

Assuming the perturbation is small ($\lambda << 1$), the wavefunction correction at the first order can be expanded on the basis of the unperturbed $|n\rangle$ states. If the system is in the non-degenerate ground state $|0\rangle$, the perturbed wavefunction $|\Psi\rangle$ writes:

$$|\Psi\rangle = c_0 \left(|0\rangle + \sum_{k \neq 0} \frac{\langle k|\mathcal{H}_{pert}|0\rangle}{E_k - E_0} |k\rangle \right) \tag{3.7}$$

with c_0 a normalisation constant. It is rather simple to show that

$$c_0 = \pm \sqrt{\frac{1}{1 + \sum\limits_{k \neq 0} \frac{|\langle k|\mathcal{H}_{pert}|0\rangle|^2}{(E_k - E_0)^2}}} \tag{3.8}$$

the actual sign of c_0 being meaningless (phase factor).
From equation (3.7), it is rather plain that the perturbation induced by an incoming ligand indeed involves the unperturbed excited states, and is weighted by the excitation energies as expected. As such, we may also expect the electron density perturbation will be weighted by the excitation energies. The perturbed electron density actually writes:

$$\begin{aligned}
\rho_{pert}(\mathbf{r}_1) &= N \int \Psi^\star \Psi d\mathbf{s}_1 d\mathbf{x}_2 \dots d\mathbf{x}_N \\
&= c_0^2 \left(\rho_0(\mathbf{r}_1) + 2 \sum_{k \neq 0} \frac{\langle k|\mathcal{H}_{pert}|0\rangle}{E_k - E_0} \rho_0^k(\mathbf{r}_1) \right) \\
&+ c_0^2 \left(\sum_{k \neq 0} \sum_{l \neq 0} \frac{\langle k|\mathcal{H}_{pert}|0\rangle \langle l|\mathcal{H}_{pert}|0\rangle}{(E_k - E_0)(E_l - E_0)} \rho_k^l(\mathbf{r}_1) \right)
\end{aligned} \tag{3.9}$$

with $\rho_0(\mathbf{r}_1)$ the unperturbed ground electron density, and $\rho_k^l(\mathbf{r}_1)$ the transition density between states k and l (note that $k = l$ corresponds to the electron density of state k). The variation of electron density from the unperturbed state to the perturbed state is then

$$\begin{aligned}
\Delta\rho(\mathbf{r}) &= \rho_{pert}(\mathbf{r}) - \rho_0(\mathbf{r}) \\
&= \rho_0(\mathbf{r}) \left(c_0^2 - 1 \right) + c_0^2 \left(\sum_{k \neq 0} \frac{|\langle k|\mathcal{H}_{pert}|0\rangle|^2}{(E_k - E_0)^2} \rho_k(\mathbf{r}) \right) \\
&+ c_0^2 \left(2 \sum_{k \neq 0} \frac{\langle k|\mathcal{H}_{pert}|0\rangle}{E_k - E_0} \rho_0^k(\mathbf{r}) + \sum_{k \neq 0} \sum_{\substack{l \neq 0 \\ l \neq k}} \frac{\langle k|\mathcal{H}_{pert}|0\rangle \langle l|\mathcal{H}_{pert}|0\rangle}{(E_k - E_0)(E_l - E_0)} \rho_k^l(\mathbf{r}) \right)
\end{aligned} \tag{3.10}$$

where we have explicitly separated the $k = l$ situation (and dropped the irrelevant 1 index on the position operator). Since we are primarily concerned with the electron density evolution in the ground state, we may at first neglect the other ($k \neq l$) terms, because they are related to "connections" between the different excited states. Using equation (3.8), we can then write

$$\Delta\rho(\mathbf{r}) = c_0^2 \left(\sum_{k \neq 0} \frac{|\langle k|\mathcal{H}_{pert}|0\rangle|^2}{(E_k - E_0)^2} (\rho_k(\mathbf{r}) - \rho_0(\mathbf{r})) + 2 \sum_{k \neq 0} \frac{\langle k|\mathcal{H}_{pert}|0\rangle}{E_k - E_0} \rho_0^k(\mathbf{r}) \right). \tag{3.11}$$

This electron density variation is expected to convey the same meaning as the DD: it translates the electron density variations upon the perturbative approach of a molecule. As we can notice, we do not retrieve a direct mapping with the state-specific formulation, because of the second term (transition densities). It is tempting to state that these terms are negligible, but no clear argument can be put forward to confirm this.

However, we can still note the explicit convergence of both terms of equation (3.11) with the excitation energy, thus suggesting the reactivity is primarily controlled by the very first excited states. Of course, this argument needs to be tempered by the impossibility to unambiguously relate the weighting parameters ω_i of the state-specific equation (3.3) to the excitation energies, and also by the presence of the matrix terms $\langle k|\mathcal{H}_{pert}|0\rangle$ in both terms of equation (3.11). These indeed suggest that higher excited states may contribute significantly to the ground state reactivity, provided that they are efficiently connected to it by the perturbation. This is actually in perfect line with published data: sometimes, one needs to consider the second or third state-specific DD in order to describe correctly the reactivity of molecules. Noteworthy, this also correlates to an older study of Pearson, who tried to link optical properties to reactivity: he eventually had to come to the conclusion that some molecules do not show a marked reactivity despite a low lying excited state, and assumed this was due to the nature of the excited state (non-reactive).[91]

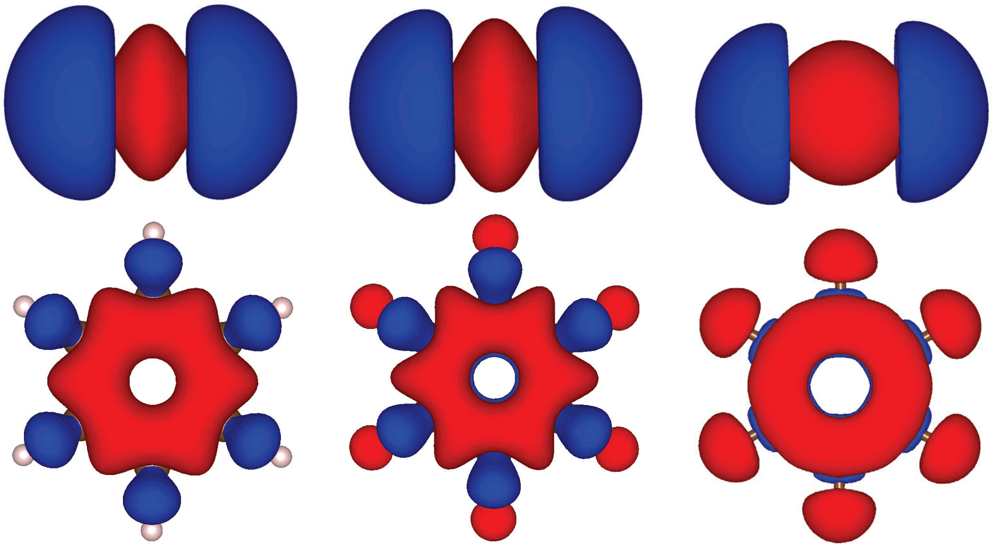

FIGURE 3.1.2: Computed isosurfaces of DD for H_2 (top) and benzene (bottom), calculated using the frontier MO densities (left), the first excited state density (middle) or an average of the ground electron densities under an electrostatic field of 0.1 a.u. (right). Method: B3LYP/6-311+G*. Colour scheme: $\Delta f(\mathbf{r}) < 0$, red; $\Delta f(\mathbf{r}) > 0$, blue.

A new computational approach of the DD. More interestingly, the previous development suggests a new way to compute the DD. In order to explicit the weight of each excitation in equation (3.3), we indeed identified the DD to the electron density variation upon the application of an electrostatic field. Actually, many quantum chemistry software offer the possibility to take into account such a field explicitly[(iv)]. It is then possible to compare directly the electron densities with and without an external field, and as such to access the DD.

In fact, this quantity will not be exactly equivalent to the one we may obtain using the finite difference scheme or the state-specific formulation. In these cases indeed, no as-

---

(iv) Or implicitly, placing point charges in space in order to create a field.

sumption is made on the geometry of approach of the incoming reagent. This means we should consider any possible orientation of the electrostatic field in order to have a complete and precise picture of the DD. Such calculations might not be used in practice, but a lot of information may already be obtained if we consider three non-coplanar directions of the field and, for each direction, 2 possible orientations – for instance, $\pm\mathbf{x}$, $\pm\mathbf{y}$, $\pm\mathbf{z}$ –. Two examples are provided on Figure 3.1.2, where we represent the DD according to the Frontier MO approximation – *cf.* formula (1.58) –, the first state-specific DD, and the electron density variation upon the application of an electrostatic field, for a molecule of dihydrogen and a molecule of benzene. The three approaches deliver similar responses, with a marked nucleophilicity due to the σ bond for H_2 and to the π electron cloud for benzene. Slight distortions are observed when comparing the "usual" DD formulations and the electrostatic response, and may likely be due to the limited number of electrostatic field orientations we considered here.

NOTE: in total line with Pearson's argument, we are linking reactivity and molecular polarisability. Most probably, the previous development may be written in terms of local polarisability.[92] This will receive our attention in a very close future.

3.2 Dual Descriptor and Molecular Electrostatic Potential: complementary tools for the study of ambiphilic ligands

In Chapter 3, we presented the basic concepts of the metal-ligand interactions in coordination complexes. Noticeably, we discussed the fact that all the concepts that are usually introduced in a MO theory framework can actually be generalised in an extended Klopman-Salem model.[61,62] We propose to develop these arguments in this part.

Our first study concerns the modelling of the coordination properties of ligands. In the simplest scheme, metal cations are perfect Lewis acids, displaying a total deficit of electrons, and ligands are perfect Lewis bases that coordinates in order to counteract the metal acidity.[51,54] Stating the obvious, this means metal cations in complexes will display a rather marked electrophilicity and ligands a strong nucleophilicity, or marked charges if the species are hard.

Nevertheless, it is also known that ligands may display some electrophilicity, and metal cations can also display a donor character.[93] Coordination is thus the resultant of different charge transfers and electrostatic interactions, and if we want to model it correctly we need to use adapted descriptors for these different phenomena. The DD seems particularly fit to describe the charge transfer phenomena. Electrostatic effects, on the other hand, can be efficiently accounted for by the Molecular Electrostatic Potential (MEP).[94,95] In the following subsection, we will explain how we may extract quantitative information from these two descriptors.

3.2.1 Theoretical model

Molecular Electrostatic Potential

MEP is defined as the electrostatic potential created at any point $\mathbf{r}_i$ by the electron density and nuclei distribution,

$$MEP(\mathbf{r}_i) = \sum_M \frac{Z_M}{|\mathbf{R}_M - \mathbf{r}_i|} + \int_{\mathbb{R}^3} \frac{\rho(\mathbf{r})}{|\mathbf{r} - \mathbf{r}_i|} d^3\mathbf{r}, \tag{3.12}$$

and can be seen as a measure of the stabilisation or destabilisation a point charge would feel if placed at any point $\mathbf{r}_i$. Regions with $MEP < 0$ are attractive for positive charges, while regions with $MEP > 0$ are repulsive. Noteworthy, if the system has a zero total charge we expect to observe both kind of regions in space. On the other hand, if the ligand is charged there may be only one type of regions – for instance, only $MEP > 0$ if it is cationic.

Condensed Grand-canonical Dual Descriptor

Here, we decided to study a set of small molecules which are known to be efficient ligands or not, and to see if the combination of the DD and the MEP allowed us to rationalise their coordination chemistry straightforwardly. We gathered them in sets of similar reactivity (expected or known), in Table 3.1.

Since we are comparing systems with different number of electrons, it is not possible to compare directly the DD values. This is because the DD is formulated in the canonical ensemble(v). A similar quantity can be defined in the grand-canonical ensemble(vi) [36,37]

$$\Delta s(\mathbf{r}) = \left(\frac{\partial^2 \rho(\mathbf{r})}{\partial \mu^2}\right)_{v(\mathbf{r})} = \frac{\Delta f(\mathbf{r})}{\eta^2} - \frac{\gamma}{\eta^3} f(\mathbf{r}) \tag{3.13}$$

where γ is the hyperhardness (N-derivative of the chemical hardness) and $f(\mathbf{r})$ the Fukui function. Since the ratio γ/η^3 is generally small (at least γ/η^3 is smaller than $1/\eta^2$), we can safely neglect the last term of equation (3.13). The grand-canonical DD (GCDD) thus approximates to the DD scaled by the square of the chemical hardness, which we will compute as the energy difference $E_{LUMO} - E_{HOMO}$.

The GC-DD, as the DD, should integrate to 0 over all space, which means the system should display both nucleophilic and electrophilic basins. In order to get a quantitative information, and at the same time to ease the interpretation, it is desirable to be able to condense the GC-DD in each nucleophilic and electrophilic basin. Vincent Tognetti recently developed a program that allows such a condensation, named *Domains*.[96] Briefly, this program follows the nodal planes of a given real function of $\mathbb{R}^3$(vii), thus defining domains into which the function can be integrated. From this condensation scheme, it is possible to obtain the integrated value over a domain, the mean value (integrated value divided by the volume), the volume of the domain, and the location of the barycentre and of each domain.

TABLE 3.1: Series of ligands.

Series	Ligands
1	H_2, ethene
2	F_2, Cl_2, Br_2, I_2
3	O_2, $O_2^{-\cdot}$, O_2^{2-}
4	NO^+, CO, CN^-
5	$NO^{\cdot}$
6	SCN^-
7	Acac, Hfac

(v) *I.e.*, for fixed N and E.

(vi) With a fixed chemical potential but a varying number of electrons.

(vii) In the Gaussian Cube format.

Computational details

Structures of ligands in Table 3.1 were fully optimised at the DFT level of theory (B3LYP). Calculations were carried out using 6-31G(d) basis sets, except for

- the thiocyanate ion SCN^-, modelled using the 6-31+G(d) basis set;
- the dihalogens, modelled using the DGDZVP basis set.

In the latter case, the DGDZVP basis set was used to ensure the internal consistency of the method (same basis set and functionnal for the whole series).

The ten first excited states were calculated at the TD-B3LYP level, and the GC-DD was – unless stated otherwise – evaluated using the first excited state. All calculations were performed with Gaussian 09, using default parameters, unless mentioned.[97]

3.2.2 Results and discussion

Series 1: H_2 and ethene. Ethene and dihydrogen usually present a similar reactivity as ligands, coordinating in a η^2 mode with their main bond. The computed DD and MEP surfaces are presented on Figure 3.2.1, and it is plain to see that we retrieve the expected chemical behaviour. Both ligands indeed present a nucleophilic development in the middle of their main bond (H-H or C=C), where they are supposed to coordinate. MEP indicates the same coordination mode, since (negative) minima are found on the same positions. In the case of ethene, the minimum value is one order of magnitude larger than that of H_2, which suggest ethene may be a more efficient ligand than hydrogen – which is actually experimentally observed.

Furthermore, electrophilic developments are seen in the vicinity of the nucleophilic contribution, and as such one could expect these two ligands to give rise to MLCT. Such back-bonding effects have actually been observed in some ethylene complexes, such as tris-ethylene nickel(0).[98] They are also consistent with the difficulty to ascertain the oxidation degree of some dihydrogen complexes,[99] and the propensity of H_2 to give rise to oxidative addition – for instance in Vaska's complex $[IrCl(CO)(PPh_3)_2]$.[100]

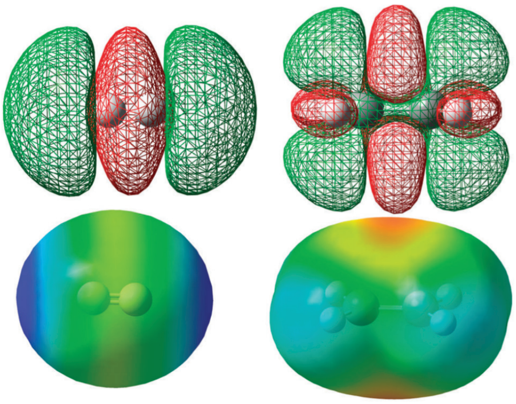

FIGURE 3.2.1: Up: DD isosurfaces for H_2 (left) and ethene (right). Isovalues: $\pm 4.10^3$ (green, positive; red, negative). Down: MEP maps on density isosurfaces (10^{-3} a.u.), values ranging from $+3.00 \times 10^{-2}$ (blue) to -3.00×10^{-2} (red) in the case of ethene, 1.00×10^{-3} to -1.00×10^{-3} (same colours) for H_2. Calculations at the (TD)-B3LYP/6-31G(d) level.

TABLE 3.2: Condensed GC-DD values for the dihalogens.

Molecule	Nucl. cont. (a.u.)	Elec. cont. (a.u.)
F_2	-9.17	9.17
Cl_2	-21.27	21.32
Br_2	-31.39	31.49
I_2	-48.06	48.12

Series 2: dihalogens. Dihalogens were gathered in the same series for rather obvious reasons. As Rogachev and Hoffmann pointed out,[101] despite having accessible lone pairs they do not tend to coordinate efficiently. Actually, they tend to oxidatively add to any complex, and only a few iodine complexes could be isolated so far.[102–105]

We represented on Figure 3.2.2 the first state-specific GC-DD and MEP maps for series **2**. Note that in these cases the two first excited states are exactly degenerate ($\pi^\star \rightarrow \sigma^\star$ excitations in a MO framework), and the corresponding state-specific DD are exactly alike but rotated along the molecular axis. For the sake of simplicity, we only display here one of them.

All dihalogens present very similar features, as could be expected. They all display electrophilicity along the molecular axis, and nucleophilic contributions on each side of the bond, where we would expect to find the lone pairs in a Lewis scheme. These features are in good agreement with the known data on iodine complexes. It is indeed displaying a donor (nucleophilic) character when coordinating in a bent "side-on" geometry, and an acceptor character when coordinating in a linear fashion. This is also corroborated by the MEP: negative MEP values are indeed only found on the sides of the halogen atoms, where the coordination is mostly expected (donor character). The maximal values of the MEP are found along the molecular axes, forming so-called σ holes.[106]

In both cases (GC-DD and MEP), the values are significantly increasing when moving from fluorine to iodine. Noticeably, it is plain from the graphical representation that the negative MEP areas are larger in the case of the heavy halogens, thus suggesting they may more efficiently stabilise cations than the lighter ones. This is also retrieved at the GC-DD level: integrated values, displayed in Table 3.2, are larger the heavier the halogen.

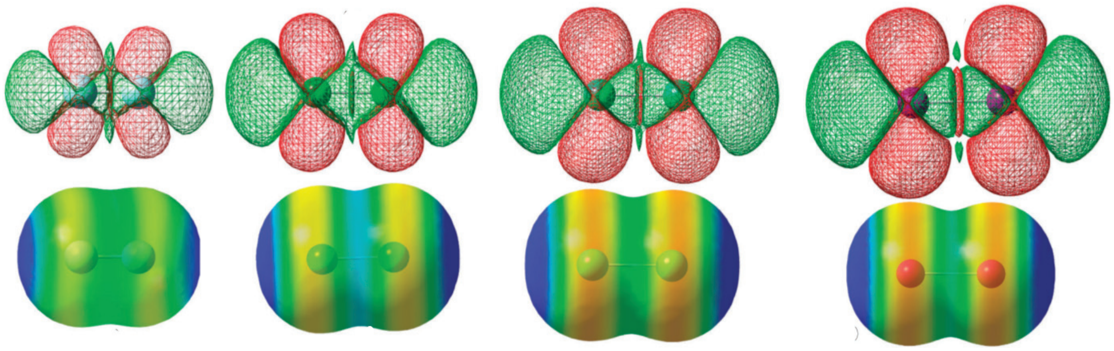

FIGURE 3.2.2: Up: DD isosurfaces for F_2, Cl_2, Br_2 and I_2 (from left to right). Isovalues: $\pm 4.10^3$. Down: MEP maps on density isosurfaces (10^{-3} a.u.), values ranging from $+1.00 \times 10^{-2}$ to -1.00×10^{-2}. Same colour scheme as in Figure 3.2.1. Calculations at the (TD)-B3LYP/DGDZVP level.

We are thus able to retrieve the coordination properties of iodine, and we may also guess why such a little number of acceptor I_2 complexes are found: linear coordination indeed leads the metal cations to approach iodine *via* its σ hole. From the viewpoint

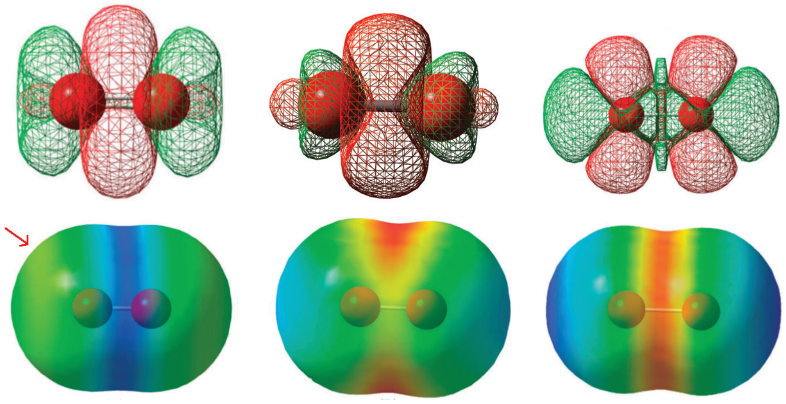

FIGURE 3.2.3: DD and MEP isosurfaces for series **3**. Same isovalues and colour scheme for the DD surfaces as previously. MEP ranges: -10^{-2} to 10^{-2} a.u. in the case of dioxo, -0.28 to -0.21 a.u. for superoxo and -0.55 to -0.45 a.u. for peroxo. Calculations at the (TD)-B3LYP/6-31G(d) level for the dioxo and peroxo ligands, and at the SA-CAS(7,4)/6-31G(d) level for superoxo.

of electrostatics, this interaction is destabilising, and will only be feasible if the covalent interactions (bonding and back-bonding) are stronger.

The rarity of dihalogen based complexes seems nevertheless unaccounted by our model. This is not a pitfall, but merely a question of viewpoint. As we noted previously, most of the time dihalogens simply oxidise coordination compounds (through oxidative addition).[103] They indeed display high redox potential[107] (standard values of +2.866 V/ECS, +1.358 V/ECS, +1.087 V/ECS and +0.536 V/ECS down the series), and from these numerical values the differentiation between iodine and the other halogens is rather plain. Here, we decided to focus on the coordination properties, and thus we implicitely assumed electron density perturbations – compared to the case of isolated ligands – would be small. Stating the obvious, an oxidative addition is *not* a small perturbation, and it is not surprising that we actually miss the point.

Series 3: from dioxo to peroxo. O_2 and its related anions, namely superoxo $O_2^{-\cdot}$ and peroxo O_2^{2-}, are of utmost importance in bioinorganic chemistry. They indeed take part in respiratory mechanisms, but also in oxidation cycles.[108,109]

Figure 3.2.3 presents the DD and MEP isosurfaces for these three molecules. As one can see, the features are very different. In the case of dioxo, the DD displays nucleophilicity mainly away from the O-O bond, but also slightly along the molecular axis. On the other hand, electrophilicity is found on the sides of the molecule, pointing out of the molecular axis with some angle. Interestingly, the GC-DD has a perfect cylindrical symmetry, as would be expected. These features can be understood rather straightforwardly in the framework of MO theory (see the MO diagram below). The nucleophilic contribution indeed displays a shape that is reminiscent of (occupied) bonding 2π and 2σ orbitals, whereas the electrophilic part resembles antibonding (semi-occupied) $2\pi^\star$ and (vacant) $2\sigma^\star$ orbitals.

In any case, dioxygen seems likely to coordinate via its main bond, in a way that resembles the coordination of H_2. However, unlike dihydrogen the MEP values on this site are quite positive (9.10^{-3} a.u.), suggesting that cations may not approach this position. The only negative MEP values are actually found on the sides of O atoms, roughly at the same position as the electrophilic lobes of the DD (red arrow on Figure 3.2.3). This means that dioxygen will likely tend to approach cations by its electrophilic areas. As such, we would expect dioxygen to behave like an acceptor ligand when coordinating in a bent side-on geometry to cations, and like a donor when coordinating by the main bond. However, even in this latter geometry dioxygen may present an acceptor character, since electrophilic basins surround the coordinating nucleophilic area.

These findings are in quite good agreement with known data on dioxygen coordination. To our best knowledge indeed, dioxygen always reduces upon coordination, either to superoxo or peroxo. For instance, in the oxygenated form of haemoglobin,[110] the Fe(II)-porphyrin complex is transformed to what is best described as a Fe(III)-superoxo complex. In the catechol-oxidase complex,[108] the two Cu(I) centres oxidise to Cu(II) upon chelation of dioxygen, which thus may be described as a peroxo ligand.

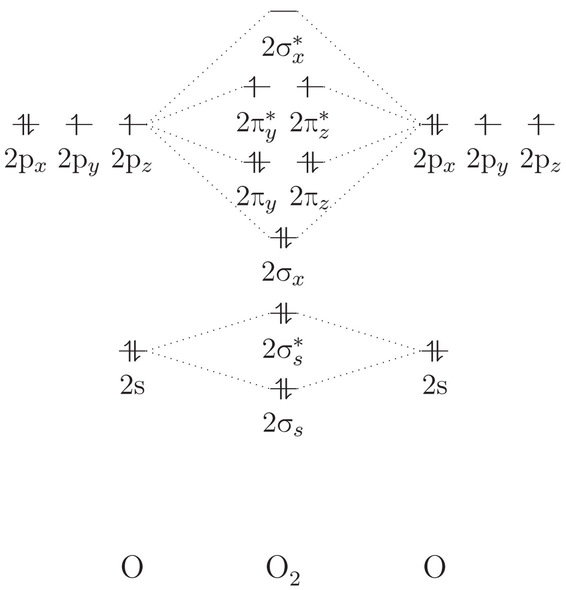

SCHEME 3.2.1: MO diagram for dioxygen in its ground triplet state.

Actually, the DD features of peroxo are very reminiscent of those of the dihalogens. This could be quite expected since O_2^{2-} and F_2 are isoelectronic, and in the framework of the MO theory their wavefunction are expect to be very similar. Similar coordination properties can be expected: acceptor character when coordinating in a linear fashion, donor when coordinating in a bent geometry. In terms of MEP, since peroxo is a dianion we would rather expect to observe only negative values on the isodensity surface. This is indeed the case, which means that any geometry of approach of a cation would virtually be stabilising. The maximal stabilisation is expected when approaching peroxo by the middle of the O-O bond, since a ring of minimum MEP is observed on this region. This in total compliance with the known geometry of coordination of peroxo in the aforementionned oxidase complex: upon coordination to the two Cu(I) centres, dioxygens reduces to peroxo, which remains fixed to the Cu(II) ions since the geometry that O_2 adopted is also stabilising for peroxo. Furthermore, our calculations suggests an explanation of the mechanism behind the reactivity of this oxidase complex. It is indeed known to oxidise phenols, which means the complex tends to accumulate more electrons. This could be achieved by taking advantage of the electrophilic basins of peroxo, which in the enzymatic pocket are pointing outside the coordination area (thus very likely in contact with the environment).

In the case of superoxo, things are slightly more complex. Indeed, it is expected to display a degenerate ground state(viii). This is actually obvious if we look at the MO diagram of

---

(viii) Which we completely yet unintentionally overlooked in the publication relative to this work. An

O_2, displayed on Scheme 3.2.1: an additional spin down electron could be placed either in the $2\pi_y^\star$ or $2\pi_z^\star$ MO, and both configurations will have the same energy. Thus, superoxo cannot be properly modelled using DFT. Here, we modelled superoxo using SA-CASSCF calculations, as implemented in ORCA 3.0.[111] From the MO diagram, we restricted the active space to the 2π and $2\pi^\star$ orbitals, thus leading to CAS(7,4) calculations. The starting set of MO was provided by a ROPBE calculation(ix). Since the degeneracy of the ground state is two, we averaged the CASSCF calculation over the two lowest doublet roots.

In this case, it seemed convenient to use our newly proposed formulation of the DD. We thus performed a set of SA-CASCCF calculations with and without a dipolar electrostatic field, set along 3 orthogonal directions, with two opposite orientations each(x). As one can see from Figure 3.2.3, the aspect of the DD for superoxo is very close to that of dioxygen. In the framework of MO theory, this is rather logical: the MO diagrams are very similar. In terms of MEP, here also only negative values are observed, which is logical since superoxo is an anion. Absolute minima are found on each side of the bond, in a way that recalls the features of peroxo. Note that on Figure 3.2.3, the MEP representation is given only for one of the two CASSCF roots, hence explaining why the cylindrical symmetry is not apparent(xi).

Overall, superoxo is expected to coordinate easily to cations (electrostatic stabilisation), and to display both donor and acceptor behaviour depending on the coordination geometry.

Series 4: nitrosium, carbonyl and cyanide. NO^+, CO and CN^- are isoelectronic species, and it is well established now they show similar coordination properties. Noticeably, they are known to provide roughly the same crystal field splitting, which indicates they tend to have the same donor and acceptor properties.[51,54] This is actually plain from the aspect of the DD, represented on Figure 3.2.4. In all cases indeed, the same shapes are obtained(xii). Nucleophilic domains are observed along the molecular axes, pointing outwards from the molecules. They are larger on the most electropositive atom (C in carbonyl and cyanide, N in nitrosium), which is generally the coordinating atom. Interestingly, these domains point exactly towards the local minima of the MEP (along the molecular axis). This suggests these species would coordinate in a linear fashion, which is actually observed.

The development of electrophilic domains in the vicinity of this coordination area furthermore suggests they would tend to display rather strong back-bonding. This is also experimentally observed, these ligands being characterised by very strong ligand fields. Actually, we may even retrieve the tendency described in the spectrochemical series: nitrosium is indeed expected to display a smaller ligand field that carbonyl and cyanide.

---

erratum will soon follow.

(ix) It is generally advised to use the output of any correlated method as input for the CASSCF calculation, thus explaining the choice of a DFT method.[16]

(x) Dipolar electrostatic fields are unfortunately not yet implemented in ORCA. We thus modelled them using two opposite point charges (magnitude 1 u.a.) placed at 4 Å and 4.5Å of the molecule. For each direction, a second calculation was performed by permutting the point charges.

(xi) A weird bug of ORCA lead the program to exit without printing the CASSCF density matrix, and thus the MEP calculations first involve the reconstruction of the latter from the MOs. The program thus computes the electron density for one of the two roots only, and there seems to be no way to get the MEP for the SA-CASSCF density matrix...

(xii) Note that, as what was observed for dihalogens, the two first excitations for these molecules are in each case degenerate, and lead exactly to same DD representation, simply rotated along the molecular axis. For the sake of simplicity, we simply represent here the first state-specific DD.

Condensation of the GCDD yields the values listed in Table 3.3, which agree with the expected tendency.

TABLE 3.3: Condensed GC-DD values for series **4**.

Molecule	Nucl. cont. (a.u.)	Elec. cont. (a.u.)
CN^-	-5.07	5.06
CO	-4.38	4.37
NO^+	-3.18	3.17

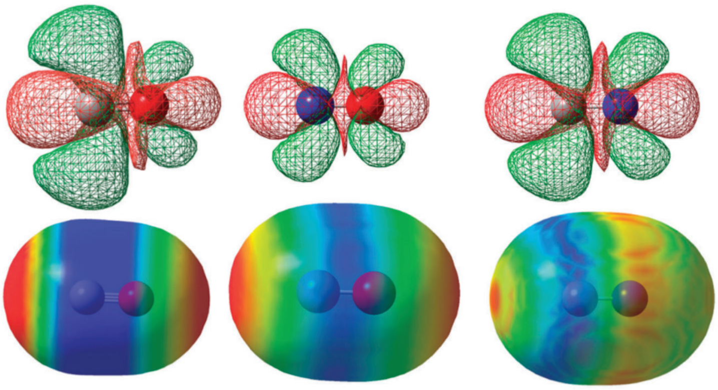

FIGURE 3.2.4: DD isosurfaces (top) and MEP maps (bottom) for series **4**. Same colour scheme and isovalues for the DD isosurfaces as Figure 3.2.3. MEP ranges: -2.10^{-2} to 2.10^{-2} a.u. in the case of carbonyl, 0.25 to 0.30 a.u. for nitrosium and -0.24 to -0.23 a.u. for cyanide. Calculations at the (TD)-B3LYP/6-31G(d) level.

Our calculations thus reproduce quite well the general behaviour of the series, but they also account for the slight differences between the different ligands. For instance, nitrosium and carbonyl tend to form isolated complexes, while cyanide is known to yield bridged entities, like the Prussian blue analogues.[112] This is probably due to the fact that MEP is negative on every point of the isodensity surface of cyanide, thus enabling coordination *via* the N atom of cyanide. Furthermore, the DD features also permit to rationalise the strong magnetic couplings that can be observed in these Prussian blue analogues: because of the marked back-bonding ability of cyanide, an efficient interaction can be engaged between the two bridged cations.[64]

We can also understand why the vast majority of cyanide and carbonyl complexes tend to be linear, while nitrosyl complexes display a much wider range of geometries. In the two former cases, there is an interplay between covalent and electrostatic control, which both suggest linear coordination should be favored. In the latter case of NO^+, on any point of the isodensity surface the MEP is positive, thus repulsive for cations. This means coordination of NO^+ will only be controled by covalent interactions, and thus will depend a lot on the relative philicity of the metal cation: when the metal centre will be rich in electrons, NO^+ will tend to act as an acceptor ligand and coordinate in a bent fashion,[51] while electron-deficient metal centres will lead NO^+ to coordinate in a linear fashion, acting principally as an electron donor.[113]

Series 5: nitrosyl. In the previous section, we discussed a few results for NO^+, which is one of the limit forms that one usually writes to describe the behaviour of a one-electron donor nitrosyl ligand. Nitrosyl is indeed known to be a non-innocent ligand, whose oxidation state is never plain: it always balances between NO^+ and NO^-.[114,115]

Usually, nitrosyl is introduced in the reaction medium in its neutral state $NO^{\bullet}$, and thus it may be relevant to study the DD and MEP feature of this species.
They are represented on Figure 3.2.5. In that case, we also had to use SA-CASSCF calculations since the ground state of $NO^{\bullet}$ is twice degenerate. This is rather plain to see from the MO diagram, displayed on Scheme 3.2.2. Here also, we limited the active space to the 2π and $2\pi^{\star}$ orbitals, thus employing SA-CAS(5,4) calculations. We also averaged over the first two doublet roots, and used the same electrostatic formulation as for superoxo. As one can see from Figure 3.2.5, we retrieve a shape that is reminiscent of what was observed for series **4**[xiii]. As already underlined in the case of superoxo, this is rather logical in the framework of MO theory: the first excitations in both cases involve the same kind of orbitals. We thus retrieve a nucleophilic contribution along the molecular axis, which is more pronounced on the N atoms. This is in a very good agreement with experimental data, nitrosyl coordinating systematically by the nitrogen atom.[xiv] We also retrieve a marked electrophilicity in the vicinity of the coordination area, which is also consistent with the strong acceptor behaviour nitrosyl displays when coordinating.

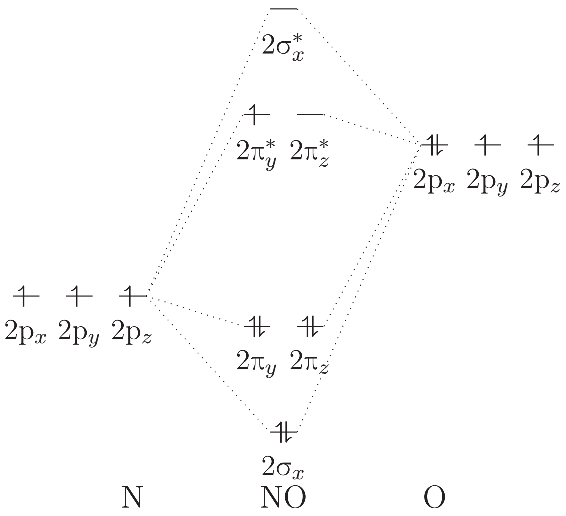

SCHEME 3.2.2: Part of the MO diagram of $NO^{\bullet}$.

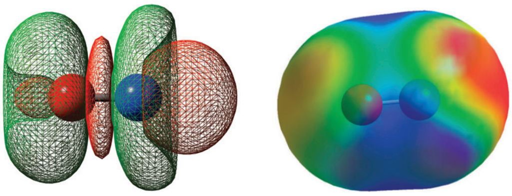

FIGURE 3.2.5: DD isosurfaces (left) and MEP maps (right) for $NO^{\bullet}$. Same colour scheme and isovalues for the DD as in Figure 3.2.4. MEP ranges: -0.012 a.u. to $+0.012$ a.u. Calculations at the SA-CAS(5,4)/6-31G(d) level.

MEP shows diffuse minima around both N and O atoms, which suggest coordination by the nitrogen atoms can be achieved in a linear or bent geometry, as experimentally

---

[xiii] Note that, since we decided to average over the two ground CASSCF roots, we actually observe a perfect cylindrical symmetry.

[xiv] O-coordination is also found, but only in metastable states, and upon light irradiation of a N-bonded complex.

observed(xv). From the shape of the DD, we can expect nitrosyl to display a much more donor character when coordinating in a linear fashion. This is actually the case, nitrosyl being found linearly coordinated to electrophilic metal cations (electron deficient), while bent coordinations are encountered in more electron-rich complexes.

Series 6: thiocyanate. Thiocyanate is an ubiquitous ligand in coordination chemistry, thanks to its ambidenticity. It is indeed known to coordinate hard species by its N atom, and in a linear geometry, while it coordinates soft metals by its S atom, usually in a bent geometry.[116] The MEP and DD are displayed on Figure 3.2.6.

As one can see, the nitrogen atom shows essentially a nucleophilic behaviour, while the sulfur atom displays both electrophilic and nucleophilic contributions. The largest contributions are found on the sulfur, which complies with our expectations: in a HSAB framework, sulfur should appear more reactive than the N atom (which is hard). Furthermore, from the shape of the nucleophilic basin on the S atom we would expect a bent coordination of thiocyanate, as observed. On the other hand, the MEP suggests linear N-coordination, since the absolute minimum on the isodensity surface is observed along the molecular axis. Once again, this is in good agreement with experimental data.

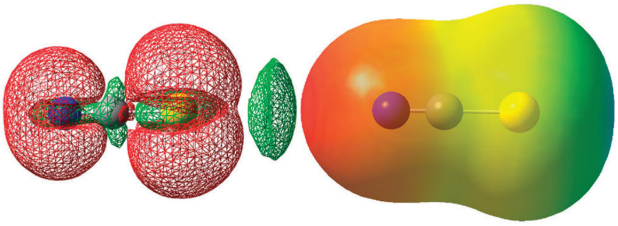

FIGURE 3.2.6: DD isosurfaces (left) and MEP map (right) for SCN$^-$. Same colour scheme and DD isovalues as Figure 3.2.5. MEP ranges: -0.2 a.u. to -0.15 a.u. Calculations at the (TD)-B3LYP/6-31+G(d) level.

Acetylacetonate and hexafluoroacetylacetonate. Acetylacetonate (acac) and its hexafluorinated analogue (hfac) are two widely used ligands in coordination chemistry. Noticeably, they are often used for their "Lewis acidity enhancement" properties: when coordinated to a metal cation, they tend to exacerbate its electrophilicity (hfac being more effective than acac).[117] This means they both need to be both good electron donors and acceptors.

This is retrieved at the DD level, as can be seen from Figure 3.2.7. In both cases indeed, nucleophilic domains are observed on the (coordinating) oxygen atoms, pointing inside the conjugated plane. They are reminiscent of oxygen lone-pairs, as expected, and are found in the same region as the MEP minima (-0.28 a.u. for acac, -0.23 a.u. for hfac). This is in very good agreement with experimental expectations: acac and hfac are expected to coordinate metal cations by their O atoms, in the molecular plane. As one may notice, electrophilic developments can be found perpendicular to the nucleophilic domains on oxygen atoms. Their shape is reminiscent of a $\pi^\star$ orbital, as could be expected, and suggest both ligands should display a marked tendency towards back-bonding. This is indeed expected from their Lewis acidity enhancement activity.

From our calculations, the difference between the hydrogenated and fluorinated form is not obvious. The value of the minimum of the MEP is smaller for hfac, as could be expected

---

(xv) The same bug as previously applies here: MEP representation here holds for one of the two CASSCF roots, thus explaining the non-cylindrical symmetry.

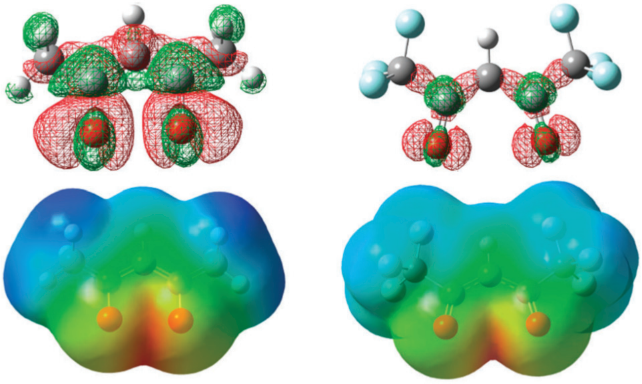

FIGURE 3.2.7: DD isosurfaces (top) and MEP maps (bottom) for acac (left) and hfac (right). Same colour scheme as Figure 3.2.5. MEP ranges: −0.28 a.u. to −0.10 a.u. (acac), −0.21 a.u. to −0.10 a.u. (hfac). Calculations at the (TD)-B3LYP/6-31G(d) level.

from the strong electron-withdrawing behaviour of trifluoromethyl group. Comparatively, one would then expect acac to show a coordination that is more driven by electrostatics than what hfac does. Furthermore, if we look more into details, we can see that the electrophilic and nucleophilic developments of hfac are very comparable, while in the case of acac the nucleophilic contributions are more extended in space than the electrophilic ones. Likely, this will make hfac a more electron withdrawing ligand than acac (relatively to the donor character), as experimentally observed.

3.2.3 Conclusion

In this section, we have seen that both the DD and the MEP allow, at the price of very simple calculations on ligands, to retrieve their coordination properties. In most cases, MEP and DD suggest the same coordination geometry. However, there are cases where both descriptors are complementary but not equivalent. For instance, in the case of dioxo we have seen that electrostatic effects lead O_2 to coordinate as a strongly acceptor ligand, because the nucleophilic areas are located in rather electropositive regions. This permitted us to explain the impossibility to isolate genuine dioxygen complexes so far: they all reduce to superoxo or peroxo. More generally, the DD permits to retrieve very simply the electronic behaviour of the ligands, but the scope is not limited to this.

As we will show in the next section, the DD may indeed be a valuable tool in the rationalisation of the chemical properties of coordination compounds, for instance allowing us to rationalise the *trans* effects in octahedral complexes.

NOTE: as already evoqued in this section, this work has been published in *Phys. Chem. Chem. Phys.* **2014**, 16, 15558-15569.

3.3 A new approach of the trans effects in octahedral complexes

In this section, we propose to show how the DD permits to rationalise and understand the chemical properties of some coordination complexes. More specifically, we will interest ourselves on the *trans* effects in octahedral complexes.

Trans effects are characterised by the modulation of a coordination bond in a complex under the influence of the ligand on the opposite position in the coordination sphere (hence the label *trans*).[51,54,118] They are mostly observed in square-planar[119] and octahedral complexes,[120] and can be divided into two distinct phenomena: the Kinetic *Trans* Effect and the Static *Trans* Effect.

In the first case, the modulation impacts the substitution kinetics of a ligand: the more *trans*-orienting a ligand is, the faster the ligand on the opposite coordination will be replaced. In the second case, the effect is purely static, and it is the metal-ligand bond lengths that are perturbed: the more *trans*-orienting a ligand is, the longer the opposite bond is. These effects are widely used in inorganic chemistry, being used in complexes with marked catalytic activities and selectivity for instance,[121–123] but also acting in natural metalloproteins[124–126] or anti-cancer drugs[127–129].

As such, understanding the origins of both STE and KTE is of paramount importance. Many experimental and theoretical studies were devoted to this task,[130–138] and it is only quite recently that KTE was firmly rationalised in the case of square planar complexes. It could be shown indeed, on a rather representative set of square-planar complexes, that two main mechanisms were acting beneath their KTE.[139,140]

First of all, as was long presumed by coordination chemists, electron donation effects have an important role: if the ligand on the *trans* position is an efficient electron donor, it may lead the opposite coordination site to be quite saturated with electrons. This leads to a marked Pauli repulsion between the electron density on the metal cation and the electron density from the ligand, which thus interacts more weakly with the metal and should be more easily replaced.

In addition to this Pauli repulsion effect, the *trans* orienting ligands can furthermore ease the metathesis on the opposite coordination position by their back-bonding properties. They can indeed withdraw electron density on the metal cation on the positions where an incoming ligand would attack, and as such they tend to stabilise the transition states of metathesis. This can be understood quite straightforwardly in a MO theory framework, as pictured on Scheme 3.3.1.

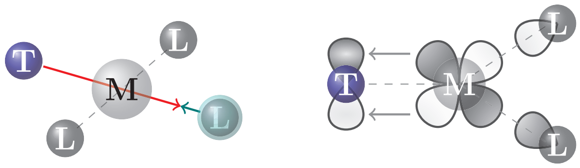

Scheme 3.3.1: Schematic representation of the Pauli repulsion (left) and back-bonding (right) mechanisms beneath the KTE in square-planar complexes.

We thus wondered whether the same lines of argument could hold in the case of the octahedral complexes; we felt there were no reasons they would not. As we can see, the two effects acting beneath the KTE of square-planar complexes involve the same kind of mechanisms as those we were discussing in the previous part: electron density reshuffles (readaptations). This suggests we could tentatively probe them using the DD.

3.3.1 Theoretical model

Theoretical tools

Here again, we employed the state-specific formalism in order to compute the DD, which we scaled using the square of the chemical hardness in order to obtain the Grand Canonical

DD. We also employed Domains condensation scheme, in order to extract quantitative information on the *trans* effects.

We also used another tool, which was not developed in the framework of conceptual DFT: the Extended Transition State - Natural Orbitals for Chemical Valence (ETS-NOCV).[141–143] When two isolated molecules are allowed to interact, the electron density of the total system can be written as a sum of the electron densitites of each separated fragment plus a deformation term. The NOCV are the eigenvectors Ψ_i of this deformation density matrix ($\Delta\rho(\mathbf{r})$). Mathematically, this translates as

$$\Delta\rho(\mathbf{r}) = \sum_m \nu_m \left[-\Psi_{-m}(\mathbf{r})^2 + \Psi_m(\mathbf{r})^2\right] \tag{3.14}$$

where it appears clearly that the NOCVs are paired.

Without getting too involved with the mathematics behind the NOCV, we can briefly state they permit to decompose the electron density reorganisation between the two fragments into well-defined orbital contributions with a given number of transferred electrons ν_m. Thus, it is possible for instance to distinguish between σ and π donation effects, and to quantitatively evaluate the effect of each, thus enabling comparisons.[144] Furthermore, thanks to the Extended Transition State formalism, it is possible to associate with each NOCV pair a given energetic stabilisation, thus helping the comparisons.[145]

Methodology and computational details

Here, we want to probe both STE and KTE in the case of octahedral complexes. In terms of reactivity, it is assumed that most of octahedral complexes undergo dissociative metatheses: first the replaced ligand leaves the coordination sphere, and then it can be replaced by another one – see Scheme 3.3.2 –.[51,54] From the viewpoint of steric hindrance, this seems to make sense: the metal cation at the centre of an octahedron is much more shielded from its environment than it is in a square planar complex.

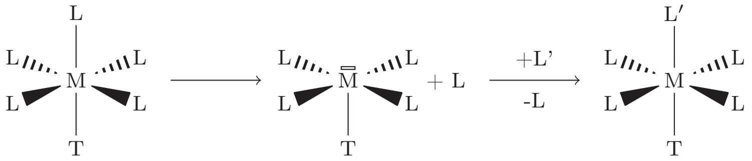

Scheme 3.3.2: Schematic representation of the dissociative mechanism of metathesis in an octahedral complex.

In turn, this means the unsaturated [ML_4T] entity might be the relevant species to study if we want to characterise the reactivity of an octahedral coordination complex. Furthermore, we can see that studying this species would allow us to gain some insight on the STE too: looking at the electronic properties of this unsaturated compound could give us information on the way it may accomodate a supplementary ligand on its vacancy.

We used a two-fold approach. First, we tried to characterise the *trans* effects by comparing, in the same complex, the *cis* and *trans* positions of coordination (relative to the most *trans*-orienting ligand), or by comparing the *trans* positions in two similar complexes. We thus chose a set of complexes that were known to display a marked STE or KTE, associated to a ligand that could also be found on the *cis* position with respect to the most *trans*-orienting ligand. They are given in Table 3.4.

TABLE 3.4: List of the studied complexes.

Label	Formula	Specifity
4.1	$[Co(NH_3)_2(NO_2)_3(CH_3)]^-$	STE, d^6, σ donors
4.2	$[NbO(NCS)_5]^{2-}$	STE, d^0, σ and π donors
4.3	$[RhL(PMe_3)_2(Cl)_3]$	STE, d^6, σ and π donors
4.4-H_2O	$[Rh(NH_3)_4(H_2O)_2]^{3+}$	KTE, d^6, σ donors
4.4-Cl	$[Rh(NH_3)_4(Cl)(H_2O)]^{2+}$	KTE, d^6, σ and π donors
4.5-OH	$[Co(en)_2(OH)(H_2O)]^{2+}$	KTE, d^6, σ and π donors
4.5-SO_3	$[Co(en)_2(SO_3)(H_2O)]^+$	KTE, d^6, π acceptors

We optimised their structure without symmetry restraint, at the B3LYP/6-311G(d) + SDD(metal) level, using Gaussian 09$^{(xvi)}$. Then, we removed either the ligand on the *trans* or *cis* position (with respect to the studied trans-orienting ligand), and we computed the GCDD of the resulting fragments. We also evaluated the NOCV associated to the coordination of the removed ligand to the corresponding fragments, using ADF2013 (B3LYP/TZV/Small Core).[146]

Second, we built two families of "theoretical" complexes having the same structures and only differing by one ligand T. We optimised their structures, then removed the ligand *trans* to T and computed the GC-DD of the corresponding unsaturated fragment. Using Domains, we condensed the GC-DD and tried to build a semi-quantitative scale of the *trans*-orienting ligands. Note that here we used the latest implementation of Domains, in which the user may define a radial threshold in order to suppress contributions from areas that are too close to nuclei (and thus supposedly not involved into reactivity). In the following, we employed the following thresholds: 0.2 a.u. for the DD (all points of the DD below 0.2 a.u. in absolute value were discarded) and 0.5 bohr as a radius threshold (all points closer than 0.5 bohr from any nucleus are discarded).

3.3.2 Results and discussion

Comparing *cis* and *trans* positions

Complex 4.1. Complex **4.1**, $[Co(NH_3)_2(NO_2)_3(CH_3)]^-$, is known to display a marked STE due to the methyl ligand.[147] The Co(III)-NO_2^- bond is indeed 0.10 Å longer when *trans* to the CH_3^- ligand. We thus here built two $[ML_5]$ fragments by removing either the *trans* (**4.1**-*trans*) or *cis* (**4.1**-*cis*) nitrito (with respect to methyl), and calculated the GC-DD for these two fragments.

As one can see from Figure 3.3.1, the GC-DD for the two species are quite similar. They noteworthy comprise a nucleophilic part recalling a non-bonding metal *d* orbital, and an electrophilic part that develops towards the coordination vacancy. This electrophilic feature could be expected: since we removed a ligand, thus very likely a nucleophile, we would expect the resulting fragment to display a marked electrophilicity, at least on the former position of the ligand.

The electrophilic domain D^+_{Co} looks much larger on the *cis* position than on the *trans* one. This is completely confirmed by the condensation with Domains, see Table 3.5. The integrated value of the GC-DD is approximately 7 times smaller for **4.1**-*trans* compared to **4.1**-*cis*, and since the volume of the corresponding basins are much more comparable

---

[(xvi)] In the case of the S and P atoms, we employed the 6-311+G(d) basis set, since it is known diffuse functions are called if one wants to correctly model these atoms.

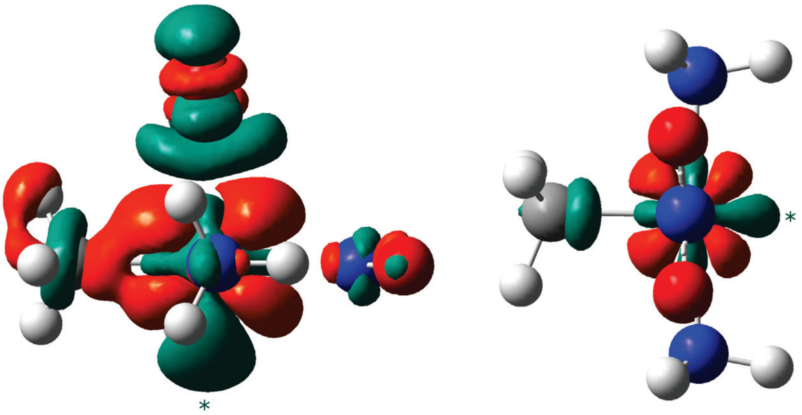

Figure 3.3.1: GC-DD isosurfaces for **4.1**-*cis* (left) and **4.1**-*trans* (right), at a ±0.4 a.u. isovalue. Electrophilic D^+_{Co} domains are highlighted with an asterisk. Colour scheme: red, negative values; green, positive values.

(30 % smaller for **4.1**-*trans*), as a result the mean value of the GC-DD is also much smaller for **4.1**-*trans*.

Table 3.5: Numerical values from the condensation of the electrophilic domains of the GC-DD, for fragments **4.1**-*cis* and **4.1**-*trans*. $\Delta s(D^+_{Co})$ is the integrated GC-DD value over domain D^+_{Co}, $\overline{\Delta s(D^+_{Co})}$ the mean GC-DD value and $V(D^+_{Co})$ the volume of the domain. All values in a.u.

Complex	**4.1**-*cis*	**4.1**-*trans*
$\Delta s(D^+_{Co})$	145.6	21.4
$V(D^+_{Co})$	24.1	17.6
$\overline{\Delta s(D^+_{Co})}$	6.0	1.2

These results mean that **4.1**-*cis* displays much more electrophilicity on the vacant coordination position, which means it binds much more to a nucleophile than **4.1**-*trans*. We would thus expect the cobalt - nitrito bond to be much stronger on the *cis* position than on the *trans* one: we retrieve a STE.

We also retrieve a similar information at the NOCV level. We represent on Figure 3.3.2 the deformation densities for the main (±1) NOCV pairs associated to the coordination of a nitrito ligand to the previous fragments. As one can see, in both cases the incoming NO_2^- ligand loses electron density, which relocates between the nitrito and the cobalt atom: a cobalt-nitrite bond is formed. Other electron density movements are seen on the rest of complex, which can be understood as the withdrawal of an excess electron density that was transferred by the remaining ligands in the $[ML_5]$ fragments, in order to counteract the vacancy.

Graphically, the relocation basin between nitrite and cobalt is smaller *trans* to the methyl, which would suggest a smaller electron density delocalisation. Actually, the NOCV pair in that case is associated to a total movement of 0.57 electrons and an energy stabilisation of 31.3 kcal.mol^{-1}, whereas in the case of the *cis* nitrito 0.66 electrons are exchanged, leading to a stabilisation of 40.1 kcal.mol^{-1}. We thus retrieve a less stabilising interaction *trans* to the methyl, and the formed bond is expected to be weaker since it involves less electrons: we retrieve the expected STE.

Complex 4.2. Complex **4.2**, $[NbO(NCS)_5]^{2-}$, is also known to show a marked STE due to the oxido ligand:[148] the thiocyanate ligand *trans* to O^{2-} is indeed located 0.18 Å further

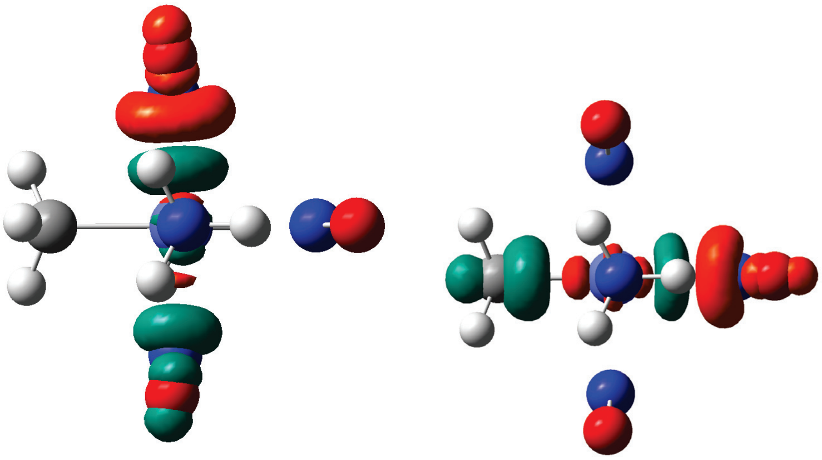

FIGURE 3.3.2: Deformation densities for the first NOCV pair associated to the coordination of a nitrito ligand to **4.1**-*cis* (left) and **4.1**-*trans* (right), at a ± 4×10^{-3} a.u. isovalue. Electron density relocation (depletion, respectively) areas are depicted in green (red).

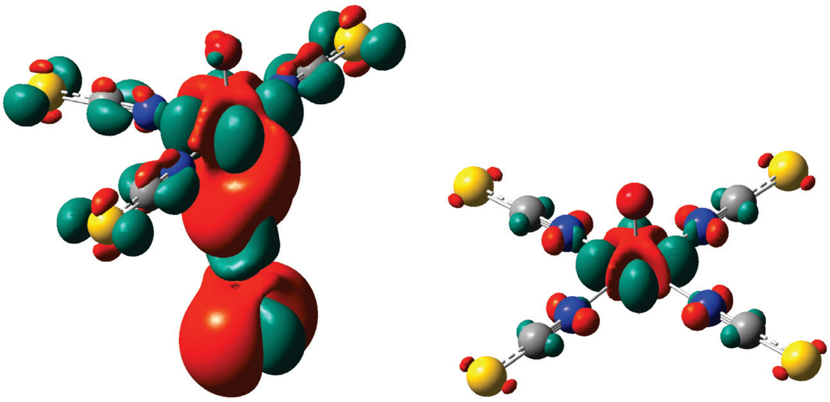

FIGURE 3.3.3: GC-DD isosurfaces for **4.2**-*cis* (left) and **4.2**-*trans* (right), at a ±0.4 a.u. isovalue. Colour scheme: red, negative values; green, positive values.

from the niobium atom than the *cis* ones.(xvii)

As for complex **4.1**, we thus built to fragments by removing one SCN^- ligand, either *trans* to the oxide (**4.2**-*trans*) or *cis* (**4.2**-*cis*). We represent on Figure 3.3.3 the GC-DD for these two fragments. Once again, the DD contributions on the metal are very similar. Noticeably, the electrophilic domains on the niobium are reminiscent of a non-bonding d_{xy} metal AO, which can be understood quite easily in the framework of ligand field theory (this is the LUMO, thus likely associated to an electrophilic behaviour).

In the case of **4.2**-*cis*, these electrophilic domains are well designed to host a π donor ligand, and thus they may stabilise efficiently a N-bonding thiocyanate. On the other hand, in the case of **4.2**-*trans* such a stabilisation is not expected: the electrophilic developments are orthogonal to the eventual thiocyanate-niobium bond. As such, we do not expect the thiocyanate *trans* to O^{2-} to actually interact in a covalent way with the rest of the complex. This could be expected from our former study, since we know N-coordination is driven mostly by electrostatic effects.

In turn, this means the *trans* thiocyanate is expected to be less strongly bound the niobium than the *cis* ones. Actually, from the shape of the GC-DD in **4.2**-*cis*, we can furthermore

---

(xvii) Note that, formally, the Nb(V) ion has a d^0 electronic configuration.

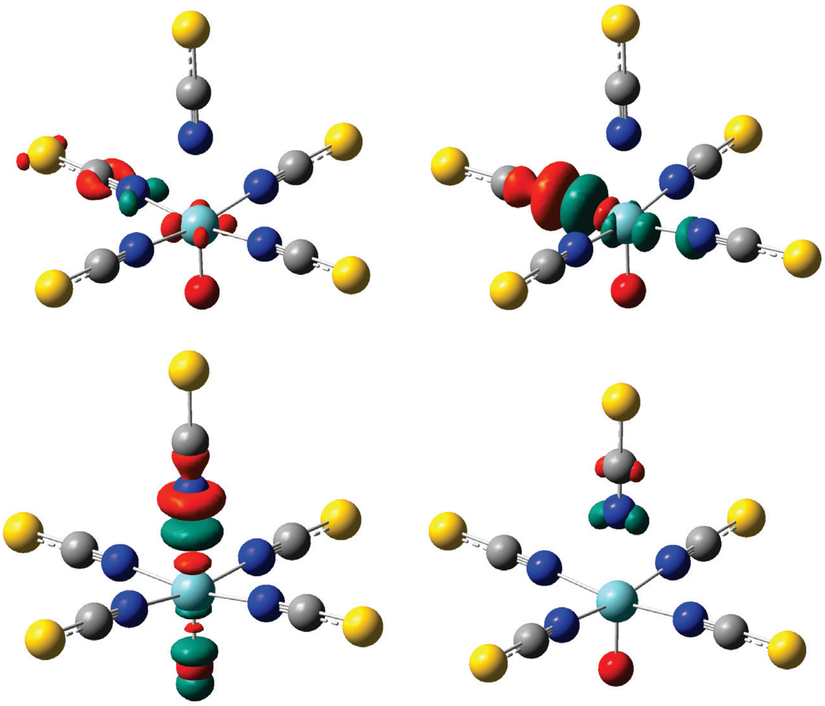

FIGURE 3.3.4: Deformation densities for the first (left) and second (right) NOCV pairs associated to the coordination of a thiocyanato ligand to **4.2**-*cis* (top) and **4.2**-*trans* (bottom), at a ± 4×10^{-3} a.u. isovalue. Electron density relocation (depletion, respectively) areas are depicted in green (red).

see that the *trans* SCN^- mostly acts as an isolated (uncoordinated) thiocyanate. Unfortunately, we cannot use the condensation scheme in that case to quantify the differences between the *cis* and *trans* positions. Nevertheless, we do still retrieve a STE.

We also retrieve it at the NOCV level. Coordination of a thiocyanate to **4.2**-*cis* or **4.2**-*trans* indeed yields two main NOCV pairs, which correspond to the formation of a σ and π bond, as shown on Figure 3.3.4. The σ bond formation leads to the exchange of 0.47 electrons in the case of **4.2**-*cis* and a stabilisation of 30.4 kcal.mol^{-1}, while only 0.34 electrons are exchanged in the case of **4.2**-*trans* and -18.0 kcal.mol^{-1} are gained. The π bond formation on the other hand leads to an exchange of 0.47 electrons in the case of **4.2**-*cis* and a stabilisation of 12.7 kcal.mol^{-1}, while 0.52 electrons are exchanged in the case of **4.2**-*trans* and 8.1 kcal.mol^{-1} are gained.

Overall, roughly the same number of electrons are exchanged in the formation of the π bonds, but the formation of the *cis* bond is energetically favoured. In the case of the σ bond, the difference between the *cis* and *trans* coordination is even more marked (both in electron numbers and energy stabilisation). We thus retrieve a weaker coordination *trans* to oxido than *cis*.

Complex 4.3. Complex **4.3**, $[RhL(PMe_3)_2(Cl)_3]$ (with L = dimethylaminocarbene), is known to present a quite marked STE:[120] the Rh(III)-Cl^- bond is 0.08 Å longer when *trans* to the carbene. Following the same approach as previously, we built two fragments by removing either the *trans* (**4.3**-*trans*) or *cis* (**4.3**-*cis*) chloride (with respect to the carbene).

As one can see from Figure 3.3.5, the shape of the GC-DD around the metal cation is very similar to what we observed for complex **4.1**. Noticeably, we retrieve the *d*-AO shaped electrophilic contribution developing towards the coordination vacancy. Here also, the volume of this domain seems bigger on the *cis* position. This is confirmed by Domains,

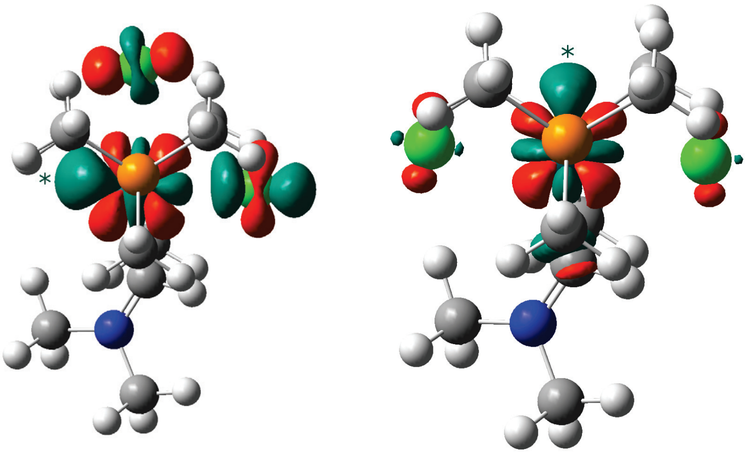

FIGURE 3.3.5: GC-DD isosurfaces for **4.3**-*cis* (left) and **4.3**-*trans* (right), at a ±0.4 a.u. isovalue. Colour scheme: red, negative values; green, positive values.

since the volume of the *cis* basin is about 50% larger than the *trans* one. As we can see from Table 3.6, once again we retrieve much larger numerical values (either integrated or averaged) for the GC-DD on the *cis* position, which suggests that coordination *trans* to the carbene is less effective: we retrieve a STE.

This also the case if we look at the NOCV associated to the coordination of a chloride to **4.3**-*trans* or **4.3**-*cis* – see Figure 3.3.6 –. In both cases, a main NOCV pair is observed, associated to an exchange of 0.76 electrons and a stabilisation of 46.7 kcal.mol^{-1} in the case of **4.3**-*cis*, and an exchange of 0.65 electrons and a stabilisation of 37.4 kcal.mol^{-1} in the case of **4.3**-*trans*. We thus retrieve a weaker coordination on the *trans* position with respect to carbene, as expected.

TABLE 3.6: Numerical values from the condensation of the electrophilic domains of the GC-DD, for fragments **4.3**-*cis* and **4.3**-*trans*. $\Delta s(D^+_{Rh})$ is the integrated GC-DD value over domain D^+_{Rh}, $\overline{\Delta s(D^+_{Rh})}$ the mean GC-DD value and $V(D^+_{Rh})$ the volume of the domain. All values in a.u.

Complex	**4.3**-*cis*	**4.3**-*trans*
$\Delta s(D^+_{Rh})$	47.3	19.8
$V(D^+_{Rh})$	30.7	20.3
$\overline{\Delta s(D^+_{Rh})}$	1.5	1.0

Comparing *trans* orienting ligands

In the three previous examples, we have compared *cis* and *trans* positions in the same complex, in order to highlight both STE and KTE. Now, we propose to focus only on one position in two related complexes, which will only differ by the ligand on the *trans* position. In principle, this should permit to compare different *trans* orienting ligands.

Complexes 4.4. Complexes (**4.4**), namely *trans*-$[Rh(NH_3)_4(H_2O)X]^{n+}$ with (X,n) = (H_2O,3) or (Cl^-,2), display a marked KTE.[149] Water substitution indeed proceeds 5000 times faster when X = Cl^-.

According to our methodology, we thus built two $[ML_5]$ fragments by removing the water ligand in both complexes (respectively, fragments $[ML_5]$-**4.4**-H_2O and $[ML_5]$-**4.4**-Cl). As one can see from Figure 3.3.7, the GC-DD for these two fragments is once again similar to

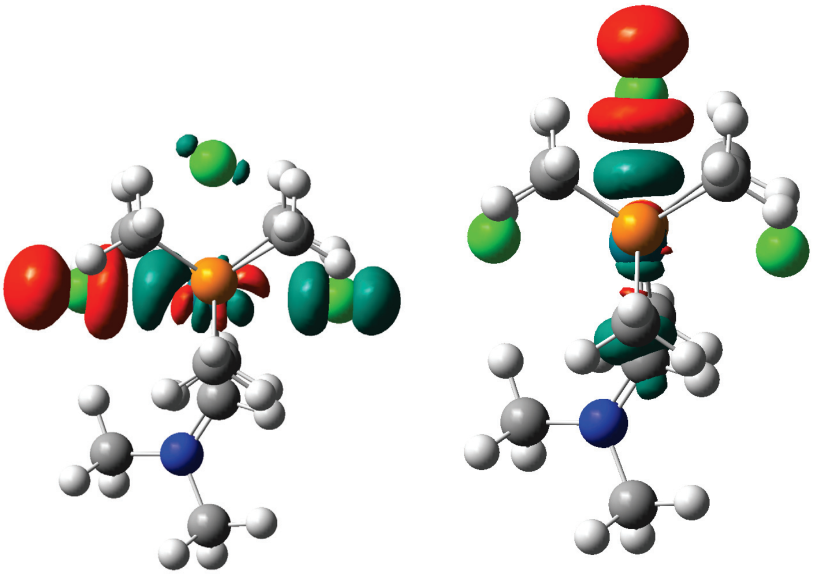

FIGURE 3.3.6: Deformation densities for the first NOCV pairs associated to the coordination of a chloride ligand to **4.3**-*cis* (top) and **4.3**-*trans* (bottom), at a ± 4×10^{-3} a.u. isovalue. Electron density relocation (depletion, respectively) areas are depicted in green (red).

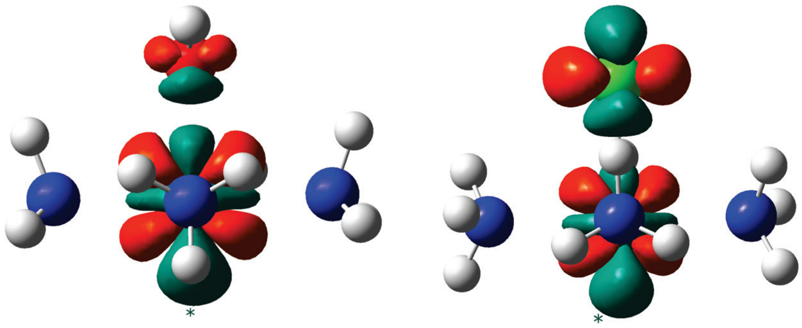

FIGURE 3.3.7: GC-DD isosurfaces for $[ML_5]$-**4.4**-H_2O (left) and $[ML_5]$-**4.4**-Cl (right), at a ±0.4 a.u. isovalue. Colour scheme: red, negative values; green, positive values. Electrophilic D^+_{Rh} domains are highlighted by an asterisk.

what we observed for complex **4.1**. In this case, it is not plain whether $[ML_5]$-**4.4**-H_2O or $[ML_5]$-**4.4**-Cl display the larger electrophilic domain on the *trans* position. Condensation is thus very helpful in this case. Condensed values, recapped in Table 3.7, indicate clearly that electrophilicity is more pronounced for X = H_2O: the integrated value of GC-DD are approximately doubled compared to X = Cl^-, and since the volumes are not that different the average value of the GC-DD is also considerably larger for $[ML_5]$-**4.4**-H_2O.

Overall, we expect a much stronger coordination of water on that position when X = H_2O, and thus a much slower substitution kinetics: we retrieve the expected KTE.

This is also confirmed at the NOCV level, as sketched on Figure 3.3.8. Coordination of water to both fragment give rise to a main NOCV pair, with a basin of electron density relocation between the O and Rh atoms (formation of a bond). When X = H_2O, 0.48 electrons are transferred, which induces a stabilisation of 31.0 $kcal.mol^{-1}$. On the other hand, when X = Cl^- 0.36 electrons only are transferred, and the stabilisation is only of 16.7 $kcal.mol^{-1}$. The water molecule in **4.4**-H_2O is thus way more stabilised than it is in **4.4**-Cl. Its replacement should thus be much slower, as observed.

TABLE 3.7: Numerical values from the condensation of the electrophilic domains of the GC-DD, for fragments [ML$_5$]-**4.4**-H$_2$O and [ML$_5$]-**4.4**-Cl. $\Delta s(D^+_{Rh})$ is the integrated GC-DD value over domain D^+_{Rh}, $\overline{\Delta s(D^+_{Rh})}$ the mean GC-DD value and $V(D^+_{Rh})$ the volume of the domain. All values in a.u.

Complex	[ML$_5$]-**4.4**-H$_2$O	[ML$_5$]-**4.4**-Cl
$\Delta s(D^+_{Rh})$	43.9	21.9
$V(D^+_{Rh})$	25.2	19.2
$\overline{\Delta s(D^+_{Rh})}$	1.7	1.1

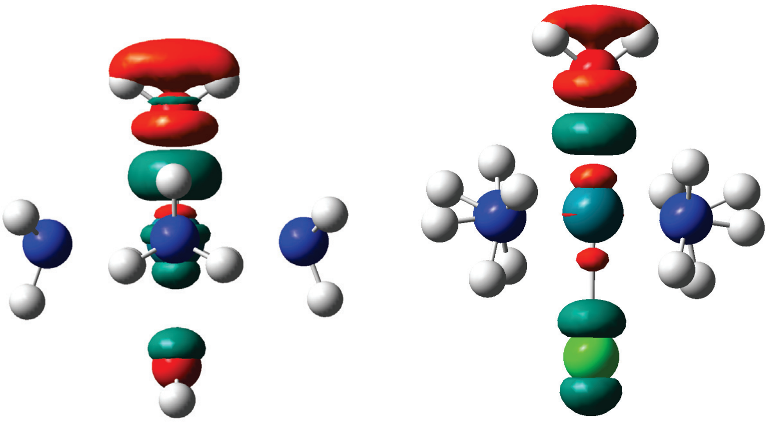

FIGURE 3.3.8: Deformation densities for the first NOCV pair associated to the coordination of an aqua ligand to [ML$_5$]-**4.4**-H$_2$O (left) and [ML$_5$]-**4.4**-Cl (right), at a ± 4×10^{-3} a.u. isovalue. Electron density relocation (depletion, respectively) areas are depicted in green (red).

Complexes 4.5. In the case of complexes **4.5**, [Co(en)$_2$(X)(H$_2$O)]$^{n+}$ with (X,n) = (OH$^-$, 2) and (SO$_3{}^{2-}$,1), a strong KTE could also be evidenced experimentally.[150,151] In this case, water substitution occurs 2000 times faster if X = SO$_3{}^{2-}$. Unfolding the same approach as previously, we thus constructed two fragments by removing the water molecule, yielding respectively [ML$_5$]-**4.5**-OH and [ML$_5$]-**4.5**-SO$_3$. The GC-DD surfaces for both fragments are represented on Figure 3.3.9.

Once again, the features are quite similar to what we observed for other complexes. As one may notice however, the features are more distorted in the case of [ML$_5$]-**4.5**-SO$_3$. This could be rather expected, since sulfite is also known to be π-acceptor ligand (and thus the shape of the DD should in principle be modified). As one may notice, the electrophilic

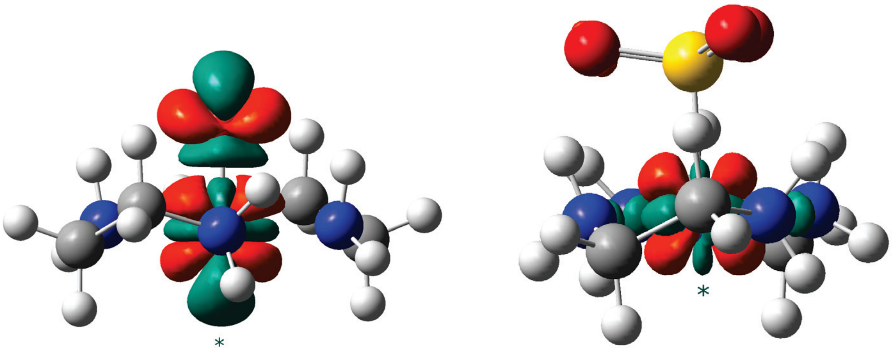

FIGURE 3.3.9: GC-DD isosurfaces for [ML$_5$]-**4.5**-OH (left) and [ML$_5$]-**4.5**-SO$_3$ (right), at a ±0.4 a.u. isovalue. Colour scheme: red, negative values; green, positive values. Electrophilic D^+_{Co} domains are highlighted by an asterisk.

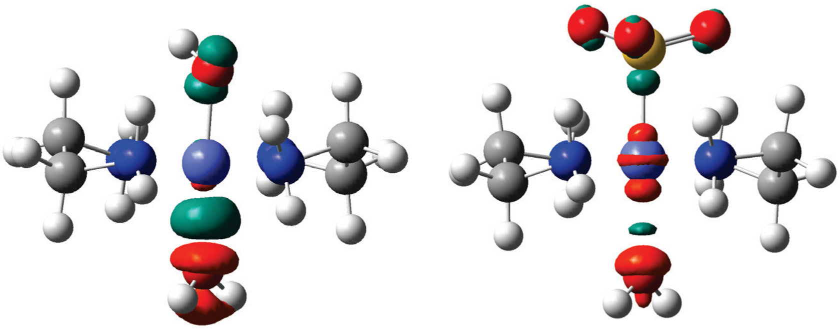

FIGURE 3.3.10: Deformation densities for the first NOCV pair associated to the coordination of an aqua ligand to [ML$_5$]-**4.5**-OH (left) and [ML$_5$]-**4.5**-SO$_3$ (right), at a ± 4×10^{-3} a.u. isovalue. Electron density relocation (depletion, respectively) areas are depicted in green (red).

basin *trans* to SO_3^{2-} is much smaller than *trans* to HO^-, which suggests electrophilicity in [ML$_5$]-**4.5**-SO$_3$ will be weaker compared to [ML$_5$]-**4.5**-OH. This is indeed the case if we look at the condensed values in Table 3.8. The integrated value of the electrophilic domain of the GC-DD is indeed 3.5 times larger *trans* to hydroxo, and since the volume of this domains is only twice larger than the volume of the basin *trans* to sulfito, the average GC-DD values are also markedly larger for hydroxo. As a result, we would expect a much stronger coordination for water when *trans* to hydroxo, as observed.

TABLE 3.8: Numerical values from the condensation of the electrophilic domains of the GC-DD, for fragments [ML$_5$]-**4.5**-OH and [ML$_5$]-**4.5**-SO$_3$. $\Delta s(D^+_{Co})$ is the integrated GC-DD value over domain D^+_{Co}, $\overline{\Delta s(D^+_{Co})}$ the mean GC-DD value and $V(D^+_{Co})$ the volume of the domain. All values in a.u.

Complex	[ML$_5$]-**4.5**-OH	[ML$_5$]-**4.5**-SO$_3$
$\Delta s(D^+_{Co})$	73.7	20.0
$V(D^+_{Co})$	33.6	13.4
$\overline{\Delta s(D^+_{Co})}$	2.2	1.5

In this case too, NOCVs for the coordination of the removed ligand are in good agreement with the GC-DD,as exemplified on Figure 3.3.10. For the two complexes, one main NOCV pair is observed, and is predictably associated to a relocation of electron density between the metal cation and the water ligand (formation of a bond). The relocation basin is much smaller in the case of sulfito, which suggests a much weaker coordination. This is retrieved in the number of transferred electrons – 0.33 electrons if X = HO^-, 0.22 electrons if X = SO_3^{2-} – as well as in the energy stabilisation – 15.6 kcal.mol^{-1} against 6.3 kcal.mol^{-1}, respectively. We thus retrieve unambiguously a *trans* effect.

Towards a quantitative scale?

From the different previous examples, it appears that our computational strategy allows to characterise the *trans* effects. Noticeably, in the last paragraphs we have seen that we could rather reliably compare different *trans*-orienting ligands using the GC-DD, in a quantitative fashion using the domains condensation. Interestingly, it appears from these examples that the *trans* effects are mostly related to a modulation of the "electron density demand" on the studied coordination positions, since the weakest electrophilicities were systematically found on the positions where STE or KTE were expected. This is actually in perfect line with the conclusions of both Chval and De Proft. Indeed, Chval and coworkers[139] proposed that the *trans* effect would be due to a "competition between the ligands [...] for the opportunity to donate their electron density to the central" metal cation, while de Proft and coworkers[140] suggested that a very efficient donation from the *trans* ligand would translate into an accumulation of electron density on the studied position and thus an enhanced Pauli repulsion. It is rather clear that both effects would translated into a decrease of the electrophilicity.

The following step is then to check whether we could use the same kind of theoretical framework to provide the first theoretically-based scale of the *trans*-orienting ligands. In many inorganic textbooks, one can indeed read that all ligands exert an influence on the other ones in the coordination sphere, and that the resulting *trans* effects are piloted by the strongest *trans*-orienting ligand. Summarising a large number of experiments, the following scale is generally assumed:

$$\mathrm{CO} \approx \mathrm{CH_3}^- \approx \mathrm{NO_2}^- > \mathrm{Cl}^- > \mathrm{Pyridine} > \mathrm{NH_3} > \mathrm{H_2O}$$

where the comparison operator > means "stronger *trans*-orienting ligand than". Note that this scale is obtained over a large set of very different experiments, which may be hardly comparable (different solvents, temperatures...). As such, many exceptions are known, and the scale may furthermore vary substantially depending on the metal cation. We thus decided to study two families of complexes, **4.4-X** $[\mathrm{Rh(NH_3)_4(H_2O)X}]^{m+}$ and**4.6-X** $[\mathrm{Ru(NH_3)_5X}]^{m+}$,[152] with X belonging to the previous series. Note that the first series derive from complexes **4.4**, hence their label **4.4-X**.

The shape of the DD for these complexes is exactly similar to what we previously observed, and as such we did not display them here. Result of the condensation of the GC-DD for complexes **4.4-X** and **4.6-X** are gathered in Tables 3.9 and 3.10, respectively.(xviii)

TABLE 3.9: GC-DD condensation for the $[\mathrm{ML_5}]$ fragments deriving from complexes **4.4-X**. All values in a.u.

X =	$\Delta s(D^+_{\mathrm{Rh}})$	$V(D^+_{\mathrm{Rh}})$	$\overline{\Delta s(D^+_{\mathrm{Rh}})}$
$\mathrm{CH_3}^-$	9.5	10.7	0.88
CO	14.1	15.8	0.89
$\mathrm{NO_2}^-$	1.6	4.5	0.36
Pyridine	36.4	24.9	1.47
$\mathrm{NH_3}$	18.5	17.9	1.03
Cl^-	21.9	19.2	1.14
$\mathrm{H_2O}$	43.9	25.2	1.74

As one can remark from these tables, the ranges of both the volumes and the integrated GC-DD values are quite large. On the other hand, the averaged values of the GC-DD are in a much narrower range (from 0.36 to 1.74), and are all close to unity. They thus seem more adapted to build a quantitative scale of the *trans*-orienting ligands. Furthermore, the chemical meaning of these values are rather simple to understand, since they have the same unit as the GC-DD: they are a measure of the mean electrophilicity in the vicinity of the metal cation.

Thus, using the averaged values, we obtain the two following ranking (from the lowest GC-DD value to the highest):

$$\mathrm{NO_2}^- < \mathrm{CH_3}^- \approx \mathrm{CO} < \mathrm{NH_3} < \mathrm{Cl}^- < \mathrm{Pyridine} < \mathrm{H_2O}$$

(xviii) Note that $[\mathrm{Ru(NH_3)_6}]^{2+}$ was not considered. The reason is rather simple: because of its perfect octahedral symmetry, no differentiation is expected between *trans* and *cis* positions: as such, it is not expected to display any *trans* effect.

TABLE 3.10: GC-DD condensation for the $[ML_5]$ fragments deriving from complexes **4.6-X**. All values in a.u.

X =	$\Delta s(D^+_{\mathrm{Rh}})$	$V(D^+_{\mathrm{Rh}})$	$\overline{\Delta s(D^+_{\mathrm{Rh}})}$
CH_3^-	22.4	28.9	0.77
CO	18.3	21.5	0.85
NO_2^-	21.0	35.2	0.60
Pyridine	29.4	26.1	1.13
Cl^-	36.3	26.4	1.37
H_2O	43.2	30.6	1.41

for complexes **4.4-X**, and

$$NO_2^- < CH_3^- < CO < \text{Pyridine} < Cl^- < H_2O$$

for complexes **4.6-X**. These rankings are in a rather good agreement with the experimental series, especially regarding the strongest *trans*-orienting ligands. Carbonyl, methyl and nitrito are indeed well placed in the series, displaying markedly small values of the GC-DD. On the other hand, weak *trans*-orienting ligands seem less well ordered. The discrepancies with the experimental series are most probably stemming from the diversity of experimental conditions in which substitution rates or structural parameters are obtained: it may be quite hard to compare a metathesis reaction in water, which is a very polar solvent, to another one occuring in THF... Furthermore, we are comparing different complexes, and differences in the values were to be expected. It should also be reminded that our approach is quite crude, in the sense that we do not allow the $[ML_5]$ species to relax, neither that we looked at a complete reaction path.

Most probably, an absolute scale of the *trans*-orienting ligands, using our theoretical approch, cannot be build. Anyhow, we are able to provide a semi-quantitative scale, which could be used as a general (though imperfect) guide.

3.3.3 Conclusion

In this section, we showed how tools from conceptual DFT and related paradigms could be used to rationalise the chemical properties of coordination complexes, noteworthy allowing to understand the physical mechanisms acting beneath the *trans* effects in octahedral complexes.

As what was observed for square-planar complexes, *trans* effecs in octahedral complexes primarily come from the differential ability of ligands to donate their electron density to the metal cation, leading certain coordination positions to be quite saturated with electron density and thus less "demanding" for a ligand. Monitoring the electrophilicity, we were able to characterise, and more importantly, to quantify the *trans* effects in a rather large set of coordination complexes.

Finally, using a local condensation scheme, we managed to build semi-quantitative scales of the *trans*-orienting ligands which happen to reproduce quite correctly the experimental trends, even though the model we used may not be the most precise.

NOTE: this work has been published in *Phys. Chem. Chem. Phys.* **2016**, 18, 982–990.

3.4 Long story short

Throughout these two studies, we aimed to examine the efficiency and adequacy of conceptual DFT in the understanding an rationalisation of the properties of coordination compounds. Starting from a very simple study on ligands, we saw that using two well designed tools, namely the electrostatic potential and dual descriptor, we were able to retrieve quite correctly the coordination geometries they would adopt, but also to gain information about their electronic properties once coordinated. Furthermore, in some cases we were able to understand experimental facts, such as the scarcity of dioxygen complexes.

The DD also proved to be a valuable tool in the study of the *trans* effects of octahedral complexes. Indeed, it appeared that these effects are essentially due to a modulation of the electrophilicity of the metal cation under the influence of the ligand on the *trans* position.

We believe the scope is much wider, and that conceptual DFT is a framework of choice for the rationalisation of the properties of coordination complexes. Noticeably, we have seen in the first study a few problems arose when the ground state of the studied molecules are degenerate. In the framework of FMO theory, such cases may be problematic. In the framework of DFT, they are even unreachable, since the fundamental hypothesis beneath the Hohenberg-Kohn theorems are no longer holding. This is not true for conceptual DFT, since we base our interpretations on electron density, no matter its origin.

Actually, this last point suggests we could imagine to perform conceptual DFT calculations basing solely on experimental data: using X-ray diffraction, it is indeed possible to obtain electron density maps, which could be used for C-DFT calculations...

Chapter 4

Amino-acid based copper complexes: from reactivity to molecular magnetism.

4.1 Introduction

Polynuclear metal complexes have attracted a large interest in research because of the fascinating physical properties they may present, among which one may find catalytic activity and magnetism.[153] For instance, as we have seen in Chapter 3, the biological properties of some enzymes are due to the presence of a polynuclear complex in their active site.[108,109] One may cite as an example the catechol oxidase, whose dinuclear copper complex is used to oxidise di-phenols into orthoquinones. Laccase[154] is another interesting copper-based example: its trinuclear complex indeed permits the activation of O_2, proceeding through what is called a "native intermediate", which is an antiferromagnetically coupled trinuclear copper(II) centre.

This intermediate is of paramount importance in the process, and many trinuclear Cu(II) complexes were synthesised as prototypes of this enzyme. Furthermore, such antiferromagnetically coupled trinuclear Cu(II) complexes may also be good candidate for spin frustration.[155,156] Indeed, there is no possible way to arrange a triangular system of three $S = 1/2$ spins in such a way that all pairs of spins will be antiferromagnetically coupled – see Scheme 4.1.1 –. Such frustrated systems are very interesting, because they present a degenerate ground state[(i)]. As such, they could be employed as molecular qubits, *i.e.*

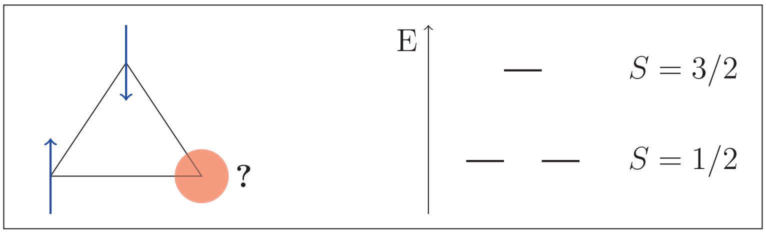

Scheme 4.1.1: Schematic representation of frustrated trinuclear Cu(II) complex, and the corresponding energy diagram.

(i) The reader may retrieve this degeneracy from equation (2.34), setting all the coupling constants to the same value J.

molecule-based quantum bits of information.(ii) Note that SMMs are also proposed to be efficient candidates for this purpose.

In 2008, our team reported the synthesis of a trinuclear Cu(II) complex based on an amino-acid derived ligand, ${L_0}^{2-}$, along with a bridging $\mu_3{-}OH^-$ ligand.[158] This complex displayed an unambiguous antiferromagnetic coupling, but because of its low symmetry no frustration was actually observed. High level calculations (DDCI-2 and approximate DDCI-3), performed by Dr. Boris Le Guennic and Prof. Vincent Robert, indeed showed the doublet states were not degenerate. Nevertheless, the complex presented another interesting feature: the lowest doublet and quartet states were indeed found to be degenerate, a rather unexpected characteristic. Furthermore, this could only be deduced at the highest level of theory – at the DDCI2 level, the computed coupling was indeed still ferromagnetic –.

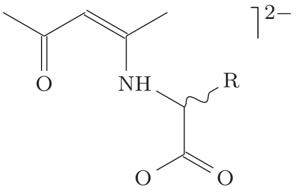

FIGURE 4.1.1: Studied amino-acids derived ligands. R = H, ${L_0}^{2-}$; R = Me, ${L_1}^{2-}$; R = ^{i}Pr, ${L_2}^{2-}$; R = ^{i}Bu, ${L_3}^{2-}$.

These very interesting results stimulated a further study on the subject. Noteworthy, the subtlety of the observed magnetic properties of the previous complex suggests a slight modification of the ligand may result in a marked effect. Interestingly, the synthetic procedure that permitted to isolate ${L_0}^{2-}$ can be easily modified, and parent ligands using different amino-acids (alanine, valine and leucine, *vide infra*) had already been obtained during the PhD theses of Sarah Petit and Amel Messai.[159,160] We thus evaluated the coordination ability of these ligands, and studied the magnetic properties of the obtained complexes. The results are presented in the following sections.

4.2 Syntheses and structures

4.2.1 Syntheses and structures of the ligands

In this study, we proposed to study the effect of subtle modifications on ligand ${L_0}^{2-}$. We thus tried to obtain these complexes using more branched versions of ${L_0}^{2-}$, replacing the starting amino-acid (glycine) by an alkylated one: alanine (R = methyl on Figure 4.1.1), valine (R = isopropyl) and leucine (R = isobutyl). Note that these amino-acids are chiral, and thus each ligand can be prepared in its enantiopure (D, L) or racemic (DL) forms.

As we have just said, the corresponding ligands had already been synthesised by Sarah Petit and Amel Messai, through a very simple procedure: acetylacetone is simply added to an aqueous solution of the corresponding amino acid with potassium hydroxide, and the mixture is left to react for a few hours at room temperature. Though being very efficient in the case of glycine and alanine – yields between 80 % and 90 % – , the method proves less successful in the case of valine (62 %), and does not afford at all the expected

---

(ii) Actually, there are more requirements to be fulfilled, which are called the "Loss-DiVincenzo criteria": the states need to be well-defined (which is the case), should be easily prepared, show low decoherence, be easily characterised and easy to manipulate.[157]

compound with leucine if room temperature is too low. Furthermore, the crude product of reaction with this procedure tend to incorporate a lot of water, as evidenced by its characteristic IR signal, which is quite hard to remove.(iii)

This led us to employ a slightly modified synthetic procedure: water is replaced by methanol, and the reaction is conducted at reflux instead of room temperature. With this method, yields are much better (98% - 99%) and the synthesised potassium salts are found pure (see Appendix A.1 for the experimental details).(iv)

Quite interestingly, our different characterisation techniques point to slightly different structures than the presumed one for L_0H^-. Indeed, IR and NMR spectra suggest our different L_nH^- (n = 0 - 3) species are better described as being enaminones (bearing both ketone and enamine motifs), rather than imino-enol, both in the solid state (IR) and in water solution (NMR in D_2O). Unfortunately, no crystallisation procedure afforded large enough crystals to directly confirm this through X-Ray diffraction.

We thus modelled $^{D}L_1H^-$ at the DFT level, using the hybrid B3LYP functional[161] and Pople's basis set 6-311++G(d),[162] and using water as an implicit solvent (PCM), with Gaussian 09.[97] In the first optimisation, the starting geometry corresponded to Figure 4.1.1. Then, we displaced the proton that was located on the nitrogen atom to the ketone oxygen, and optimised once more the geometry. Moreover, we also considered another conformation of the carbon backbone of this ligand. Indeed, the drawn formula on Figure 4.1.1 is such that the two successive unsaturated bonds are in a relative *cis* conformation, but it is known that such systems may also present a *trans* configuration (which would consist here in turning the ketone oxygen upwards).[50] We then performed two supplementary geometry optimisations, starting from the corresponding *trans* guess configurations.

Table 4.1: Relative energies (in kcal/mol) of the different optimised geometries of ligand $^{D}L_1H^-$, at the B3LYP/6-311++G(d)/PCM(H_2O) level.

	NH	OH
cis	0.00	+13.98
trans	+4.23	+26.66

Overall, we obtained four different geometries, that we label *cis*-NH, *cis*-OH, *trans*-NH and *trans*-OH, respectively.(v) Frequency calculations were performed in each case to ensure they correspond to genuine energy minima, and were also used to compute the free energies corresponding to these four geometries. They are listed in Table 4.1.

As one may remark, the minimum value is found for the *cis*-NH form, in good agreement with our characterisations. Noticeably, even though the energy differences between the all the conformers seem rather small, they are nonetheless significant. For instance, if we presume conversion between *cis*-NH and *trans*-NH may happen(vi) at room temperature, the ratio between the two forms should be given by the corresponding Boltzmann population factor. In that case, this factor leads to a partition into 99.92% of *cis*-NH and 0.08% of *trans*-NH: we can safely neglect all conformations but *cis*-NH in the liquid state. This

---

(iii) Water could still be evidenced by IR after 2 weeks of desiccation in vacuum.

(iv) In addition, chirality of ligands $^{D}L_1H^-$ and $^{L}L_1H^-$ was confirmed by circular dichroism measurements on methanol solutions.

(v) Note that we did not consider the iminone form (both ketone and imine motifs), since ^{1}H NMR unambiguously points to a sp^2 hybridation of the central carbon of the acetylacetone backbone (only one H is observed).

(vi) *I.e.*, that the energy barrier for this process is small enough – which our calculations does not confirm or infirm –.

is furthermore confirmed by the consistency of the experimental and calculated ^{1}H NMR chemical shifts and coupling constant for this conformation (using the GIAO formalism as implemented in Gaussian), as shown in Appendix A.1.

4.2.2 Coordination properties

In summary, we isolated 9 different ligands (as potassium salts):

- $^{D}L_1HK$, $^{L}L_1HK$, $^{DL}L_1HK$, starting from the corresponding alanines,
- $^{D}L_2HK$, $^{L}L_2HK$, $^{DL}L_2HK$, starting from the corresponding valines,
- $^{D}L_3HK$, $^{L}L_3HK$, $^{DL}L_3HK$, starting from the corresponding leucines,

and looked for their coordination properties towards transition metals. As we have seen in the previous chapter, DFT calculations can provide appreciable information for this. Since we know the glycine analogue coordinates when deprotonated, in a geometry that is close to the one of *cis*-NH, we here considered a deprotonated form of this latter structure, by simply removing the hydrogen atom from the amine group. We then computed the DD without geometry optimisation, using the state-specific formalism,[89] focusing on the first excited state and using the same level of theory as previously. We also performed the same calculation for the non-deprotonated form, and in both cases we also evaluated the MEP.[94]

We represent on Figure 4.2.1 the result of these calculations. First, at the DD level we notice similarities between the two compounds. We indeed observe a marked electrophilicity on the imine and ketone groups, together with a non negligible nucleophilicity on the central carbon. This latter characteristic is more pronounced in the deprotonated form, indicating a relocation of charge density on this carbon. We retrieve a similar characteristic in the case of the nitrogen atom, that becomes much more nucleophilic upon the H abstraction – which is quite logical. On the other hand, the ketone oxygen show the reverse tendency: it appears to be much more nucleophilic in the protonated form that in the deprotonated one. This can be understood rather simply: since the DD integrates to zero over space, an increase of nucleophilicity on one site must be accompanied either by an increase of electrophilicity or a reduction of nucleophilicity elsewhere in the molecule. As we do not observe an increase in electrophilicity through deprotonation – which is rather logical, since we increased the charge of the system –, we understand why the nucleophilicity of the ketone oxygen is decreasing.

At the MEP level, we observe an interesting feature: in the protonated form, the negative charge tends to locate on the carboxylate group, and also on the ketone oxygen, as evidenced by the large negative values on these sites. In the deprotonated form, we retrieve these negative charges, but they are somehow masked by the much larger one on the nitrogen atom, which bears the lowest MEP values.

If we summarise, these two species involve a hard negative charge on the carboxylate – low MEP values and no significant DD contribution –, which may be quite fitted to stabilise lanthanide cations.[21] On the other hand, they also present softer sites, which display both low values of the MEP, non negligible nucleophilic DD contributions with electrophilic contributions in their vicinity. They are thus quite fitted to stabilise transition metal cations.[63]

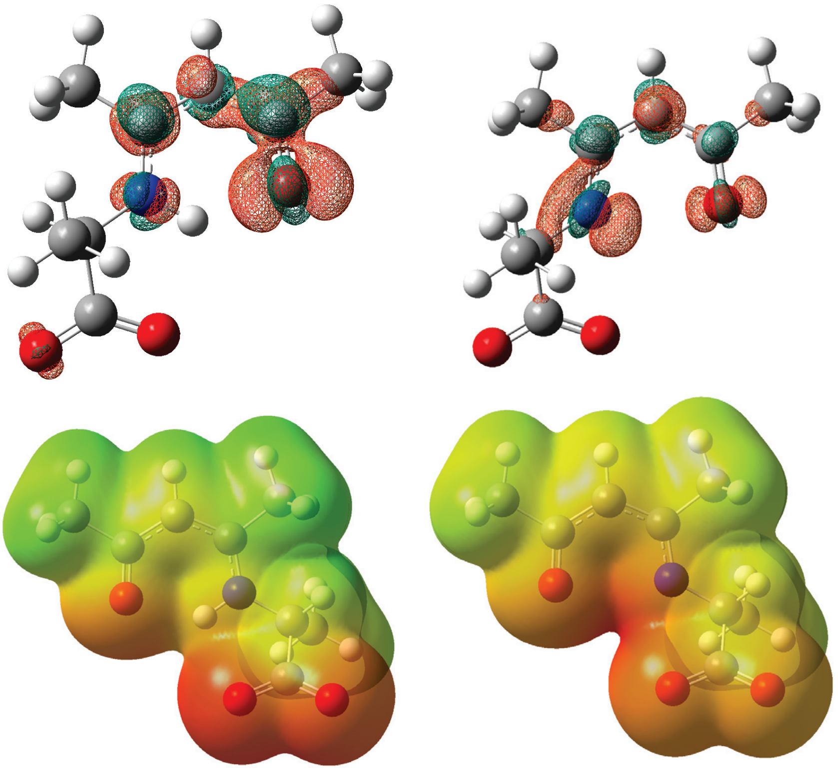

FIGURE 4.2.1: Up: DD isosurfaces for ${}^{D}L_1H^-$ (left) and ${}^{D}L_1{}^{2-}$ (right), as computed at the B3LYP/6-311++G(d)/PCM(H_2O) level. Isovalue: $\pm 4 \times 10^{-3}$. Positive values are depicted in green, and negative values in orange.
Down: MEP projection on density isosurfaces ($\rho(\mathbf{r}) = 4 \times 10^{-3}$ a.u.) for ${}^{D}L_1H^-$ (left) and ${}^{D}L_1{}^{2-}$ (right), at the same level of theory. Colour gradient: red, lowest MEP values; green: highest MEP values.

4.2.3 Complexations

We then tried to coordinate different metal cations, using a similar synthetic procedure as the one previously employed for the trinuclear Cu(II) complex of $L_0{}^{2-}$: a simple mixture of methanolic solutions of the ligand and the metal salts, in a 1:1 ratio, in the presence of a weak base (here triethylamine). The following metal cations were scrutinised: Cu^{2+}, Cr^{3+}, Co^{2+}, Mn^{2+}, VO^{2+}, Ni^{2+} and Zn^{2+}.(vii) For all these ions, a marked change of colour is observed without addition of base. For instance, addition of an acid green $CuCl_2 \cdot 2\,H_2O$ solution to a pale yellow solution of ${}^{D}L_1HK$ leads to a dark green mixture. In the case of Zn^{2+}, the resulting solution shows a slightly more intense yellow colour. Upon addition of triethylamine, a further colour change is observed; for instance, the previous dark green solution turns to a deep and dark blue. In the case of Zn^{2+}, a colour change is also observed, the resulting solution turning to a much stronger yellow.

Such colour changes suggest coordination takes place, in two steps. First, in the absence of base we already observe a coordination, which likely involves the conjugated enaminone part of our ligands (more intense colour of the Zn(II) complex). Second, upon addition of base it is very likely that we deprotonate the ligand, thus changing drastically the electronic structure of the resulting complex and as such its absorption properties.

Nevertheless, crystallisation of these complexes proved nearly impossible. Indeed, we never managed to isolate any crystalline material in the case of Cr^{3+}, Co^{2+}, Mn^{2+}, VO^{2+},

---

(vii) Note that a trinuclear complex of Cu(II) was already obtained by Sarah Petit, basing on the alanine derivative, but was not thoroughly studied because of a lack of time.

Ni^{2+} and Zn^{2+}. In the case of Cu(II), depending on the counter-ion and the experimental conditions, we managed to characterise four crystal structures, which are presented hereafter.

Trinuclear complexes 4.1 and 4.2

Reaction of ${}^{D}L_1HK$ and ${}^{L}L_1HK$ with $CuCl_2 \cdot 2\,H_2O$ affords compounds **4.1** and **4.2** as single crystals, suitable for X-Ray diffraction. Both compounds crystallise in the non enantiogenic $P2_12_12_1$ space group, and the found formulas are $K_2[Cu_3(\mu_2{-}{}^{D}L_1)_3(\mu_3{-}OH)]_2 \cdot 5\,H_2O$ for **4.1** and $K_2[Cu_3(\mu_2{-}{}^{L}L_1)_3(\mu_3{-}OH)]_2 \cdot 5\,H_2O$ for **4.2**. The crystallographic parameters are listed in Table B.1. In both crystal structures, two independent trinuclear complexes are found within the unit cell, along with two K^+ ions and five crystallised water molecules. Interestingly, **4.1** and **4.2** are not exactly enantiomorphic, since the lattice parameters are slightly different from one structure to the other. Also, the obtained crystal structures do not match the one that was isolated by Sarah Petit (which incorporated four water molecules).

We represent on Figure 4.2.2 the molecular structure of one complex of the asymmetric unit of **4.2**. It is highly reminiscent of the one that was obtained with ${L_0}^{2-}$, showing a half-cubane-like Cu_3O_4 core. As one may note from Tables B.2 and B.3, the complexes are quite asymmetric, all coordination bonds showing slightly different properties (distances and angles). Nevertheless, they all present similar global aspects, and the observed variations in angle or bond length remain rather small. We may then discuss the coordination geometries basing on one complex only.

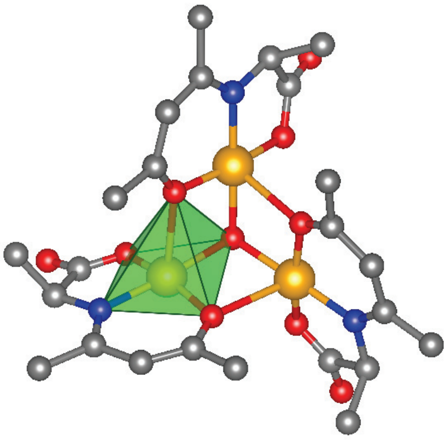

FIGURE 4.2.2: Representation of one of the complexes in the asymmetric unit of **4.2**. H atoms were omitted for the sake of clarity.

It is plain from Figure 4.2.2 that the Cu(II) ions are penta-coordinated, with a O_4N environment. The local geometry can be described as a distorted square-based pyramid, as evidenced by the Addison parameters (ranging from 0.09 to 0.22).(viii) The basal plane of this pyramid is constituted by a ${L_1}^{2-}$ ligand, in addition to the bridging hydroxyde. Axial coordination is ensured by the ketone oxygen of the neighbouring ligand, and the measured bond lengths are much longer than those measured in the basal plane (around 2.5 Å, to be compared to the 1.9 Å on the basal plane).

(viii) We remind that the Addison parameter, defined as $\tau = \Delta\theta/60$ with $\Delta\theta$ the difference between the two largest angles in the coordination sphere, characterises the geometry of penta-coordinate complexes: perfect square-based geometry corresponds to $\tau = 0$, while trigonal bipyramid corresponds to $\tau = 1$.[163]

Interestingly, the basal planes of the three Cu(II) ions within a trinuclear complex are almost perpendicular (calculated angle between the mean planes of 81° to 87°). This was actually already observed in the case of ${\mathrm{L}_0}^{2-}$, and was partially responsible for the very weak antiferromagnetic coupling. If we indeed consider the crystal field diagram of Cu(II) in a square-based pyramid geometry, we indeed expect the unpaired electrons to locate in the $d_{x^2-y^2}$-based orbitals, which will be quasi-orthogonal here. As such, the overlap between these magnetic orbitals is expected to be weak, and according to Kahn's argument so must be the antiferromagnetic coupling.[64] We may then expect a very weak antiferromagnetic coupling for **4.1** and **4.2**. Noteworthy, bridging through the ketone oxygens is not expected to convey any efficient magnetic coupling, as the axial coordination bonds are long and the Cu-O-Cu angles close to 90 °.

Polymeric complexes 4.3 and 4.4

Surprisingly, reacting $^{\mathrm{L}}\mathrm{L}_1$HK with another Cu(II) salt, namely $\mathrm{CuSO_4{\cdot}5\,H_2O}$, permitted to isolate another complex: $[\mathrm{Cu}(\mu_3{-}^{\mathrm{L}}\mathrm{L}_1)]_\infty$ (**4.3**). The same reaction with $^{\mathrm{L}}\mathrm{L}_3$HK yielded a similar compound, $[\mathrm{Cu}(\mu_3{-}^{\mathrm{L}}\mathrm{L}_3)]_\infty$ (**4.4**). The two complexes are monodimensional coordination polymers, the monomeric unit being simply composed of one Cu(II) ion and one ligand – see Figure 4.2.3.

We may actually understand why we do not retrieve the former trinuclear complexes: they were anionic complexes, and as such needed positive counter ions (K^+ ions from the ligand salt in this case, but triethylammonium ions were also present) in order to crystallise. Here, we employed a sulfate salt of Cu(II), and ammonium or alkaline sulfates are not expected to be soluble in methanol: we thus precipitated all the counter-ions (massive white precipitate as a side product), which prevented the formation of the trinuclear complex.

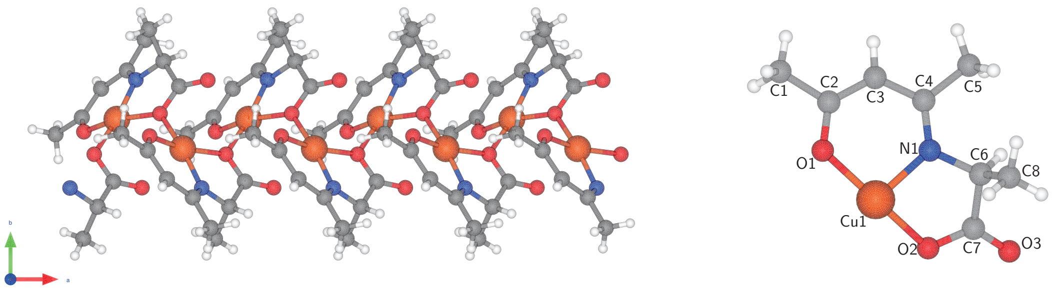

FIGURE 4.2.3: Structure of the $[\mathrm{Cu}(\mu_3{-}^{\mathrm{L}}\mathrm{L}_1)]$ polymer 4.3, seen along the $\vec{c}$ axis (left), and detail on the asymmetric unit numbering scheme (right).

The crystallographic parameters of both **4.3** and **4.4** are gathered in Table B.4. The structures of both complexes are very similar (nearly isostructural). In both cases, the Cu(II) ions are located in the coordinating pocket of one ligand, and the coordination sphere is completed by the carboxylate oxygens of two neighbouring ligands. This leads to a slightly distorted square-based pyramid geometry around Cu(II), as shown by the low values of the Addison parameter (0.10 and 0.06, respectively).

Interestingly, unlike what could be observed in the case of the trinuclear complexes, the basal planes of neighbour Cu(II) ions in the polymer are far from being orthogonal (calculated angle between the mean planes of 68° for **4.3**, 71° for **4.4**). A marked antiferromagnetic coupling could be expected. We depict on Figure 4.2.4 the two successions of bonds that could serve as support for a magnetic coupling. We remind that, in order to promote a strong antiferromagnetic coupling, one needs to have a strong overlap of the

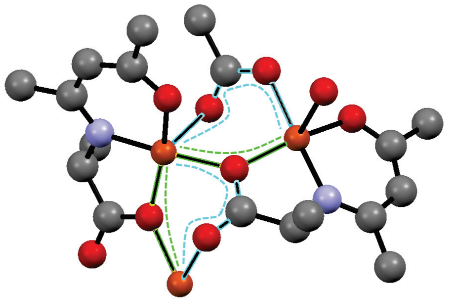

FIGURE 4.2.4: Possible magnetic coupling pathways in **4.3**, highlighted in cyan and green.

magnetic orbitals, which can be achieved if the path is short (monoatomic bridge) and the successive coordination bonds not orthogonal. Here, quite obviously the cyan path will not lead to a strong antiferromagnetic coupling, as it is long (and the two coordination bonds are quasi orthogonal). On the other hand, the green paths fulfils both criteria (the angle between the two successive coordination bonds is 128.4(1)° in both structures, and the associated dihedral angle is 113.0(1) ° in **4.3** and 111.0(1) in **4.4**).
As such, we may expect complexes **4.3** and **4.4** to present a strong antiferromagnetic coupling and, because of their polymeric nature, a 1D magnetic order at low temperature.

Structure in solution

So far, we have presented and discussed the crystal structures we could evidence using our different ligands and Cu(II) salts. Actually, these complexes were not the only compounds in the reaction mixture. Each time, an off-white (from white to pale blue) powder could also be isolated, and sometimes beautiful blue crystals could also be found. These were shown to be [Cu(Acac)$_2$] complexes (with Acac = acetylacetonate) by X-Ray diffraction. The observation of this Acac complex suggests our ligands hydrolysed in the reaction medium. Indeed, we remind our syntheses are akin to Schiff base condensations[50] (condensation of an amine on a carbonyl group, with the release of water), and these reactions are known to be reversible. Nevertheless, our ligands are rather original since they can be synthesised in water – while Schiff base usually decompose in water –. They thus seem to be quite water-resistant, at least as potassium salts. We may then wonder if it is not coordination (or deprotonation) that triggers the hydrolysis. This could explain why we did not manage to isolate most of the complexes.
We thus decided to model the hydrolysis reaction at the DFT level, in order to determine its feasibility. But prior to that study, we need to know the structure of our complexes in solution. We first looked at the absorption spectra of both **4.1**, **4.2**, **4.3** and **4.4** in methanol. Surprisingly, **4.3** and **4.4** dissolved quickly and easily – a rather unexpected feature for coordination polymers –. More surprising is the strong similarity of the spectra, irrespectively of the trinuclear or polymeric structure. For instance, we report on Figure 4.2.5 the absorption spectra for **4.2** and **4.3**. An almost perfect superimposition is seen, with in both cases a large absorption band around 645 nm ($\epsilon = 84(1)$ L.mol^{-1}.cm^{-1} for **4.2**), as well as a strong absorption in the UV region.
Such a strong similarity suggests the absorbing species in the two solutions are the same, which is rather unexpected. Actually, UV spectra for all crude reaction mixtures are similar, regardless of the Cu(II) salt or the ligand. Very likely, all our complexes have the same general structure in solution.
The effect of the solvent on the absorption spectra of **4.2** and **4.3** was also studied, and only small shifts were observed. For instance, the maximum of absorption of **4.3** moves

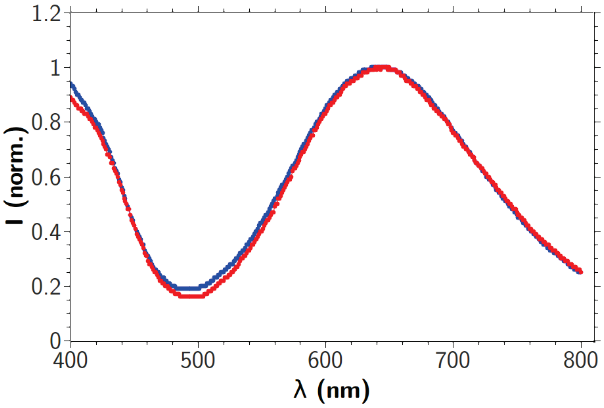

FIGURE 4.2.5: Absorption spectra for **4.2** (blue) and **4.3** (red), in methanol.

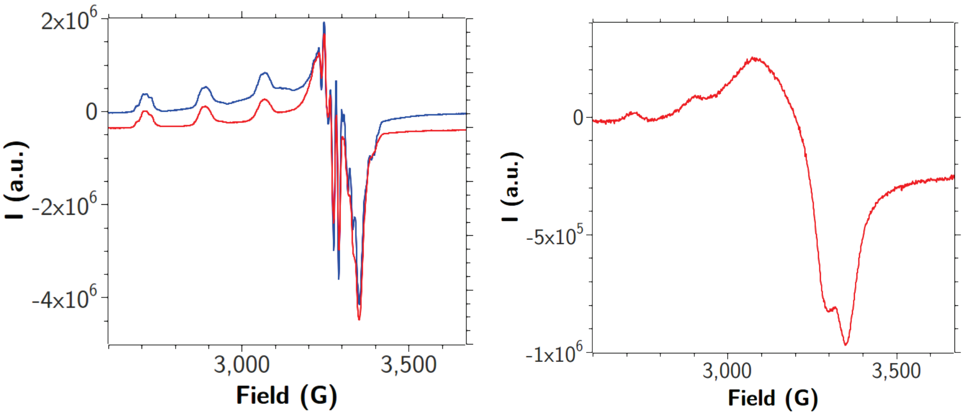

FIGURE 4.2.6: Left: X-band EPR spectra ($\nu = 9.41$ GHz) for frozen methanol solutions of **4.2** (red) and **4.3** (blue), at 118 K. Right: EPR spectrum of **4.2** at the same frequency and temperature, measured on a powder sample of **4.2**.

from 645 nm in methanol to 634 nm in pyridine and 612 nm in chloroform. The fact that the absorption features remain nearly unchanged upon change in the solvent indicates the latter is not involved in the first coordination sphere of our complexes.(ix) Furthermore, the good solubility of our complexes in chloroform suggests they are neutral in solution.

In order to gain more insight on the molecular structure, we then turned ourselves to EPR measurements on methanolic solutions. In good agreement with the UV measurements, the X-band spectra for **4.2** and **4.3** are very similar, as shown on Figure 4.2.6. One may also notice the major difference between the solution and solid spectra, which suggest completely different geometries should be considered.(x) Actually, similar results were obtained for the glycine analogue, and also for the alanine derivative synthesised by Sarah Petit. At that time, interpretation of the spectra proved tricky. Indeed, the four first peaks of the EPR spectra (2600 G - 3200 G) can be attributed to a hyperfine splitting pattern of a $g_Z = 2.26$ peak, with the $I = 3/2$ nuclear spin of one copper atom ($A(Cu) = 169G$). Only one copper atom thus seems to be seen, which was unexpected because of the solid state structure. Two hypotheses were then presented to account for this: either the complexes display a perfect C_3 symmetry in solution, thus rendering all three Cu(II) ions

---

(ix) And the weak solvatochromism, in addition to the low ϵ value for the visible range absorption, suggest the observed transition is of the $d - d$ type.

(x) In the case of **4.3**, no solid state spectra could be recorded, because of a lack of signal. As we will show in section 4.4, this is due to a strong antiferromagnetic coupling.

equivalents, or a mononuclear complex is formed in solution. The latter hypothesis is the most probable, considering the results of the UV measurements (how could a μ_3-hydroxo complex form from the polymer structures?).

In the second region of the spectra (3200 G - 3500 G), a more complicated pattern is seen, which was formerly interpreted as being the result of two $g_X = 2.06$ and $g_Y = 2.01$ signals split by a superhyperfine coupling with the nuclear $I = 1$ spin of nitrogen. We may invoke the same interpretation here, noteworthy since the field separation between successive peaks is almost constant (*ca.* 17(2) G), and is thus consistent with a unique superhyperfine coupling. One may also note the good agreement with the previously deduced superhyperfine coupling constant (*ca.* 16 G).

Overall, EPR measurements point to a mononuclear Cu(II) complex, involving a single coordinating nitrogen atom, and thus most presumably a single tri-coordinating ligand. Other ligands must be found in the coordination sphere, as Cu(II) ions usually display coordination numbers of four, five or six. We can presume they are water molecules, since it is the only common compound in all our syntheses (the Cu(II) salts being hydrated).(xi) The corresponding formula is thus expected to be $[\mathrm{CuL_n(H_2O)_m}]$.

We then tried to perform geometry optimisations at the DFT level, in order to determine the exact geometry. We first employed B3LYP as functional and D95V basis sets[164] for all elements but Cu, which was modelled using a Los-Alamos pseudo-potential and the corresponding double-zeta basis set (LANL2DZ). Optimisations with one to four water molecules were undertook, using an implicit solvent model (methanol, PCM) and in every cases in the final geometry only one water molecule remains coordinated, in a distorted square-planar geometry. The remaining water molecules arrange around the complex, forming H-bonds with the coordinated water but also with the different functional groups of the ligand. Noteworthy, when four water molecules are involved, we observe a H-bond between one uncoordinated water molecule and the central (malonic-like) carbon of the ligand (this water molecule being itself H-bonded to another one). This latter feature is rather simply understood from our previous DD calculations, as this carbon is expected to be quite nucleophilic in $\mathrm{L_1}^{2-}$, but is nevertheless very interesting. It indeed suggests the backbone of our ligand is able to interact with water molecules, which a necessary condition to be fulfilled if we look for an hydrolysis pathway.

Confidence in this structural model is furthermore given from the rather good reproduction of the EPR parameters: $g_1 = 2.04$, $g_2 = 2.05$, $g_3 = 2.16$, $A(Cu) = 225G$ and $A(N) = 19G$, as computed at the B3LYP/def2-TZVPP/DKH level,[165] using an implicit solvent correction (COSMO) for methanol (ORCA 3.0).[166]

We then turned to a much higher level of theory, optimising our structures with the dispersion-corrected ωB97xD functional,[167] and using 6-311++G(d) for all elements, plus Stuttgart-Dresden pseudopotentials on the copper atom,[168] with the same implicit solvent correction as previously. Such a high level may indeed be needed, as H-bonds are seen (and may not be properly described using B3LYP). Interestingly, in that case the optimised geometries show a square-based pyramid geometry around the Cu(II) ion, with a weakly axially coordinated water molecule (*ca.* 2.32 Å away from Cu, compared to 2.03 Å in the basal plane). The B3LYP and ωB97xD geometries are thus quite different, though we may state that somehow an agreement exists between both descriptions, as the axial coordination seems rather weak. Furthermore, we retrieve the same kind of H-bonding between an uncoordinated water molecule and the "malonic" central carbon atom of the ligand, this water molecule being here also stabilised by another water molecule (but, in

---

(xi) And in the case of the coordination polymers, we may assume that the needed water molecules are withdrawn from the atmosphere or from the solvents, which may indeed incorporate a non negligible proportion of water.

that case, coordinated to the Cu(II) ion).

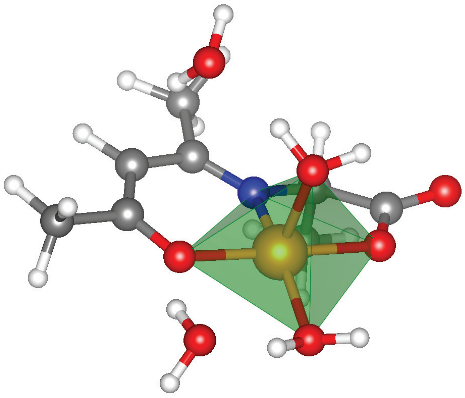

FIGURE 4.2.7: Solution structure of the Cu(II) complex of ${}^{D}L_1{}^{2-}$, with four explicit water molecules.

Actually, from the computed EPR properties, we may indeed see that the structural discrepancies do not seem to have a dramatic effect; we indeed find $g_1 = 2.04$, $g_2 = 2.06$, $g_3 = 2.17$, $A(Cu) = 206G$ and $A(N) = 18G$, using the same level of theory as previously. We may then assume that our lower level description is already rather good, though naturally fine effects (and eventually geometrical effects) could be missed.

4.3 Reactivity studies

As such, we decided to first model the hydrolysis reaction using the lower level of theory, in order to obtain a first, rough estimate of the Potential Energy Surface for our system. The basic idea here was to ease the search of Transition States, which is a rather complicated task already at our lower level of theory, and which becomes incredibly complex with ωB97xD (which presents here slow and problematic SCF and geometry convergences). We present hereafter the results.

4.3.1 First approach with B3LYP

REMINDER: all calculations were performed at the B3LYP/D95V/LanL2DZ level of theory, with inclusion of an implicit solvent (methanol, PCM + keywords "*Dis*, *Rep*, *Cav*"(xii) for a more accurate energetic representation of the solvent cavity). In every cases, transition state structures were optimised, and the PES were computed using the Intrinsic Reaction Path (IRC)[170] as implemented in Gaussian09. Systematically, the reagent and product structures determined from these IRC calculations were fully optimised.

First step: protonation of the ligand. In the previously optimised structure, a H-bond could be seen between one water molecule and the central carbon of our ligand. This particular structure suggested the first step in our hydrolysis mechanism would likely be the protonation of this carbon. Among the products of this first step, we indeed expect to find an hydroxide ion, which is a much better nucleophile than water, and which may attack the enamine carbon, as pictured on Scheme 4.3.1.

(xii) "*Dis*" computes and includes the total solute-solvent dispersion interaction energy,[169] "*Rep*" includes the solute-solvent repulsion dispersion energy and "*Cav*" includes the solute cavitation energy.

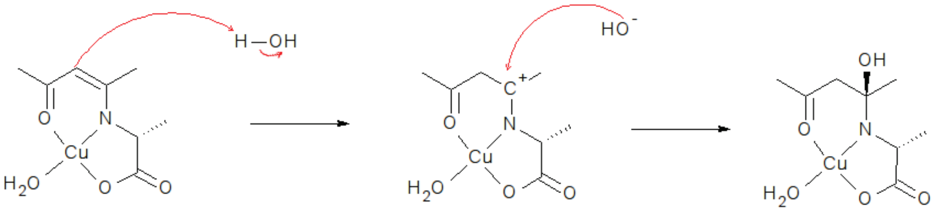

SCHEME 4.3.1: Proposed mechanism for the first step of the reaction. The molecular structure is here simplified for the sake of clarity.

Quite surprisingly, in our calculation these two processes occur almost simultaneously, the protonation of the carbon being quickly followed by the nucleophilic attack of hydroxide on the enamine carbon. The structures of the starting reagent (R1), transition state (TS1) and product (P1) are given on Figure 4.3.1. As one may note, the TS structure actually corresponds to the addition of OH^-, the protonation occurring just before TS1 (thus yielding a rather unusual shape of the IRC curve). Interestingly, we retrieve a six-centre intermediate for the reaction, with an additional water molecule, which are depicted on Scheme 4.3.2. This supplementary H_2O actually helps the proton transfer, and stabilises the hydroxide group on a reactive position, thus permitting the following nucleophilic attack.

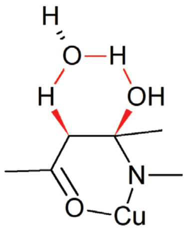

SCHEME 4.3.2: Simplified representation of the six-centre structure of TS1.

Product P1 is less stable than R1 (+31 kcal/mol), and despite the additional water molecule, the free energy activation barrier is high: +40 kcal/mol. Such a high barrier mechanism is hardly feasible at room temperature, whereas our reaction occurs spontaneously in such conditions. Nevertheless, we may expect a large stabilisation of the TS with the inclusion of dispersion, as it involves many water molecules. In turn, we should observe a decrease in the energy barrier, which may render this reaction feasible.

Second step: prototropy. As such, we kept on studying the reaction pathway with our low level method. Product P1, which serves as a starting point for the second elementary step, has a rather remarkable structural feature. The proton on the alcohol group (that was formerly added to the ligand backbone) is indeed pointing towards the imino nitrogen atom. From a chemical point of view, we know that our reactions must, at some point, lead to the addition of two protons on this nitrogen atom, in order to retrieve the starting deprotonated amino-acid. We thus looked if a direct 1,3 protonation from the hydroxyl to the imine was possible.

As shown on Figure 4.3.2, we indeed manage to optimise a TS structure for such a 1,3 proton transfer, displaying a four centres core. The deduced IRC curve here shows a more usual aspect, and product P2 has the same free energy as P1 (computed difference of only 0.02 kcal/mol). The energy barrier for this process is much lower than previously, *ca.* 17.4 kcal/mol, and thus quite feasible at room temperature.

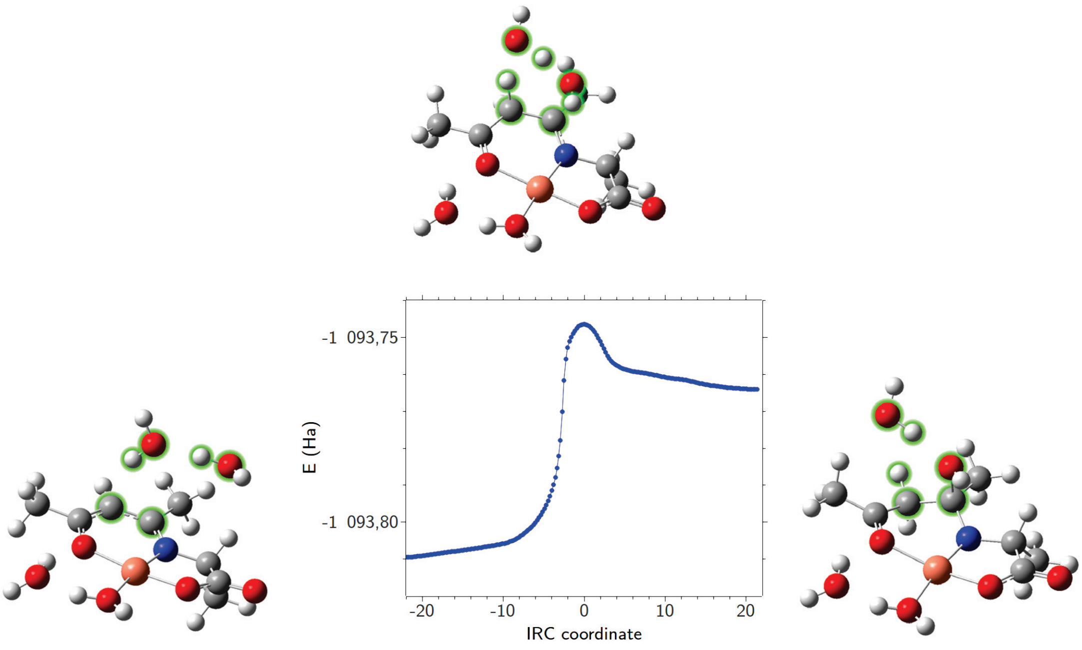

FIGURE 4.3.1: Structures of the reagent, transition state and product for the first reaction step, and corresponding IRC curve. The six centres intermediate sub-structure is highlighted in green.

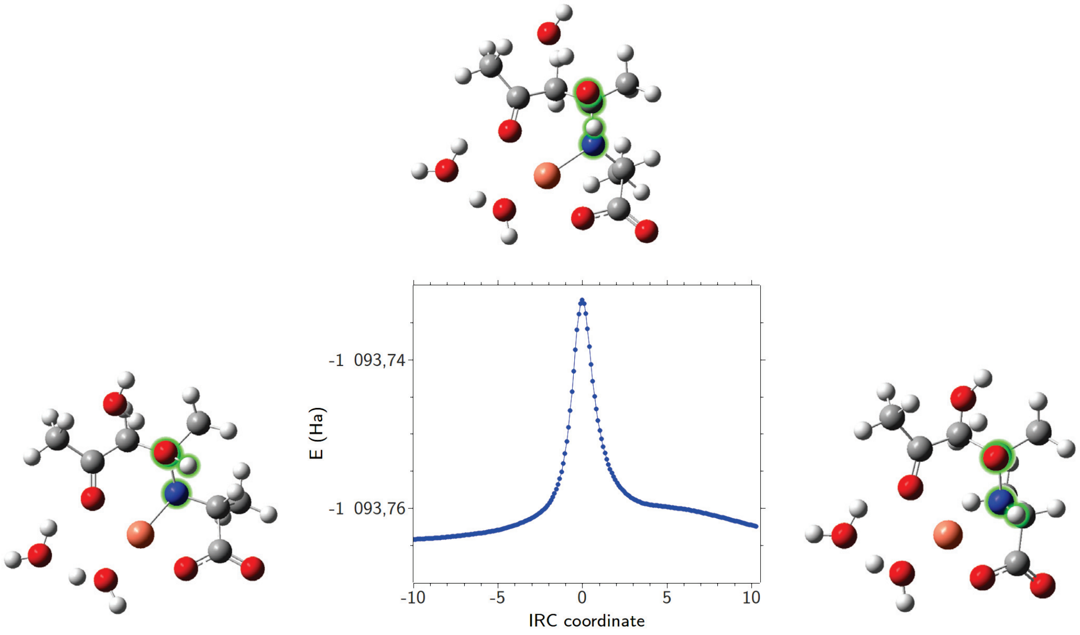

FIGURE 4.3.2: Structures of the reagent, transition state and product for the second reaction step, and corresponding IRC curve. The four centres intermediate sub-structure is highlighted in green.

Third step: another prototropy. In order to complete our reaction, as we said we need to add another proton on the nitrogen. It is rather plain in the structure of product P2 that no acidic proton is found in the vicinity of the N atom. However, a water molecule is found near the deprotonated alcohol group, and the latter seems to interact with one of its proton (distance of 1.48 Å). We thus wondered if the alkoxy group could be protonated once again and be used to transfer an additional proton on the nitrogen.

A TS structure could here also be optimised (though it proved a bit more difficult to find), and is represented on Figure 4.3.3. As one can remark, we retrieve here also a six-centres core, the water molecule being used once again as a proton channel. Interestingly, we thus deprotonate the central carbon of the ligand, rather than the water molecule.

The free energy barrier for this process is 9.5 kcal/mol, and noticeably product P3 is more stable than reagent R3 (-12 kcal/mol), but still less stable than the starting reagent (+20 kcal/mol).(xiii)

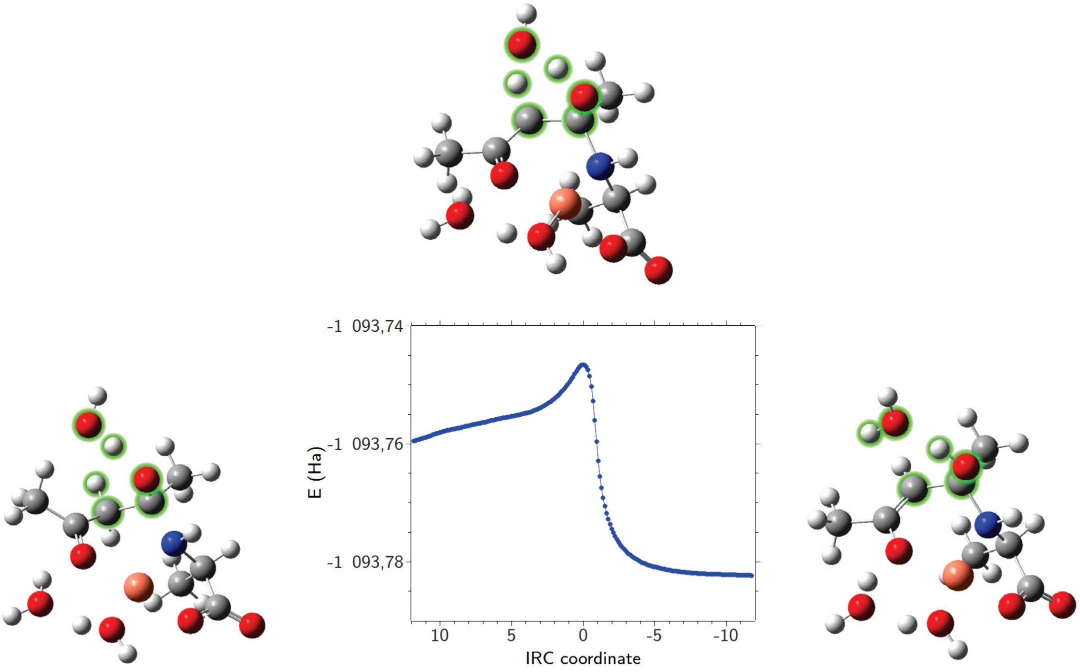

FIGURE 4.3.3: Structures of the reagent, transition state and product for the third reaction step, and corresponding IRC curve. The six centres intermediate sub-structure is highlighted in green.

Fourth step: intramolecular metathesis. From product P3, there is no simple way to transfer a proton to the nitrogen: any approach of an acidic proton is prevented by the presence of the first transferred H atom on this group, which is quite rigidly oriented because of the coordination with copper.

We thus looked for a reaction path that would decoordinate this nitrogen and make the second protonation more probable. Starting from the geometry of P3, a possibility would rely on an intramolecular metathesis: in the vicinity of this coordination position, we indeed also have an alcohol group, which can coordinate too. We thus searched a TS for this metathesis (depicted on Scheme 4.3.3), and found one. Its geometry is depicted on Figure 4.3.4.

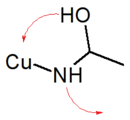

SCHEME 4.3.3: Simplified representation of the searched fourth reaction path..

(xiii)Note that, on Figure 4.3.3, the IRC coordinate axis is inverted. This is not a mistake, but is due to the fact that there is no way to precise in which direction the reaction should be unfolded, and as such the program somehow picks the direction at random.

Here again, the free energy barrier is quite low (24.2 kcal/mol), and the P4 product is found to be less stable than P3 (+13.6 kcal/mol).(xiv)

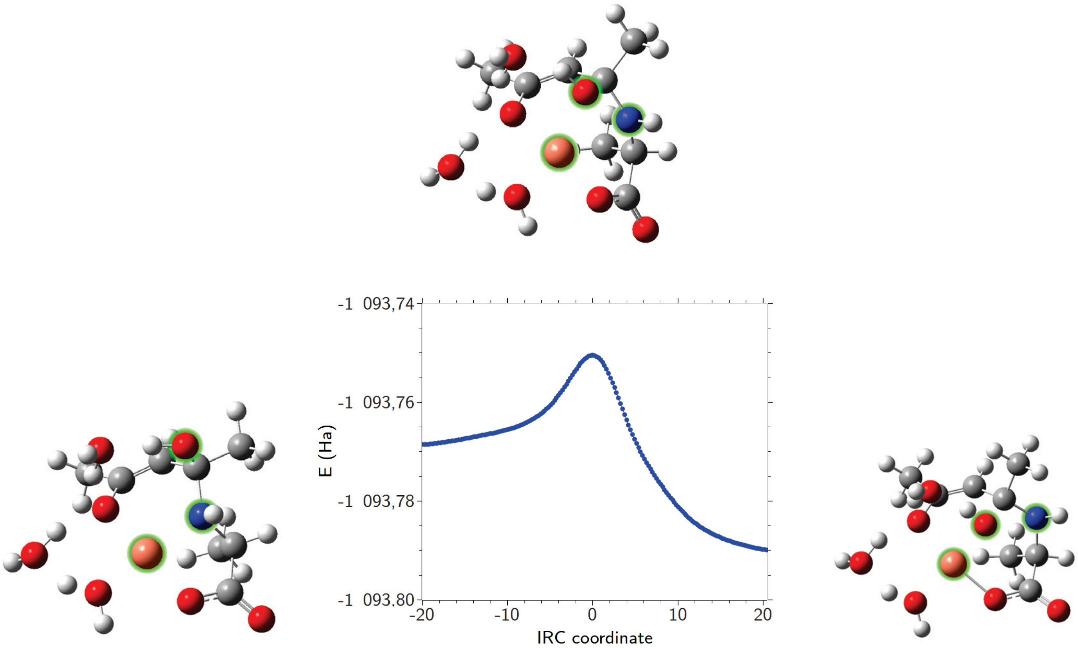

FIGURE 4.3.4: Structures of the reagent, transition state and product for the fourth reaction step, and corresponding IRC curve. The six centres intermediate sub-structure is highlighted in green.

Final step: prototropy and rearrangement. From product P4, we can then quite straightforwardly see how to proceed in order to transfer a second proton on the nitrogen atom: the alcohol group is indeed now well positioned to interact with the amine group, and the proton transfer should be quite easy. We thus looked for a reaction path that would allow to perform directly this proton transfer (with a four-centre structure).

We represent on Figure 4.3.5 the obtained R5, TS5 and P5 geometries. In this case also, the energy barrier is not high (25.5 kcal/mol), and more importantly the reaction in that case is found to be exothermic (-33 kcal/mol). Actually, product P5 has a slightly lower free energy than the initial reagent (-2 kcal/mol).(xv)

Furthermore, we can see that this product corresponds to the expected products of hydrolysis: we indeed retrieve the starting amino acid (in the carboxylate form) and the acetylacetonate moiety, coordinating the Cu(II) ion.

Long story short. We represent on Scheme 4.3.4 the total free energy profile for our reaction. The weak exothermicity suggests the degradation should indeed take place in a sensible manner, as it is thermodynamically slightly favoured. Actually, the thermodynamic stabilisation of degradation is largely underestimated in this approach, as the aminoacid complexes of copper (and the potassium salts, also) are sparingly soluble in methanol.

(xiv) In that case, the IRC curve seem to show an opposite tendency, but it only displays the electronic energy and not the free energy (with thermodynamic corrections.

(xv) Note that here, optimisation after the IRC calculation proves to be very important. Following the reaction coordinate defining our TS does not indeed allow to retrieve product P5, since the C-N bond is not fully broken yet (distance of 1.72 Å).

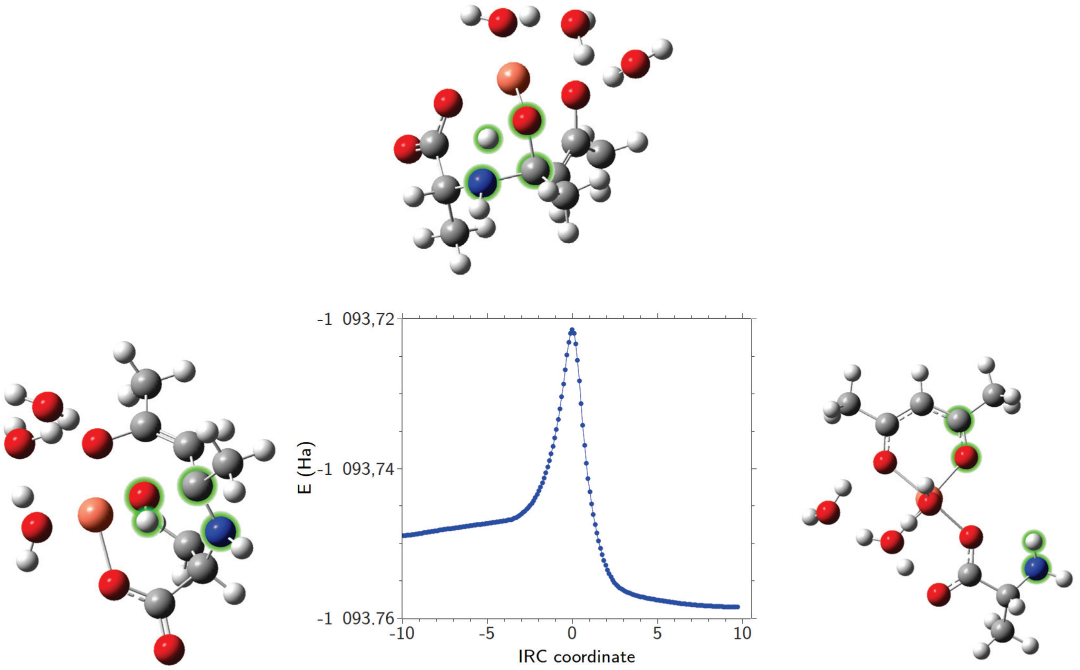

Figure 4.3.5: Structures of the reagent, transition state and product for the fifth reaction step, and corresponding IRC curve. The four centres intermediate sub-structure is highlighted in green.

On the point of view of kinetics, the first energy barrier is of course too high to allow the reaction to actually take place in solution. The other energy barriers on the other hand are acceptable, being sufficiently high to prevent the reaction to occur too quickly at room temperature, in good agreement with experimental evidences: the complexes do not decompose at once, but slowly and during the recrystallisation process.
We thus turned ourselves to the higher level modelling, namely at the ωB97xD/6-311++G(d) + SDD level. The results are presented hereafter.

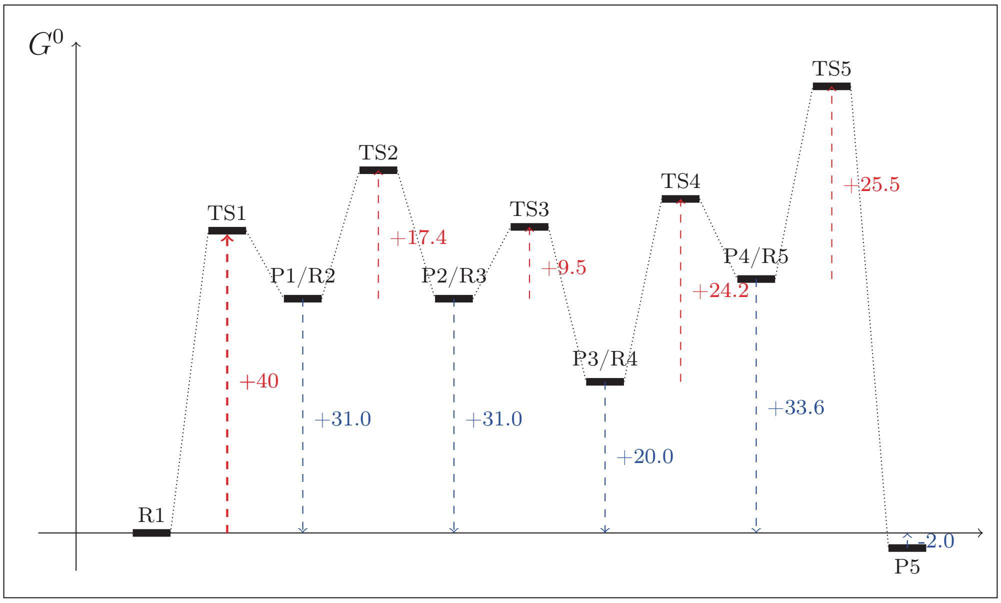

Scheme 4.3.4: Complete energy profile for the hydrolysis reaction of $[\mathrm{Cu}^{\mathrm{D}}\mathrm{L}_1(\mathrm{H}_2\mathrm{O})]$ in methanol, with four explicit water molecules, at the B3LYP/D95V/LanL2DZ level.

4.3.2 Refining with ωB97xD.

First step: protonation of the ligand. In this case too, the optimised structure in solution presents a marked H-bond between a water molecule and the central carbon atom, and thus we searched a transition state corresponding to this protonation.
Starting from TS1 structure, we are unable to locate a transition state. However, we manage to optimise one, which interestingly corresponds only to the protonation (and not to a protonation + nucleophilic attack on the hydroxide). We represent the optimised geometry on Figure 4.3.6, as well as the reagent (R1ω) and product (P1ω) structures.

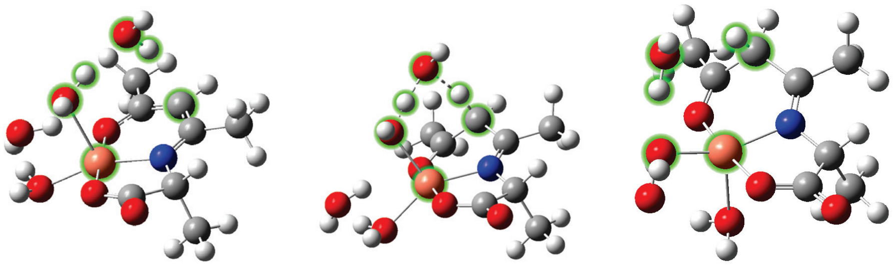

FIGURE 4.3.6: Structures of the reagent, transition state and product for the first reaction step, calculated at the ωB97xD/6-311++G(d)/SDD level. The six centres intermediate sub-structure is highlighted in green.

As one can notice, TS1ω involves a six-centres structure, and the overall proton transfer is achieved between the coordinated water molecule and the carbon (the initially H-bonded water molecule serving only as a proton channel). The free energy barrier for this process is only 22.7 kcal/mol, and P1ω is found 13.0 kcal/mol above the initial reagent. Note that in this case, IRC calculations proved to be very tricky, and inevitably crash after a few points on both directions. We thus directly optimised the reagent and product structures, and as such cannot provide IRC curves.

Second step: second prototropy and nucleophilic attack. In the previous reaction path, protonation of the central carbon was immediately followed by a nucleophilic attack of OH^- on the imino carbon. Here, the reaction does not follow immediately, and the product of the first step is not in an appropriate geometry to allow this: the hydroxide ligand is indeed in *trans* position with respect to the nitrogen, and a water molecule is located on the axial coordination position (thus blocking any hydroxide displacement). Nevertheless, a proton transfer between this water molecule and the coordinated hydroxide could possibly allow the nucleophilic attack, and thus we looked for the corresponding

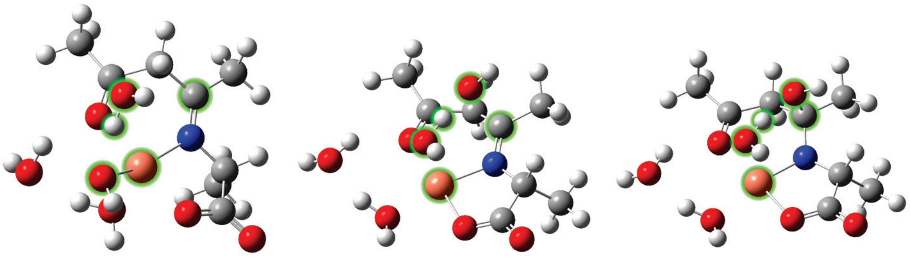

FIGURE 4.3.7: Structures of the reagent, transition state and product for the second reaction step, calculated at the ωB97xD/6-311++G(d)/SDD level. The five centres intermediate sub-structure is highlighted in green.

transition state TS2ω. We represent on Figure 4.3.7 the geometries for this TS and the corresponding product and reagent structures. In that case too, IRC calculations proved unsuccessful, and we had to fully optimise the geometries.
As one may note, here again we observe a two-steps phenomenon, with a first proton transfer between the coordinated hydroxide and the water molecule, followed by the nucleophilic attack of the resulting OH^- on the enamine group. The activation energy for this process is also rather low, *e. g.* 20.8 kcal/mol, and after optimisation product P2ω is found lying 11.0 kcal/mol below P1ω.

Third step: nitrogen protonation. Basing on our previous results, we would expect the next step to consist in a proton transfer from the hydroxyl group towards the nitrogen atom, though we apparently do not retrieve the former H-bond between hydroxyl and nitrogen. Nevertheless, scanning the N-H distance(xvi) permitted to isolate a TS for this prototropy. In this case, IRC calculations were quite complicated, crashing within a few steps, and we thus had to directly optimise both reagent (R3ω) and product (P3ω) geometries. The corresponding structures are provided on Figure 4.3.8. As one can notice, we retrieve a four-centres intermediate species, as was observed at the B3LYP level.
Here also, the activation energy is rather modest, *ca.* 22.6 kcal/mol, and product P3ω is found 0.7 kcal/mol above reagent R3ω and 2.9 kcal/mol above the initial reagent R1ω. However, a striking difference with the B3LYP calculations must be noted: in the geometry of P3ω, no water molecule is found in the vicinity of the "deprotonated hydroxyl group". As such, we cannot follow the same reaction scheme from this point, as the following step in B3LYP was a proton transfer from a water molecule to this oxygen – a proton that was afterwards transferred to the nitrogen atom, leading to the breaking of the C-N bond –.

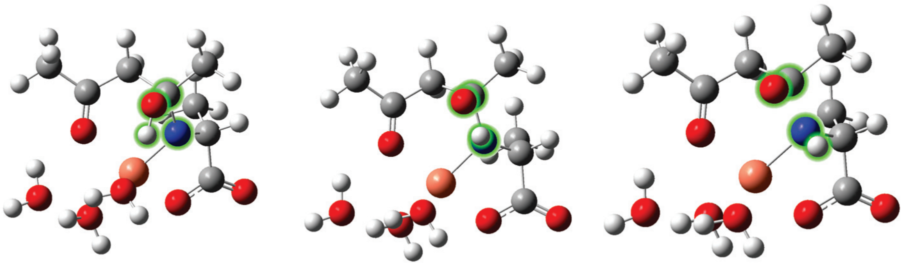

FIGURE 4.3.8: Structures of the reagent, transition state and product for the third reaction step, calculated at the ωB97xD/6-311++G(d)/SDD level. The four centres intermediate sub-structure is highlighted in green.

Fourth step: second nitrogen protonation. Nevertheless, as careful inspection of the molecular structure of P3ω reveals the presence of an acidic proton in the vicinity of the protonated imino group. Indeed, because of the different reactions, the ligand backbone started to fold, and one of the protons on the initally protonated carbon is now pointing toward the nitrogen atom, and is found a 2.66 Å from it, as pictured on Figure 4.3.9.
We thus considered the possibility of a direct proton transfer from the carbon atom to the nitrogen, and first performed a relaxed geometry scan on the N-H distance. The result of this scan is provided on Figure 4.3.10.

(xvi) Using the relaxed scan in Gaussian 09.

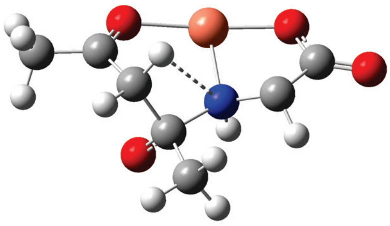

Figure 4.3.9: Detail on the geometry of product P3ω, highlighting the proximity of an acidic proton to the nitrogen atom (dashed line). For the sake of clarity, water molecules and the amino-acid methyl groups were omitted.

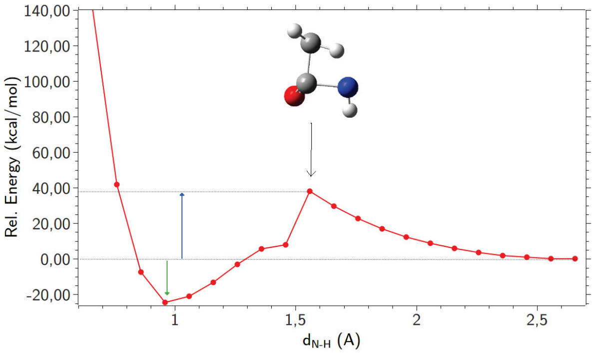

Figure 4.3.10: Relaxed geometry scan on the N-H distance, computed at the ωB97xD/6-311++G(d)/SDD level. Inset: detail of the molecular structure at the cusp.

A cusp is clearly observed on this curve, at a N-H distance of 2.55 Å, suggesting that a transition state may be found on the potential energy surface close to this point. We can notice that the relative energy of this point is rather high (*ca.* 38.0 kcal/mol), but it does not imply the potential energy barrier will be large. Indeed, it is only a rough estimate of the electronic energy of the TS, and does not take into account thermodynamic corrections.

We thus tried to optimise a TS structure starting from this point, but the only structure we found for the moment does not permit to retrieve product P3ω as a starting reagent. As one can see on Figure 4.3.11, in this TS the C-N bond is indeed already broken, and the H atom is found lying exactly in between the central carbon atom and the nitrogen. Actually, this TS corresponds to an intermolecular prototropy between the two expected products of reaction (acetylacetonate and alanine), rather than the expected intramolecular prototropy.

We are thus still working on this TS structure, but as one can note from Figure 4.3.10 protonation of the nitrogen is accompanied by a large electronic energy stabilisation (*ca.* 20.0 kcal/mol). The corresponding reaction will thus very likely be thermodynamically favoured. Actually, a free geometry optimisation starting from the minimum of the scan curve – represented on Figure 4.3.12 – yields a total stabilisation of 28.2 kcal/mol with respect to P3ω, and thus of 25.3 kcal/mol with respect to R1ω. The overall reaction is then indeed strongly favoured from the viewpoint of thermodynamics.

Summary

We report on Scheme 4.3.5 the resulting energy profile for our reaction at the ωB97xD/6-311++G(d)/SDD level.

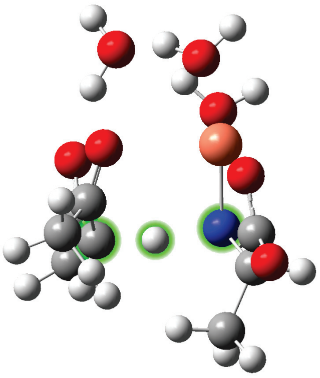

FIGURE 4.3.11: Found TS structure for the fourth reaction step. C, H and N atoms involved in this reaction are highlighted in green.

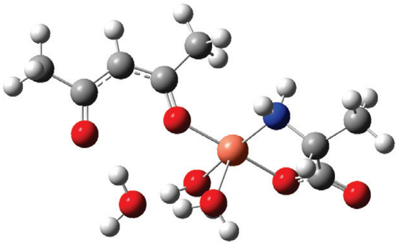

FIGURE 4.3.12: Optimised structure for the minimum of the scan curve 4.3.11, at the ωB97xD/6-311++G(d)/SDD level.

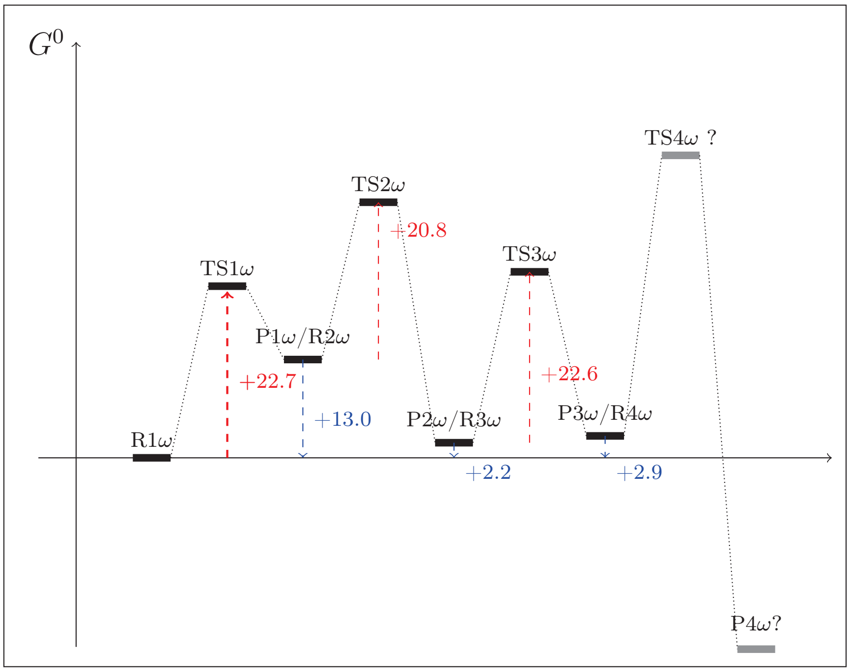

SCHEME 4.3.5: Energy profile for the hydrolysis reaction of $[Cu^{D}L_1(H_2O)]$ in methanol, with four explicit water molecules, at the ωB97xD/6-311++G(d)/SDD level.

The overall exothermicity suggests the hydrolysis reaction should indeed take place, and provided that the last energy barrier is not too high, the reaction should also be quite favoured from the viewpoint of kinetics. As expected, dispersion interactions have a major impact on our reaction: energy barriers are systematically lower compared to the ones we obtained with B3LYP, but the reaction path is also quite different. For instance, the first reaction step in B3LYP (protonation of the central carbon and hydroxylation of the enamine carbon) can be decomposed into two steps with ωB97xD. The last step also seems to be slightly different, because the starting reagent geometries in ωB97xD and B3LYP do not match. Nevertheless, both computational methods point to the same final hydrolysis products, and also to the overall feasibility of the process.

In our experiments, we thus very likely witness a competition between two processes: on one hand, the evaporation of the solvent and the crystallisation of the desired complexes, and on the other hand the degradation of the mononuclear complexes in solution because of water. Performing the synthesis in rigorously anhydrous conditions should allow to isolate only the desired compounds. Corresponding experiments are planned in the near future.

4.4 Magnetic properties

As we mentioned in the introduction of this chapter, we synthesised complexes **4.1** and **4.2** noteworthy since they may display interesting magnetic properties, among which is spin frustration. We thus performed static magnetic measurements on these compounds, which we present in the following subsections. Nevertheless, in the course of our syntheses, we also isolated coordination polymers **4.3** and **4.4**, and we also studied their magnetic properties.

4.4.1 Coordination polymers 4.3 and 4.4

Let us then first consider coordination polymers **4.3** and **4.4**. As we formerly saw, their structures are very similar, and noteworthy they present very close bridging patterns, which seem fitted to promote a strong antiferromagnetic coupling. As such, we said we could expect these complexes to present a 1D order, behaving as monodimensional antiferromagnets.[64]

We present on Figure 4.4.1 the thermal evolution of susceptibility for these two compounds. Both curves present very similar aspects, with a slow increase from room temperature to intermediate temperatures, a local maximum at 80(5) K for **4.3** and 100(5) K for **4.4**, and a marked increase at very low temperature. The two first features are rather characteristic of antiferromagnetic 1D chains, the presence of an antiferromagnetic coupling being furthermore confirmed by the continuous decrease of $\chi_m T$ with temperature for both complexes. The low temperature divergence, on the other hand, is not an expected feature of 1D antiferromagnetic chains. It may be due to a paramagnetic impurity or border effects, as seen in the case of $[Cu(C_2O_4)].1/3H_2O$.[171] In any case, fittings with a spin 1/2 chain model proved unsuccessful here.

Anyway, from the location of the maxima of the two curves, we may get an estimate of the coupling parameter, as we expect to have

$$\frac{k_B T_{max}}{|J|} = 0.641. \tag{4.1}$$

Here, this leads to $|J| = 87(5)$ cm^{-1} for **4.3** and 108(5) cm^{-1} for **4.4**: we indeed observe a rather strong antiferromagnetic coupling. Note that the difference in magnetic coupling between both compounds is very marked, despite the similarity of the structures. Actually, from Table B.5 we can see that the bridging pattern in both structure is nearly identical; for instance, the angle between successive Cu(II) ions through the bridging O atom is

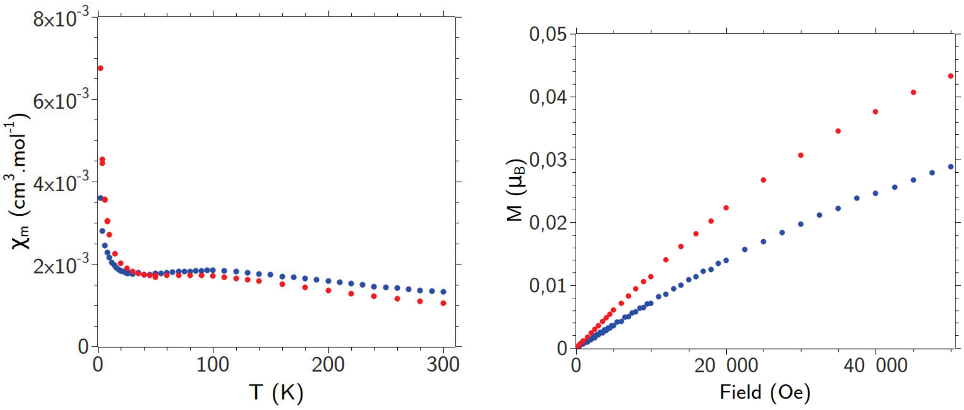

FIGURE 4.4.1: $\chi_m = f(T)$ (left) and $M = f(H)$ curves (right) for complexes **4.3** (red) and **4.4** (blue). Susceptibility measurements were performed under a static field of 1000 Oe, and magnetisation was measured at 2 K.

128.4(1)° in both cases. However, the coordination sphere around Cu(II) varies slightly from one complex to the other, as evidenced for instance by the Addison parameter (0.10 for **4.3**, 0.06 for **4.4**), and is a probable cause for the observed difference in the magnetic coupling. We thus retrieve the line of arguments of O. Kahn: subtle changes in the geometry, especially on the bridging part of our complexes, can lead to marked differences in the magnetic behaviour.

4.4.2 Trinuclear complexes

Foreword

As we have seen previously, in the crystal structures of both **4.1** and **4.2** there are two crystallographically independent complexes. The magnetic study of both complexes is thus expected to be a quite complicated task, and for the sake of simplicity we decided to focus on **4.2** only. The study of **4.1** will be undertaken in the near future.

Experimental data

Let us now focus on trinuclear complex **4.2**. We present on Figure 4.4.2 the temperature dependence of its susceptibility and field dependence at 2 K of its magnetisation.

From the $\chi_m T = f(T)$ curve, it is rather plain to see that a weak antiferromagnetic coupling is acting: the $\chi_m T$ product is indeed almost constant between 300 K and 100 K, and drops abruptly below 50 K, to reach 0.31 $cm^3.K.mol^{-1}$ at 2 K. The room temperature value, 1.20 $cm^3.K.mol^{-1}$, is in the expected range for 3 uncoupled $S = 1/2$ spins with a Landé factor $g \geq 2$, here equal to *ca.* 2.06. On the other hand, the 2 K value is too low for a single $S = 1/2$ spin (expected value of 0.375 $cm^3.K.mol^{-1}$).[64] Interestingly, such a low 2 K value was not observed in the case of the glycine derivative (0.42 $cm^3.K.mol^{-1}$), and we may wonder if it is a sign of anisotropic or antisymmetric (Dzyaloshinski-Moriya) couplings, themselves being signs of frustration or of the relaxation of a frustration.[156](xvii)

We then tried to fit the magnetic data assuming a unique magnetic coupling between all our three Cu(II) ions (using the Van Vleck formula and equations (2.29) and (2.34), setting all couplings equal to J). Doing so, we managed to model quite correctly the

---

(xvii) Yet, such couplings might also have been observed for the glycine derivative, since it is chiral (though the ligand is not).

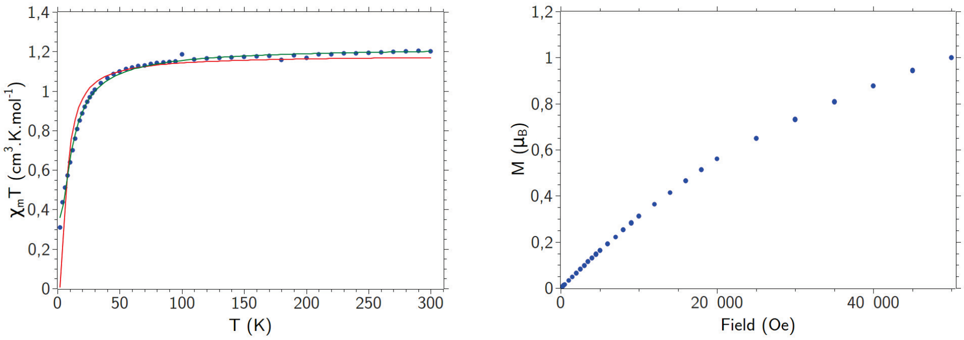

FIGURE 4.4.2: $\chi_m T = f(T)$ (left) and $M = f(H)$ curves (right) for complex **4.2**. Susceptibility measurements were performed under a static field of 1000 Oe, and magnetisation was measured at 2 K. The solid lines on the susceptibility curve correspond to fittings with two Van Vleck equations for an equilateral triangle (see text for more details).

experimental data with an antiferromagnetic coupling $J = -9.1(5)$ cm^{-1} and a Landé constant $g = 2.51(1)$. This last value is rather high for a Cu(II) based complex – one expecting a value much closer to 2.003 – and suggests this fitting is only a mathematical artefact. If we let g take different values in the doublet (g_D) and quartet (g_Q) states, thus rewritting the Van Vleck equation as

$$\chi T = \frac{N_A \mu_B^2}{4k_B} \frac{g_D^2 + 5g_Q^2 \exp\left(\frac{3J}{2k_B T}\right)}{1 + \exp\left(\frac{3J}{2k_B T}\right)}, \tag{4.2}$$

we obtain a better agreement with the experimental data and more "physical" values: $g_D = 1.96(3)$, $g_Q = 2.11(1)$, $J = -7.4(2)$ cm^{-1}. We can remark that the coupling is here also rather weak. Nevertheless, we know from X-Ray diffraction that our complexes are rather unsymmetrical, and as such the physical meaning of these fittings is rather dubious. Unfortunately, as we showed in Chapter 2 we cannot deduce from our experimental data three different magnetic couplings, as the Van Vleck equation for an asymmetric triangular complex bases only on two energy differences.

Theoretical modelling

We thus decided to study **4.2** with the tools of theoretical chemistry, in the same spirit as what was previously done in the case of the glycine derivative. Here, we are interested in modelling the lowest energy states of our trinuclear complexes, and more specifically we will focus on the first quadruplet and the two first doublet states. To do so, many different methods have been used in the literature, but three of them appear to be most frequently used: Broken-Symmetry DFT (BS-DFT), DDCI and CASPT2/NEVPT2 calculations.

A few words on BS-DFT. As suggested by the name, BS-DFT[172–174] is based on Density Functional Theory, and is thus a relatively "cheap" method (from a computational point of view). The basic idea beneath it is very simple: one first evaluates the ground state energy for a given spin multiplicity, for instance in our case the quartet state of one of the trinuclear complexes, and computes the associated wavefunction. Then, one spin (for instance on any of our Cu atom) is flipped and the energy of this new (doublet) "state" is computed, without any orbital relaxation nor SCF cycle. The energy difference between the high spin state and this spin-flip state is directly related to the magnetic coupling.

Formally, this flipping is equivalent to the reversal of one spin in the MO diagram *ceteris paribus*, and as such the obtained wavefunction is not an eigenfunction of the spin operator S^2: it does not respect the symmetry of the Hamiltonian, hence the label BS.

BS-DFT calculations have already been successfully applied in the case of trinuclear complexes,[175–177] noticeably of Cu(II), and we wondered whether they could be used in our case. We got in touch with Dr. Jean-Marie Mouesca (CEA Grenoble), a specialist of BS-DFT calculations, and quickly realised our complexes cannot be efficiently described with this approach. There indeed exists a strong *caveat* in BS-DFT calculations: not only the magnetic orbitals symmetry is broken, but also is the symmetry of the bridge orbitals.[178] This may result in a potentially non negligible overlap of the magnetic orbitals through the bridge, which should be orthogonal for the calculations to make sense. In our case, the bridging ligand is very small (monoatomic connexion), and thus a strong overlap is likely to occur, preventing the use of BS-DFT.

Multireference modelling. We then turned ourselves to wavefunction based-methods, and we first considered DDCI calculations,[24,26] which we performed in collaboration with Dr. Marie-Bernadette Lepetit (Institut Néel, Grenoble). As we mentioned in Chapter 2, DDCI calculations are based on a CI expansion of CASSCF wavefunctions for different spin multiplicities, in which most of the excitations are not explicitly treated as they are redundant in the different spin states. Overall, three classes of excitations only are considered in DDCI calculations:

- mono-excitations: LMCT, *i.e.* excitations from the inactive space to the active space (labelled $1h$), MLCT (from the active space to virtual orbitals, labelled $1p$), and direct inactive to virtual excitations ($1p - 1h$);
- di-excitations: double excitations from the inactive space towards the active space ($2h$), or from the active space towards the virtual orbitals ($2p$);
- tri-excitations: coupling of $1p - 1h$ excitations with LMCT ($1p - 2h$) or MLCT ($2p - 1h$);

and further simplifications also exist: DDCI-1 (which only incorporates the mono- excitations) and DDCI-2 (which incorporates mono- and di-excitations). Here, as was previously done in the case of the glycine derivative, we considered the successive levels of approximation. This comes from two reasons: first, this allows to get information on the different mechanisms acting beneath the magnetic couplings in our trinuclear complexes.[179] Second, our complexes are huge systems, and the highest level calculations could simply be unaffordable because of the high computational cost.(xviii) For this reason, we also considered NEVPT2 calculations,[22] which are known to be much less computationally demanding, and proved to be rather efficient in the modelling of magnetic couplings. They indeed involve formally similar excitations as the DDCI-3 calculation, however it is known that they tend to miss higher order effects which are included in the DDCI procedure, and thus may underestimate the magnetic couplings.[25,180]

In any case, we did not model the whole crystal asymmetric unit at once, but considered each complex separately. For both of them, the same chain of calculations was applied: first, we converged the unrestricted Hartree-Fock wavefunction for the quartet state. This UHF wavefunction was used as an input for a restricted-open shell calculation, which was itself used as a starting point for a CASSCF calculation. Here, our active space will consist in the three highest orbitals, occupied by three electrons (the 3 $d_{x^2-y^2}$ orbitals

---

(xviii) Actually, several crashes on the laboratory cluster led us to this conclusion...

one would expect in a crystal-field approach). Finally, the CASSCF wafunction was used as a starting point either for a DDCI-n or SA-CASSCF/NEVPT2 calculation.(xix) All computations were made using ORCA 3.0, and both DDCI-n and NEVPT2 calculations were performed at the CINES. All elements were modelled using a triple-zeta quality basis set with polarisation (TZVP),[165] and core electrons of the Cu atoms were replaced by Stuttgart-Dresden pseudopotentials (ECP10MDF).[168] In the case of the DDCI-n and NEVPT2 calculations, RI approximation was employed and, correspondingly, the auxiliary TZV/C basis set was used. In order to give an idea of the complexity of the system, we may simply say that we deal here with 1006 basis functions...

Let us first focus on the CASSCF results. We represent on Figure 4.4.3 the optimised active orbitals for one complex. As one can note, the MOs all involve the three Cu(II) ions, as well as the central hydroxo bridge. The metal contributions are very reminiscent of $d_{x^2-y^2}$ AOs, as expected from crystal field theory; we may thus expect our different descriptions to bear some physical meaning.

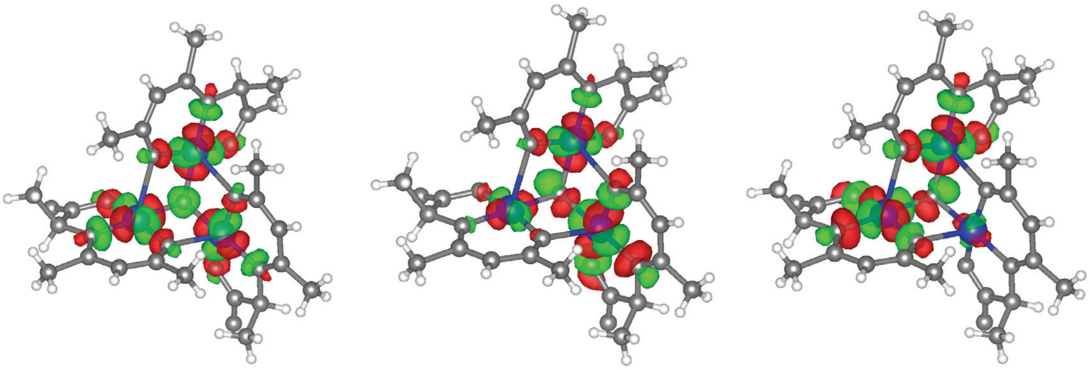

FIGURE 4.4.3: Representation of the active space for one complex in the asymmetric unit of **4.2**, as computed at the CASSCF level. The same orientation is given for the three MOs, and for the sake of clarity all heavy atoms but Cu are depicted in gray.

At the SA-CASSCF level of theory, a total ferromagnetic coupling is seen, as evidenced by the stabilisation of the quartet state over the doublets. Nevertheless, the energy splitting is very small: 9.6 cm^{-1} between the quartet and the first doublet (8.3 cm^{-1} for the second complex in the asymmetric unit), 12.8 cm^{-1} between the quartet and the second doublet (respectively 13.1 cm^{-1}). As such, already at the SA-CASSCF level we are able to reproduce the low magnitude of the magnetic exchange, if not its sign.

At the RI-DDCI-1 level, the calculations converge without any difficulty, since the number of Configuration State Functions (excitations) is low, *e.g.* 8594. Nevertheless, the correction on the energies differences is quite moderate, not to say negligible: only -0.7 cm^{-1} for the first doublet, and -0.5 cm^{-1} for the second. This tends to suggest that, in our case, single excitations do not contribute significantly to the antiferromagnetic exchange. Interestingly, the energy differences are quite close to those obtained in the case of the glycine analogue (+7.0 cm^{-1} and +14.0 cm^{-1}, respectively), which suggests that maybe the same line of argument already held for this compound.

At the RI-DDCI-2 level, things are much more complex, as the number of CSF explodes: 3824070 CSF per complex! Several tests were performed at the CINES, but even one

---

(xix) Note that we employed state-specific orbitals for the NEVPT2 calculations.

hundred and twenty hours of computation on one hundred and sixty eight cores (20160 CPU hours!) did not allow the first iteration to finish.
Among all these CSF, some may not be relevant for our system: excitations from C-H bonds for instance should not contribute significantly to the magnetic coupling. We may thus consider suppressing some excitations from our CI space, in order to alleviate the computational effort. However, selecting them by hand would be a tremendous task (as there are 1006 orbitals to consider). Furthermore, ORCA does not permit to do this for the moment, as it only allows to select excitations within a MO energy window. Still, using this energy window selection we may already simplify a bit our CI space: MOs 5 to 37 (occupied) and 953 to 1005 (virtual) indeed involve only non-coordinating atoms. We could thus select only MOs 37 to 953 in the CI procedure (saving eighty-nine MOs), the correction from the four first MOs being most presumably negligible.(xx)
Doing so, the number of CSF reduces slightly (moving to 3635542), which is seemingly not enough for the calculation to proceed. We could crop a little more the CI space, but we would not be able then to evaluate the relevance of the computed energies. As such, DDCI calculations for our system seem to be out of reach for the moment.

At the RI-NEVPT2 level on the other hand, no convergence problem is seen. The correction on the energy differences is much more marked than what was seen at the DDCI-1 level: the first doublet is now only 2.8 cm^{-1} above the quartet state, and the second one is found at $+8.1$ cm^{-1}. Overall, the second-order corrections thus enhance the antiferromagnetic character of the coupling, as was observed in the case of the glycine analogue. More information can be gained from a comparison of the energy corrections in the quartet (Q1) and doublet (D1 and D2) states. The results are summed up in Table 4.2.

TABLE 4.2: Detail of the NEVPT2 energy corrections for doublets states D1 (Δ_1) and D2 (Δ_2), with respect to the quartet state corrections (values in cm^{-1}), based on a CAS(3,3) reference wavefunction. Notation: $V_{ab}^{rs,[0]}$, excitation from two inactive orbitals a, b towards two virtuals orbitals r, s; $V_{ai}^{rs,[-1]}$, inactive-virtual and active-virtual excitation; $V_{ab}^{is,[1]}$, inactive-active and inactive-virtual excitation; $V_{ab}^{ij,[2]}$, double inactive-active excitation; $V_{ij}^{rs,[-2]}$, double active-virtual excitation; $V_{ai}^{rj,[0]}$, inactive-virtual and active-active excitation; $V_{ii}^{rj,[-1]}$, active-virtual and active-active excitation; $V_{aj}^{ik,[+1]}$, inactive-active and active-active excitation. The DDCI equivalent notation is also given.

Excitations	"DDCI equivalent"	Δ_1	Δ_2
$V_{ab}^{rs,[0]}$	$2h-2p$	-0.4	-0.3
$V_{ai}^{rs,[-1]}$	$1h-2p$	**2.0**	**1.3**
$V_{ab}^{is,[+1]}$	$2h-1p$	**-3.5**	**-2.8**
$V_{ab}^{ij,[+2]}$	$2h$	**-3.3**	**-3.4**
$V_{ij}^{rs,[-2]}$	$2p$	**-1.2**	**-1.2**
$V_{ai}^{rj,[0]}$	$1h-1p$	0.0	**2.2**
$V_{ij}^{rk,[-1]}$	$1p$	-0.5	-0.4
$V_{aj}^{ik,[+1]}$	$1h$	-0.1	-0.1

First of all, we may note the similar and low impact of the double inactive-virtual excitations $V_{ab}^{rs,[0]}$ on the energy differences. In the DDCI scheme , these excitations are

---

(xx) Indeed, the corrections to the energy difference at the DDCI-2 level evolve as $1/\Delta E\Delta E'$, where ΔE and $\Delta E'$ are the $2h$ or $2p$ excitation energies. In the case of the four lowest MOs, these energy difference should be very high, thus rendering the correction very small.

not explicitly computed as they are expected to be provide the same energy variation on every spin state, thus simply shifting the energy levels without changing their relative separations.[180] Here, the value is not exactly zero as we employ different sets of orbitals for each state (canonical orbitals for the NEVPT2 calculations).

Second, we may note that for both D1 and D2 the essentials of the antiferromagnetic contribution stem from three excitations, which are akin to the DDCI $2h$, $2p$ and $2h-1p$ excitations. Interestingly, in the case of dinuclear Cu(II) complexes it has been observed that $2h$ and $2p$ contributions are antiferromagnetic but weaker than the other ones.[25] This is obviously not the case here. Another interesting thing is the opposite sign of the $2h-1p$ and $1h-2p$ contributions, which is in good agreement with previously published studies.[180]

Finally, as one can note for doublet D1 the $V_{ai}^{rj,[0]}$, $V_{ij}^{rk,[-1]}$ and $V_{aj}^{ik,[+1]}$ excitations only have a small stabilising effect. This is very interesting, since these excitations correspond to the ones that are evaluated at the DDCI-1 level, where a very weak stabilisation of the doublets was observed. On the other hand, for doublet D2 the $V_{ai}^{rj,[0]}$ ("$1h-1p$") component is more marked, with a positive value (ferromagnetic action). This was not expected, as at the DDCI-1 level the overall correction for both doublet states is very similar. Nevertheless, we need to remind that these two types of calculations are not based on the same reference wavefunction, and as such direct comparison is tricky. Furthermore, we know higher order effects are neglected in the NEVPT2 formulation, which are not in the DDCI calculations, and as such the weights of the ionic determinants in D2 are possibly underestimated. According to Malrieu,[25] this mechanically reduces the antiferromagnetic (stabilising) contributions in this state, and thus may yield a total ferromagnetic behaviour. In his 2002 publication, he offers a possibility to overcome this difficulty: "enlarging the CAS to include in this way part of the higher order effects".

We thus enlarged the active space, including the three lowest doubly occupied MOs (CAS(9,6)SCF). At the SA-CASSCF level, the energy differences remain exactly the same, which is rather logical from the composition of the CAS wavefunctions. They indeed merely develop on the determinants where these MOs are doubly occupied, as such they behave mostly as "inactive" orbitals. At the NEVTP2 level on the other hand, results are more interesting. Both doublets are indeed found at lower energies: $+2.3$ cm^{-1} for D1, $+7.6$ cm^{-1} for D2. Furthermore, we can observe in Table 4.3 that all components but $V_{ai}^{rj,[0]}$ remain rather unchanged, for both doublets. Most of the stabilisation thus stems from these $1h-1p$ like contributions, which tends to suggest that indeed the weights of the ionic determinants in D2 were underestimated, but also in D1.

We then wondered how we could further increase the active space, without making the computational effort too high. According to Malrieu, higher order effects are especially missed when the ligands are polarisable.(xxi) Incidentally, this statement hints a way to rationally enlarge the active space: as we already mentioned in Chapter 3, polarisability and reactivity are close concepts, and we know reactivity can be described at first order using the frontier MOs.[40] Here, we could thus include in the active space orbitals corresponding to the frontier MOs of $^{\mathrm{L}}\mathrm{L}_1{}^{2-}$.

Actually, in the previous CAS(9,6) calculation, the three additional (nearly inactive) orbitals involved only two of the ligands, two of these MOs corresponding to the expected π-like HOMO, and the third one being a combination of a π contribution on the enaminone part of a ligand and a $\sigma^\star$ contribution on its carboxylate group. In this configuration, the highest inactive orbital proved to be the expected third ligand-based HOMO, and thus

---

(xxi) From the DD computation on ligand $\mathrm{L}_1{}^{2-}$, we may indeed expect the latter to be quite polarisable.

Table 4.3: Detail of the NEVPT2 energy corrections for doublets states D1 and D2, with respect to the quartet state corrections (values in cm^{-1}), based on a CAS(9,6) reference wavefunction. Same notations as in Table 4.2.

Excitations	"DDCI equivalent"	Δ_1	Δ_2
$V_{ab}^{rs,[0]}$	$2h-2p$	-0.4	-0.3
$V_{ai}^{rs,[-1]}$	$1h-2p$	**1.9**	**1.3**
$V_{ab}^{is,[+1]}$	$2h-1p$	**-3.3**	**-2.7**
$V_{ab}^{ij,[+2]}$	$2h$	**-3.3**	**-3.3**
$V_{ij}^{rs,[-2]}$	$2p$	**-1.2**	**-1.2**
$V_{ai}^{rj,[0]}$	$1h-1p$	-0.6	**1.5**
$V_{ij}^{rk,[-1]}$	$1p$	-0.5	-0.4
$V_{aj}^{ik,[+1]}$	$1h$	-0.1	0.0

Table 4.4: Detail of the NEVPT2 energy corrections for doublets states D1 and D2, with respect to the quartet state corrections (values in cm^{-1}), based on a CAS(11,7) reference wavefunction for the second trinuclear complex. Same notations as in Table 4.2.

Excitations	"DDCI equivalent"	Δ_1	Δ_2
$V_{ab}^{rs,[0]}$	$2h-2p$	-0.5	-0.4
$V_{ai}^{rs,[-1]}$	$1h-2p$	**2.8**	**1.4**
$V_{ab}^{is,[+1]}$	$2h-1p$	**-4.6**	**-2.9**
$V_{ab}^{ij,[+2]}$	$2h$	**-3.6**	**-3.5**
$V_{ij}^{rs,[-2]}$	$2p$	**-1.2**	**-1.2**
$V_{ai}^{rj,[0]}$	$1h-1p$	**-2.8**	0.9
$V_{ij}^{rk,[-1]}$	$1p$	-0.7	-0.5
$V_{aj}^{ik,[+1]}$	$1h$	-0.3	0.2

was included in the active space of a supplementary SA-CAS(11,7)/NEVPT2 calculation. As a result, the lowest doublet state shows a further stabilisation, being found only $+2.0$ cm^{-1} above the ground quartet state. D2 on the other hand is found at the same energy, and overall the contributions from each excitation class remain rather constant.

Interestingly, for the other complex in the unit cell an antiferromagnetic behaviour is already retrieved at the SA-CAS(11,7)/NEVPT2 level: doublet D1 is found to be the ground state, Q1 is found 2.6 cm^{-1} above the latter and doublet D2 is found at $+9.3$ cm^{-1}. Such a difference of behaviour is remarkable because of the strong similarities these two complexes presented at the SA-CASSCF level. This is quite in line with Kahn's findings: subtle structural effects lead to marked changes in the magnetic properties. We report in Table 4.4 the different relative NEVPT2 corrections for doublets D1 and D2. As one may note, the total correction is principally piloted by the same contributions as those involved for the first trinuclear complex. We may however notice that values for D1 are markedly more negative, which results in the observed antiferromagnetic character.

Nevertheless, these results are not sufficient to reproduce the $\chi T = f(T)$ curves, as an overall slightly ferromagnetic behaviour is observed. Further extension of the active spaces to include the ligands-based LUMOs (CAS(11,10)) were attempted but proved for the moment rather unsuccessful, convergence of the CASSCF wavefunctions being very problematic in these case (close to zero occupations). Nevertheless, we seem to be on the right direction, with a global tendency towards antiferromagnetism. Further efforts will then be devoted to converge the CAS(11,10) calculation (with inclusion of the LUMOs) in the very close future. Note also that the ill reproduction of the experimental curves may also be due to orientations effects. The two trinuclear complexes in the lattice indeed display different relative orientations, and their magnetic moments may thus somehow cancel out. However, this would imply an Ising (non Heisenberg)-like behaviour of spins, which is quite unexpected: we indeed do not expect any magnetic anisotropy in this system, and as such the molecular magnetic moments should, at all times, align with the magnetic field.

4.5 Conclusion

Through this study, we have seen how computational chemistry could be used as a strong support to experiments. First, DFT calculations were successfully employed to determine unambiguously the structural formula of our ligands in solution. Then, we employed the same kind of approach as in Chapter 3 to rationalise their coordination properties.

We thus employed these ligands to synthesise coordination complexes with various transition metal cations, and in the case of Cu(II) we were able to characterise four crystal structures (two coordination polymers and two trinuclear complexes). We were also able in that case to elicit the structures in solution, through a series of spectroscopic characterisations and DFT calculations. We also tentatively rationalised the reactivity of these species, using DFT calculations at two different levels of theory. We could show that there may be a competition between the crystallisation of our complexes and their degradation by water. Indeed, a reaction mechanism for hydrolysis could be computed, and in both cases the hydrolysis products are more stable than the starting reagents, thus rendering the reaction thermodynamically favourable. Inclusion of dispersion in our theoretical model proved critical here, lowering considerably the energy barriers for the different elementary steps of reaction – and in some cases, modifying the steps themselves –. For the moment, the last transition state structure could not be optimised, but calculations are still undertaken to correct this.

Finally, we studied the magnetic properties of the crystalline compounds, and in the case of the trinuclear complexes employed high level *ab initio* calculations to gain a better understanding on these systems. They indeed display a weak antiferromagnetism, and we wondered whether magnetic frustration could be observed. In agreement with the previously published results on the glycine-based analogue, the lower levels of theory do not permit to retrieve the experimental magnetic properties: almost no variation is observed between the SA-CASSCF and DDCI-1 levels, which both yield a ferromagnetic coupling.

The DDCI-2 level of theory is merely unaffordable in our case, the system being way too large. This lead us to consider a different theoretical approach, based on perturbation theory, namely NEVPT2 calculations. They indeed formally contain all the excitations involved in the DDCI-3 formalism, but at a reduced computational cost, and could thus be employed here. At this level of theory, a much better description is obtained, especially when the active space is enlarged to include ligands polarisation effects: at the CAS(11,7)/NEVPT2 level, we indeed retrieve a very small energy gap between the first doublet and the ground quadruplet for one of our complexes, while for the second one an antiferromagnetic behaviour is even seen. Though these results do not allow, for the moment, to reproduce correctly the magnetic properties of our complexes, they are very encouraging and suggest a further enlargement of the active space might be sufficient to get a sound description of our system. These calculations are currently considered, but

marked convergence issues hamper their realisation for the moment.
In a concluding remark, these results seem to comfort the fact that NEVPT2 calculations are adapted to the modelling of weak magnetic couplings, as previously stated. This is very interesting, since in the past years NEVPT2 calculations were quite overlooked on this topic, DDCI methods being generally preferred – but being not always applicable, because of the size of the systems under study –. We thus hope our study may encourage others to use such calculations.

Chapter 5

Lanthanide-based mononuclear complexes: experimental and theoretical studies of single molecule magnets

In Chapter 3, we introduced the basics of molecular magnetism, and noticeably we presented Single Molecule Magnets. These compounds have attracted a large interest in research due to the slow relaxation of magnetisation they present at the single molecule scale, which is up to date not completely mastered. Indeed, though the different mechanisms behind magnetic relaxation are known, we still do not know how to finely control them.

In this context, we propose here to study the magnetisation dynamics of some very simple lanthanide complexes. The first section deals with a thorough study of the [$LnTp_2NO_3$] family, which present a rather exceptional dynamics. The second section, more preliminary, shows how we may rather straightforwardly extend this family of complexes through adequate modifications in the synthetic process. The first results on the "new" complexes suggest more efficient and/or more exotic SMMs are at reach.

5.1 Study of [$LnTp_2NO_3$], a family of mononuclear complexes

5.1.1 Syntheses and crystal structures

The [$LnTp_2NO_3$] complexes (Ln = Dy (**5.1**), Ho (**5.2**), Er (**5.3**), Yb (**5.4**) and Y (**5.5**)) were obtained through a very simple synthetic procedure: a simple mixture of two methanolic solutions of a rare earth nitrate $Ln(NO_3)_3 \cdot xH_2O$ (x = 5 or 6) and KTp (potassium hydrotrispyrazolylborate)[181] affords the complexes at relatively high yields (see Appendix A.2.2 for the synthetic details). Their crystal structures are presented on Figure 5.1.1.

They all crystallise in the monoclinic $P2_1/c$ space group, and their single crystals always present the same shape (elongated platelet). Crystallographic data is gathered in Table B.8 in Appendix B.4. The asymmetric unit consists of a mononuclear complex, with two N,N,N-bound tridentate Tp^- ligands and one O,O-bound bidentate nitrate ligand, coordinated to the central Ln(III) ion. The coordination polyhedron around the Ln(III) ion is highly unsymmetrical (see Table B.6 for more details). It may be described as a distorted square antiprism, with a strong distortion stemming from the biting angle between the nitrate and the Ln(III). This yields a final C_1 symmetry. Noteworthy, no π-stacking nor H-bond are seen in the packing and the lanthanide ions are quite remote from each other. For instance, the shortest Yb(III)-Yb(III) distance is 8.4864(2) Å. Complexes within the unit cell may thus likely be considered isolated.

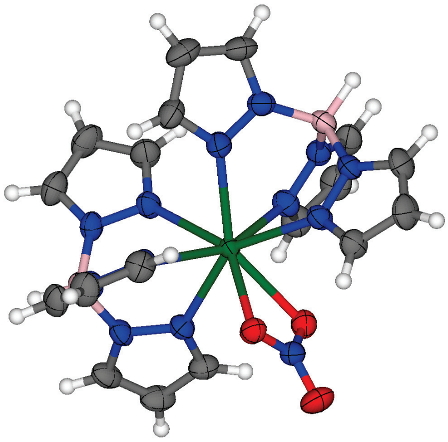

FIGURE 5.1.1: ORTEP drawing of the [$LnTp_2NO_3$] complexes 5.1 to 5.5, ellipsoids drawn at 50% probability. Example: [$YbTp_2NO_3$] **5.4**.

Quite interestingly, we did not manage to obtain the same complexes with other lanthanide ions. Attempts with any lanthanide between La and Gd proved unsuccessful, while in the case of Tb we only managed to obtain a few milligrams of [$TbTp_2NO_3$] in a single occasion, which furthermore degraded over a recrystallisation attempt. In another occasion, we managed to isolate transient [$LnTp_2NO_3(H_2O)$] species (Ln = Tb, Gd, La), which also degraded over time and recrystallisation. The crystal structures of the [$LnTp_2NO_3(H_2O)$] complexes are presented on Figure 5.1.2, and the XRD parameters are displayed in Table B.8. These complexes crystallise in the triclinic $P\bar{1}$ space group, the asymmetric unit consisting of a single complex.

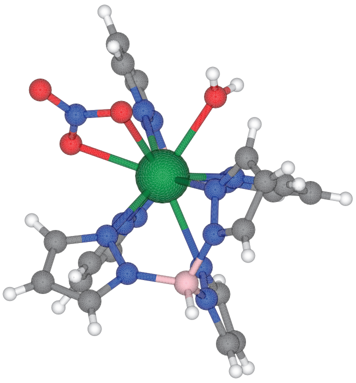

FIGURE 5.1.2: Molecular structure of the [$LnTp_2NO_3(H_2O)$] complexes (Ln=Tb, Gd, La). Example: Tb.

The [$LnTp_2NO_3(H_2O)$] molecular structure is quite reminiscent of that of the [$LnTp_2NO_3$] complexes, but with the addition of a coordinating water molecule. In Chapter 3, we claimed that lanthanide ions all presented a similar reactivity, behaving mostly as +3 point charges. Actually, it would be more accurate to state that they act almost as +3 *diffuse* charges. Indeed, it is known that the ionic radii of the Ln^{3+} ions are strongly decreasing from La^{3+} (1.16 Å in 8-coordinence) to Yb^{3+} (0.985 Å): this is the so-called lanthanide contraction.(i) [21,182] This contraction leads the early lanthanides to prefer higher coordinences, which permit to stack more ligands in the coordination sphere in order to shield their positive charge.

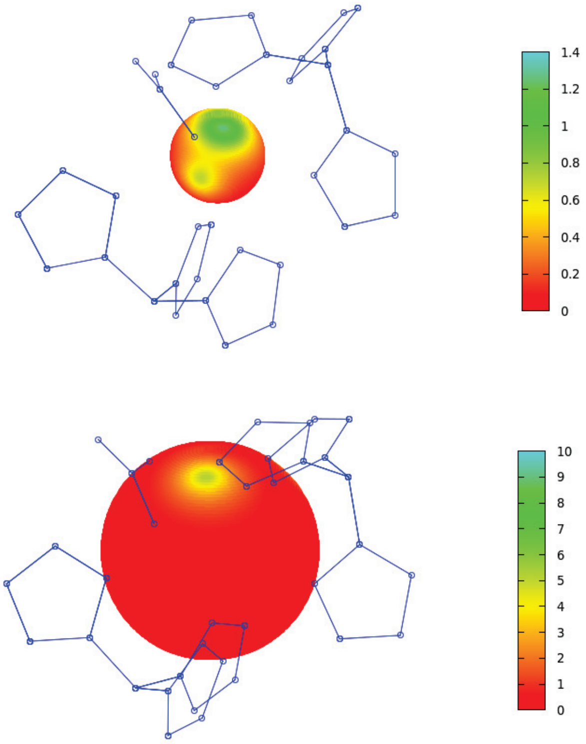

FIGURE 5.1.3: Electrostatic potential maps for [YTp_2NO_3], projected on a sphere of 1 Å (top) and 2.4 Å (bottom) of radius, as calculated at the PBE-DKH/TZVP level in ORCA. Colour scale is indicated next to each Figure (in atomic units). Images were build using Gnuplot, and for the sake of simplicity and clarity only the backbone of the ligands was represented in blue lines.

We thought this simple effect could lead the [$LnTp_2NO_3(H_2O)$] structure to be much more stable for the early lanthanide than the 8-coordinated one. We thus ran a very simple DFT calculation(ii) on [YTp_2NO_3] in order to get a better insight on this. On Figure 5.1.3, we represent the computed molecular electrostatic potential, projected onto a sphere centred around the yttrium cation, with a radius of 1.0 Å and 2.4 Å. From these two images, it is rather clear that the potential on any point of these surfaces is positive, thus electro-attractive. A maximum of potential appears between the coordination position of the nitrate and one Tp^- ligand, and a negative charge or a properly oriented dipole would be quite stabilised on this position. Interestingly, it roughly corresponds to the position the additional water molecule occupies in the [$LnTp_2NO_3(H_2O)$] complexes, but in the case of the yttrium derivative the coordination sphere is such that this position is obstructed by the Tp^- and nitrate ligands.

(i) To the expected diminution in ionic radius – ionic radii decreasing as one moves to right in the periodic table, for instance $r(Ti^{2+}) = 0.86$ Å $> r(Zn^{2+}) = 0.74$ Å – adds a relativistic effects, that over-expresses the reduction.

(ii) PBE-DKH/TZV with a geometry optimisation, using ORCA.

If now we increase the ionic radius of the lanthanide, the coordination sphere should relax in such a way that the potential hole may become accessible for a supplementary ligand, thus explaining why we rather obtain the [$LnTp_2NO_3(H_2O)$] structure for the early lanthanides.(iii)

5.1.2 Probing the lanthanide contraction

The lanthanide contraction thus seems to have a direct impact on the synthesis of our complexes, and we thought it may be interesting to try to probe it, more or less quantitatively.(iv)

Raman spectroscopy should, in principle, allow such a study. Quite surprisingly, we only found one literature reference that looked explicitly for the impact of the lanthanide contraction on the Raman spectra,[183] and this further motivated this study. In collaboration with the group of Prof. C. Reber at the University of Montréal, we measured the Raman spectra of complexes **5.1** to **5.5**, at both room temperature and 80 K, in the solid state, using a 785 nm laser excitation. The room temperature spectra in the 200 cm^{-1} - 1800 cm^{-1} region are provided on Figure 5.1.4.

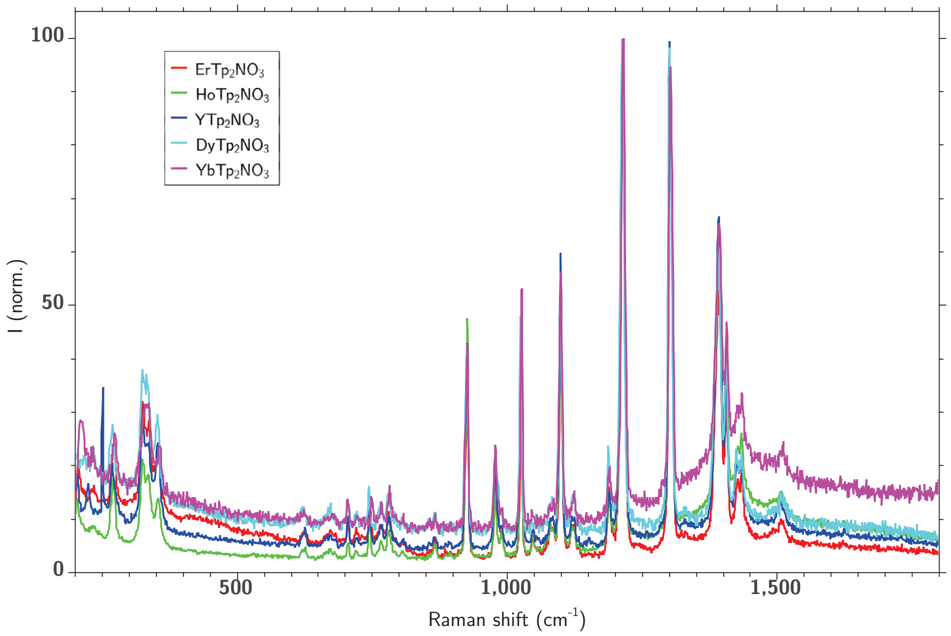

FIGURE 5.1.4: Room temperature Raman spectra for complexes **5.1** to **5.5**. Colour scheme is provided in caption. Excitation ad 785 nm, 10% of laser intensity, 4 accumulations and 10 seconds of exposition.

As one may remark, the spectra are very similar from one complex to another, which could be expected. However, if we zoom we can see that the maxima of several transitions shift depending on the lanthanide. This is the case, for instance, of the transition around 1025 cm^{-1} on Figure 5.1.5. We have thus plotted the Raman shifts of these peaks with respect to the ionic radii of the lanthanide in 8-coordinence,[182] and a quite general trend appears,

---

(iii) As for the degradation of these complexes, it is maybe due to an hydrolysis of the Tp^- ligands. The water molecule in the [$LnTp_2NO_3(H_2O)$] structure is indeed quite well located to interact with the borohydride.

(iv) At a global level, this can be achieved quite straightforwardly. Indeed, it rather obvious that there exists a linear relationship between the volume of the crystal lattice and the cube of the ionic radii of the lanthanide (see Figure B.4.2 in Appendix): the larger the radius, the larger the volume.

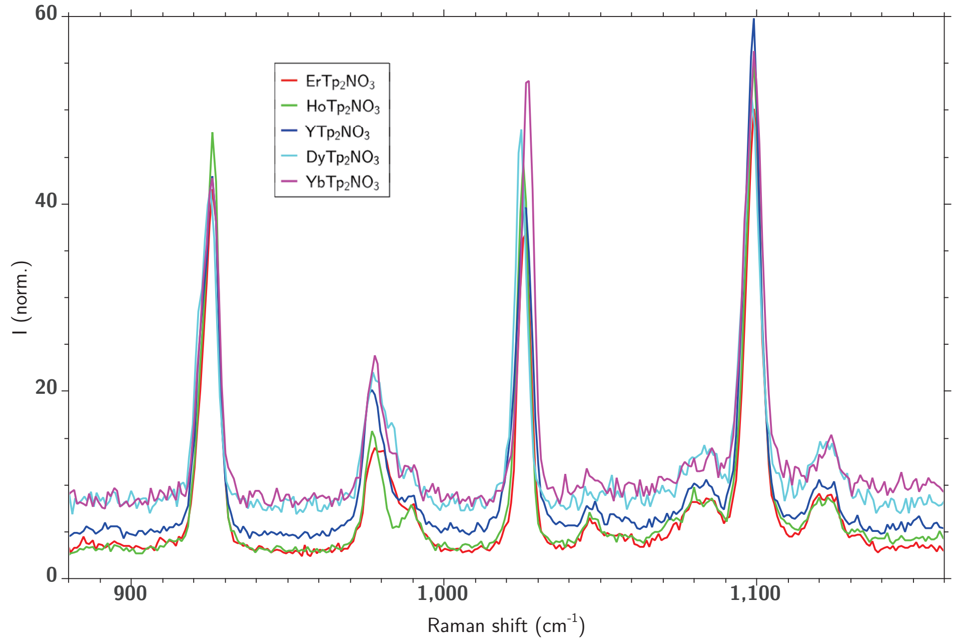

FIGURE 5.1.5: Zoom in the 880 cm^{-1} - 1160 cm^{-1} region of the room temperature Raman spectra for complexes **5.1** to **5.5**.

as exemplified on Figure 5.1.6. In all cases, an almost linear relationship is observed. It not clear whether the Raman shift should actually display a linear dependence with the ionic radius of the lanthanide, but the decreasing tendency is quite easy to understand. A larger ionic radius indeed means a smaller charge density (at constant charge), and in turn this means the electrostatic interaction with the ligands is expected to be significantly smaller the higher the radius. Raman peaks are thus expected to shift to the left when moving from Yb to Dy, which is observed.

The fact that shifts are not observed for all vibrations is also quite simple to understand: molecular vibrations involving atoms that are far away from the lanthanide (C-H vibrations of the cycles, for instance) should not be much perturbed by its replacement. In turn, large shifts will likely indicate that the vibration involves atoms in the first coordination sphere of the lanthanide. In order to confirm this idea, and also to ease the attribution of the peaks, we performed a DFT modelling of the Raman spectrum of **5.5**(v) at the B3LYP-DKH level, choosing 6-311++G(d) as a basis set for all elements[184] but Y, which was modelled using the def2-TZVP basis set (ORCA). Note that this calculation, though seemingly simple, took about 982 hours to complete on the laboratory cluster (on a 12 cores node)!

We present on Figure 5.1.7 the calculated Raman spectrum. As one may notice, a certain degree of agreement between the calculated and experimental curves is obtained, noticeably in the low frequencies region.(vi) On the other hand, larger discrepancies are seen in the intermediate region (1000 - 1500 cm^{-1}) of the spectrum, the computed peaks being shifted by up to 80 cm^{-1} with respect to the experimental ones. Actually, we could expect such an energy mismatch(vii) here, as the experimental Raman spectra were recorded on powder samples, whereas the calculations are performed on an isolated molecule in a

---

(v) Being a lighter element, and displaying a closed shell, [YTp$_2$NO$_3$] seemed a much simpler system to study than any other complex in the family.

(vi) Here, we will not discuss the relative intensities of the peaks, since it is strongly dependent on both the chosen FWHM and the apparatus sensitivity.

(vii) Even on simple systems, more or less marked mismatches are observed.[184–186]

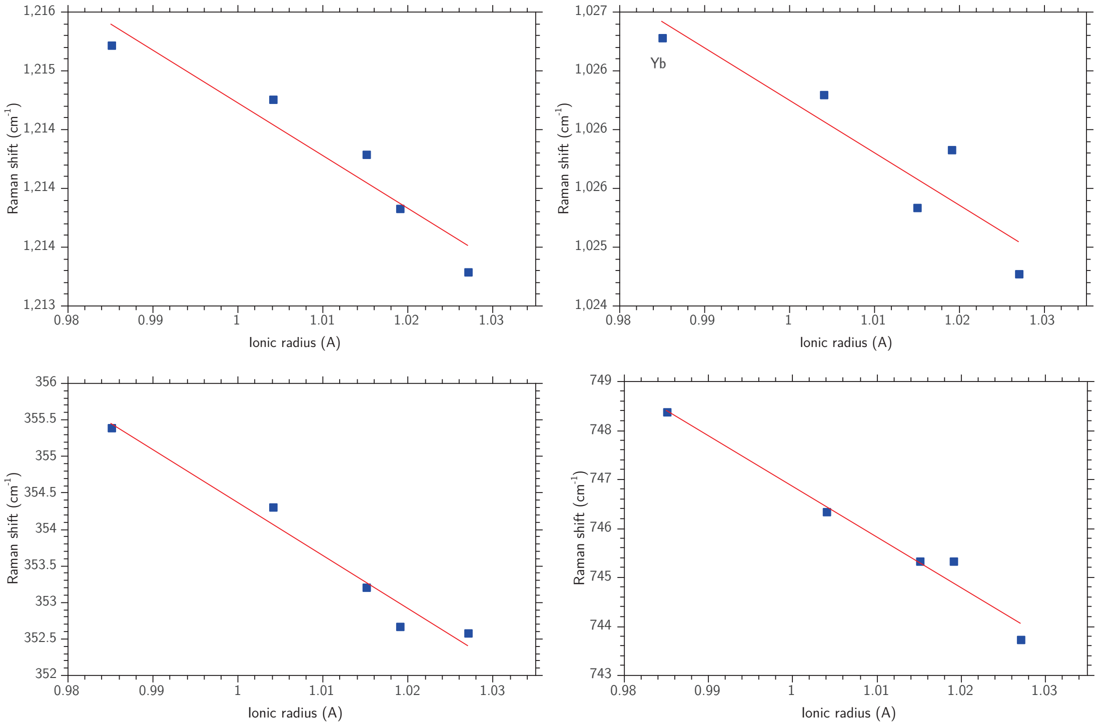

FIGURE 5.1.6: Plot of the Raman shifts with respect to the ionic radii of the corresponding lanthanide for 4 transitions, at room temperature. The solid red line is simply a guide for the eye..

vacuum. We thus miss all the crystal state effects: collective vibrations, electrostatic and dispersion embedding...

Nevertheless, despite the energy shift we may expect the "isolated molecule in a vacuum" description to provide relevant information on the vibrations of **5.5** in the solid state, thus helping us to assign the different vibration peaks. Let us focus on the four peaks of Figure 5.1.6. To the first vibration mode, observed at 353 cm^{-1}, corresponds a series of intermediate to weak computed vibrations, between 271 cm^{-1} and 339 cm^{-1}. These different peaks all correspond to out-of-plane vibrations of the pyrazole groups of the Tp^{-} ligands, as exemplified on Figure 5.1.8.

To the second vibration mode, centred around 745 cm^{-1}, correspond three principal vibrations, computed at 770 cm^{-1}, 778 cm^{-1} and 783 cm^{-1}. The first one corresponds to a scissoring movement of the nitrate ligand, in good agreement with published data.[187] The second and third ones, on the other hand, are mainly associated to a rocking movement of the hydride.

The third vibration mode, around 1025 cm^{-1}, may be associated to a series of vibrations at 1071 cm^{-1}, 1082 cm^{-1}, 1086 cm^{-1}, 1087 cm^{-1} and 1092 cm^{-1}, respectively. The four first modes correspond to streching vibrations of the pyrazole rings, characterised by a strong modulation of the coordination bonds Y - N. The last mode, on the other hand, is associated to a symmetric streching of the nitrate ligand, also in good agreement with previously published data.[188,189]

Finally, to the 1214 cm^{-1} experimental peak corresponds four vibrations at *ca.* 1216 cm^{-1}, 1220 cm^{-1}, 1232 cm^{-1} and 1248 cm^{-1}. The two first modes are associated to a wagging movement of two pyrazole of each Tp^{-} ligand, while the two last modes are associated to the associated twisting vibration.

In summary, the four shifting vibration modes of Figure 5.1.6 seem in any case to involve

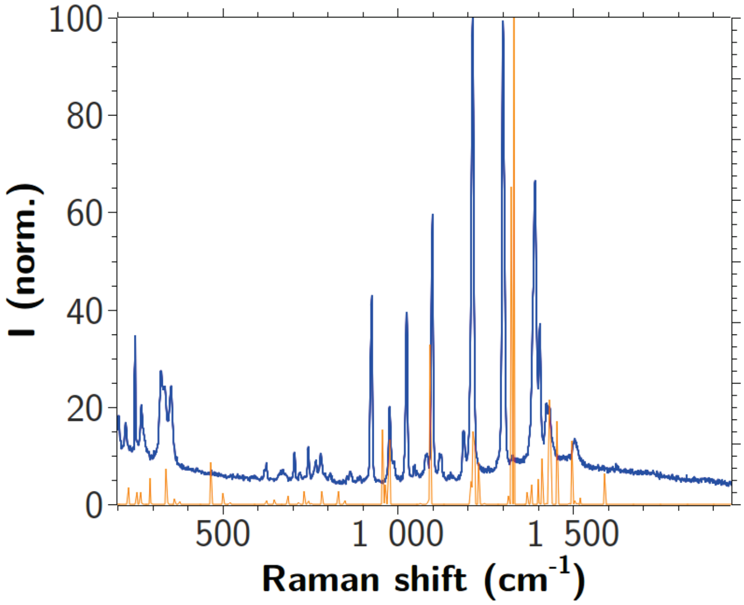

FIGURE 5.1.7: Experimental (blue) and calculated (orange) Raman shifts for **5.5**, at the B3LYP/6-311++G(d)/def2-TZVP level. For the sake of clarity, the full width at half maximum was set to 1.0 cm^{-1} for the calculated curve.

coordination atoms. This correlates very well with our expectations, and gives support to our discussion: there indeed is a non negligible impact of the lanthanide contraction on the Raman spectra of the [LnTp$_2$NO$_3$] complexes.

5.1.3 Luminescence of the [LnTp$_2$NO$_3$] complexes.

At first, we synthesised complexes **5.1** to **5.5** for their magnetic properties. However, they also display interesting visible and near-IR luminescence, which can furthermore help to understand the magnetic properties we observed.[190–198]

It is indeed known that lanthanide ions may display a metal-centred luminescence.[199] Thanks to the efficient shielding of the 4f AOs, non-radiative de-excitations are indeed severely reduced and internal 4f → 4f transitions can be observed. In collaboration with Dr. Olivier Maury and Dr. François Riobé (ENS Lyon), we thus studied the luminescence properties of complexes **5.1** to **5.4** – note that we did not consider the yttrium derivative here, since it is not a lanthanide element and as such may not present any 4f → 4f transition –.

Under a 300 nm excitation(viii), only the Dy and Yb derivatives **5.1** and **5.4** did display luminescence. We represent on Figure 5.1.9 and 5.1.10 the room temperature and 77 K luminescence spectra for these two complexes.

The room temperature spectrum of **5.1** displays two principal series of transitions, at *circa* 475 nm and 575 nm. They correspond to the expected $^4F_{9/2} \rightarrow {}^6H_{15/2}$ and $^4F_{9/2} \rightarrow {}^6H_{13/2}$ transitions of the Dy^{3+} ion, respectively.[199] A better resolution is observed at 77 K, yet it is not possible to fully resolve the different transitions. The $^6H_{15/2}$ and $^6H_{13/2}$ states are indeed expected to be splitted in, at most, 8 and 7 Kramers doublets (KD) by the ligand field. One could thus expect to distinguish up to 8 and 7 peaks, respectively, for the two

---

(viii) This corresponds roughly to the wavelength domain where ligands are absorbing. Direct excitation of the lanthanide is indeed expected to be quite inefficient, and it is assumed that generally luminescence occurs *via* an energy transfer from the ligands to the lanthanide – the so-called antenna effect–.

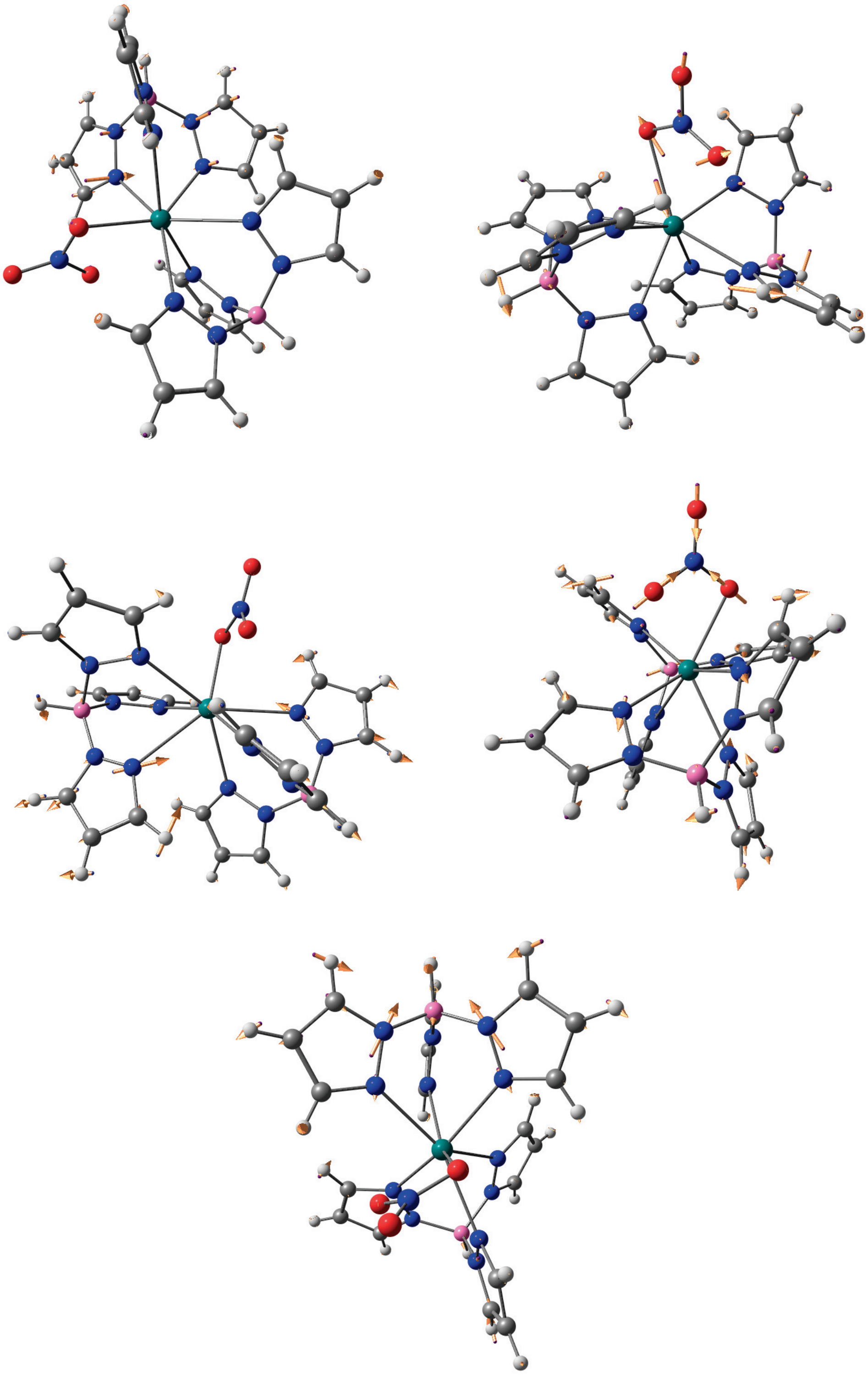

FIGURE 5.1.8: Molecular representation of the computed vibration modes of **5.5**, at 339 cm^{-1} (top left), 770 cm^{-1} (top right), 1071 cm^{-1} (center left), 1092 cm^{-1} (center right) and 1216 cm^{-1} (bottom).

transitions. Here, we may only observe 3 peaks and 5 shoulders in the first massive, and 6 peaks in the second one. In the first case, one may try to isolate the 8 peaks through a deconvolution of the spectrum into Gaussian functions. Unfortunately, this procedure is not working here. This could be due to the fact that the emitting $^4F_{9/2}$ state is also expected to be splitted into several (here 5) KD, and it is not clear whether luminescence

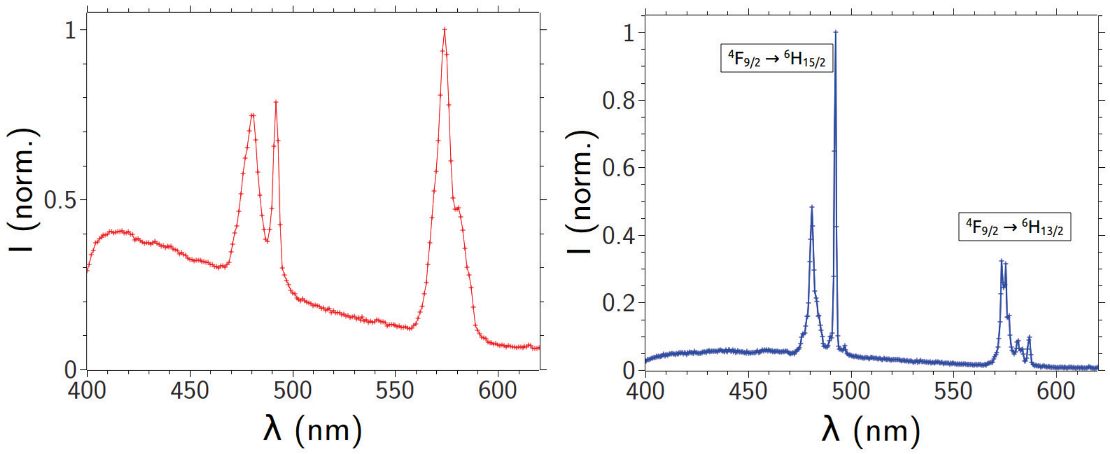

FIGURE 5.1.9: Luminescence spectra of **5.1** under a 300 nm excitation, at room temperature (red) and 77K (blue), in the solid state.

should originate only from the lowest energy KD. It is indeed known that Kasha's rule[200] may not be strictly observed in the case of lanthanide luminescence, and thus assigning the peaks and shoulders in the luminescence spectrum is a fairly complicated task.[192,193,196]

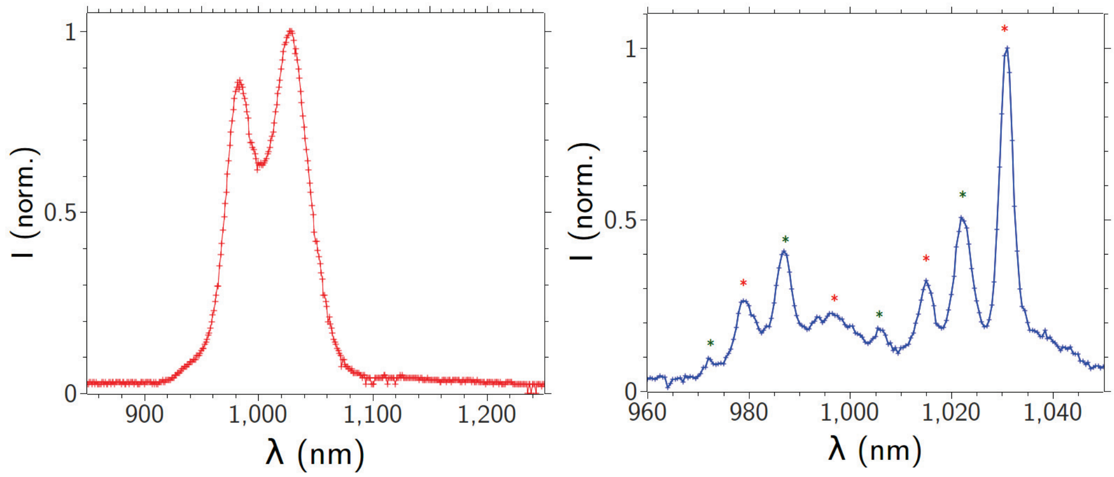

FIGURE 5.1.10: Luminescence spectra of **5.4** under a 300 nm excitation, at room temperature (red) and 77K (blue), in the solid state. Coloured asteriks in the 77 K spectrum correspond to the assignation of the peaks as two different transitions.

Such a breaking in Kasha's rule may actually be acting in the case of **5.4**. The two room temperature peaks, observed at 985 cm^{-1} and 1030 cm^{-1} respectively, indeed resolve into 7 well-defined peaks and a large one – the corresponding wavelengths and wavenumbers are given in Table 5.1 –. However, we would only expect to observe 4 peaks, since they correspond to the $^2F_{5/2} \rightarrow {}^2F_{7/2}$ transition, and the ground $^2F_{7/2}$ state should not resolve into more than 4 KD. The fact that the luminescence spectrum does not change when **5.4** is in solution in CH_2Cl_2 ensures the doubling does not originate from the existence of two different emitters in the solid state(ix). The uniqueness of the emitting species is

---

(ix) This hypothesis was proposed since in the $P2_1/c$ space group two non equivalent positions are found in the lattice. As such, even if the molecular structure for these two positions are exactly the same, they also confirmed by the luminescence decay measurements, which fit nicely with a unique monoexponential function $\tau = y_0 + A_0 \exp\left(-t/\tau_{\mathrm{Yb}}\right)$ with $\tau_{\mathrm{Yb}} = 10(1)$ μs.

Altogether, these facts suggest that we actually observe a luminescent deexcitation from two KD of the excited $^2F_{5/2}$ state towards the 4 KD of the ground $^2F_{7/2}$ state. This hypothesis is supported by the fact that successive transitions are separated by the same energy splitting, of *ca.* 85(12) cm^{-1}. The observed spectrum thus very likely consists of two series of 4 transitions that are simply shifted by 85 cm^{-1}. The consistency of the obtained energy diagrams for the ground state, considering either one series or the other, seems to confirm this idea. *Ab initio* calculations at the SA-CASPT2[x] level also provide a rather good agreement with this hypothesis, yielding a similar energy diagram and an energy splitting in the $^2F_{5/2}$ state of 71 cm^{-1}.

TABLE 5.1: Wavelength and associated transition energies corresponding to the luminescence peaks of **5.4**.

λ (nm)	$\bar{\nu}$ (cm^{-1})
972.0(5)	10288(5)
979.0(5)	10215(5)
987.0(5)	10132(5)
996(2)	10040(20)
1006.0(5)	9940(5)
1015.0(5)	9852(5)
1022.0(5)	9785(5)
1031.0(5)	9699(5)

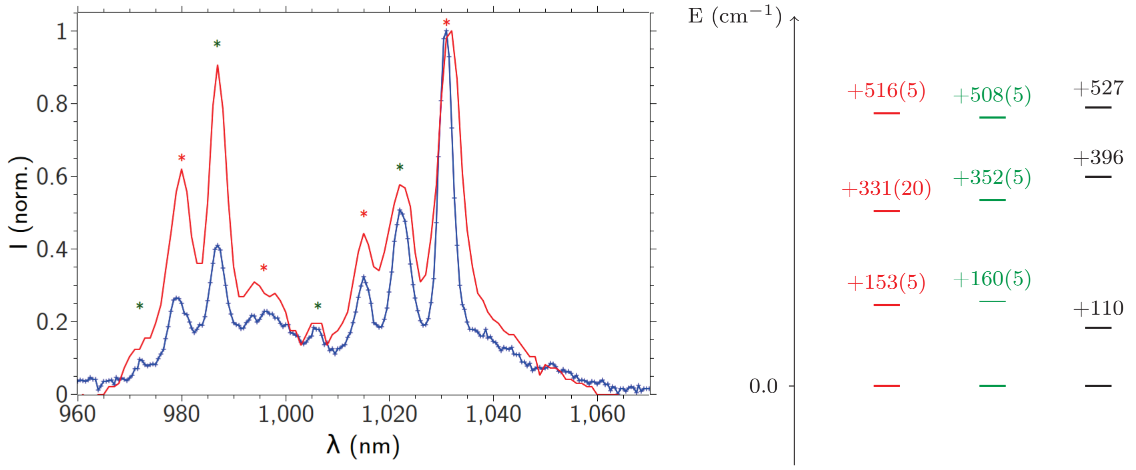

FIGURE 5.1.11: Left: luminescence spectra of **5.4** under a 300 nm excitation, at 77K in the solid state (blue) and in a frozen CH_2Cl_2 solution (red). Right: deduced energy diagrams considering the first (red) or second (green) series of peaks, and calculated (black) at the SA-CASPT2 level.

Actually, we can devise an experiment that would confirm or infirm our hypothesis. The relative luminescence intensities between the two series of transitions should indeed obey a Maxwell-Boltzmann distribution,

$$\frac{I_2}{I_1} = \exp\left(-\frac{\Delta E_{5/2}}{k_B T}\right) \tag{5.1}$$

---

are bathed in potentially different Madelung fields and as such may present slightly different physical properties.

[x] See below for the computational details.

with I_i the intensity of a given transition from the ith KD of state ${}^2F_{5/2}$, and $\Delta E_{5/2}$ the energy difference between the two emitting KD of this state. This could be checked in a survey of the temperature dependence of the luminescence. Unfortunately, the equipment at the moment does not afford such a study – the 77 K spectra were indeed recorded on a powder sample immersed in liquid nitrogen –. It is nevertheless planned in future, a cryostat being installed on the spectrometer at the ENS Lyon.(xi)

Anyhow, as can be seen from the energy diagrams in Figure 5.1.11, large energy gaps are expected between the different KD of the ${}^2F_{7/2}$ state. They may constitute energy barriers for the reversal of magnetisation, thus turning **5.4** into a potential candidate for a SMM behaviour.

5.1.4 Static magnetic properties

We thus studied the magnetic properties of complexes **5.1** to **5.4**; once again, **5.5** was not considered since it is expected to be diamagnetic (closed shell).

Powder measurements

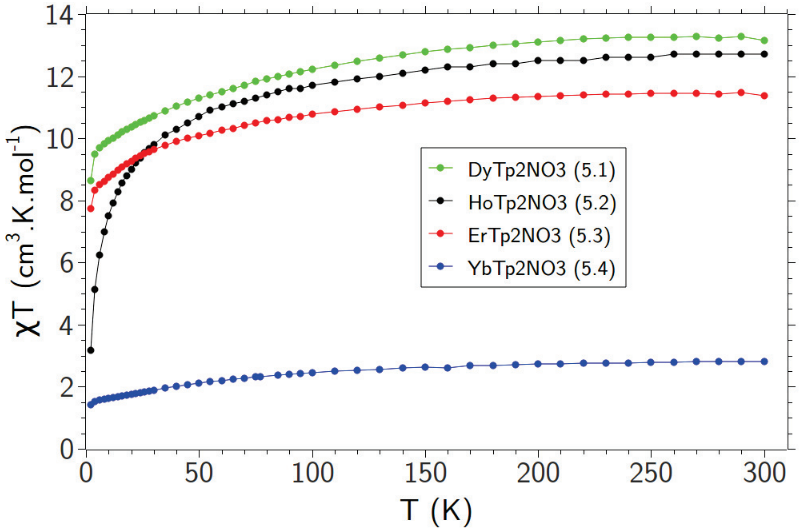

FIGURE 5.1.12: $\chi_m T = f(T)$ curves for complexes **5.1** to **5.4**, measured on powder samples under a 1000 Oe static field.

The temperature dependence of the $\chi_m T$ product for these complexes is displayed on Figure 5.1.12. In every cases, the $\chi_m T$ product decreases with temperature, and rather slowly at high temperatures. The lanthanide-lanthanide distances in the crystal lattice being quite large – above 8 Å –, we may presume this thermal evolution is primarily controlled by the progressive depopulation of the CF levels. We indeed remind that magnetic coupling in lanthanide complexes is almost always dipolar (weak to negligible orbital overlap), and that such a magnetic coupling decays strongly with distance.

Yet, it may be actually acting in the case of the Ho(III) derivative **5.2**, since the 2 K value of $\chi_m T$ is much smaller (of about 75%) than the room temperature one, and the thermal variations are more pronounced for this complex. Nevertheless, this could also

---

(xi) This new installation actually raised many questions, noticeably whether it is possible to actually control the temperature of the illuminated sample. First measurements tend to show that, when turning the irradiation on, samples may heat by as much as 25 K!

be due to the presence of a non magnetic state lying close in energy to the ground one – if it is not even the ground state –. We believe this last hypothesis to be more probable. Indeed, complexes **5.1** and **5.2** have comparable room temperature $\chi_m T$ values and as such should present similar single-ion magnetisation. They should then display similar dipolar magnetic couplings, whereas they are not expected to present similar CF patterns – Ho(III) being a non Kramers ion, while Dy(III), Er(III) and Yb(III) are –.
The room temperature $\chi_m T$ values for all these complexes depart slightly to the ones we would expect in the free ion model.[64] The discrepancies are very likely related to the inadequacy of this free ion model. For instance, as we have seen from the luminescence measurement, the 4 KD of the ground $^2F_{7/2}$ state of **5.4** are split by more than 500 cm^{-1}. As such, we cannot state that the thermal energy at room temperature (207 cm^{-1} at 298 K) is much larger than the CF splitting for this complex, which would be a necessary condition to the application of the free ion model.

TABLE 5.2: $\chi_m T$ values for complexes **5.1** to **5.4**, at 2 K and 300 K, in cm^3.K.mol^{-1}.

Complex	$\chi_m T$ at 2 K	$\chi_m T$ at 300 K	Free ion value
5.1	8.63	13.16	14.17
5.2	3.17	12.7	14.07
5.3	7.74	11.38	11.48
5.4	1.41	2.82	2.57

Field dependence of magnetisation at 2 K is presented on Figure 5.1.13. Here also, a strong similarity is observed between the Dy(III), Er(III) and Yb(III) derivatives. They all display a monotonous increase and a saturation at high fields – above 2 T – to markedly low values: 4.77 μ_B for **5.1**, 4.78 μ_B for **5.3** and 2.06 μ_B for **5.4**.(xii) Such low saturation values are usually observed when the complexes display a marked anisotropy[201]. This suggests complexes **5.1**, **5.3** and **5.4** could behave as SMMs, and as we will see in the following paragraphs they indeed do.

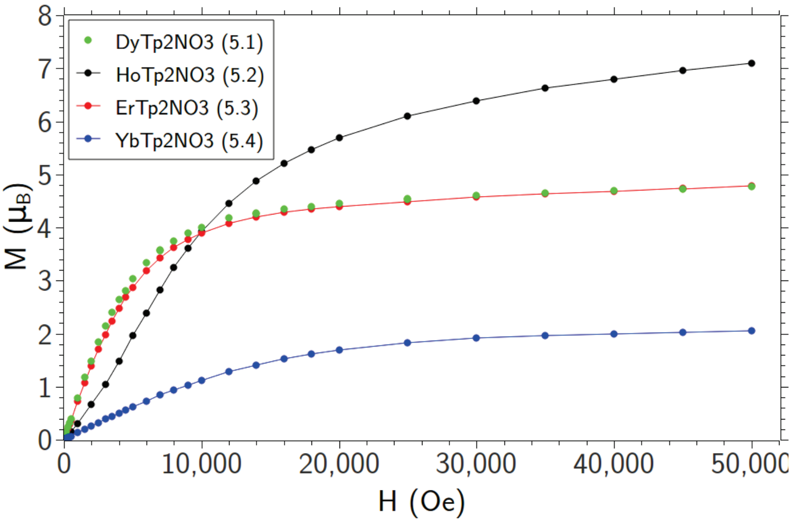

FIGURE 5.1.13: Magnetisation versus field curves for complexes **5.1** to **5.4**, measured on powder samples at 2 K.

(xii) In the free ion model, we would indeed expect saturation values of 10 μ_B for **5.1** and**5.2**, 9 μ_B for **5.3** and 4 μ_B for **5.4**.[64]

In contrast, the Ho(III) derivative does present not a marked saturation, even at 5 T. In the low field region, a remarkable feature is observed: the increase of magnetisation is not monotonous, an inflexion point being found around 0.4 T. Such a sigmoidal aspect of the curve is often observed when the studied compound presents two states that are very close in energy, such that the Zeeman splitting can invert their order in the energy diagram. Altogether, the static magnetic data on **5.2** tend to suggest that a low, non magnetic state should be found in its energy diagram. Magnetic relaxation at low temperature is thus expected to be quite fast for this complex, which should not display any SMM behaviour. This is actually what is observed, as we will show in the following paragraphs.

Single crystal measurements

Magnetic measurements on powder samples for complexes **5.1**, **5.3** and **5.4** suggest they may display rather large anisotropies. As we have seen in Chapter, because of the monoclinic structure of these compounds, only Polarised Neutron Diffraction may allow to characterise their magnetic anisotropy at the molecular level.

We thus decided to study the [LnTp$_2$NO$_3$] complexes using Polarised Neutron Diffraction experiments. Nevertheless, we saw in Chapter 2 that the magnetic susceptibility tensor approach is only applicable when magnetisation evolves linearly with field. The field dependence of the single crystal magnetisation thus needs to be known prior to any PND experiment, because we will need to apply the highest possible field in order to measure the least ambiguous flipping ratios, yet with a linearity constraint.[87,88]

Angular resolved magnetometry. As such, we first performed angular resolved magnetometry measurements on complex **5.4**, in collaboration with Dr. Jean-François Jacquot (CEA Grenoble). The shape of the studied single crystal is given on Figure 5.1.14, orientations being deduced from an X-Ray diffraction experiment.

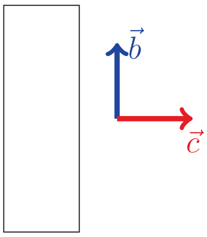

FIGURE 5.1.14: Shape of the studied single crystal of **5.4**, with the crystallographic axes highlighted.

Since both $\vec{b}$ and $\vec{c}$ axes can be easily related to a geometric feature of the crystal ($\vec{b}$ is found along the longest direction, $\vec{c}$ is parallel to the second longest direction), we decided to set them as rotation axes. We thus glued the sample by first setting the rotation axis along the $\vec{c}$ direction and with $\vec{b}$ vertical, and then by setting $\vec{b}$ as the rotation axis and $\vec{c}$ vertical. We report on Figure 5.1.15 the measured magnetisation at 2 K for these two experiments.

It is rather plain to see that a marked anisotropy is found in both cases. In the first experiment, a minimum is found at 20° (value of 0.40 μ_B at 2.0 T), and accordingly a maximum is found 90° further (value of 2.39 μ_B at 2.0 T). This suggests a crystal hard axis of magnetisation is found near $\vec{b}$, while a crystal easy axis if found in the vicinity of the reciprocal $\vec{a^\star}$ axis.

This is confirmed by the second experiment, where a maximum value (of 2.22 μ_B at 2.0 T) is observed at a 80° angle, thus near the $\vec{a^\star}$ axis, while a minimum (of 0.68 μ_B at

2.0 T) is seen near the $\vec{c}$ axis (at 170°). The discrepancies between the maximal values of magnetisation in both experiments furthermore suggest that the crystal easy axis is not located precisely along the $\vec{a^\star}$ axis, but that it rather has components along each lattice vector. Note also that a part of the difference may stem from the incertainty on the starting position of the crystal, since it might have slightly moved when the glue was drying. We can actually try to evaluate that shift: at a 90° angle, for the same field magnitude we would expect to measure the same magnetisation in both experiments, since it corresponds to a situation where the field is parallel to $\vec{a^\star}$. At 2.0 T, we indeed get 2.27 μ_B for the first experiment, and 2.20 μ_B for the second one, thus suggesting the considered field orientations are quite precise.

NOTE : the curves for the second experiment seem to present a slight asymmetry, which is unexpected. This is due to a weariness of the rotating sample holder, that impacted the first angles on each measurements (and which ended in a breakdown of the apparatus at the end of the collection). As such, we have a limited confidence in the first portion ($\theta < 20°$) of the curves for the second measurement, because of the uncertainty on the actual angle value. Nevertheless, the remaining data points can be trusted. Additional measurements are planned in the close future.

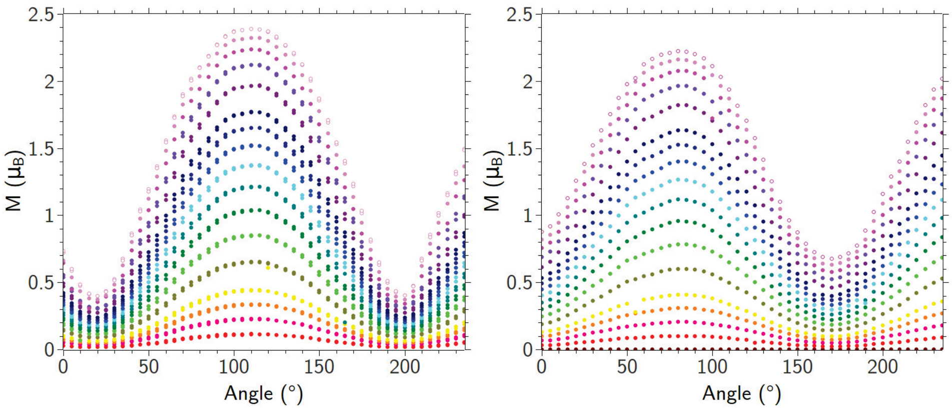

FIGURE 5.1.15: Magnetisation at 2 K for [YbTp$_2$NO$_3$] **5.4**, for static fields between 0.0 T (brown) and 2.0 T (light magenta). Left panel: rotation along the crystal $\vec{c}$ axis, $\vec{b}$ initially set vertical. Right panel: rotation along the $\vec{b}$ axis, $\vec{c}$ initally set vertical.

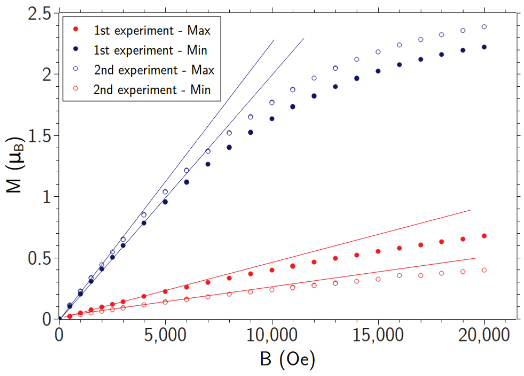

FIGURE 5.1.16: Field dependence of the magnetisation of **5.4** at 2 K along the easy and hard axes projections determined in the first (●) and second (○) angular-resolved magnetometry measurement. Solid lines are a guide for the eye.

Polarised Neutron Diffraction. Anyhow, a marked crystal magnetic anisotropy is observed, which suggest a strong molecular magnetic anisotropy could also be found. We thus studied complex **5.4** by the means of PND on the 5c1 and 6T2 lines at the Laboratoire Léon Brillouin (Saclay), in collaboration with Dr Béatrice Gillon. As we already said in Chapter 2, these experiments are performed by rotating the single crystal along a particular axis where the magnetic field is applied. Three collections, for three non coplanar directions of the field are required in order to reconstruct the magnetic susceptibility tensors.[87,88]

Here, because of the particular shape of the crystals three field directions seemed to impose: along $\vec{a^\star}$, $\vec{b}$ and $\vec{c}$[(xiii)]. We thus set a single crystal of **5.4** with these orientations, in an aluminium sample holder filled with quartz wool (which does not interact with the neutron beam, and permits to prevent any reorientation of the sample in the magnetic field), and collected the diffracted intensities at 2 K, for alternating up and down polarisation of the neutron beam.

The magnitudes of the applied magnetic fields were deduced from the single crystal SQUID measurements (see Figure 5.1.16). They are recapped in Table 5.3, along with their real orientation in the lattice. Here, we must mention the rather exceptional character of these measurements. The sample we studied was indeed rather large from the viewpoint of standard crystallography – about 1.5 mm^3 –, but rather small in the frame of PND, which calls for samples larger than 3 mm^3. Because of this, data treatment proved challenging, since many diffraction peaks were hidden by the powder diffraction of aluminium (from the sample holder).

We furthermore had to perform the collections several times, in order to obtain a better statistics on the diffraction peaks. When the field was applied along the hard axes, the flipping ratios were actually so small that we had to switch to the thermal line 6T2 – with a much higher neutron flux – in order to extract significant signal from our experiments. Overall, 139 inequivalent Bragg peaks with $|1-\mathcal{R}| > 2\sigma$ could be extracted and used for the refinement of the magnetic susceptibility tensor. Note that we employed the room temperature X-Ray structure to perform the data treatment. In principle, we should have solved the structure at 2 K prior to the PND experiment, but major delays at the LLB hampered this experiment – which was planned – to happen. However, indexation of the diffraction peaks with the room temperature lattice cell parameters proved successful, which suggest no phase transition occurs in the 300 K - 2 K temperature range and that the cell parameters, overall, do not evolve much with temperature.

TABLE 5.3: Field magnitude, orientations and number of relevant reflections used in the PND experiments. Orientations are given in the so-called CCSL reference frame ($\vec{a^\star}/a^\star, \vec{b}/b, \vec{c}/c$).

λ (Å)	Field (T)	Orientation	Type of axis	No. of equiv. reflns.
0.84	0.67	(-0.973 ; -0.009 ; 0.232)	easy	29
1.40	1.70	(-0.051 ; -0.992 ; -0.116)	hard	67
1.40	1.50	(0.095 ; 0.074 ; 0.993)	mean	43

We then refined the magnetic susceptibility tensor of the Yb atoms stepwise, in the CCSL reference frame ($\vec{i} = \vec{a^\star}/a^\star, \vec{j} = \vec{b}/b, \vec{k} = \vec{c}/c$).[202] First, we evaluated the diagonal term χ_{ll} corresponding to each collection; for example, in the first experiment we set the field roughly along the $\vec{a^\star}$ axis, and as such this collection should permits us to access χ_{ii}.

[(xiii)] They are indeed all associated to a specific feature of the crystal, respectively being perpendicular to the largest face, parallel to the longest axis and parallel to the second longest axis.

TABLE 5.4: Eigenvalues (in μ_B/T) and components of the corresponding eigenvectors of the local susceptibility tensor in the orthonormal $(\vec{i}, \vec{j}, \vec{k})$ basis.

Eigenvalues (μ_B/T)	$\vec{i}$ component	$\vec{j}$ component	$\vec{k}$ component
2.454(1)	0.895	-0.414	-0.166
0.2992(2)	-0.133	0.107	-0.985
0.007(2)	0.425	0.904	0.040

Then, we treated doublets of collections in order to refine the corresponding off-diagonal terms – for instance, the first and second experiments in order to refine χ_{ij} –. Finally, all the collections were merged and the total tensor was refined, which yields in the CCSL frame:

$$\bar{\bar{\chi}} = \begin{pmatrix} 1.97(10) & -0.91(5) & -0.33(6) \\ & 0.43(1) & 0.14(3) \\ & & 0.36(2) \end{pmatrix}. \tag{5.2}$$

This tensor can be easily diagonalised, yielding the magnetic axes directions and the corresponding eigenvalues, as listed in Table 5.4. It is rather plain to see that we indeed observe a strong single-ion anisotropy on the Yb(III) ion. It is principally uniaxial, although a non negligible (12%) transverse component is observed. From the components in the CCSL frame, we can see that indeed the easy axis is located near the reciprocal $\vec{a^\star}$ axis, while the hard axes are closer to the $\vec{b}$ and $\vec{c}$ axes.

As one may notice, the eigenvalues in Table 5.4 are given with error bars. Contrarily to the diagonalisation procedure, evaluating the uncertainty on the eigenvalues of a 3 × 3 symmetric and real matrix is a quite tedious task. Since no general procedure was found$^{(\text{xiv})}$, we developed a small Fortran program – expectedly called *Uncertainties* – to compute the error bars. The source code can be found in Appendix. Very simply, this program discretises the problem: for each component $\chi_{ab} \pm \Delta\chi_{ab}$ of the non-diagonalised tensor, we build a (user-defined) number of values comprised betwen $\chi_{ab} - \Delta\chi_{ab}$ and $\chi_{ab} + \Delta\chi_{ab}$, and for each of these values we diagonalise the matrix. This is done for each of the 6 tensor components, independently but keeping the symmetry condition $\chi_{ab} = \chi_{ba}$. The program thus computes the eigenvalues for all of the possible matrices, and isolates their extrema. It also computes the variance, which we used as an error bar$^{(\text{xv})}$.

We can also try to represent this tensor in the form of an ellipsoid (as what is generally done for the thermal displacements of atoms in XRD). This is achieved on Figure 5.1.17. The anisotropy is rather plain from this figure. As one may notice, the easy axis follows a direction that is roughly perpendicular to the Yb-NO_3 direction. The overall tensor seems to be "sandwiched" between the two Tp^- ligands, but no further correlation with structure al features can be found. Susceptibility tensor could also be calculated at the CASPT2/RASSI-SO level,[47,48] and is represented on the same figure. As one may notice, differences are observed between the two models, but the general tendency remains similar. Noticeably, the easy axes point in quite similar directions. The discrepancies on the hard axes may be due to the actual computational conditions: the calculations are performed on an isolated complex in a vacuum, while the measurements are performed on molecules within a crystal.

(xiv) And the mathematicians we contacted ensured us there were none. They suggested to discretise the problem, and also stressed that error bars on the orientations (eigenvectors) would probably be out of reach, since small variations in the eigenvalues can lead to marked changes in orientation.

(xv) Extremal eigenvalues are indeed found quite different from the average ones, but they appear to have a negligible weight.

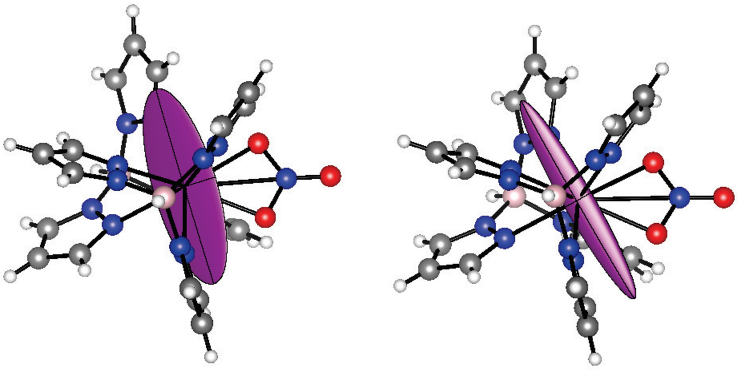

FIGURE 5.1.17: Ellipsoid representation of the PND (left) and *ab initio* (right) susceptibility tensor.

Comparing PND and single-crystal SQUID measurements. As we have just seen, the susceptibility tensor we deduced from PND experiments agrees qualitatively well with the computed one, and also with the single crystal SQUID measurements. Actually, we can even push the comparison further. We should indeed be able to evaluate the magnetisation for any orientation of a magnetic field, starting from the PND or *ab initio* susceptibility tensor. This means we can try to reproduce the single crystal SQUID curves of Figure 5.1.15, through the evaluation of

$$m = \frac{\vec{H}(\theta) \cdot \bar{\bar{\chi}} \cdot \vec{H}(\theta)}{|\vec{H}(\theta)|} \tag{5.3}$$

with θ the rotation axis$^{(\mathrm{xvi})}$.

In the first experiment, we measured magnetisation while rotating the crystal around the $\vec{c}$ axis, with $\vec{b}$ initially vertical. This means the magnetic field in this experiment can be written, in the CCSL frame,

$$\vec{H}_{exp1} = \begin{pmatrix} H \ \sin\theta \\ H \ \cos\theta \\ 0 \end{pmatrix} \tag{5.4}$$

with θ the rotation angle. Similarly, in the second experiment the field writes

$$\vec{H}_{exp1} = \begin{pmatrix} H \ \sin\theta \\ 0 \\ H \ \cos\theta \end{pmatrix}. \tag{5.5}$$

We thus developed another program, called *Conversion*, to compute the magnetisation for a list of user-defined orientations of the magnetic field, basing either on a PND or *ab initio* susceptibility tensor. The source code can be found in Appendix. In the current implementation, field orientations can be given either in the CCSL or crystal frame. In the case of a PND susceptibility tensor, the tensor must be expressed in the CCSL frame – which is the default in the refinement procedure we used –. In the case of *ab initio* data, the tensor is given in the calculation frame, and the change of basis is performed using the positions of three non-coplanar atoms in the lattice and calculation frame. The different equivalent positions in the lattice must also be given, in a matrix form, in order to evaluate the average magnetisation over one unit cell.

(xvi) The first scalar product yields the magnetisation vector, and the second yields the projection of magnetisation along the field direction, which is what we actually measure in such SQUID experiment.

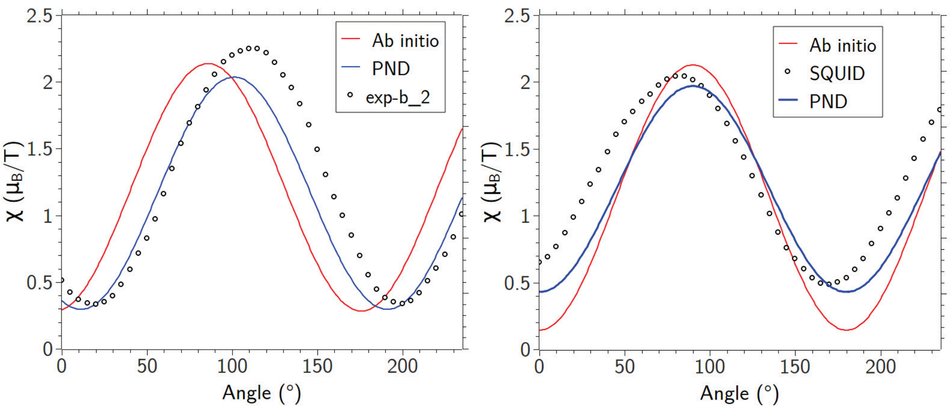

FIGURE 5.1.18: Comparison between the experimental (∘) and calculated (–, *ab initio*; –, PND) magnetisation versus angle curves, for a rotation around the $\vec{c}$ axis with $\vec{b}$ initially vertical (left) and a rotation around $\vec{b}$, with $\vec{c}$ initially vertical (right).

We represent on Figure 5.1.18 the outcome of this program. As one can see, the qualitative agreement is retrieved, though deviations are observed. In the first experiment, the maximum in the experimental curve is observed at 115°, while PND and *ab initio* deduced curve present a maximum at 101° and 86°, respectively. In the case of the second experiment, the maximum is found at 80° from the experimental curves, and at 90° in both PND and *ab initio* deduced curves.

Several factors may be involved in these deviations. First of all, as we already noticed, there is a slight mismatch between the expected and actual orientations of the crystal in the SQUID experiments, because of the experimental setup. Furthermore, we also noticed a slight disagreement between PND and *ab initio* susceptibility tensor, which is most likely due to the simplifications in the CASPT2 calculations. Finally, we also employed some simplifications in the PND approach, which yield a certain uncertainty. Noticeably, we used the room-temperature structure to perform the susceptibility tensor refinement. Small deviations could likely be expected, and as we already noticed small deviations in the tensor component can result in marked differences in the orientations of the eigenvectors.

Nevertheless, the agreement is quite correct, noticeably on the second experiment. Our different approaches are thus rather self-consistent, and noteworthy we may trust the *ab initio* model to be quite correct.

NOTE: for the moment, we only managed to study **5.4** by the means of PND. This is partly due to the proposals procedure, which yields incompressible delays, but it is also the consequence of the numerous experiments we had to perform on our Yb(III) sample. Nonetheless, studies of **5.1** and **5.3** are planned in the close future.

5.1.5 AC magnetic properties

As we have seen, the Yb(III) derivative **5.4** displays a marked magnetic anisotropy, and powder measurements on **5.1** and **5.3** suggest they may also do. From the luminescence measurements, we also saw a strong energy splitting between the Kramers Doublets (KD) of **5.4** in the ground state – *circa* 150 cm^{-1} –.

Together, these characteristics suggest this complex – if not the whole [LnTp_2NO_3] family – may present a slow dynamics of magnetisation at low temperature, at least under a static magnetic field. We thus performed AC squid measurements on powder samples for all complexes, under a static field of 0 Oe and 2000 Oe. No signal is observed in zero field, while at 2000 Oe a non zero out-of-phase magnetic moment is measured for **5.1**, **5.3** and **5.4**, as shown on Figure 5.1.19. Quite expectedly, nothing is observed in the case of the Ho(III) derivative, as suggested by the static measurements.

On the other hand, the observation of a non zero AC component for both Dy(III), Er(III) and Yb(III) derivatives is quite unexpected. In the framework of Rinehart and Long's model,[79] these ions are indeed expected to display markedly different magnetic behaviours, since their $4f$ electron density is not expected to interact in a similar fashion with the ligand field. More precisely, Er(III) and Yb(III) ions show a prolate deformation of their $4f$ electron density in the $M_J = \pm J$ substate, while Dy(III) shows an oblate deformation.

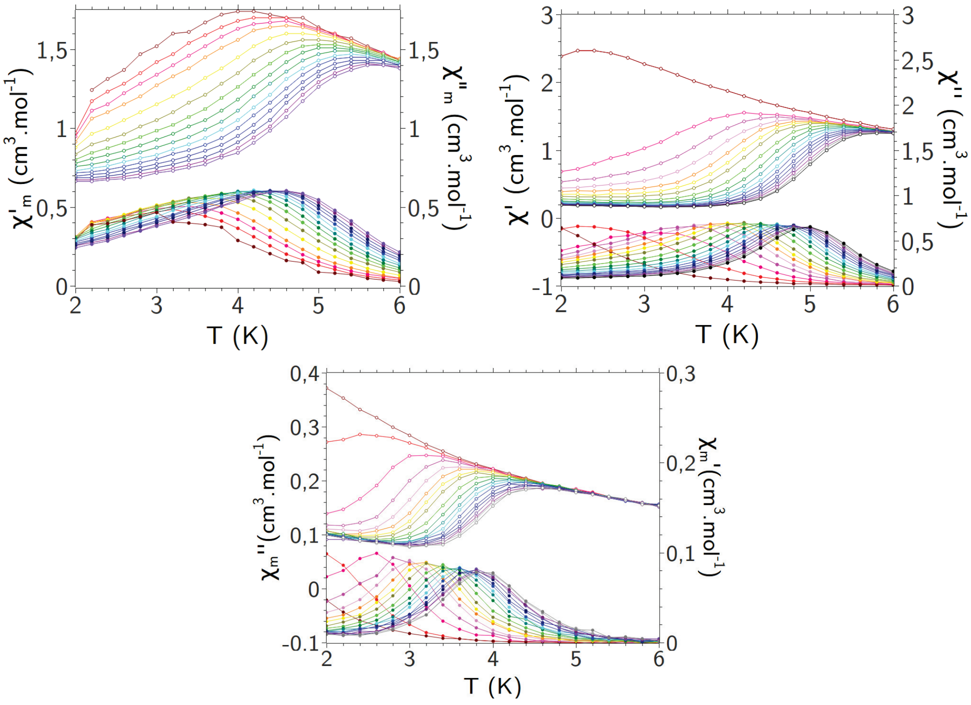

FIGURE 5.1.19: AC susceptibility curves for complexes **5.1** (upper left), **5.2** (upper right) and **5.4** (bottom), under a static field of 0.2 T and in the frequency range [1 Hz; 1400 Hz] (brown to gray).

At first, this observation was very surprising(xvii), but soon Sessoli and coworkers reported a similar behaviour in the [Ln(trensal)] family of complexes[203] (with trensal = 2,2',2"tris(salicylideneiminato) triethylamine). More specifically, they observed a similar slow dynamics of magnetisation for the Er and Dy derivatives at low temperature, and using a combination of spectroscopies they were able to rationalise it. In that case indeed, magnetisation dynamics is not solely governed by a "single-ion" energy barrier mechanism, but also by other direct and Raman spin-phonon relaxations (see Chapter 2 for a reminder on these mechanisms), and as such Rinehart and Long model does not apply.[80,81]

Following this inspiring example, we studied in more details the magnetisation dynamics of our complexes. On Figure 5.1.20, we represent the Arrhenius plots $ln\ \nu = f(T)$, deduced from the maxima of the $\chi''_m = f(T;\nu)$ curves. A marked deviation from linearity is seen in these plots, suggesting that the dynamics is not solely governed by energy-barrier (Arrhenius-like) mechanisms. Frequently, these deviations are assigned to quantum tunnelling of magnetisation (QTM), and one uses the linear portion of the curve to determine

---

(xvii) The first magnetic measurements on these complexes were performed in 2013, and no literature example was then published.

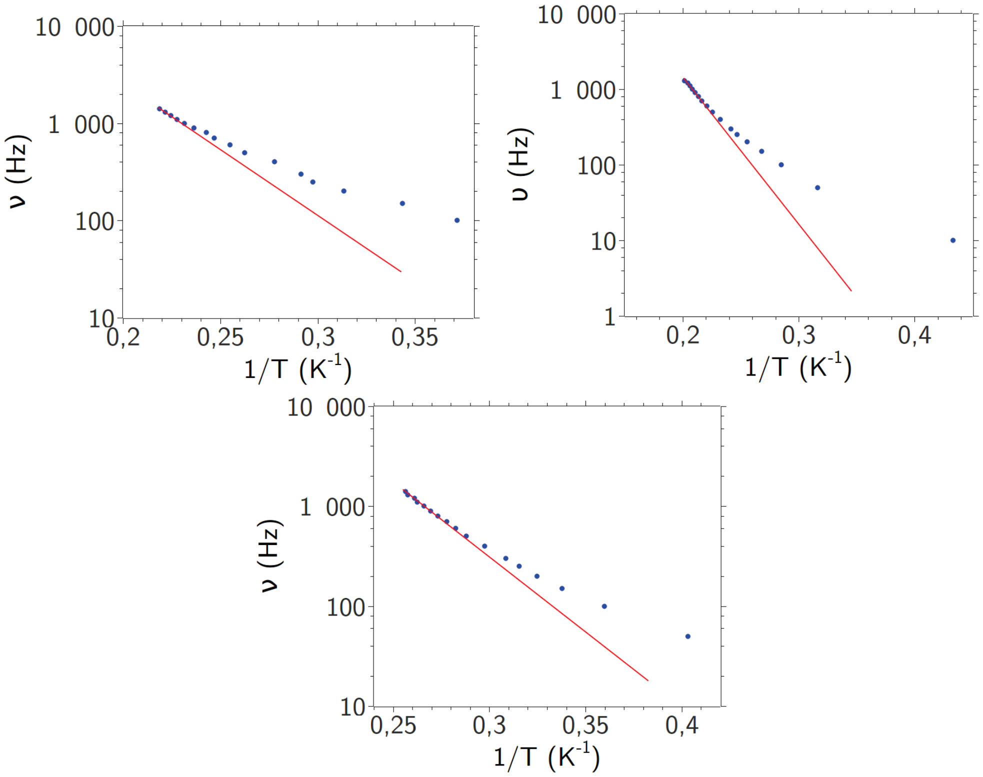

FIGURE 5.1.20: Arrhenius plots $ln\ \nu = f(/T)$ for complexes **5.1** (upper left), **5.3** (upper right) and **5.4** (bottom), as deduced from the maxima of the out-of-phase susceptibility at 2000 Oe. The solid red lines are a guide for the eye.

the energy barrier.[204–206] Here, since we applied a static magnetic field of a rather high magnitude (2000 Oe), we would not expect to observe any remaining QTM, and as such it is quite unlikely that such an approach would yield meaningful energy barriers. In fact, doing so we obtain in this case energy barriers of 25.8(6) K for **5.1**, 40.0(5) K for **5.3** and 30(1) K for **5.4**. This last value does not correlate at all with the CF splitting we deduced from luminescence (which was around 100 cm^{-1}), and the other two values do not correlate either with the calculated ones (see Tables 5.6 and 5.7 below). As such we have little to no confidence in these energy barriers.

We thus decided to analyse the experimental data using a more complete description, involving also Raman and direct relaxation mechanism.[203] To do so, we fitted the $\nu = f(T)$ curves using

$$\nu = aT + bT^n + \nu_0 \ \exp\left(-\frac{\Delta E}{k_B T}\right). \tag{5.6}$$

Yet, as one can remark this last equation involves a rather large number of parameters compared to the number of data points. In order to avoid any overparametrisation, we then fixed some of them. First of all, in the case of the Yb(III) derivative **5.4** we know the possible values for ΔE, thanks to the luminescence spectrum, and as such we may keep this parameter fixed. In the case of the Er(III) and Dy(III) derivative, we do not have these experimental values, but we may also employ the *ab initio* energy barriers to do so.

Doing so, we obtained the following equations as best fits:

$$\nu_{\mathrm{Dy}} = 38(2)T + 2.99(5) \times 10^{-2} T^7, \tag{5.7}$$

$$\nu_{\mathrm{Er}} = 11(2)T + 6.97(7) \times 10^{-4}T^{9}, \quad (5.8)$$

$$\nu_{\mathrm{Yb}} = 13(2)T + 6.36(5) \times 10^{-3}T^{9}. \quad (5.9)$$

Let us interpret these results. First of all, it is rather striking that no energy-barrier mechanism is involved here. To the best of our knowledge, this is the third time such an unexpected magnetic behaviour is reported.[190,191]
Furthermore, we also remark that the Raman exponent is equal to 7 for **5.1**, and 9 for **5.3** and **5.4**. We may wonder if we actually retrieve the expected differentiation between Dy(III) on one hand and Er(III) and Yb(III) on the other hand. Moreover, these values also bear much information on the magnetisation dynamics. Indeed, when $n = 7$ the magnetic relaxation occurs between two states $|a\rangle$ and $|b\rangle$ that are not related by Kramers conjugation – for instance, $|a\rangle = |+5/2\rangle$ and $|b\rangle = |-3/2\rangle$. On the other hand, when $n = 9$ the two quantum states involved in the relaxation of magnetisation are Kramers conjugate.[81] At this stage, it thus seems the magnetic relaxation of **5.1** is fundamentally different from the one of **5.3** and **5.4**.

NOTE: an additional support to our model for the dynamics of magnetisation comes from the field dependence of the out-of-phase susceptibility. The corresponding curves are given in Appendix. In short, for complexes **5.3** and **5.4** no marked variation is observed at high frequencies, as could be expected from a T^9 Raman relaxation (field-independent). On the other hand, at lower frequencies small shifts can be observed, also in good agreement with our model: the direct relaxation is preponderant at lower temperature (thus lower frequencies), and it is field dependent. In the case of **5.1**, variations are observed both at low and high frequencies, here again in good agreement with our model: at low frequency, the direct contribution dominates, and it is field dependent. At higher frequencies, the rate of relaxation is governed by the T^7 Raman contribution, which is also field dependent.
We also gain support from the study of the $\chi''_m = f(\chi'_m)$ curves at constant temperature – the so-called Cole-Cole plots.[207] When the relaxation of magnetisation occurs through a unique mechanism, these curves are indeed expected to be perfect semi-circles. When several mechanisms are involved, because of the distribution of relaxation rates these curves distort. If the different relaxation rates are very different, we may expect the Cole-Cole plot to consist in juxtaposed and separated semi-circles, while in the case of comparable rates the different semi-circles would be fused and the overall curve would present a distorted semi-circular shape. In this latter case, one may characterise the distortion *via* a phenomenological parameter α, which tends to zero for a single relaxation process, and to one when the distribution of relaxation rates is wide.[208]
Here, in the case of the Yb(III) derivative **5.4** we obtain slightly distorted semi-circles, which can be fitted by a Cole-Cole equation with α values ranging from 0.25(3) at 2 K to 0.13(4) at 4 K. These values are in good agreement with our expectation: at lower temperature, both direct and Raman mechanisms contribute significantly to the relaxation rate (89 % and 11 % respectively, at 2 K), thus yielding a marked deviation of α from 0. When increasing the temperature, the contribution of the Raman process becomes largely predominant (96% at 4 K, for instance), and the systems tends to ideality, with α tending to 0. On the other hand, in the case of **5.1** and **5.3** the curves present a more complex shape. In both cases, at low χ'_m values (*i.e*, high frequencies) we observe a semi-circular shape, while for the higher χ'_m values (lower frequencies) additional points are seen, which seem to belong to a second semi-circle (though more data points would be needed to ascertain this). This correlates nicely with the characteristic of the direct and Raman relaxation processes of these two complexes. Indeed, for both **5.1** and **5.3**

the Raman process is less involved at low temperature (5% and 2% at 2K, respectively), and the transition between the two relaxation processes is more abrupt than what it is the case of **5.4**. As such, the two processes are quite separated, which translates into two peculiar Cole-Cole plots.

5.1.6 Ab initio modelling

Here again, theoretical support is very valuable. We thus modelled complexes **5.1**, **5.3** and **5.4** at the SA-CASSCF/RASSI-SO level, using basis sets from the ANO-RCC library, and with the following contractions:

- [8s7p4d3f2g1h] for Dy, Er, Yb;
- [4s3p2d] for the coordinating atoms (N, O);
- [3s2p1d] for the non-coordinating C, N, O, B atoms;
- [2s] for the H atoms.

In all cases, the active spaces consisted of the 7 $4f$ orbitals. In the case of **5.1**, we computed 21 sextets, 224 quadruplets and 300 doublets(xviii) at the SA-CASSCF level.[15] Among all these roots, 21, 128 and 107 of them were, respectively, included in the state-interaction procedure. Similarly, for **5.3** 35 quadruplets and 112 doublets were computed at the SA-CASSCF level, and were all included in the RASSI-SO calculation. Finally, for **5.4** 7 doublets were optimised at the MS-CASPT2[18] level, and allowed to interact in the RASSI-SO procedure.

We performed the calculations using Molcas 8.0,[210] in collaboration with Dr. Boris Le Guennic and Dr. Julie Jung (Université Rennes 1). For these three complexes, the accuracy of the model was checked by comparison between computed and experimental data. As we have already seen, in the case of **5.4** the calculation provides a nice agreement with the single crystal SQUID data and the luminescence spectrum. The agreement with the powder magnetic measurements can also be obtained quite directly (the Single_Aniso routine of MOLCAS[211] indeed permits to compute susceptibility and magnetisation at different fields ans temperatures). As one can see from Figure 5.1.21, it is quite correct for the three complexes, though the calculations seem to overestimate the $\chi_m T$ value for **5.1** at low temperature. Nevertheless, magnetisation seems quite correctly reproduced, which suggest the theoretical models can be trusted.

In Table 5.5, 5.6 and 5.7, we give the $|M_J\rangle$ decomposition of the wavefunctions of the KD in the respective ground states of complexes **5.1**, **5.3** and **5.4**. Though quite tedious to read, these tables yield valuable information. It is indeed rather plain that both **5.3** and **5.4** present a high degree of mixing in all their KD(xix), while **5.1** presents a ground KD with a relatively low extent of mixing. These marked mixing are a likely cause for the strong QTM[212] – we indeed remind that, though we did not consider any QTM contribution in the analysis of the magnetisation dynamics under 2000 Oe, we still do not observe any out-of-phase peak in the AC susceptibility at zero constant field, thus implying a strong QTM is acting here.

Single_Aniso also permits to compute the Transition Dipole Moments (TDM), which give information about the feasibility of the transitions between the different substates in the energy diagram. Here, these TDM may allow us to understand the QTM and direct

---

(xviii) 490 doublets should be included,[209] but the current implementation of MOLCAS restricts the number of roots to 300.

(xix) *I.e.*, the wavefunction of a given KD involves different $|M_J\rangle$ basis vectors.

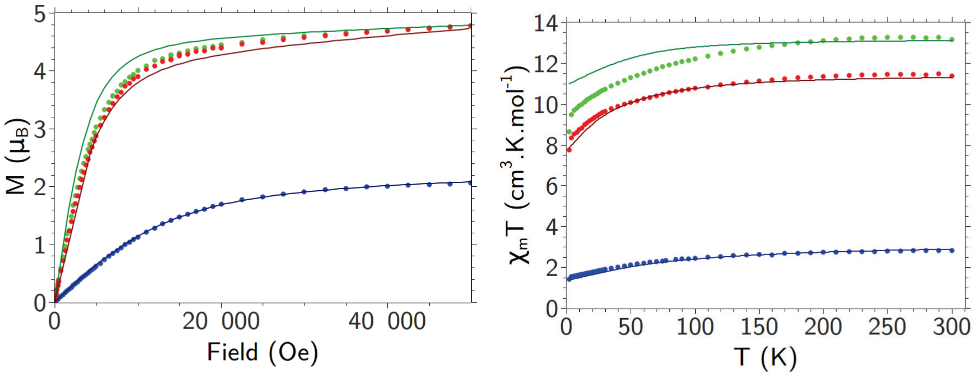

FIGURE 5.1.21: Comparison between the calculated (solid lines) and experimental (bullets) $M = f(B)$ (left) and $\chi_m T = f(T)$ curves (right). Colour scheme: **5.1**, green; **5.3**, red; **5.4**, blue.

TABLE 5.5: Decomposition of the wavefunctions corresponding to the 8 KD of the ground $^6H_{15/2}$ state of **5.1**, on the basis of the $|M_J\rangle$ vectors, and relative energies (in cm^{-1}). Convention: n in Ψ_n^+ indexes the KD (the higher in energy, the larger n), and + indicates that only substates associated to a positive magnetic moment are represented (the conjugated substates are deduced by changing the sign of M_J). To ease the reading, only the norms of the (complex) coefficients are displayed, and values above 0.5 are highlighted (bold font).

	Ψ_1^+	Ψ_2^+	Ψ_3^+	Ψ_4^+	Ψ_5^+	Ψ_6^+	Ψ_7^+	Ψ_8^+
Rel. E	0	87	124	134	162	183	241	546
$\|+15/2\rangle$	**0.96**	0.15	0.07	0.01	0.11	0.01	0.01	0.00
$\|+13/2\rangle$	0.03	0.04	0.20	0.35	0.32	0.10	0.22	0.07
$\|+11/2\rangle$	0.21	0.23	0.36	0.22	0.37	0.24	0.11	0.03
$\|+9/2\rangle$	0.06	0.08	0.26	0.45	0.23	0.14	0.30	0.21
$\|+7/2\rangle$	0.10	0.34	0.14	0.24	0.19	0.25	0.18	0.10
$\|+5/2\rangle$	0.01	0.11	0.33	0.33	0.37	0.19	0.28	0.40
$\|+3/2\rangle$	0.07	0.28	0.19	0.06	0.43	0.42	0.23	0.20
$\|+1/2\rangle$	0.01	0.03	0.26	0.19	0.13	0.23	0.14	**0.55**
$\|-1/2\rangle$	0.05	0.30	0.07	0.08	0.13	**0.56**	0.08	0.24
$\|-3/2\rangle$	0.00	0.04	0.31	0.09	0.08	0.13	0.22	0.49
$\|-5/2\rangle$	0.04	0.34	0.07	0.17	0.14	0.34	0.24	0.15
$\|-7/2\rangle$	0.01	0.12	0.42	0.43	0.25	0.12	0.34	0.30
$\|-9/2\rangle$	0.03	**0.50**	0.06	0.28	0.17	0.20	0.34	0.06
$\|-11/2\rangle$	0.00	0.12	0.26	0.29	0.30	0.13	0.48	0.14
$\|-13/2\rangle$	0.02	0.48	0.42	0.17	0.32	0.24	0.27	0.01
$\|-15/2\rangle$	0.00	0.01	0.02	0.10	0.07	0.03	0.11	0.02

processes, but not the Raman ones (since they involve virtual states which cannot be computed explicitly). Analysis of these TDM can also be a fairly tedious task (in the case of Er and Dy, 60 values should be considered), but we may summarise quite simply the results. First of all, for all three complexes we can observe a non negligible TDM within all the KD, noticeably in the ground ones. As a result, a strong QTM is expected for these three complexes, as observed.

If this QTM is suppressed (application of an external field), then other relaxations should be sought. The rule of thumb in these cases is to find the shortest path, associated to the highest TDM values. As one can imagine, in the cases of Er and Dy the matter may be quite complicated, and indeed it is. For the sake of simplicity, on Schemes 5.1.1, 5.1.2

Table 5.6: Decomposition of the wavefunctions corresponding to the 8 KD of the ground $^4I_{15/2}$ state of **5.3**, on the basis of the $|M_J\rangle$ vectors, and relative energies (in cm^{-1}). Convention: n in Ψ_n^+ indexes the KD (the higher in energy, the larger n), and + indicates that only substates associated to a positive magnetic moment are represented (the conjugated substates are deduced by changing the sign of M_J). To ease the reading, only the norms of the (complex) coefficients are displayed, and values above 0.5 are highlighted (bold font).

	Ψ_1^+	Ψ_2^+	Ψ_3^+	Ψ_4^+	Ψ_5^+	Ψ_6^+	Ψ_7^+	Ψ_8^+
Rel. E	0	49	83	153	189	236	283	312
$\lvert +15/2\rangle$	**0.80**	0.24	0.14	0.10	0.10	0.01	0.28	0.00
$\lvert +13/2\rangle$	0.19	0.49	0.49	0.15	0.14	0.04	0.43	0.02
$\lvert +11/2\rangle$	0.43	0.21	**0.53**	0.15	0.02	0.03	0.33	0.04
$\lvert +9/2\rangle$	0.20	0.31	0.45	0.38	0.21	0.04	0.22	0.14
$\lvert +7/2\rangle$	0.27	0.37	0.30	0.21	0.30	0.06	0.17	0.06
$\lvert +5/2\rangle$	0.10	0.44	0.23	0.23	0.26	0.13	0.48	0.20
$\lvert +3/2\rangle$	0.03	0.24	0.29	**0.51**	0.07	0.27	0.34	0.11
$\lvert +1/2\rangle$	0.03	0.07	0.12	0.24	0.33	0.46	0.28	0.28
$\lvert -1/2\rangle$	0.03	0.12	0.03	0.47	0.26	0.25	0.15	0.24
$\lvert -3/2\rangle$	0.03	0.13	0.03	0.24	0.24	0.25	0.11	0.43
$\lvert -5/2\rangle$	0.05	0.23	0.02	0.25	0.12	0.38	0.20	0.13
$\lvert -7/2\rangle$	0.02	0.13	0.02	0.15	**0.52**	0.33	0.09	0.34
$\lvert -9/2\rangle$	0.03	0.21	0.05	0.10	0.33	0.41	0.17	0.20
$\lvert -11/2\rangle$	0.00	0.06	0.10	0.07	0.16	0.23	0.07	0.50
$\lvert -13/2\rangle$	0.02	0.16	0.11	0.05	0.26	0.20	0.05	0.33
$\lvert -15/2\rangle$	0.00	0.05	0.00	0.04	0.22	0.23	0.05	0.26

Table 5.7: Decomposition of the wavefunctions corresponding to the 4 KD of the ground $^2F_{7/2}$ state of **5.4**, on the basis of the $|M_J\rangle$ vectors, and relative energies (in cm^{-1}). Convention: n in Ψ_n^+ indexes the KD (the higher in energy, the larger n), and + indicates that only substates associated to a positive magnetic moment are represented (the conjugated substates are deduced by changing the sign of M_J). To ease the reading, only the norms of the (complex) coefficients are displayed, and values above 0.5 are highlighted (bold font).

	Ψ_1^+	Ψ_2^+	Ψ_3^+	Ψ_4^+
Rel	0	110	396	527
$\lvert +7/2\rangle$	**0.53**	0.00	0.04	0.00
$\lvert +5/2\rangle$	**0.73**	0.15	0.17	0.13
$\lvert +3/2\rangle$	0.36	0.12	0.34	0.39
$\lvert +1/2\rangle$	0.11	0.04	0.12	**0.57**
$\lvert -1/2\rangle$	0.04	0.12	0.45	**0.65**
$\lvert -3/2\rangle$	0.16	0.18	**0.68**	0.27
$\lvert -5/2\rangle$	0.14	**0.57**	0.22	0.10
$\lvert -7/2\rangle$	0.08	**0.77**	0.35	0.05

and 5.1.3 we represented the energy diagram for the ground states of **5.1**, **5.3** and **5.4**, and we symbolised the different TDM values using a colour code: in gray, we depict the lowest quartile, in blue the second, in green the third and in red the highest one.

From these three schemes, it appears that many different pathways are eligible. It is then quite hard to pinpoint exactly which states are involved in the direct relaxation mechanisms, but nonetheless these mechanisms are quite feasible.

Finally, we may also gain information on the Raman relaxation process. In the case of the Yb(III) and Er(III) derivatives, we indeed observe a T^9 dynamics, which according to Stevens is expected when the relaxation takes place within a KD.[81] Said otherwise, for these two complexes the relaxation process would be associated to a horizontal transition in Schemes 5.1.2 and 5.1.3 (passing through a virtual state). If we assume our magnetic system is at equilibrium with the thermal bath, we may then postulate that the relaxation occurs within the ground KDs. In the case of the Dy(III) derivative on the other hand, a T^7 dynamics is observed, which is expected when the relaxation process links two substates that are not forming a KD. This means that, in Scheme 5.1.1, the (rate limiting) process would be associated to a diagonal or vertical transition. Using the same assumption as previously, we may postulate that the starting state for this transition will belong to the ground KD.

We may even try to push this development further, wondering whether there is a link between the strong mixing in all the KD of the ground states of the Yb(III) and Er(III) derivatives and the efficient "horizontal magnetic relaxation" they present. Indeed, one usually considers mixing "increases the communication" within the two components of a KD, eventually leading to a more efficient QTM. Here, we may wonder if the same line of argument holds for other relaxation processes. It could indeed account for the fact that the Dy(III) derivative does not show such "horizontal relaxation" processes, because of the low extent of mixing in its ground KD. Nevertheless, three experimental evidences are not sufficient to build such a model, and in order to confirm or infirm this hypothesis we would need to gather more data...

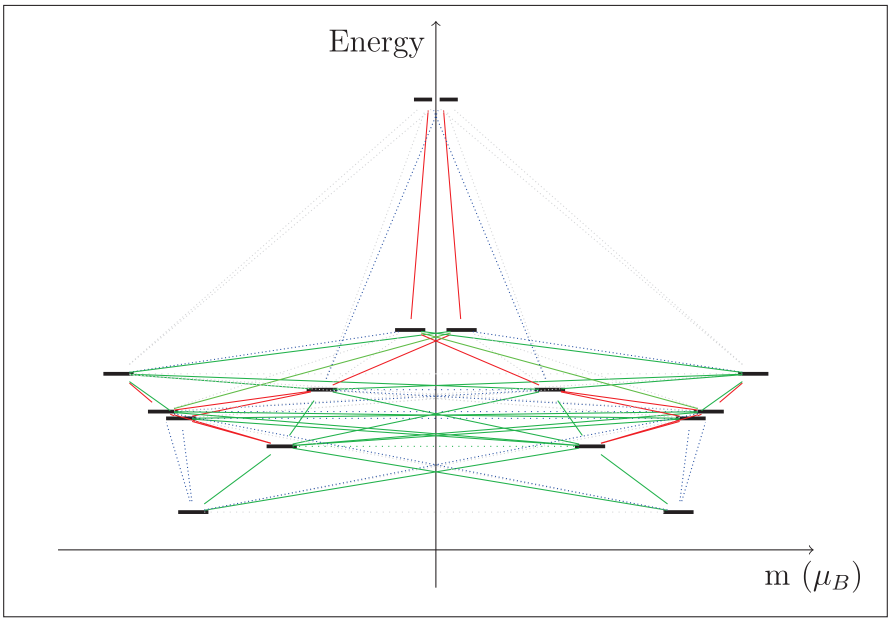

Scheme 5.1.1: Energy diagram and TDM of **5.1**, as computed at the SA-CASSCF/RASSI-SO level.

5.1.7 Long story short

In short, we have synthesised and characterised a new family of lanthanide mononuclear complexes, [LnTp$_2$NO$_3$], which present interesting magnetic properties. Indeed, though they do not present a genuine SMM behaviour, they display a slow dynamics of magnetisation under the application of a static magnetic field, which is quite unexpected in the framework of Rinehart and Long's model. Using a combination of experimental and

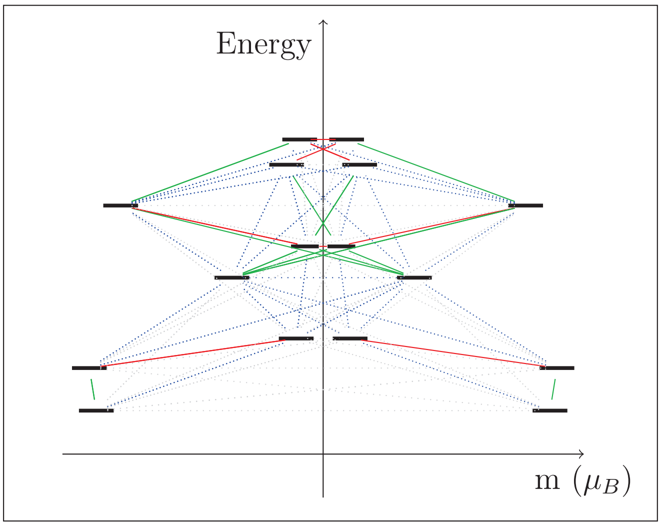

Scheme 5.1.2: Energy diagram and TDM of **5.3**, as computed at the SA-CASSCF/RASSI-SO level.

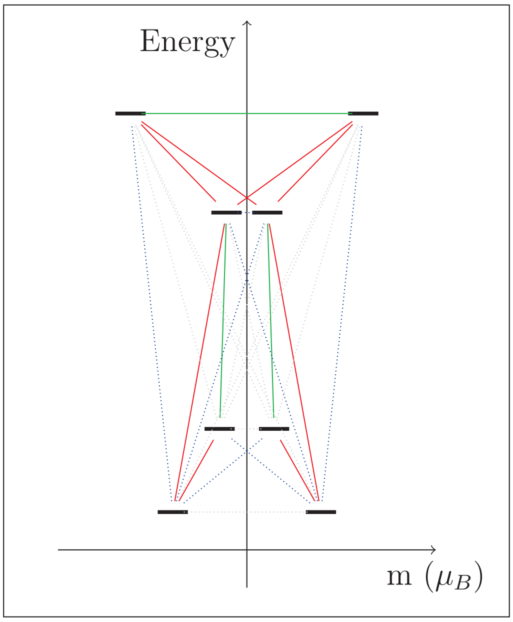

Scheme 5.1.3: Energy diagram and TDM of **5.4**, as computed at the SA-CASPT2/RASSI-SO level.

theoretical characterisations, we have been able to show this is due to the fact that the dynamics of magnetisation for these complexes is not governed by any Arrhenius-like behaviour, but is rather entirely controlled by Raman and direct mechanism. To the best of our knowledge, such a peculiar magnetisation dynamics was only reported twice, and not for a family of complexes, thus making these compounds rather original.

Furthermore, we have also been able to tentatively rationalise this exotic magnetic behaviour. In both cases, *ab initio* calculations reveal a marked propensity towards QTM as well as many possible direct relaxation pathways. On the other hand, the temperature dependence of the Raman mechanism indicates a fundamental difference between the Dy(III) derivative and the Er(III) and Yb(III) derivatives. In the first case, the relaxation mechanism links two states that are not conjugated by Kramers theorem, while in the latter case a horizontal relaxation is likely involved. Interestingly, this differentiation can be tentatively correlated to the extent of mixing in the wavefunctions of the ground KD: it is strong in the cases of the Er(III) and Yb(III) derivatives, suggesting an efficient "communication" can be observed between the two components of the ground KDs, whereas almost no mixing is observed in the case of the Dy(III) derivative, indicating a much less efficient "interplay" within the ground KD. Notwithstanding, we remind that caution must be taken with these interpretations, as they are based on a rather limited set of experimental evidences.

Nevertheless, and quite surprisingly, they would lead to retrieve a connection with Rinehart and Long's model. Indeed, the lower mixing in **5.1** could be interpreted as the fact that the ligand field of our complexes suits more the oblate Dy(III) ion than the prolate Er(III) and Yb(III) ions, at least in their ground KD.

Because of the potentially strong importance of such a model, we wanted to gather more experimental evidences, and we thus considered a closely related family of mononuclear complexes(xx), which we present hereafter.

5.2 The [LnTp$_2$Acac]: towards more efficient SMM?

As we have just seen, the [LnTp$_2$NO$_3$] complexes present very interesting magnetic properties, which are likely related to their structure. As chemists, we then wondered whether we could finely tune these properties by an appropriate modification on the ligands. Similar complexes structures were already reported in the literature,[213,214] and noticeably we found an interesting family of complexes whose properties were left unexplored: the [LnTp$_2$(Acac)] family. Formally, they can be seen as [LnTp$_2$NO$_3$] complexes where the nitrate ligand has been substituted by an acetylacetonate. These complexes seemed easy to synthesise, and also to functionalise, the acetylacetonate moiety presenting several functionalisable carbons. We thus decided to synthesise these complexes and to study their luminescent and magnetic properties. We remind here that the results are preliminary, noticeably because of a series of breakdowns on the different apparatuses we used (magnetometer, spectrometer).

5.2.1 Syntheses and crystal structures.

The details of the synthetic procedures are given in Appendix A.2.3, and are adapted from the previously published methods. They are both quite reminiscent of the one used to obtain the [LnTp$_2$NO$_3$] complexes: a solution of the lanthanide salt – here, a chloride

---

(xx)Hoping their magnetic properties would be similar to those of the [LnTp$_2$NO$_3$] complexes, as their structures are rather resemblant.

– is added to a solution of the ligands, leading to a precipitate that is recrystallised either in a CH_2Cl_2/heptane or $CHCl_3$/heptane mixture.[214]
Different crystal structures are obtained, depending on the solvent and the lanthanide ion. They can be separated into three families.

Complexes 5.6 to 5.12. The first family of complexes crystallises in the monoclinic $P2_1/c$ space group, and they were obtained for Ln = Ce **5.6**, Pr **5.7**, Nd **5.8**, Sm **5.9**, Gd **5.10**, Tb **5.11**, Dy **5.12**. All these complexes are isostructural, and correspond to the published one for Ce(III).[215] They were crystallised using either dichloromethane or chloroform as solvent. The asymmetric unit consists of a single [LnTp$_2$Acac] complex and is depicted on Figure 5.2.1, and the crystallographic parameters are gathered in Table B.9. The coordination geometry here also can be viewed as distorted square-base antiprism, though it has been shown previously that it is more accurately described as a bicapped trigonal prism.

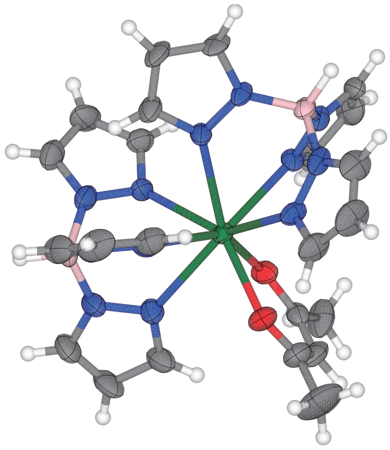

FIGURE 5.2.1: ORTEP drawing of the [LnTp$_2$Acac] complexes 5.6 to 5.12 (ellipsoids drawn at 50% probability). Example of [DyTp$_2$Acac] **5.12**.

Complexes 5.13 to 5.16. This second family of complexes is not isomorphic, but they are all crystallising in a primitive monoclinic space group and the unit cell contains a co-crystallised solvent molecule. **5.13**, **5.14** and **5.15** are isostructural ($P2_1/c$), and were obtained using chloroform as solvent. The formula of the asymmetric unit for these three complexes is [LnTp$_2$Acac] · $CHCl_3$. Complex **5.16** crystallises in the monoclinic $P2_1/n$ space group, and its asymmetric unit is composed of a [LnTp$_2$Acac] complex plus a crystallised CH_2Cl_2 molecule. Noteworthy, the solvents molecules in these four structures are not disordered, and in the case of **5.13** to **5.15**, a 2D-lamellar structuration is actually observed (see Appendix B.5.1). Noteworthy, these structures were not reported previously.

Complexes 5.17 to 5.19. The third family of complexes is also not isomorphic, but they are all crystallising in the triclinic $P\bar{1}$ space group. The asymmetric units of **5.17** and **5.18** contain two independent [HoTp$_2$Acac] and [YbTp$_2$Acac] complexes respectively, while in the case of **5.19** only one [YbTp$_2$Acac] complex and a crystallised chloroform molecule are found. Note that the structure of **5.19** was also not reported previously.
Overall, the molecular structures of all these complexes are rather similar. Yet, because of the marked differences in their crystal packing, we may not directly compare their physical properties in the solid state. For instance, if we recall the magnetic properties of

our previous [LnTp$_2$NO$_3$] complexes, we saw that the slow dynamics at low temperature was not governed by single-molecule properties but entirely by vibrations (either molecular or collective). In such case, a modification of the environment of the complexes will very likely impact the observed property, since many vibration modes will be perturbed.
As such, we will focus in the following on the first family of complexes only. In contrast with the [LnTp$_2$NO$_3$] family, here the structures are found only for the lighter lanthanide ions.(xxi) In agreement with our former approach, we studied their luminescent and magnetic properties. Because of a lack of time, we have not yet studied them at the CASSCF level. This study is planned in a close future.

5.2.2 Luminescence spectra.

We first studied the luminescence properties of complexes **5.6** to **5.12**, at both room and liquid nitrogen temperatures. To the exception of the Ce(III) **5.6** and Gd(III) **5.10** derivatives, they present moderate to strong luminescence peaks in the 400 nm - 1200 nm range.

Complex 5.7, [PrTp$_2$Acac]. We report on Figure 5.2.2 the luminescence spectra of **5.7**. As one can see, a signal is already observed at room temperature, but presents a very low resolution. A large background noise is also observed, which to date remains unexplained.(xxii) At low temperature, the resolution is slightly better, though the background contribution remains rather intense. In order to increase the signal over noise ratio, we thus focused on parts of the spectral range and performed several acquisitions with very long collection times (up to half an hour for a 30 nm window).

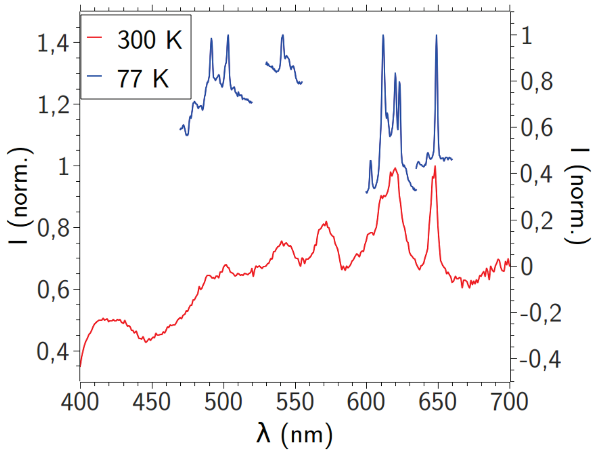

FIGURE 5.2.2: Visible luminescence spectra of **5.7** under a 300 nm irradiation, at room temperature (red curve) and 77 K (blue).

This allows us to identify four $4f \to 4f$ transitions:[199] $^3P_0 \to ^3 H_4$ around 490 nm, $^3P_0 \to ^3 H_5$ around 545 nm, $^3P_0 \to ^3 H_6$ around 615 nm and $^3P_0 \to ^3 F_2$ around 650 nm. As one may note, these are all fluorescent transitions ($\Delta S = 0$). Noteworthy, an additional peak seemed to be observed at 575 nm at room temperature, but is not seen at 77 K and

---

(xxi) Note that we also retrieve the effect of the lanthanide contraction in the lattice cell volumes, as exemplified in Figure B.5.2

(xxii) Note that the large bump between 400 nm and 450 nm corresponds to the residual ligand fluorescence. This band is not usually observed, since the lanthanide luminescence is much more intense. Here, the Pr(III) signal is weak enough to permit its observation.

does not correspond to any expected transition of the Pr(III) ion. We may then suppose it also was a part of the unexplained background noise. A new campaign of measurement is planed in the close future in order to ascertain this fact, but a spectrometer breakdown delays it for the moment...

Complex 5.8, [NdTp$_2$Acac]. We present on Figure 5.2.3 the near-IR luminescence spectrum of **5.8**. A broad band is observed at room temperature around 1073 nm, which resolves into three peaks at 77 K, at 1062 nm, 1073 nm and 1090 nm respectively. According to literature, they correspond to the expected $^4F_{3/2} \rightarrow ^4 I_{11/2}$ transition of Nd(III).[199] Two interesting things may be noted here. First, we only observe 3 separated peaks on the spectrum, while we could expect to observe at least – assuming Kasha's rule is obeyed – 6 transitions. Most probably, these transitions are simply not observable with our experimental conditions, being too weak – although we also employed very long measurements here –.
Second, we do not either observe the $^4F_{3/2} \rightarrow ^4 I_{9/2}$ transition, which would be expected around 900 nm. As such, our luminescence study does not allow us to gain any information on the ground $^4I_{9/2}$ state.

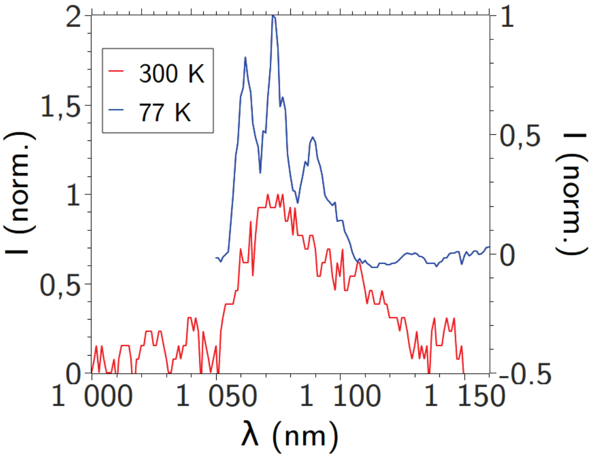

FIGURE 5.2.3: Near-IR luminescence spectra of **5.8** under a 300 nm irradiation, at room temperature (red curve) and 77 K (blue).

Complex 5.9, [SmTp$_2$Acac]. On the other hand, the luminescence spectra of the samarium derivative **5.9** are rich in information. They are depicted on Figure 5.2.4.
As one can see, three series of peaks are observed at room temperature, respectively around 565 nm, 603 nm and 648 nm, corresponding to the expected $^4G_{5/2} \rightarrow\ ^4H_{5/2}$, $^4H_{7/2}$ and $^4H_{9/2}$ transitions.[199] A fourth one around 705 nm ($^4G_{5/2} \rightarrow\ ^4H_{11/2}$) can also be guessed, but it shows a very low intensity and as such was not represented here. At 77 K, the three series are nicely resolved, yielding massifs of three, four and five peaks respectively. The corresponding wavelengths and wavenumbers are given in Table 5.8.
These numbers of peaks are exactly the one we would expect to observe, since they correspond to the degeneracy of the ^4H_J states. If we then assume Kasha's rule is obeyed, we can tentatively draw the energy diagram for the three first ^4H_J states of **5.9**.This is achieved on Figure 5.2.8. Note that in the case of the second series of transitions (towards the $^4H_{7/2}$ state), the second luminescence peak seems to be split in two components at 77 K, and as such there is a larger uncertainty on the position of the corresponding KD in the diagram. Two phenomenon may cause this apparent splitting: the lifting of Kasha's rule,

TABLE 5.8: Wavelengths, absolute and relative wavenumbers associated to the luminescence peaks of **5.9** at 77 K, measured under an irradiation at 300 nm. The relative values are calculated with respect to the highest energy peaks of each transition.

Transition	λ (nm)	$\bar{\nu}$ (cm^{-1})	$\bar{\nu}_{rel}$ (cm^{-1})
$^4G_{5/2} \rightarrow {}^4H_{5/2}$	562.0(5)	17794(16)	0
	567.0(5)	17637(16)	+157(32)
	575.0(5)	17391(15)	+403(31)
$^4G_{5/2} \rightarrow {}^4H_{7/2}$	597.0(5)	16750(14)	0
	604(1)	16556(28)	+194(42)
	607.0(5)	16474(14)	+276(28)
	610.0(5)	16393(14)	+357(28)
$^4G_{5/2} \rightarrow {}^4H_{9/2}$	644.5(5)	15516(12)	0
	647.5(5)	15444(12)	+72(24)
	651.5(5)	15349(12)	+167(24)
	655.5(5)	15256(12)	+260(24)
	659.0(5)	15175(12)	+341(24)

or vibronic effects. We may postulate the second hypothesis is the right one, since we do not observe any peak below the minimum wavelength (560 nm) for this transition[xxiii]. In any case, we can see that we obtain a nicely resolved energy diagram for the ground state, and we can observe a rather strong CF splitting: +403(31) cm^{-1} between the first and last KD. As such, this complex might be a good candidate for the observation of a SMM behaviour, provided it is magnetically anisotropic – and setting aside the problem of the very weak paramagnetism of Sm(III) –.[64]

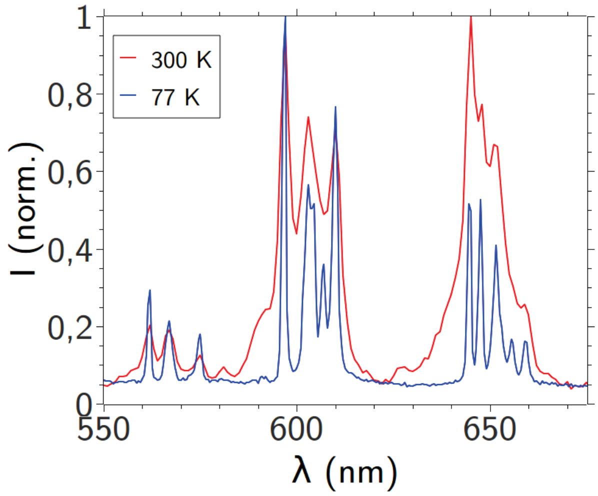

FIGURE 5.2.4: Visible luminescence spectra of **5.9** under a 300 nm irradiation, at room temperature (red curve) and 77 K (blue).

Complex 5.11, [TbTp$_2$Acac]. We present on Figure 5.2.5 the luminescence spectra of **5.11** at room and liquid nitrogen temperatures. The observed pattern is very characteristic of Tb(III), with four series of peaks centred around 490 nm, 545 nm, 585 nm and

---

[xxiii] Which would be the case if luminescence from excited KD of the $^4G_{5/2}$ state were active: deexcitation towards the lowest energy KD of the ground state would occur at a higher energy than expected if the emitting state is not the lowest energy KD, thus at lower wavelengths.

620 nm, respectively corresponding to the $^5D_4 \rightarrow\ ^7F_6$, $^7F_5$, $^7F_4$ and $^7F_3$ transitions.[199] Interestingly, resolution does not increase much when cooling to 77 K, but luminescence become stronger – though it already was very strong at room temperature –. Anyway, luminescence of the Tb(III) ion does not generally convey much information on the coordination geometry or the crystal field: one says that Tb(III) luminescent transitions are "insensitive" of the coordination sphere. Changes in the coordination sphere will indeed impact principally the overall luminescence efficiency (the so-called quantum yield) and the lifetimes of the emitting state, through modifications of the non-radiative deexcitation mechanisms, but not much the emission wavelengths.

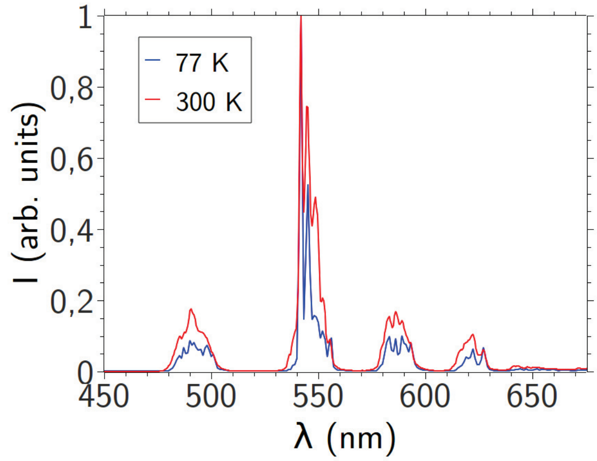

FIGURE 5.2.5: Visible luminescence spectra of **5.11** under a 300 nm irradiation, at room temperature (red curve) and 77 K (blue).

Complex 5.12, [DyTp$_2$Acac]. On the other hand, the luminescence of the Dy(III) ion can be quite markedly modulated by the crystal field. We represent on Figure 5.2.6 the measured spectra for **5.12** at room and liquid nitrogen temperatures.

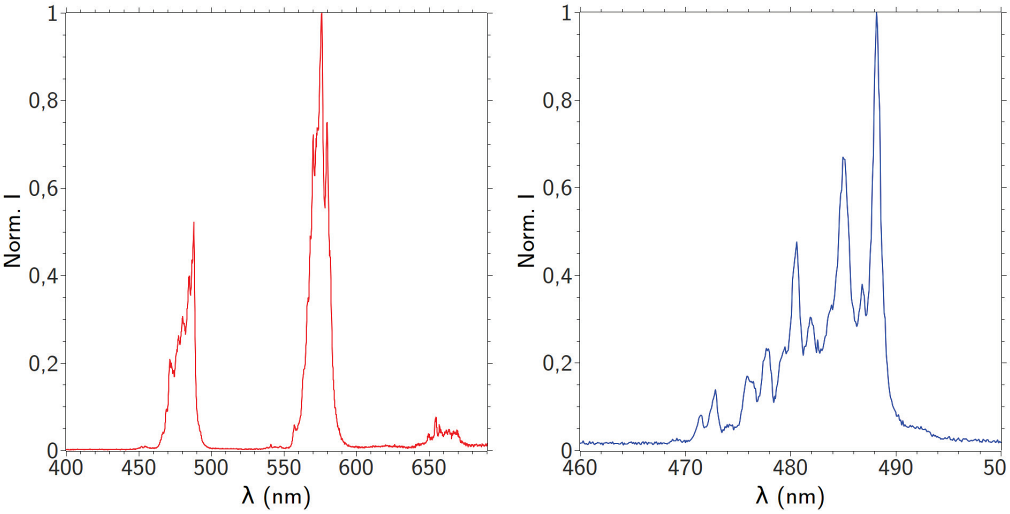

FIGURE 5.2.6: Left: visible luminescence spectra of **5.12** under a 350 nm irradiation, at room temperature. Right: zoom on the first series of peaks, measured at 77 K.

As one can remark, the room temperature spectrum recalls the one we obtained for [DyTp$_2$NO$_3$], though striking differences are observed. We indeed retrieve two principal transitions at 480 nm and 575 nm, corresponding to the expected $^4F_{9/2} \rightarrow {}^6H_{15/2}$ and $^4F_{9/2} \rightarrow {}^6H_{13/2}$ deexcitations, and a third one around 650 nm, corresponding to the $^4F_{9/2} \rightarrow {}^6H_{11/2}$ emission.[199]

At 77 K, we observe a marked increase in resolution for these transitions. More specifically, if we focus on the first series we may observe twelve clear luminescence peaks, indicating that Kasha's rule is most probably not obeyed in this case. Yet, we do not observe a doubling of the number of luminescence peaks, and as such we cannot propose an unambiguous and direct attribution of each transition, as we did in the case of [YbTp$_2$NO$_3$]. Nevertheless, and unlike in the case of [DyTp$_2$NO$_3$], we may presume that among these twelve peaks we may find the eight expected transitions of the $^4F_{9/2} \rightarrow {}^6H_{15/2}$ deexcitation, plus four so-called hot bands.(xxiv) As such, it could still be possible to deduce the energy diagram of **5.12** in the ground state, provided that we could determine which peaks in the emission spectrum correspond to hot bands.

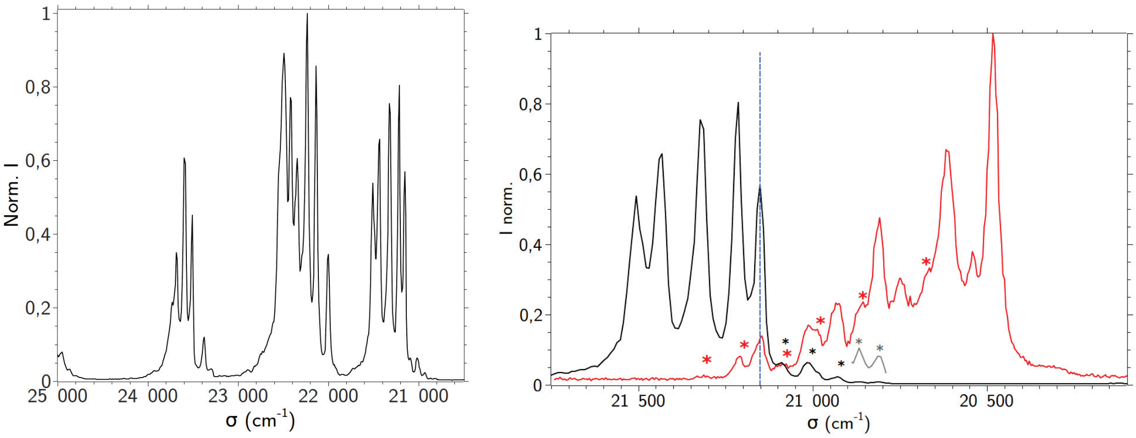

FIGURE 5.2.7: Left: excitation spectrum of **5.12**, measured at 576 nm and 77 K. Right: superimposition of the excitation (black curve) and luminescence (red curve) spectra at 77 K. The blue dashed line indicates the (0,0) transition in both spectra, the asterisks denote the hot-bands in the luminescence spectrum and the empty circles the hot-bands in the excitation spectrum.

To do so, we measured the excitation spectrum of **5.12** at 77 K, at 576 nm. We remind that such a measurement consists in varying the wavelength of the exciting (incident) beam on the sample and studying how this impacts the luminescence intensity at a fixed λ. Here, we chose the wavelength to correspond to the emission maximum at room temperature, which itself corresponds to the $^4F_{9/2} \rightarrow {}^6H_{13/2}$ transition of Dy(III). As such, any maximum in the spectrum will be associated to an absorption transition from the ground state of our complex towards an excited state that is located above (or equal to) the emitting $^4F_{9/2}$ state of Dy(III) – thus, to a ligand- or Dy(III)-centred excited state –.

From the curve in Figure 5.2.7, three series of fine transitions can be observed, approximately centred around 21500 cm^{-1}, 22500 cm^{-1} and 23500 cm^{-1} respectively.(xxv) These peaks all correspond to $4f-4f$ absorptions, and can be respectively assigned to $^6H_{15/2} \rightarrow {}^4F_{9/2}$, $^6H_{15/2} \rightarrow {}^4I_{15/2}$ and $^6H_{15/2} \rightarrow {}^4G_{11/2}$ transitions.[21,199]

The first of these transitions is of particular interest for us, as its reciprocal ($^4F_{9/2} \rightarrow {}^6H_{15/2}$) is also observed in the luminescence spectrum. Both massifs of peaks should thus

---

(xxiv) The term "hot band" underlines the fact that these supplementary transitions are permitted by the non-negligible thermal population of the excited states.

(xxv) Actually, a fourth one may be guess above 25000cm^{-1} as well, likely corresponding to the $^6H_{15/2} \rightarrow {}^4H_{21/2}$ absorption of Dy(III).

partly overlap, ideally on a single peak corresponding to the transition between the lowest KDs of both states (highest energy emission and lowest energy absorption). As one can observe on the right side of Figure 5.2.7, several peaks actually overlap, complicating the assignment of each band.

Let us denote the transitions by (n, m) where n and m respectively label the KDs in the ${}^6H_{15/2}$ and ${}^4F_{9/2}$ states (0 standing for the lowest energy KD). In the excitation spectrum, five intense bands are observed at 21150(9), 21213(9), 21321(9), 21431(9) and 21505(9) cm^{-1} respectively, and five much weaker transitions are observed at 20816(9), 20868(9), 20929(9), 21017(9) and 21088(9) cm^{-1}. Since ${}^4F_{9/2}$ is expected to be split in five KD because of the low symmetry of our complex, and as the lowest KD of ${}^6H_{15/2}$ will most probably display the largest statistical population at 77 K, we may presume that the five intense bands actually correspond to the $(0, m)$ transitions with $0 \leq m \leq 4$, and the following ones to (n, m) transitions with $n \neq 0$. With this assumption, the band at 21150(9) cm^{-1} can be attributed to the $(0, 0)$ transition, and any absorption (*resp.* emission) band at lower (higher) energy will thus be associated to a hot band.

If we now focus on the luminescence spectrum, we can see that two peaks are found above the $(0, 0)$ transition, at 21317(9) and 21209(9) cm^{-1} respectively, and correspond to the second and third intense excitation bands. They may thus be respectively attributed to the $(0, 2)$ and $(0, 1)$ (hot bands) transitions. The fourth luminescence peak, found at 21088(9) cm^{-1}, is associated to the first weak excitation band, and thus corresponds to a $(1, m)$ transition. Since its intensity is also weak in the luminescence spectrum, we may presume that the emitting KD is weakly statistically populated at 77 K, suggesting that $m = 1$.

The fifth luminescence peak, found at 21013(9) cm^{-1}, also corresponds to a weak excitation band and thus can be associated to a $(1, m)$ transition. The observed luminescence intensity being non negligible, we may postulate in that case that $m = 0$. Actually, knowing the position of the $(0, 0)$, $(0, 1)$ and $(1, 1)$, we could alread deduce the energy of the $(1, 0)$ luminescent transition:

$$E(1,1) - E(1,0) = E(0,1) - E(0,0) \tag{5.10}$$

which yields $E(1, 0) = 21025(27)$ cm^{-1}, in very good agreement with our assignment. Furthermore, one may note that in both the excitation and luminescence spectra this transition presents a shoulder around 20998(9) cm^{-1}, which very likely corresponds to a hot-band.

The sixth luminescence band, found at 20934(9) cm^{-1}, is associated to a rather strong intensity and very likely corresponds to a $(n, 0)$ transition, and we may state that $n = 2$ here. As one may note, we also retrieve an excitation band at this energy, which is rather unexpected: the $(2, 0)$ absorption band should indeed be very weak, as the third KD of ${}^6H_{15/2}$ should display a very small statistical population at 77 K. Here, this is most probably the very strong luminescence intensity that permits to observe such weak transitions.

At 20860(9) cm^{-1}, we find a shoulder in the luminescence spectrum, which very likely corresponds to a hot-band (thus, a $(n, 1)$ transition). We may thus presume it actually consists in the (3,1) excitation band, and that the following intense peak at 20807(9) cm^{-1} is the corresponding (3,0) transition. As one may note, the energy gap between these two bands (*ca.* 56 cm^{-1}) is very close to the one between the (0,1) and (0,0) transition (*ca.* 63 cm^{-1}), supporting this hypothesis.

The next four intense bands at 20751(8), 20614(8), 20542(8) and 20483(8) cm^{-1} are also very likely associated to $(n, 0)$ transitions, and we may attribute them to the (4,0), (5,0), (6,0) and (7,0) excitations respectively. As one may note, we furthermore observe a shoulder at 20670(8) cm^{-1} (on the second peak), which very likely corresponds to an additional hot-band. It is indeed found 56 cm^{-1} above the second transition, thus suggesting it may be the $(5, 1)$ transition.

We summarised the luminescence data in Table 5.9 and drew the energy diagram in Figure 5.2.8. As one may note, the energy splitting in the ground $^6H_{15/2}$ state is very marked, with a total energy span of 663(17) cm^{-1}. Furthermore, we also notice a strong energy splitting between the two first KD, which indicates **5.12** might be a good candidate for the observation of a SMM behaviour. As we will see in the following, it is indeed the case.

Table 5.9: Absolute and relative luminescence energies associated to the $^6H_{15/2} \rightarrow {}^4F_{9/2}$ transition of **5.12** at 77 K, measured under an irradiation at 350 nm. The relative values are calculated with respect to the (0,0) transition, and the values in bold font highlight the energy splitting in the ground state.

E (cm^{-1})	E_{rel} (cm^{-1})	Attribution
21317(9)	-171(18)	(0,2)
21209(9)	-63(18)	(0,1)
21146(9)	**0**	(0,0)
21088(9)	58(18)	(1,1)
21013(9)	**133(18)**	(1,0)
20986(9)	160(18)	(2,1)
20934(9)	**212(18)**	(2,0)
20863(9)	283(18)	(3,1)
20807(9)	**339(18)**	(3,0)
20751(8)	**395(17)**	(4,0)
20670(8)	476(17)	(5,1)
20614(8)	**532(17)**	(5,0)
20542(8)	**604(17)**	(6,0)
20483(8)	**663(17)**	(7,0)

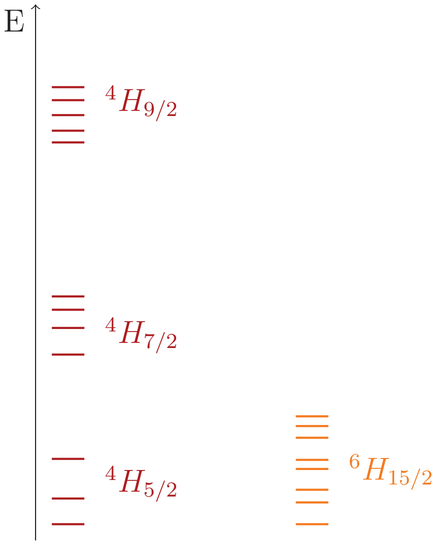

Figure 5.2.8: Detail of the relative energy diagrams of **5.9** and **5.12**, deduced from the 77 K spectra.

5.2.3 Static magnetic properties

We thus studied the magnetic properties of these complexes, and first focused on the static responses. The thermal dependence of the $\chi_m T$ product is presented on Figure 5.2.9. As one can remark, to the exception of the Gd(III) derivative we retrieve a thermal evolution for these complexes that is similar to the one we observed for the [LnTp$_2$NO$_3$] complexes, with a monotonous decrease with temperature.(xxvi) In the case of **5.10**, the $\chi_m T$ product is nearly constant between 300 K and 6 K – with a value of 7.63 cm^3.K.mol^{-1} –, and then presents an abrupt decrease between 6 K and 2 K, to a final value of 5.23 cm^3.K.mol^{-1}. These features are very classical of an isolated Gd(III) ion,[64] and suggests strongly that no significant intermolecular magnetic coupling is acting. As such, we may postulate the thermal variations of the $\chi_m T$ product for all these complexes are due to crystal field effects only.

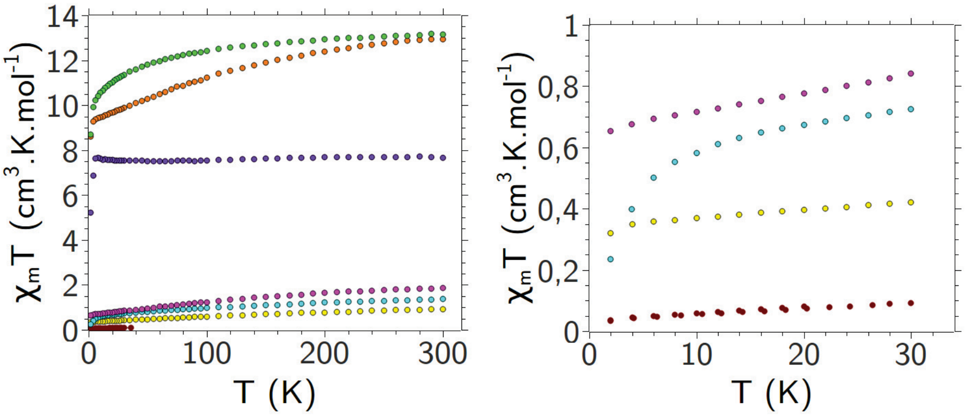

FIGURE 5.2.9: Left: $\chi_m T = f(T)$ curves for complexes **5.6** to **5.12**, measured under a static field of 0.2 T on powder samples. Right: focus on the low temperature-low susceptibility area. Colour scheme: **5.6**, yellow; **5.7**, cyan; **5.8**, pink; **5.9**, brown; **5.10**, violet; **5.11**, green; **5.12**, orange.

TABLE 5.10: Measured and expected $\chi_m T$ values at 300 K for complexes **5.6** to **5.12**, in cm^3.K.mol^{-1}. Note that, for the Sm(III) derivative, the 300 K was not accessible and thus the 30 K value is given instead.

Complex	$\chi_m T$ (300 K)	Free ion value
5.6	0.92	0.80
5.7	1.36	1.60
5.8	1.87	1.64
5.9	0.11 (30 K)	0.09
5.10	7.63	7.88
5.11	13.16	11.82
5.12	12.93	14.17

The observed room temperature values are in rather good agreement with the expected ones in the free ion model, as highlighted in Table 5.11. The discrepancies may here also be due to the inadequacy of the free ion model, since we know from the interpretation of the luminescence spectra of **5.9** and **5.12** that the crystal field splitting may be much larger than the thermal energy.

(xxvi)Note that, in the case of the Sm(III) derivative **5.9**, the paramagnetic moment is too low to be measured above 30 K.

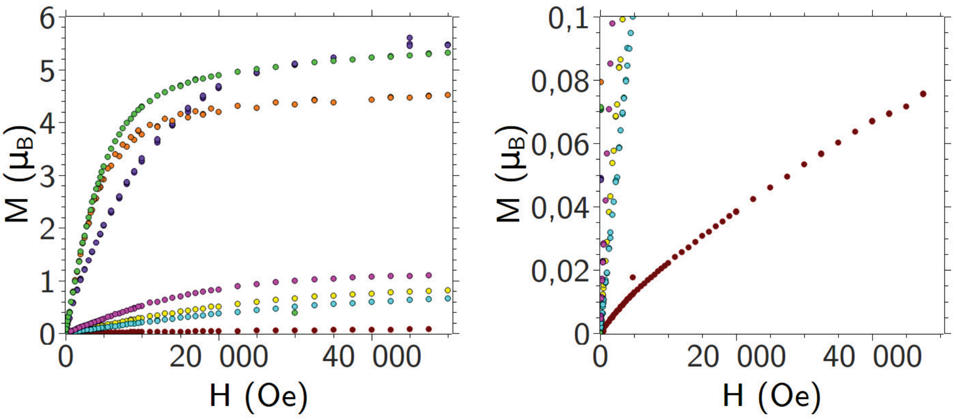

FIGURE 5.2.10: Left: magnetisation versus field curves for complexes **5.6** to **5.12**, measured at 2K on powder samples. Right: focus on the signal of **5.9**. Same colour scheme as Figure 5.2.9.

TABLE 5.11: Measured and expected (in the free ion model) magnetisation values at 2 K and 5 T for complexes **5.6** to **5.12**, in μ_B.

Complex	m	Free ion value
5.6	0.81	2.14
5.7	0.66	3.20
5.8	1.10	3.27
5.9	0.08	0.71
5.10	5.46	7.00
5.11	5.32	9.00
5.12	4.51	10.00

On Figure 5.2.10, we represent the field dependence of magnetisation at 2 K for complexes **5.7** to **5.12**. As one may notice, the Gd(III) derivative **5.10** does not seem to present a marked saturation of its magnetisation, as expected. It indeed usually behaves like an ideal and isotropic $S = 7/2$ spin, and thus presents a slow saturation of its magnetisation with field. The Sm(III) derivative **5.9** does also not present a clear saturation of its magnetisation, which is not surprising either. The fact that the $^4H_{7/2}$ excited state of Sm(III) is very close in energy to the ground $^4H_{5/2}$ state indeed often leads Sm(III) complexes to present an original magnetic behaviour compared to other lanthanide ions. Here, we know from the luminescence measurements that the lowest KD of the excited $^4H_{7/2}$ state of Sm(III) lies only 641(30) cm^{-1} above the highest KD of the ground $^4H_{5/2}$ state, an energy difference that is of the order of magnitude of the CF splitting in the ground state (403(31) cm^{-1}). Very high fields are then required in order to reach the saturation of magnetisation.

For the other complexes, magnetisation is nearly saturated at 5 T, and it is plain from Table 5.11 that the final values are far from the ideal ones. As we previously said, this is the likely sign of magnetic anisotropy, and since we saw that the CF splitting may be quite large for these complexes – at least, we now this is the case of the Sm(III) and Dy(III) derivative – they may present a slow relaxation of magnetisation at low temperature.

5.2.4 AC magnetic properties

We thus studied the susceptibility dynamics of all these complexes, to the exception of the Gd(III) derivative. Indeed, as we formerly said Gd(III) is not expected to present any single-ion anisotropy because of its zero orbital momentum. As such, we would not expect **5.10** to present any SMM behaviour.

Complex 5.6, [CeTp$_2$Acac]. In the case of the Ce(III) derivative **5.6**, we did not observe any out-of-phase signal in the absence of a static magnetic field, neither did we observe any modification of the in-phase signal. Hence, **5.6** does not display any genuine SMM behaviour. We may presume this is, once again, the consequence of a strong QTM. However, if we turn a static field on, a lag in the magnetic response starts to appear. Noteworthy, this complex is, to our best knowledge, the second mononuclear Ce(III) complex to present such a property, and only three other Ce(III)-based SMMs or field-induced SMM were reported so far in the literature.[216–218]

We present on Figure 5.2.11 the $\chi''_m = f(T;\nu)$ curves measured under a static field of 500 Oe. We retrieve the same kind of aspect as what we observed for the [LnTp$_2$NO$_3$] complexes, though striking differences are seen. First of all, the signal over noise ratio is much lower here than previously. This is the consequence of the overall weaker magnetism of complex **5.6**, as evidence by the low values of susceptibility (maximum around 0.04 cm^3.mol^{-1} for the out-of-phase component). Additional measurements are called, but unfortunately[(xxvii)] the magnetometer also broke down, delaying these measurements until further notice.

Second, we may also notice that the high frequency curves display an interesting characteristic at low temperature: χ''_m does not decrease to zero, but rather seems to saturate at a positive value. Usually, this is associated to a remnant QTM effect,[219] which would here not be completely suppressed at 500 Oe.

The dynamics of magnetisation of **5.6** may thus, at least at low temperature, be partially controlled by QTM. At higher temperatures, other phenomena are likely involved, and the temperature-frequency dependence of the maxima of the $\chi''_m = f(T;\nu)$ curves may yield valuable information. We represent on the right side of Figure 5.2.11 the $\nu = f(T)$ curves for **5.6**, in a log-log scale. It is plain from this Figure that there is an almost linear dependency of $ln\ \nu$ with respect to $ln\ T$, which would be in good agreement with either direct or Raman mechanisms. A marked deviation from linearity in the corresponding Arrhenius plot furthermore suggests that barrierless mechanisms may be acting (see Appendix D.2.1).

We thus tried to fit the $\nu = f(T)$ data using these different mechanisms, in a stepwise approach. First, we used the higher temperature points in the Arrhenius plot $ln\ \nu = f(1/T)$ in order to determine the eventual energy barrier, using a linear fitting. This yielded $\Delta E = 33(2)$ K. Then, we tried to fit the $ln\ \nu = f(ln\ T)$ curves using a linear approach too, in order to determine the eventual Raman exponent n. Letting n be a real number, we obtain $n = 6.7(2)$, thus suggesting a T^7 Raman mechanism should be involved. Then, we tried to fit the whole data set using a combination of this T^7 Raman mechanism, an Orbach relaxation with $\Delta E = 33$ K (fixed, thus we will not obtain an error bar on this parameter), a direct relaxation mechanism (cT) and a remnant QTM contribution (d):

$$\nu = aT^7 + \nu_0\ \exp\left(-\frac{\Delta E}{k_B T}\right) + cT + d. \tag{5.11}$$

As a result of this fitting procedure, we obtain

$$\nu = 0.9(1) \times 10^{-2}\ T^7 + 0.8(1) \times 10^6\ \exp\left(-\frac{33}{T}\right) + 13(2), \tag{5.12}$$

[(xxvii)] Well, we may definitively say we are quite unlucky with machines...

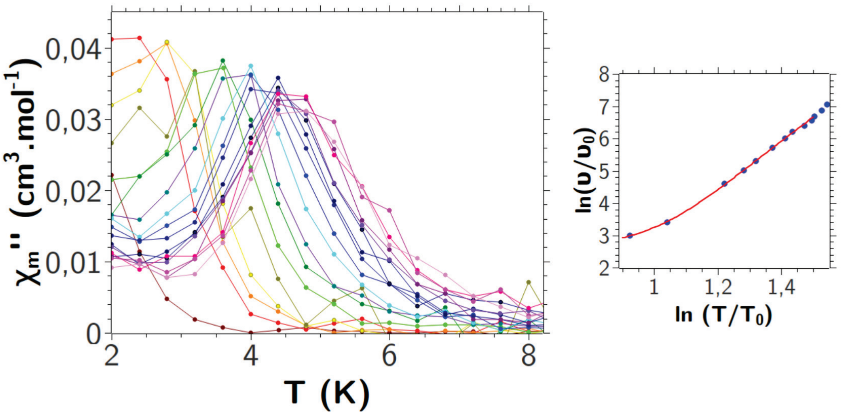

FIGURE 5.2.11: Left: $\chi''_m = f(T;\nu)$ curves for complex **5.6**, under a static field of 500 Oe and for frequencies ranging from 1 Hz (brown) to 1200 Hz (pink). Right: frequency versus temperature plots for the maxima of the $\chi''_m = f(T;\nu)$ curves, in log-log scale. The solid red line corresponds to the best fit.

and we can see from Figure 5.2.11 that the agreement with the experimental data is very good.(xxviii) Noteworthy, no direct contribution seems to be involved here.

Furthermore, we find here a T^7 Raman contribution, which is a very interesting result. Indeed, we already observed such a Raman mechanism in the case of [DyTp$_2$NO$_3$], whose structure is akin to the one of **5.6**. In this latter case, the predominance of this T^7 mechanism could be linked to the quasi-null mixing in the ground KD (leading to a negligible Kramers conjugation with any other state in the energy diagram), which itself may be related to the adequacy of the ligand field with respect to the $4f$ electron density deformation in this KD. We thus retrieved the same line of arguments as in Rinehart and Long's model, but applied to the Raman mechanisms.

Here, since **5.6** and **5.1** have similar structures, we may presume their ligand fields would show a certain extent of similarity. Moreover, we also know that Dy(III) and Ce(III) ions are expected to present similar magnetic properties in the framework of Rinehart and Long's model(xxix). Thus, using our findings on **5.1** we could already propose that, provided that the magnetisation dynamics of **5.6** occurs – at least partially – *via* a Raman mechanism, this latter would present the observed T^7 temperature dependence.

It thus seems that Rinehart and Long's model, which was initially formulated to rationalise energy-barrier dependent dynamics of magnetisation, can be extended to the rationalisation of Raman relaxation mechanisms. Nevertheless, we do not know the generality of such findings: can this extended model be applied on any complex, or is it only working here because of the specificities of our complexes? The answer to such a question requires a huge work, but we may already try to see if this model applies on the other [LnTp$_2$Acac] complexes.

Complex 5.7, [PrTp$_2$Acac]. In the case of complex **5.7**, no out-of-phase signal is seen in the absence or presence of a static field. Furthermore, the in-phase susceptibility does not either present any frequency dependence, thus suggesting that **5.7** does not present any SMM or field-induced SMM behaviour. This is maybe not surprising: Pr(III) is indeed a non-Kramers ion, as is Ho(III). As such, it may not present a two-fold degenerate ground state, which is a necessary requirement for the observation of a SMM behaviour. Actually,

---

(xxviii) Unfortunately, due do the low signal over noise ratio, we cannot exploit the $\chi''_m = f(\chi'_m)$ (Cole-Cole) plots in order to add a supplementary confirmation. Complementary measurements are thus truly needed here.

(xxix) They indeed present an oblate deformation of their electron density in the $M_J = \pm J$ KD.

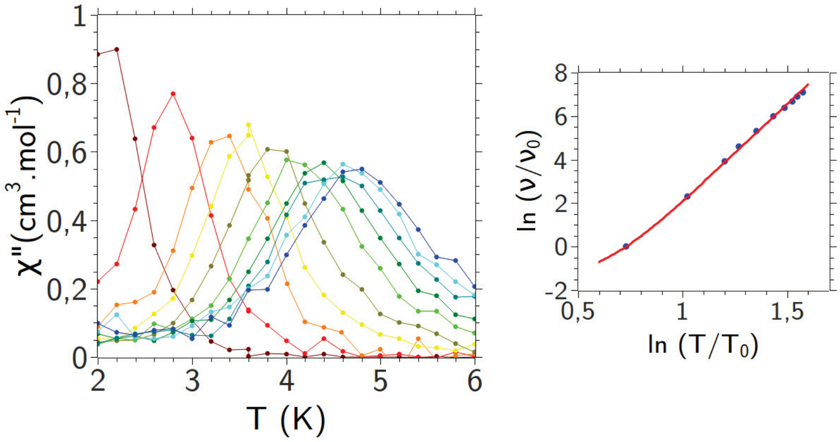

FIGURE 5.2.12: Left: $\chi''_m = f(T;\nu)$ curves for complex **5.8**, under a static field of 2000 Oe and for frequencies ranging from 1 Hz (brown) to 1200 Hz (blue). Right: frequency versus temperature plots for the maxima of the $\chi''_m = f(T;\nu)$ curves, in log-log scale. The solid red line corresponds to the best fit.

if we look more carefully to the static magnetic properties, we can notice a drop in the $\chi_m T$ product at very low temperature, similar to what we observed in the case of the Ho(III) complex **5.2**. Most probably, **5.7** presents a non magnetic state low lying state, which leads to a very fast magnetic relaxation at low temperature.

Complex 5.8, [NdTp$_2$Acac]. In the case of **5.8**, we also observe a non-zero out-of-phase signal under an applied static field. Noteworthy, only three other Nd(III) based SMM or field-induced SMM were reported up to date, and they are all polynuclear complexes.[217,220,221] Complex **5.8** is thus, as **5.6**, a rather original and unusual compound.
Here, we first set the field at 2000 Oe, which yielded us the curves represented on Figure 5.2.12.(xxx) As one can see, we retrieve the same kind of aspect as previously for the out-of-phase component, with two noticeable facts. First, the signal over noise ratio is much better here, because of the much larger magnetic moment of **5.8**. Furthermore, we can also remark that χ''_m tends to zero at low temperature for the highest frequencies, thus suggesting any remnant QTM process can be safely neglected here. Actually, this is not much surprising, since the applied field is rather high (and we know QTM is strongly decreasing with magnetic field).
On the other hand, the $ln\ \nu = f(ln\ T)$ plot on the right side of Figure 5.2.12 strongly suggests Raman or direct mechanisms are involved in the dynamics of magnetisation of **5.8**, since a marked linearity is observed. Deviations from linearity in the Arrhenius ($ln\ \nu = f(1/T)$) plot are furthermore seen, which supports the action of barrierless processes. We thus unfold the same procedure as for complex **5.6**: first, we tried to fit the high temperature points of the Arrhenius plot using a linear function, which yields an apparent energy barrier of 35.0(5) K. Then, we also performed a linear fitting on the $ln\ \nu = f(ln\ T)$ curve, which yields a slope of around 8.50(8), hence suggesting a T^9 Raman mechanism should be involved here.
Then, we tried to fit either the $ln\ \nu = f(ln\ T)$ and $ln\ \nu = f(1/T)$ curves using

$$\nu = \nu_0 \exp\left(-\frac{35.0}{T}\right) + aT^9 + bT \tag{5.13}$$

(xxx) We planned measurements at different static fields, and also at zero field, but the SQUID broke down before we could perform them...

(with a fixed energy barrier). In this case, the fitting procedure proved quite tricky, and we had to try several starting sets of parameters to find a good agreement with both curves. Eventually, we obtained:

$$\nu = 9,5(3) \times 10^{-4}\ T^9 + 0.16(4)T. \tag{5.14}$$

As one can see, we do not retrieve an Arrhenius contribution in this case, as what was observed for the [$LnTp_2NO_3$] complexes. Nevertheless, we observe a two-process magnetisation dynamics, which agrees qualitatively well with the shape of the Cole-Cole $\chi''_m = f(\chi'_m)$ curves in Appendix D.2.2. We indeed retrieve a semi-circular shape, and the quality of the data at higher temperature allows to fit the curves with a Cole-Cole equation, with α ranging from 0.03(2) at 4 K to 0.14(2) at 3.2 K. These values are in the range of those we obtained for the [$LnTp_2NO_3$], and meet our expectations: at higher temperatures, the T^9 Raman relaxation dominates, leading α to tend to zero, while at lower temperature both phenomena are active and thus the range of relaxation rates is larger (hence α is greater).

Interestingly, the temperature dependence of the Raman relaxation (T^9) implies the magnetic relaxation occurs within two states that are conjugated by Kramers theorem. As such, as previously we may presume this is due to a marked mixing in the different KD of the ground $^4I_{9/2}$ state of Nd(III), and noteworthy in the states that are involved in the relaxation of magnetisation. Such an extended mixing implies the ligand field in **5.8** does not suit any of the pure M_J substates perfectly, in contrast to what we deduced for **5.6**. This can actually be once again understood in the framework of Rinehart and Long's model. Indeed, if we consider the $4f$ electron density distortions in the different M_J substates of Ce(III) and Nd(III) (as evaluated for perfectly isolated ions), we can notice a marked difference between these two ions. In the case of Ce(III), the $4f$ electron density is markedly prolate when $M_J = \pm 1/2$, and becomes markedly oblate when $M_J = \pm 5/2$ ($M_J = \pm 3/2$ being an intermediate case). If we presume the ligand field in **5.6** will suit oblate $4f$ electron density deformations, we could then expect the ground KD to be a nearly pure $| \pm 5/2\rangle$ state.

In the case of Nd(III), in all the M_J substates the $4f$ electron density deformation is intermediate between prolate and oblate. Since the ligand field for this complex should be same as the one of **5.6**, it is not expected to be adequate for any of these substates, and in turn we expect to observe a high degree of mixing in every KD, which should lead an eventual Raman process to display a T^9 temperature dependence, as observed.

Complex 5.9, [$SmTp_2Acac$]. We then turned to complex **5.9**, which despite its weak magnetism may be an interesting – if not exotic – compound to study. Indeed, a literature survey revealed only one Sm(III)-based SMM has been reported so far, and it appears this compound is a polynuclear Mn(III)-Sm(III) complex, whose SMM behaviour may not be exclusively due to the lanthanide cation.SmSMM

In zero field, a frequency dependence of the in-phase susceptibility can be evidenced, as shown on Figure 5.2.13. Here, we focused only on a limited temperature and frequency range, because of the very low magnetic moment of the sample (below 10^{-8} emu, which is near the sensitivity limit of a MPMS Squid). We indeed had to perform long measurements (averaging over 5 values, long collection), and despite these drastic conditions we could not measure any significant out-of-phase signal. Nonetheless, complex **5.9** is very likely a SMM, and we would need additional measurements on a high-sensitivity magnetometer in order to confirm this.

Noteworthy, the application of a static magnetic field (of 500 Oe) in this case seems to deteriorate the signal. Most probably, this comes from the fact that a part of the in-

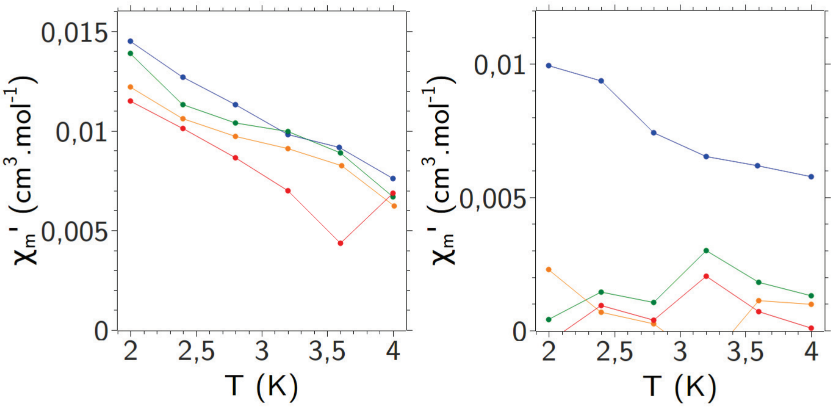

Figure 5.2.13: $\chi''_m = f(T; \nu)$ curves for complex **5.9**, under a static field of 0 Oe (left) and 2000 Oe (right), measured at 1 Hz (blue), 200 Hz (green), 600 Hz (orange) and 1200 Hz (red).

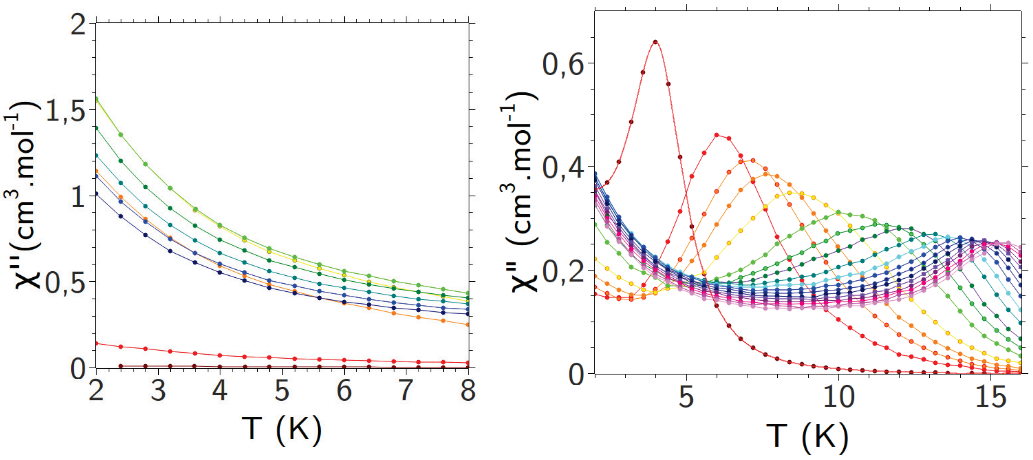

Figure 5.2.14: $\chi''_m = f(T; \nu)$ curves for complex **5.12**, under a static field of 0 Oe (left) and 500 Oe (right), for frequencies ranging from 1 Hz (brown) to 1200 Hz (pink).

phase signal moves to the out-of-phase component, thanks to the suppression of QTM, and as such the in-phase component becomes smaller – thus harder to measure – while the out-of-phase component remains too small to be characterised...

Complex 5.11, [TbTp$_2$Acac]. In the case of complex **5.11**, no out-of-phase component is observed either under a zero or 2000 Oe dc field. Furthermore, no frequency dependence of the in-phase susceptibility can be evidenced, thus suggesting **5.11** does not present a SMM or field-induced SMM behaviour. This may not be surprising since Tb(III) is, as Pr(III) or Ho(III), a non Kramers ion, thus expected to display a completely different magnetism with respect to Kramers ions.

Complex 5.12, [DyTp$_2$Acac]. Finally, we also studied the AC response of **5.12**, both under a static field and in zero field. We represent the result of these measurements on Figure 5.2.14.
It is plain to see that a frequency dependent out-of-phase signal is measured in both cases, thus suggesting **5.12** behaves as a genuine SMM. The zero field curves do not display any visible maximum, which we assume to be lying below 2 K. Interestingly, we can notice that the frequency dependence of these curves is not monotonous: at constant temperature, between 1 Hz and 400 Hz the χ''_m values are increasing, and above 400 Hz they start to

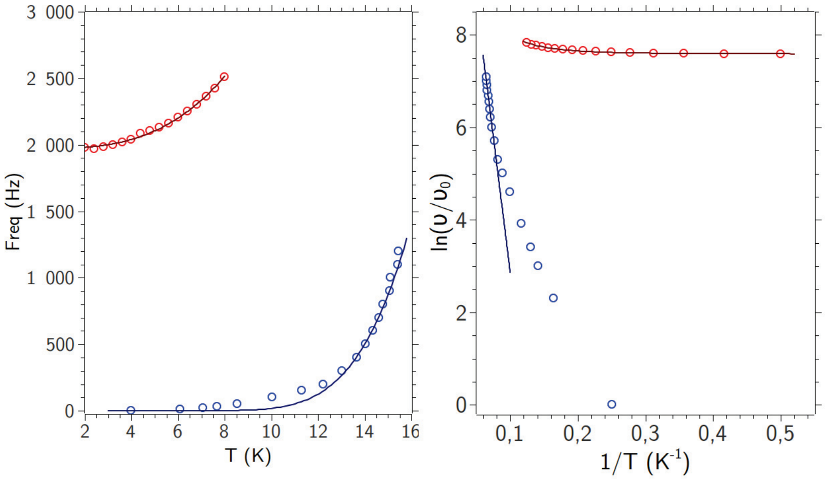

FIGURE 5.2.15: Frequency/temperature curves for the relaxation of magnetisation of complex **5.12**, measured under a zero (red) and 500 Oe (blue) dc field. Right panel: Arrhenius (log-reciprocal) representation. Solid lines correspond to the best fits (see the text for more details).

decrease – to reach, at 1200 Hz, values that are close to those measured at 100 Hz. Obviously, here we cannot employ the same methodology as previously to analyse the dynamics of magnetisation$^{\text{(xxxi)}}$. Fortunately, an analytical expression exists for the out-of-phase component, at constant temperature, as a function of the frequency of the field (ν) and the relaxation time (τ):[222]

$$\chi''_m = (\chi_T - \chi_S)\,\frac{(2\pi\nu\tau)^{1-\alpha}\cos(\pi\alpha/2)}{1 + 2(2\pi\nu\tau)^{1-\alpha}\sin(\pi\alpha/2) + (2\pi\nu\tau)^{2-2\alpha}} \tag{5.15}$$

where χ_T is the limit value of susceptibility for $\nu \to 0$, χ_S the limit value for $\nu \to +\infty$, and α the Cole-Cole distortion parameter. Using this equation to fit the $\chi''_m = f(\nu)$ curves for all the temperatures thus permitted us to obtain the rate/temperature data for **5.12** at 0 Oe, which we represent on Figure 5.2.15.

Expectedly, the corresponding frequencies are high (above 2000 Hz), thus explaining why we were not able to observe any maximum. We can also notice on the Arrhenius plot a clear saturation of the relaxation rate at low temperature, in good agreement with the expected prevalence of QTM. Interestingly, QTM does not seem to be the only active mechanism in this regime, since a clear temperature dependence is seen. Additional support comes from the α values, which range between 0.13(4) at 2 K and 0.11(2) at 8 K, thus suggesting a (narrow) distribution of relaxation rates is present. The Cole-Cole plots seem to confirm this, the curves showing in all cases a rather semi-circular shape (see Appendix D.2.2).

We then tried to model the dynamics of magnetisation using a combination of QTM, Raman and Arrhenius mechanisms, using the same approach as previously.

Linear fitting of the high temperature region of the Arrhenius plots yielded an apparent energy barrier of 4.3(6) K. This value does not correspond at all to the energy spectrum we deduced from luminescence, and bears little meaning, thus suggesting no Arrhenius contribution is actually involved here. On the other hand, no linearity is seen is the $ln\ \nu = f(ln\ T)$ plot, which does not permit us to propose any n value for an eventual Raman contribution. From Figure 5.2.15, it appears that the temperature dependence of

---

(xxxi) It is indeed rather difficult to analyse the temperature/frequency dependence of maxima that do not exist...

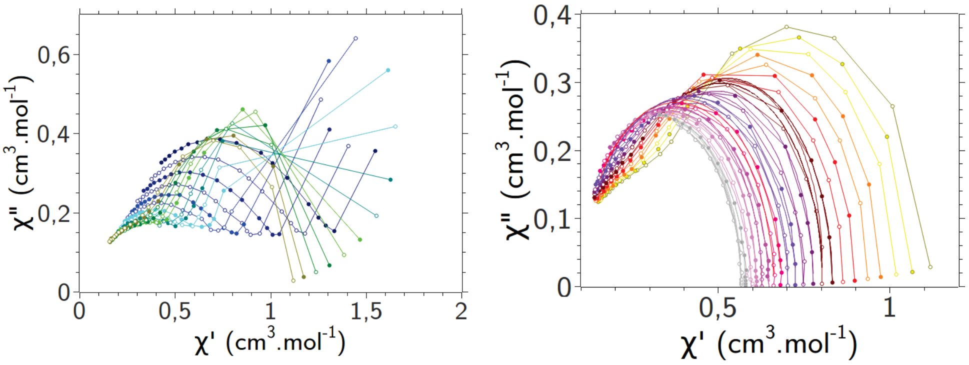

FIGURE 5.2.16: Cole-Cole plots for **5.12**, measured under a static field of 500 Oe, between 2 K (dark blue) and 16 K (gray). For the sake of clarity, the low ($T < 8K$) and high ($T > 8K$) temperature plots were separated. Solid lines in the high temperature plots correspond to the best fits.

the relaxation rate is slow, suggesting a low n value. Fitting of the data with

$$\nu = \nu_0 + aT^n + bT \tag{5.16}$$

setting n as a real parameter yields $n = 2.7(1)$. This very low value is quite surprising. Indeed, as we have seen previously, Raman processes usually display a T^9 or T^7 temperature dependence, with some accounts of T^5 dynamics when the phonon energy is much larger than the energy difference between the magnetic states.[81] A T^3 Raman dynamics is thus rather unexpected, but it is generally assumed that n values between 1 and 6 are acceptable, and may reflect deviations from the Debye phonon model.[223] Here, fixing $n = 3$ leads to a rather nice reproduction of the experimental data, and we finally obtain a QTM frequency of 1972(4) Hz.

If now we consider the 500 Oe data, the dynamics of magnetisation is even more interesting. First, as one may see from Figure 5.2.14, the temperature range in which the AC signal is observed is much larger than previously, with an out-of-phase response up to 16 K. Furthermore, several mechanisms are likely involved here, since at high frequencies a marked increase of χ''_m is seen at low temperatures, in addition to the maxima at higher temperatures. This becomes plain if we look at the Cole-Cole plots, depicted on Figure 5.2.16. At low temperature, we indeed retrieve a semi-circular shape, plus additional points at the lowest frequencies (right side of curves), as we observed for [DyTp$_2$NO$_3$]. As temperature increases, the semi-circles get buried and the "tail" points shift to the left, seemingly forming a new semi-circle. This becomes more obvious above 8 K, where the first semi-circles are completely suppressed, while the second fully develop.[219]

We thus seem to observe a transition between a low temperature process (or mixture of processes) and a high temperature one. This becomes more obvious on Figure 5.2.17, where we represent explicitly the temperature dependence of the Cole-Cole plots. We indeed observe a first relaxation process at very low temperatures and high frequencies, which is progressively replaced by a second relaxation process, that is much slower (lower frequency) at low temperature. In three dimensions (T, χ'_m, χ''_m), this results in a "mountain" landscape, the summits being associated with these two processes.

Quite likely, the low temperature process is – at least partially – driven by a remnant QTM. We indeed remind that QTM in zero field was found to be rather strong (1908 Hz), and if we assume – as was observed for other mononuclear Dy(III) SMM – that the QTM rate of relaxation varies as $\nu_{0Oe}/(1 + bH^2)$ with $b \sim 10^{-5}$ Oe^{-2}, then at 500 Oe the remnant QTM should still be non negligible (around 1500 Hz).[191,203]

On the other hand, the high temperature process may be driven by Arrhenius, Raman or direct processes. Nevertheless, fitting of the $\nu = f(T)$ curves in the whole temperature

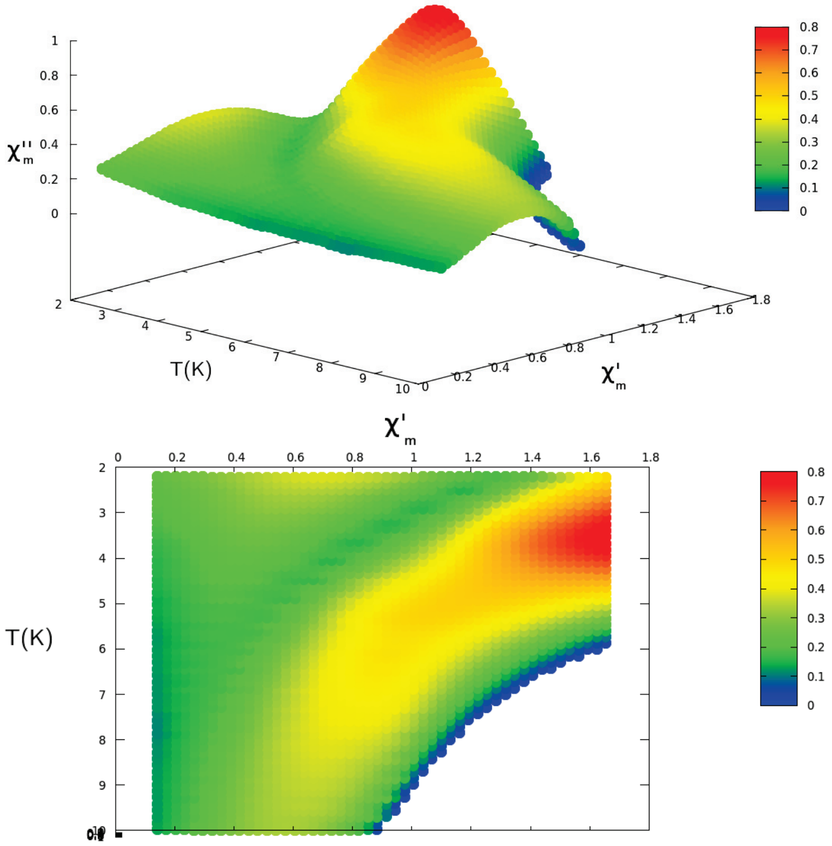

FIGURE 5.2.17: Top: 3D plot of the temperature dependence of the Cole-Cole curves for **5.12**, measured under a static field of 500 Oe. Bottom: corresponding top view. High values of χ''_m are depicted in red, intermediate values in yellow, and low values in blue.

range case may be a quite complicated task, because of the admixture of relaxation mechanisms. We may still try to focus on the highest temperature region (13.2 K to 16.0 K), where the Cole-Cole plots seem to present little to no distortion, suggesting the first mechanism is definitively turned off.

Fitting of the Cole-Cole plots proves possible in that temperature region, and the corresponding α values range, respectively, between 0.05(2) to 0.01(1). First of all, the possibility to fit the data confirms the admixture of the low and high temperature regimes is not encountered any more. Furthermore, the low α values point to a unique relaxation process in this temperature region.

$ln\ \nu = f(1/T)$ and $ln\ \nu = f(ln\ T)$ plots both present a marked linearity in this temperature range. In the first case, we obtain an energy barrier of 117(5) K, whereas in the second case we obtain a slope of $n = 8.8(3)$, thus implying a T^9 Raman mechanism could be active in that case. Interestingly, the deduced energy barrier does not match exactly the one we obtained using luminescence (87(5) cm^{-1}, to be compared to the expected 133(18) cm^{-1}). We may thus consider that the high temperature regime is principally driven by T^9 Raman mechanism, though we cannot unambiguously opt for one mechanism or the other basing solely on experimental evidences...

5.2.5 Ab initio modelling

In order to clarify this, we thus tried to unfold the same computational methodology as for the [LnTp$_2$NO$_3$] complexes, *i.e.* SA-CASSCF+RASSI-SO calculations with nine electrons spanning the seven $4f$ orbitals of Dy(III). We employed the same ANO basis sets and contractions, and used the same number of roots (21 sextets, 224 quartets and 300 doublets) in the RASSI-SO calculation.

However, in that case the reproduction of the magnetic properties is rather poor, and we do not retrieve the same crystal field splitting of the ground $^6H_{15/2}$ state of Dy(III). Actually, we did not manage either to reproduce the magnetic properties of **5.8** and **5.9**, as exemplified on Figure 5.2.18. It thus seems that our approach, though quite standard, fails to correctly reproduce the physical behaviour of these [LnTp$_2$Acac] complexes. For the moment, we do not know the exact reason of these difficulties, but they seem quite systematic over the family, and might be related to the specificity of the [LnTp$_2$Acac] complexes.

We discussed this problem with Dr. B. Le Guennic, and we are currently performing a series of calculations in order to identify the cause of these problems. Possibly, this is related to the definition of the active space. In our calculations, the only degrees of freedom are indeed the occupations (and composition) of the $4f$ orbitals, assuming that the ligands can be efficiently represented by a unique set of orbitals and occupations in all the CASSCF states we are computing. This may actually not be a good approximation, as the electronic structure of our ligands may vary from one state to another, in order to stabilise the different CASSCF roots. Here, we may presume that Acac will tend to present this kind of behaviour, as it is a rather polarisable ligand (with an extended π-conjugated system). As such, we should include some ligands orbitals in our active space (both occupied and virtual) in order to permit such polarisation effects. These calculations are currently performed.

5.2.6 Long story short

In short, basing on the interesting properties of the [LnTp$_2$NO$_3$] complexes, we synthesised and studied a similar family of lanthanide complexes, [LnTp$_2$Acac]. Though virtually

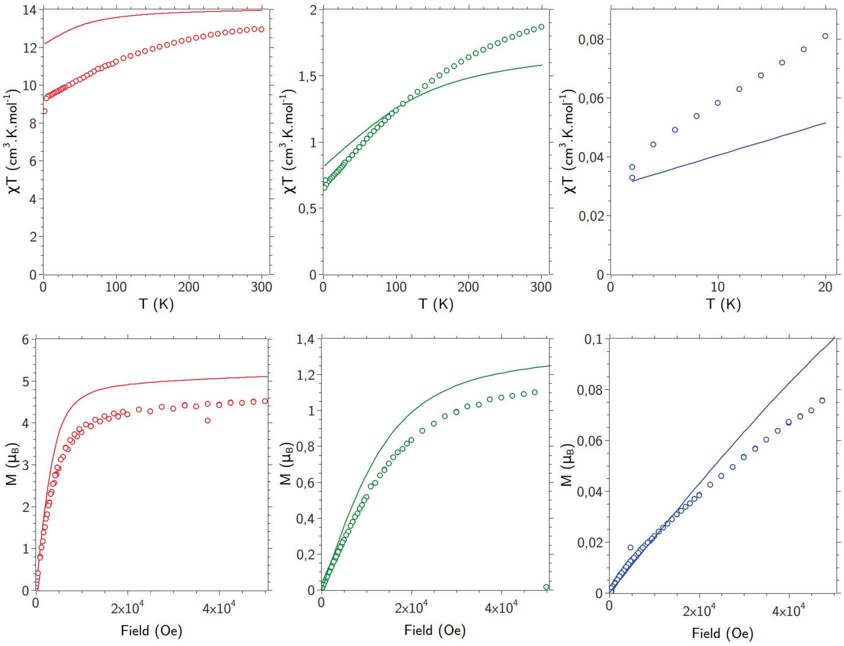

FIGURE 5.2.18: Comparison between the experimental (bullet points) and computed (solid lines) magnetic properties of **5.12** (left, red curves), **5.8** (middle, green curves) and **5.9** (right, blue curves).

any Ln(III) ion can be used to obtain these complexes, we observed a non negligible polymorphism for the heavier ones, which forced us to restrict the study to the lighter lanthanides (Ce - Dy). To the exception of the Ce(III) and Gd(III) derivatives, these complexes present moderate to strong luminescence upon excitation at 300 nm, in the near IR range – Nd(III) derivative **5.8** – or in the visible range. In the case of the Sm(III) **5.9** and Dy(III) **5.12** derivatives, a very high resolution can be obtained on the $4f \rightarrow 4f$ transitions, allowing to draw their energy diagrams in the ground state on an experimental basis. Note that one often has to use deconvolution procedure to achieve this, which is not the case here.

From the viewpoint of magnetism, these complexes proved also very interesting. In the case of the Ce(III) and Nd(III) derivatives, we were indeed able to evidence a field-induced SMM behaviour, which up to date was only reported once for mononuclear complexes based on these lanthanide ions. More interestingly, we could tentatively rationalise the observed temperature dependence of the relaxation rate using the same line of arguments as in Rinehart and Long's model. In the case of the Ce(III) complex, the slow relaxation is indeed partially piloted by a T^7 Raman relaxation, as was also observed for [DyTp$_2$NO$_3$]. In that latter case, we could show this T^7 process stemmed from the adequacy of the ligand field towards the oblate electron density deformation in the ground $M_J = \pm 15/2$ KD. In the case of Ce(III), the $M_J = \pm 5/2$ KD also presents a similar oblate deformation of the $4f$ electron density, and since the [LnTp$_2$Acac] and [LnTp$_2$NO$_3$] structures are rather alike, we may expect the same line of argument to hold. In the case of Nd(III) on the other hand, a T^9 dynamics is observed, consistent with the fact that no M_J substate presents a clear oblate deformation of the $4f$ electron density (no M_J is specifically strongly stabilised, and large extents of mixing can be expected).

We also seem to observe a slow relaxation in the case of the Sm(III) derivative, even in the absence of a static magnetic field. However, in this latter case the signal is too low to draw any conclusion, and we would need to measure the AC response of this sample again. In the case of the Dy(III) derivative, a genuine SMM behaviour is observed. In zero field, the slow relaxation is piloted by a fast QTM, in addition to a phonon-bottleneck limited direct process. Turning on a static field drastically changes the AC response, two regimes of relaxation being evidenced. The first regime is observed at very low temperatures, and most presumably corresponds to the zero-field processes. The second regime is observed at much higher temperatures, and its nature is less clear. A strong temperature dependence is indeed observed, originating from a single process that can be analysed as stemming either from an Arrhenius or Raman (T^9) mechanism. Using the same line of argument as previously, we might suppose the dynamics of magnetisation is actually piloted by the Arrhenius mechanism, since we would rather expect a T^7 Raman contribution. Nevertheless, a non negligible mismatch is observed between the deduced energy barriers from luminescence spectroscopy and fitting of the magnetic data, and we thus strongly need the support of theoretical calculations.

5.3 Conclusion

In this section, we showed how a combination of experimental – magnetism, luminescence, X-ray diffraction – and theoretical studies allowed to rationalise the physical properties of two related series of lanthanide coordination complexes, [LnTp$_2$NO$_3$] and [LnTp$_2$Acac]. In both cases, field-induced or genuine SMM behaviours could be evidenced, even though quite unexpected in the framework of Rinehart and Long's model, since they involve lanthanide ions with very different $4f$ electron density deformations in their KD. We could show that, as already reported, these unexpected slow magnetisation dynamics are the consequence of the presence of barrierless relaxation processes, noticeably Raman and direct mechanisms, which were not considered in the former model.

Nevertheless, our findings seem to suggest one of these mechanisms – the Raman relaxation – could be rationalised using a similar line of argument as in this model. More explicitly, a T^9 Raman dynamics could be expected when the ligand field is not well adapted to the $4f$ electron density deformation in any $\pm M_J$ substate, because this induces a strong mixing in all the possible KD – thus all relaxation pathways connect Kramers conjugated states. On the other hand, if the ligand field is adapted to the $4f$ electron density deformation in one of the $\pm M_J$ substate – ideally, the $M_J = \pm J$ one, as it leads to the highest magnetic moment – we may expect a T^7 Raman dynamics, since the ground KD will be a pure M_J substate.

Of course, we would need to complete this study in order to confirm or infirm this hypothesis. Further theoretical modelling of the [LnTp$_2$Acac] complexes is planned in the close future, as well as complementary measurements(xxxii). We would also need to study supplementary complexes, in order to accumulate evidence for (or against) our model. Here, we may use the high tunability of the acetylacetone ligand. We could indeed employ different β-diketonate ligands in order to enlarge the family of [LnTp$_2$L] complexes, with L a bis-oxygenated ligand. Actually, a first attempt of synthesis involving 1,5-diphenylacetylacetone proved successful, thus comforting us in this approach.

(xxxii) Though we principally wait for the apparatuses to be fixed, which may take some times unfortunately...

General conclusion

Throughout this thesis, our work focused on the description and rationalisation of the properties of coordination complexes, by combining experiments and quantum calculations, with the underlying goal of installing a fruitful dialogue between both approaches.

To do so, we first employed tools from the framework of conceptual Density Functional Theory in order to rationalise the coordination properties of ligands, thus revisiting the ligand field theories in the words of Parr and Pearson (*i.e.* philicities and chemical hardness). The success of this first survey led us to study the *trans* effects in octahedral complexes within the same framework. With a very simple theoretical model, we managed to characterise and rationalise these effects using a very similar line of arguments. Briefly speaking, we could show that *trans* effect is simply the translation of a reduction in the electrophilicity of the *trans* position, which itself very likely originates from the ability of certain ligands to efficiently donate their electron density to the metal cation. A rule of thumb thus appeared, in good agreement with experiment: the more donor, the more *trans*-orienting. More interestingly, using a real space partition of the Dual Descriptor, we could quantify this electrophilicity modulation and, for the first time, contemplate the possibility to build a purely theoretical scale of the *trans*-orienting ligands. Though only semi-quantitative, as a consequence of the different approximations lying within our theoretical approach, this scale proved nevertheless to correlate nicely with experimental data.

We then turned ourselves to the syntheses and characterisation of transition metal complexes of amino-acids based Schiff base analogues. Though syntheses of the ligands proved very simple, isolation of the corresponding complexes was very challenging, and for all transition metal ions we used but Cu(II), was impossible. In that latter case, only two trinuclear complexes and two 1D coordination polymers could be isolated, and in all cases side compounds were found, suggesting hydrolysis took place.
To explain this, resorting to both experimental and computational studies proved very valuable. This indeed allowed to determine the solution structure of the free ligands and their Cu(II) complexes, which in turn allowed to initiate a survey of the reactivity of the latter towards water. To do so, we employed a two-steps approach: first finding the reaction mechanism at a relatively low level of theory (in this case, B3LYP plus double-zeta basis sets and pseudopotentials on Cu), and use this first path as an input for a higher level calculation (ωB97xD, triple zeta basis sets with diffuse and polarisation functions, and pseudopotentials on Cu). At the lower level, we managed to find a reaction mechanism that indeed leads to the formation of the starting amino-acid and acetylacetone moieties, but its first step is too energetically expensive to take place. At the higher level of theory, this first step decomposes into two elementary processes, with much lower energy barriers, thus rendering the process rather feasible. Nevertheless, we did not manage yet to retrieve the full reaction path at the higher level of theory – after nearly two years of work –, and

more calculations are called in order to confirm our results. It could also be interesting to perform the same kind of survey for the other transition metal cations we employed.
We also studied the magnetic properties of the four aforementioned crystalline compounds. In the case of the coordination polymers, a strong antiferromagnetism is seen, whereas in the case of the trinuclear complexes a weak antiferromagnetic coupling is observed. Because of the triangular geometry of these complexes, we wondered whether this antiferromagnetic coupling would result in a frustrated magnetism or, as was already observed in the case of the glycine-based analogue, in a much more exotic situation with quasi degenerate quartet and doublet states. We thus tried to model these complexes using very high level *ab initio* calculations. In agreement with what was observed in the case of the glycine derivative, only the highest level calculations seem to properly model our system. At the SA-CASSCF or DCCI-1 level of theory, a total ferromagnetic picture is indeed obtained, and a tendency towards antiferromagnetism is only observed at the NEVPT2 level – the DDCI-2 and DDCI-3 approaches being out of reach because of the size of our system. Interestingly, in agreement with Malrieu's conclusion we seem to tend to a more accurate description by a systematic enlargement of the active space in the NEVPT2 calculations, and using the outcome from our first study we proposed a rational way to perform these enlargements. Unfortunately, convergence becomes more and more problematic as the active space size increases, but we have good hope that this approach will eventually succeed.

In a third time, we turned ourselves to lanthanide-based mononuclear Single Molecule Magnets. In the first family of complexes we studied, based on late lanthanide ions, a rather unexpected similar field-induced slow dynamics of magnetisation could be evidenced for Dy(III), Er(III) and Yb(III) ions. Using a combination of magnetic and luminescence measurements, in addition to SA-CASSCF(PT2)/RASSI-SO calculations, we managed to identify the cause of this apparent similarity: the slow dynamics, in these three cases, is not governed by any energy-barrier dependent mechanism, but by Raman and direct processes, and as such Rinehart and Long's model does not hold. Nevertheless, we managed to rationalise the temperature dependence of the Raman processes using the very same lines of argument as those involved in this model, thus suggesting it could be extended.
Unfortunately, we did not manage to isolate the same kind of complexes with earlier lanthanides in order to confirm it. Using very simple DFT calculations, we could show that most probably this is due to the lanthanide contraction, which renders the structure unstable for larger (earlier) ions. Incidentally, we could prove by Raman spectroscopy that, indeed, the lanthanide contraction has a sensible impact on our complexes.
We thus turned ourselves to a closely related family of complexes, changing the nitrate for a 2,4 pentanedionate ligand. Though already reported in the literature, these complexes were not fully characterised, and noteworthy their magnetic and luminescence properties were not studied. We synthesised the complexes for all the lanthanide ions we had at our disposition, and focused in this preliminary study on the earlier elements (La-Nd, Sm, Gd-Dy) which are isostructural. Most of these complexes displayed a field-induced SMM behaviour, and in the case of the Dy(III) derivative the slow dynamics of magnetisation could still be observed under a zero static field. Evidences tend to suggest the same is true for the Sm(III) derivative, but the signal was too low to be unambiguously assigned. Interestingly, the field-induced SMM behaviour of the Nd(III) and Ce(III) derivative is also partly piloted by Raman relaxation, and could be rationalised using the same line of arguments as previously. More interestingly, the Dy(III) derivative displays a complex dynamics under a static field, with two distinct regimes of relaxation. Interestingly, the

nature of both the low temperature and high temperature regimes remains elusive, and further measurements and *ab initio* calculations are needed in order to fully rationalise this slow dynamics of magnetisation.

Conclusion générale

Au travers de cette thèse, nous nous sommes attachés à décrirer et rationaliser les propriétés de complexes de coordination par l'emploi simultané de la chimie expérimentale et théorique, avec pour but sous-jacent d'instaurer un dialogue fructueux entre les deux approches.

Pour ce faire, nous avons dans un premier temps employé les outils de la théorie de la fonctionnelle de la densité conceptuelle afin de rationaliser les propriétés de coordination des ligands, revisitant de fait les théories de type "champ de ligand" dans une approche de type Parr-Pearson (*i.e.*, en termes de philicités et dureté chimique). Le succès de cette première étude nous a ensuite amené à analyser les effets *trans* dans les complexes octaédriques par le même genre d'approche. A partir d'un modèle théorique très simple, nous avons alors pu caractériser et rationaliser ces effets par des raisonnements très similaires. En bref, nous avons pu montrer que ces effets *trans* traduisent simplement une réduction de l'électrophilie au niveau de la position de coordination *trans*, originant elle-même de la faculté qu'ont certains ligands de pouvoir efficacement "donner" de la densité électronique au cation métallique. Une règle générale s'est alors dessinée, en bon accord avec les données expérimentales : plus un ligand est donneur de densité électronique, et plus il est *trans* orienteur. De manière plus intéressante, nous avons pu quantifier cette modulation de l'électrophilie grâce à une partition du descripteur dual par domaines, et pour la première fois pu envisager la constitution d'une échelle purement théorique des ligands *trans*-orienteurs. Malgré son caractère semi-quantitatif, conséquence directe des nombreuses simplifications induites par notre approche théorique, cette échelle concorde néanmoins efficacement aux données expérimentales.

Nous nous sommes ensuite intéressé à la synthèse et à la caractérisation de complexes d'éléments de transition et de ligands de type "base de Schiff" dérivant d'acides aminés. Bien qu'il se soit révélé très simple d'isoler les ligands, la synthèse des complexes a en revanche été une tâche particulièrement ardue. En effet, de tous les éléments de transition employées, seul le Cu(II) nous a permis d'isoler quatre solides cristallins (deux polymères de coordination monodimensionnels, et deux complexes trinucléaires), et des co-produits d'hydrolyse ont systématiquement été observés.
Dans ce cas, l'utilisation jointe de méthodes expérimentales et computationnelles s'est avérée payante. En effet, nous avons pu de ce fait déterminer la structure adoptée en solution par les ligands libres mais aussi par les complexes de cuivre, ce qui nous a ensuite laisser envisager la possibilité d'étudier la réactivité de ces derniers vis-à-vis de l'eau. Pour ce faire, nous avons employé une stratégie en deux étapes : dans un premier temps, chercher le mécanisme de la réaction d'hydrolyse en solution à un relativement bas niveau de théorie (ici, B3LYP et des bases de qualité double-zêta, les électrons de cœur du cuivre étant représentés par un pseudopotentiel), puis utiliser le chemin ainsi déduit comme point de départ d'une série de calculs de plus haut niveau (ici, ωB97xD, bases triple-zêta avec

inclusion de polarisation et de fonctions diffuses, et pseudopotentiel sur le cuivre). Au plus bas niveau, nous avons effectivement pu déterminer un chemin réactionnel menant à la formation des réactifs initiaux – acide aminé et acétylacetonate –, mais le coût énergétique de la première étape est trop haut pour être envisageable en pratique. Au plus haut niveau, cette première étape se décompose en deux processus élémentaires, auxquels sont associés de bien plus faibles barrières d'énergie et donc bien plus envisageables en pratique. Néanmoins, nous n'avons pas pu retrouver l'entièreté du chemin réactionnel à ce niveau de théorie – malgré deux ans de travail –, et des calculs supplémentaires sont donc nécessaires avant de pouvoir confirmer définitivement la validité de ces résultats. Il serait aussi intéressant de pratiquer le même genre d'étude dans le cas des autres éléments de transition employés expérimentalement.
Quoiqu'il en soit, nous avons aussi étudié les propriétés magnétiques des quatre solides cristallins précédemment mentionnés. Dans le cas des polymères de coordination, un antiferromagnetisme marqué est observé, comme attendu, tandis que dans le cas des complexes trinucléaires un faible couplage antiferromagnétique semble agir. Du fait leur géométrie triangulaire, nous nous sommes demandés si ce couplage antiferromagnétique se pouvait se traduire par de la frustration magnétique, ou si – de manière similaire à ce qui avait été vu dans le cas d'un complexe analogue dérivé de la glycine – un magnétisme plus exotique encore n'était pas à l'œuvre, avec deux états quadruplet et doublet quasi dégénérés. Nous avons donc cherché à modéliser ces complexes par des calculs *ab initio* de très haut niveau. En accord avec les résultats précédemment obtenus dans le cas de l'analogue à base de glycine, seuls les plus hauts niveaux de théorie semblent fournir une description correct de nos complexes. En effet, au niveau SA-CASSCF comme DDCI-1, un comportement ferromagnétique est obtenu, et seuls les calculs NEVPT2 montrent une tendance vers l'antiferromagnétisme – les calculs de type DDCI-2 et DDCI-3 étant interdits par la trop grosse taille de notre système –. De manière intéressante, en accord avec les conclusions de Malrieu nos calculs semblent montrer une meilleure description au fur et à mesure de l'élargissement de l'espace actif. Par ailleurs, les résultats de notre première étude nous ont permis de suggérer une méthode rationnelle pour réaliser ces élargissements, mais des problèmes de convergence nous ont pour le moment empêché de confirmer pleinement ces hypothèses. Nous avons néanmoins bon espoir que ces résultats soient confirmés dans un futur proche.

Dans un troisième temps, nous nous sommes intéressés à d'autres composés au magnétisme original : les molécules aimants mononucléaires à base d'ion lanthanides. Au sein de la première famille de complexes que nous avons étudié, basés sur les lanthanides tardifs, nous avons pu mettre en évidence une similaire lente dynamique de l'aimantation pour les composés de Dy(III), Er(III) et Yb(III). Par la combinaison de mesures magnétiques, de luminescence et de calculs SA-CASSCF(PT2)/RASSI-SO, nous avons pu mettre en évidence la cause de cette apparente similarité : dans ces trois cas, la dynamique de l'aimantation à basse température n'est pas gouvernée par des mécanismes de type Arrhénius, mais plutôt par des mécanismes Raman et direct. De fait, le modèle de Rinehart et Long (qui n'incorpore pas ces mécanismes) ne s'applique *a priori* plus. Néanmoins, nous avons pu rationaliser la dépendance en température des mécanismes Raman en invoquant le même genre d'arguments que ceux utilisés dans ce modèle, suggérant ainsi qu'il pourrait possiblement être étendu.
Malheureusement, il n'a pas été possible d'isoler le même genre de complexes avec d'autres ions lanthanides (du début de la série), et donc de confirmer ou d'infirmer directement notre hypothèse. Un simple calcul DFT nous a permis de suggérer que cette impossibilité est une conséquence de la contraction des lanthanides, la structure cherchée devenant

instable pour les trop gros ions lanthanides. Incidemment, nous avons aussi pu mettre en évidence l'impact de la contraction des lanthanides sur nos complexes par spectroscopie Raman.

Nous nous sommes donc tournés vers une seconde famille de complexes, apparentée à la précédente (le ligand nitrate étant remplacé par un acetylacetonate). Bien que déjà décrits dans la littérature au cours des années 1980, ces complexes n'avaient pas été étudiés en détail, et en particulier leurs propriétés magnétique ou de luminescence n'avaient pas été caractérisées. Nous avons donc synthétisé les complexes correspondant à l'ensemble des ions lanthanides à notre disposition, et nous nous sommes tout particulièrement intéressés aux lanthanides du début de la série (La-Nd, Sm, Gd-Dy) pour cette étude préliminaire, puisque les complexes ainsi isolés sont isostructuraux. La plupart de ces complexes ont présenté un comportement de molécule-aimant induit par le champ, et dans le cas du dérivé de dysprosium une dynamique lente de l'aimantation a même pu être mise en évidence en l'absence de champ. Les premières mesures sur l'analogue de samarium suggèrent qu'il présente aussi un véritable comportement SMM, mais le signal s'est avéré trop faible pour être traité en détail.

De manière intéressante, la dynamique lente de l'aimantation sous champ des complexes de Nd(III) et Ce(III) s'avère partiellement pilotée par un mécanisme Raman, dont la dépendance en température peut se rationaliser par les mêmes arguments que précédemment. De façon plus intéressante encore, la dynamique de l'aimantation du dérivé de Dy(III) sous champ est très complexe, impliquant deux régimes distincts de relaxation. La nature de ces deux régimes reste assez mystérieuse, et des mesures complémentaires, ainsi que des calculs *ab initio* sont donc nécessaires.

Appendix A

Syntheses

Mass spectra were performed at the "Centre commun de spectrométrie de masse de l'Université Claude Bernard - Lyon 1". NMR spectra were recorded at the "Centre Commun de RMN de l'Université Claude Bernard - Lyon 1", on a AVS 300 Bruker apparatus (300 MHz).

A.1 Schiff bases deriving from α amino acids

A.1.1 Ligands syntheses

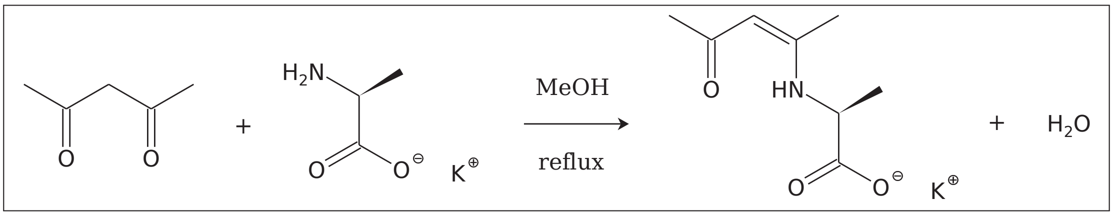

FIGURE A.1.1: Reaction scheme corresponding to the synthesis of ${}^{L}L_1HK$. The same procedure was used for all the α amino-acids listed in Chapter 4.

The procedure is adapted from S. Petit,[159] and was used for alanine, leucine and valine (D, L and DL):
1.114 g (12.5 mmol) of L-alanine are suspended in 12.5mL of a 1 M solution of KOH in methanol (1 equivalent), at room temperature. After 30 minutes of stirring, the solid partly dissolves and yields a fine suspension. 1.252 g (1 equivalent) of 2,4-pentanedione are dissolved in 5 mL of methanol and added dropwise to the mixture. The solution quickly becomes yellow. It is then refluxed overnight (typical experiment, 17 hours), yielding a yellow-orange clear solution (no traces of solid remaining). The reaction mixture is allowed to cool down, and the solvent is removed under reduced pressure (rotary evaporator). The resulting yellow solid is washed with petroleum ether, then extracted with methanol and filtered. Methanol is removed under reduced pressure, yielding 2.561 g of ${}^{L}L_1HK$ as a white-yellow solid. Yield: 98%.

NMR spectroscopy of ${}^{D}L_1HK$ and ${}^{D}L_2HK$ (in D_2O):

${}^{D}L_1HK$: $\delta = 1.33$ ppm (d, J=7.16 Hz, 3H - **f**), $\delta = 1.85$ ppm (s, 3H - **a** or **c**), $\delta = 1.90$ ppm (s, 3H - **c** or **a**), $\delta = 4.02$ ppm (q, J=7.16 Hz, 1H - **e**), $\delta = 5.07$ ppm (s, 1H - **b**).

Table A.1: ESI mass spectrometry (in MeOH) and IR (powder sample).

Ligand	IR: $\bar{\nu}_{\mathrm{C=O}}$	$\bar{\nu}_{\mathrm{C-N}}$	ESI (u)
$^{\mathrm{L}}\mathrm{L_1HK}$	1595 $\mathrm{cm^{-1}}$	1515 $\mathrm{cm^{-1}}$	+172.1, $[^{\mathrm{L}}\mathrm{L_1H_3}]^+$
		1537 $\mathrm{cm^{-1}}$	−170.0, $[^{\mathrm{L}}\mathrm{L_1H}]^-$
$^{\mathrm{D}}\mathrm{L_1HK}$	1593 $\mathrm{cm^{-1}}$	1515 $\mathrm{cm^{-1}}$	+172.1, $[^{\mathrm{D}}\mathrm{L_1H_3}]^+$
		1538 $\mathrm{cm^{-1}}$	−170.0, $[^{\mathrm{D}}\mathrm{L_1H}]^-$
$^{\mathrm{DL}}\mathrm{L_1HK}$	1598 $\mathrm{cm^{-1}}$	1515 $\mathrm{cm^{-1}}$	+172.1, $[^{\mathrm{DL}}\mathrm{L_1H_3}]^+$
		1535 $\mathrm{cm^{-1}}$	−170.0, $[^{\mathrm{DL}}\mathrm{L_1H}]^-$
$^{\mathrm{L}}\mathrm{L_2HK}$	1599 $\mathrm{cm^{-1}}$	1511 $\mathrm{cm^{-1}}$	+200.1, $[^{\mathrm{L}}\mathrm{L_2H_3}]^+$
		1537 $\mathrm{cm^{-1}}$	−198.1, $[^{\mathrm{L}}\mathrm{L_2H}]^-$
$^{\mathrm{D}}\mathrm{L_2HK}$	1598 $\mathrm{cm^{-1}}$	1514 $\mathrm{cm^{-1}}$	+200.1, $[^{\mathrm{D}}\mathrm{L_2H_3}]^+$
		1535 $\mathrm{cm^{-1}}$	−198.1, $[^{\mathrm{D}}\mathrm{L_2H}]^-$
$^{\mathrm{DL}}\mathrm{L_2HK}$	1597 $\mathrm{cm^{-1}}$	1517 $\mathrm{cm^{-1}}$	+200.1, $[^{\mathrm{DL}}\mathrm{L_2H_3}]^+$
		1541 $\mathrm{cm^{-1}}$	−198.1, $[^{\mathrm{DL}}\mathrm{L_2H}]^-$
$^{\mathrm{L}}\mathrm{L_3HK}$	1595 $\mathrm{cm^{-1}}$	1516 $\mathrm{cm^{-1}}$	+214.1, $[^{\mathrm{L}}\mathrm{L_3H_3}]^+$
		1546 $\mathrm{cm^{-1}}$	−212.3, $[^{\mathrm{L}}\mathrm{L_3H}]^-$
$^{\mathrm{D}}\mathrm{L_3HK}$	1597 $\mathrm{cm^{-1}}$	1516 $\mathrm{cm^{-1}}$	+214.1, $[^{\mathrm{D}}\mathrm{L_3H_3}]^+$
		1545 $\mathrm{cm^{-1}}$	−212.3, $[^{\mathrm{D}}\mathrm{L_3H}]^-$
$^{\mathrm{DL}}\mathrm{L_3HK}$	1597 $\mathrm{cm^{-1}}$	1518 $\mathrm{cm^{-1}}$	+214.1, $[^{\mathrm{DL}}\mathrm{L_3H_3}]^+$
		1538 $\mathrm{cm^{-1}}$	−212.3, $[^{\mathrm{DL}}\mathrm{L_3H}]^-$

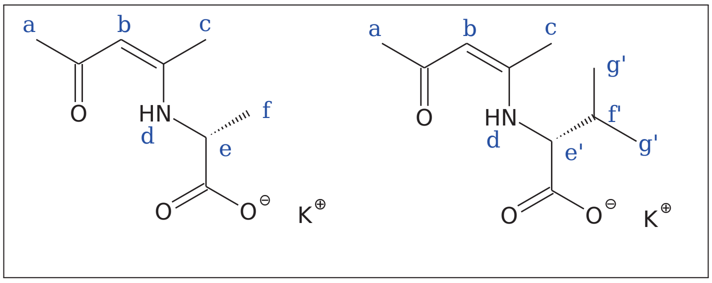

$^{\mathrm{D}}\mathrm{L_2HK}$: δ = 0.76 ppm (d, J=6.78 Hz, 1H - **f'**), δ = 0.84 ppm (t, J=5.93 Hz, 6H - **g'**), δ = 1.81 ppm (s, 3H - **a** or **c**), δ = 1.88 ppm (s, 3H - **c** or **a**), δ = 3.81 ppm (qd, J=4.14 Hz, 1H - **e'**), δ = 5.07 ppm (s, 1H - **b**).

Calculated: δ = 1.27 ppm (J=6.10 Hz, **f**), δ = 1.86 ppm (**c**), δ = 1.90 ppm (**a**), δ = 3.88 ppm (J=6.10 Hz, **e**), δ = 4.85 ppm (**b**).
For $^{\mathrm{D}}\mathrm{L_1H^-}$, on an optimised structure with an implicit solvent ($\mathrm{H_2O}$, PCM), at the B3LYP/6-311++G(d) level, using the GIAO method. Chemical shifts are relative to TMS, computed at the same level of theory.

A.1.2 Complexations

The procedure is derived from S. Petit, and was applied for the D, L and DL enantiomers of ligands L_1HK, L_2HK and L_3HK:[159]
87 mg (0.5 mmol) of $\mathrm{CuCl_2 \cdot 2\,H_2O}$ (or 125 mg of $\mathrm{CuSO_4 \cdot 5\,H_2O}$) are dissolved in 5 mL of methanol, and added dropwise to a solution of 105 mg (1 equivalent) of $^{\mathrm{L}}\mathrm{L_1HK}$ in 5 mL of methanol. The resulting solution is of a deep emerald green colour, which changes to dark blue upon addition of 0.15 mL (2 equivalents) of triethylamine. After filtration, this solution is left to slowly evaporate. Within a few weeks, the reaction mixture is

almost dry and, in the cases of L_1HK and L_2HK ligands, several crystals are seen as well as an off-white powder. The two solids are easily separated using sonication in heptane, affording single crystals amenable for X-ray diffraction.

Powder X-ray diffraction: Comparison between the calculated and experimental powder X-ray diffractograms reveal the uniqueness of the obtained crystalline phases.

A.2 Hydrotris-pyrazolylborohydride based lanthanide complexes

A.2.1 KTp synthesis

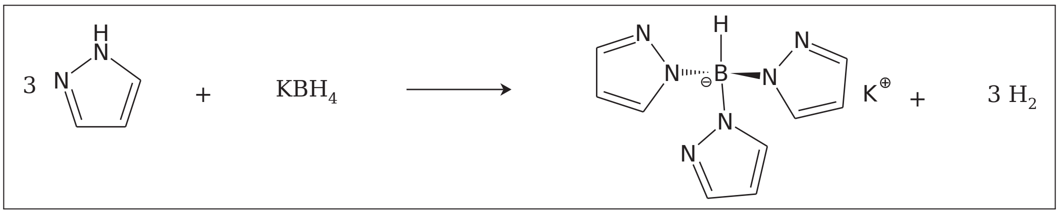

FIGURE A.2.1: Reaction scheme corresponding to the synthesis of KTp.

The procedure is adapted from S. Trofimenko:[181]
1.079 g (0.02 mol) of KBH_4 and 5.438 g (0.08 mol, 4 equivalents) of pyrazole are mixed together in a 100 mL round bottomed flask, and placed in an oil bath. The flask is connected to an air condenser, itself connected to a safety flask and a 2 L measuring cylinder filled with water and inverted in a reservoir of water (apparatus for collection of gas over water). The mixture is stirred and the temperature is increased progressively to 190 °C, with 30 min. plateaux at 105 °C and 125 °C. After 4 to 6 hours, a total volume of 1340 mL of H_2 is collected (3 equivalents). The slurry, consisting of KTp in molten pyrazole, is then cooled down to room temperature. 20 mL of toluene are added, and the mixture is stirred and heated until the solid pyrazole has completely dissolved (around 90 °C). The resulting fine suspension is filtered, washed with 2×20 mL of toluene, 2×20 mL of heptane, 2×10 mL of pentane and let to dry in air. The procedure affords 3.117 g of KTp as a white, crystalline solid. Yield: 62%.

ESI mass spectrometry (in MeOH):

m/Z (u)	Intensity (%)	Ion
-213.2	100	$[Tp]^-$
-449.2	60	$[NaTp_2]^-$
-685.0	20	$[Na_2Tp_3]^-$

NB: no signal is observed in the positive m/Z area.

^{1}H NMR in CD_3OD, 300 MHz: δ = 6.15 ppm (t, 3H); δ = 7.15 ppm (d, 2H); δ = 7.50 ppm (d, 3H).
NB: The hydride H is not seen, as underlined by Trofimenko.

A.2.2 [LnTp$_2$NO$_3$] complexes

The following method has been employed for Ln = Dy, Ho, Er, Yb and Y.
234 mg of Yb(NO$_3$)$_3$ $\cdot$ 6 H$_2$O (0.5mmol) were dissolved in 10 mL of methanol, and added dropwise to a solution of 252 mg of KTp (2 equivalents) in 10mL of methanol. Precipitation occurs during the addition. The resulting suspension is stirred for 5 to 10 minutes at room temperature, then evaporated to dryness (rotary evaporator). The solid is then extracted with 2×10 mL of dichloromethane, or 2×15 mL of chloroform, and the remaining solid is washed with an additional aliquot of the same solvent. The solution is then layered with heptane (2 to 5 mL) and left to slow evaporation. Single crystals are obtained within 5 to 10 days.

ESI mass spectrometry (in CH$_2$Cl$_2$): each time a single peak is observed, corresponding to a [LnTp$_2$]$^+$ ion: +589.1 u (Dy), +591.3 u (Ho), +592.4 u (Er), +600.1 u (Yb), +515.3 u (Y). Nothing is observed in the negative m/Z region.

Powder X-ray diffraction: Comparison between the calculated and experimental powder X-ray diffractograms reveal the uniqueness of the obtained crystalline phases.

A.2.3 [LnTp$_2$Acac] complexes

The following methods have been employed for Ln = La - Nd, Sm - Er, Yb and Y.

Non-aqueous way. 252 mg of KTp (1 mmol), 0.5 mL of a 1M solution of KOH in methanol (0.5 equivalent) and 0.05 mL of 2,4-pentanedione (AcacH, 0.5 equivalent) are mixed in 10 mL of methanol. 187 mg of DyCl$_3$ $\cdot$ 6 H$_2$O (0.5 equivalents), dissolved in 10 mL of methanol, are added dropwise to the previous solution. Precipitation occurs during the addition, and the resulting suspension is stirred at room temperature for 10 additional minutes. Afterwards, the solvent is removed under reduced pressure (rotary evaporator). Then, the solid is extracted in 3×10 mL of CH$_2$Cl$_2$, and the solution is layered with heptane (5 mL). It is then left to slowly evaporate. Single crystals are obtained within one week, possibly after recristallisation (La, Sm).

Aqueous way. *Adapted from J. Moss*[215]. 252 mg of KTp (1 mmol), 0.05 mL of AcacH (0.5 equivalents) and 0.5 mL of a 1M solution of KOH in water are mixed in 10 mL of water. 187 mg of DyCl$_3$ $\cdot$ 6 H$_2$O (0.5 equivalents), dissolved in 10 mL of water, are added to the previous solution. Precipitation occurs immediately, and the resulting suspension is stirred for 10 minutes. 20 mL of dichloromethane is then added, and the mixture is vigorously stirred for 10 minutes. The resulting two liquid phases are separated, and the organic layer is dried with Na$_2$SO$_4$. It is then filtered, layered with heptane (5 mL) and left to slowly evaporate. Single crystals are obtained within one week.

ESI mass spectrometry (in CH$_2$Cl$_2$): nothing is seen in the negative nor positive m/Z region.

Powder X-ray diffraction: Comparison between the calculated and experimental powder X-ray diffractograms reveal the uniqueness of the obtained crystalline phases.

Appendix B

Crystal structures

B.1 Single crystal X-ray diffraction: details

Single crystal X-ray diffractions were performed at the LMI. Diffracted intensities were collected on a 4-circles XCalibur apparatus (Oxford Diffraction), at room temperature, under a Mo Kα radiation ($\lambda = 0.7107$ Å). Data reduction and absorption corrections were computed using CrysAlis. Unless otherwise stated, structure solutions were calculated by the charge flipping method, using Superflip (as implemented in the software suite Crystals). In a few cases, the structure solutions were found by direct methods, using SIR97.
In both cases, missing H atoms were found by difference Fourier density mapping. All but H atoms were then anisotropically refined by least squares on F, using Crystals. When relevant, disordered solvent effects were taken into account using the SQUEEZE option of the PLATON program.
All the figures were drawn using VESTA 3.3.2.

B.2 Trinuclear copper(II) complexes 4.1 and 4.2

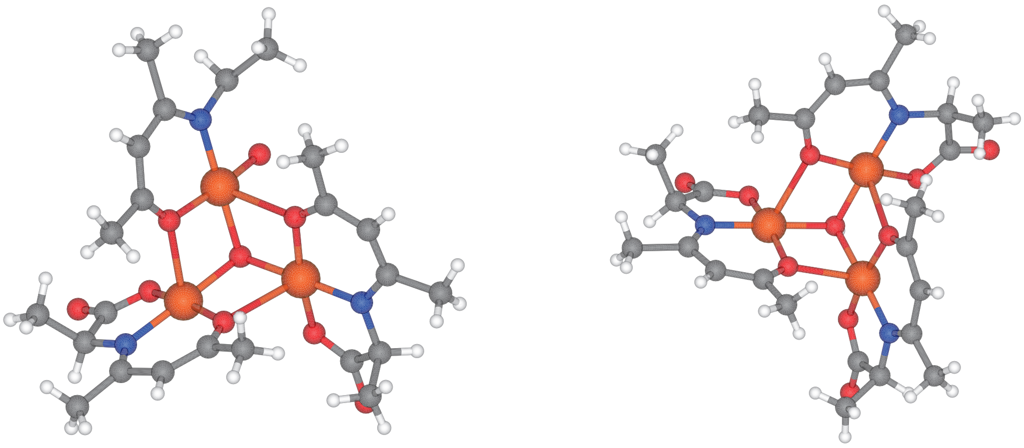

FIGURE B.2.1: Structure of the two $[\mathrm{Cu_3}(\mu_2{-}{}^{\mathrm{L}}\mathrm{L}_1)_3(\mu_3{-}\mathrm{OH})]^-$ complexes found within the asymmetric unit of structure 4.1. The relative orientations are different.

Notice relative to tables B.2 and B.3:

- ▷ geometrical parameters and their error bars were computed using Mercury;

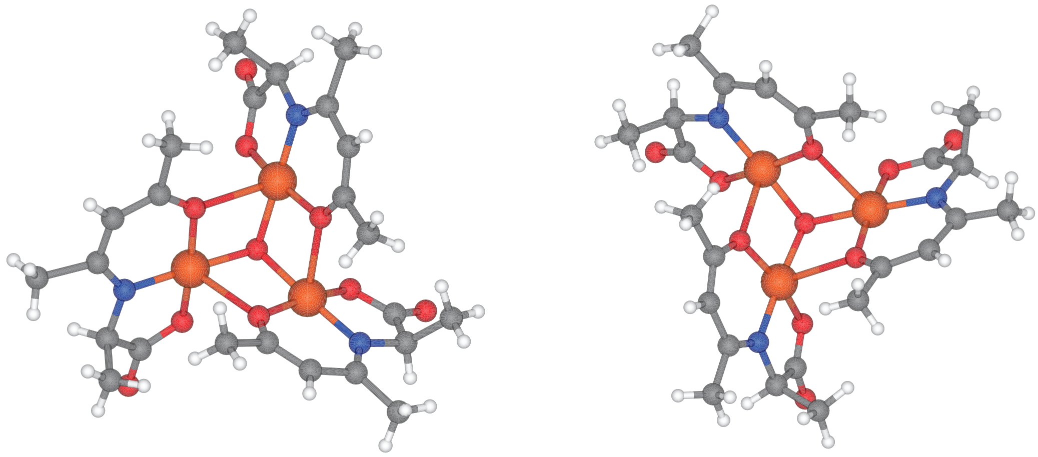

FIGURE B.2.2: Structure of the two $[Cu_3(\mu_2-{}^{D}L_1)_3(\mu_3-OH)]^-$ complexes found within the asymmetric unit of structure 4.2. The relative orientations are different.

TABLE B.1: Cell and refinement parameters for the single crystal X-Ray diffraction study of $K_2[Cu_3(\mu_2-{}^{L}L_1)_3(\mu_3-OH)]_2 \cdot 5\,H_2O$ (4.1) and $K_2[Cu_3(\mu_2-{}^{D}L_1)_3(\mu_3-OH)]_2 \cdot 5\,H_2O$ (4.2). $N_{IR}/N_{R.R}$: number of independent reflections versus number of refined reflections.

Complex	4.1	4.2
Formula	$C_{48}H_{78}Cu_6K_2N_6O_{25}$	$C_{48}H_{78}Cu_6K_2N_6O_{25}$
FW (g.mol^{-1})	1598.64	1598.64
a (Å)	23.715(1)	14.3538(6)
b (Å)	20.8777(8)	23.7444(7)
c (Å)	13.1738(6)	20.8813(7)
α, β, γ (°)	90	90
V (Å^3)	7017.6(5)	7116.8(4)
Z	4	4
Space group	$P2_12_12_1$	$P2_12_12_1$
μ *(cm^{-1})*	1.978	1.951
F_{000}	3280	3280
$N_{IR}/N_{R.R}$	16350/8360	16444/9033
N. parameters	785	785
Flack	0.03(3)	0.05(2)
$R(F, I > 3\sigma(I))$	8.06%	6.77%
$R_w(F, I > 3\sigma(I))$	7.85%	4.42%
GooF	1.0004	0.9069

- when relevant, these parameters are given for each trinuclear complex within the asymmetric unit (the three first values corresponding to one complex, the three last to the second complex);
- d(Cu-X) are the distances between a given copper atom and its neighbours. $O_{ket,s}$ labels the closest ketone-like O atom, $O_{ket,l}$ the bridging ketone-like O atom from the other ligand, O_{COO} the coordinating O atom from the carboxylate group, and O_{OH} the O atom from the bridging hydroxide;
- $\widehat{XCuX}$ and $\widehat{CuXCu}$ are the associated coordination angle, X being defined similarly to the previous case;
- d($\overline{Cu}$-O_{OH}) represents the calculated distance between the hydroxide and the mean plane defined by the three copper atoms of a given trinuclear complex.

Table B.2: Selected distances (in Å) related to the coordination sphere of the Cu atoms in complexes 4.1 and 4.2.

Parameter	Complexes 4.1	Complexes 4.2	Average for 4.1	Average for 4.2
d(Cu-N)	1.927(9)	1.924(6)	1.90(3)	1.91(1)
	1.893(9)	1.910(6)		
	1.880(9)	1.903(7)		
	1.929(9)	1.931(6)	1.91(2)	1.91(2)
	1.92(1)	1.908(6)		
	1.89(1)	1.889(7)		
d(Cu-$\mathrm{O_{ket,s}}$)	1.904(7)	1.906(6)	1.898(7)	1.904(6)
	1.900(9)	1.903(5)		
	1.891(6)	1.902(4)		
	1.921(9)	1.922(6)	1.91(2)	1.91(1)
	1.920(9)	1.918(5)		
	1.897(6)	1.90(1)		
d(Cu-$\mathrm{O_{ket,l}}$)	2.501(9)	2.562(4)	2.47(3)	2.48(4)
	2.463(7)	2.477(5)		
	2.451(8)	2.464(6)		
	2.545(9)	2.556(4)	2.5(1)	2.50(9)
	2.54(1)	2.535(7)		
	2.389(7)	2.418(5)		
d(Cu-$\mathrm{O_{COO}}$)	1.93(1)	1.950(5)	1.92(1)	1.93(2)
	1.926(7)	1.941(6)		
	1.921(9)	1.916(6)		
	1.963(9)	1.964(5)	1.95(3)	1.93(3)
	1.963(9)	1.916(4)		
	1.926(9)	1.913(6)		
d(Cu-$\mathrm{O_{OH}}$)	3.213(2)	3.219(1)	3.15(6)	3.13(6)
	3.131(2)	3.138(1)		
	3.117(2)	3.130(1)		
	3.183(2)	3.185(1)	3.16(2)	3.16(2)
	3.159(2)	3.163(1)		
	3.131(2)	3.138(1)		
d($\overline{\mathrm{Cu}}$-$\mathrm{O_{OH}}$)	0.751	0.727	0.73(3)	0.72(2)
	0.700	0.706		

B.3 Copper(II) coordination polymers

Table B.3: Selected angles (in °) related to the coordination sphere of the Cu atoms in complexes 4.1 and 4.2.

Parameter	Complexes 4.1	Complexes 4.2	Average for 4.1	Average for 4.2
$\mathrm{Cu\widehat{O_{OH}Cu}}$	108.9(3) 107.3(3) 106.9(3)	110.0(2) 106.2(2) 105.2(2)	108(1)	107(3)
	109.1(4) 105.6(3) 104.4(3)	109.3(2) 107.5(2) 107.0(2)	106(3)	108(2)
$\mathrm{Cu\widehat{O_{ket}Cu}}$	92.0(3) 91.4(4) 87.9(4)	91.5(4) 90.9(2) 90.9(2)	108(1)	107(3)
	92.1(3) 91.6(3) 91.1(3)	91.6(2) 90.9(2) 89.0(3)	91.6(5)	90(2)

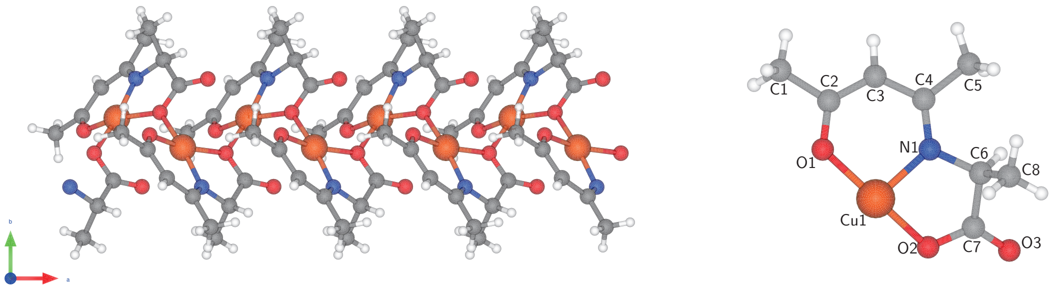

Figure B.3.1: Structure of the $[\mathrm{Cu}(\mu_2{-}^{\mathrm{L}}\mathrm{L}_1)]$ polymer 4.3, seen along the $\vec{c}$ axis (left), and detail on the asymmetric unit numbering scheme (right).

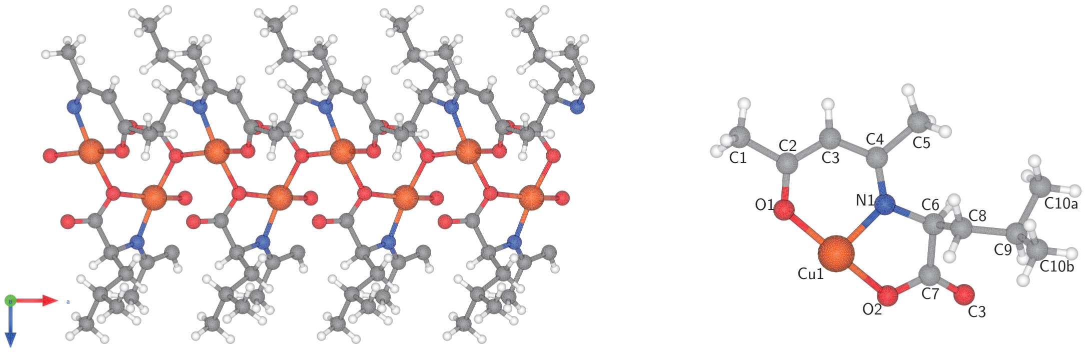

Figure B.3.2: Structure of the $[\mathrm{Cu}(\mu_2{-}^{\mathrm{L}}\mathrm{L}_1)]$ polymer 4.4, seen along the $\vec{c}$ axis (left), and detail on the asymmetric unit numbering scheme (right).

Table B.4: Cell and refinement parameters for the single crystal X-Ray diffraction study of $[\mathrm{Cu}(\mu_2{-}{}^{\mathrm{L}}\mathrm{L}_1)]$ (4.3) and $[\mathrm{Cu}(\mu_2{-}{}^{\mathrm{D}}\mathrm{L}_1)]$ (4.4). $\mathrm{N}_{IR}/\mathrm{N}_{R.R}$: number of independent reflections versus number of refined reflections.

Complex	4.3	4.4
Formula	$C_8H_{11}Cu_1N_1O_3$	$C_{11}H_{17}Cu_1N_1O_3$
FW (g.mol^{-1})	232.73	274.81
a (Å)	5.0016(3)	4.9606(4)
b (Å)	12.7365(9)	8.9692(9)
c (Å)	14.7029(8)	27.702(2)
α, β, γ (°)	90	90
V (Å^3)	936.6(1)	1234.5(2)
Z	4	4
Space group	$P2_12_12_1$	$P2_12_12_1$
μ *(cm^{-1})*	2.304	1.764
F_{000}	476	572
$\mathrm{N}_{IR}/\mathrm{N}_{R.R}$	2180/1797	2826/2227
N. parameters	119	146
Flack	0.04(2)	-0.01(3)
$R(F, I > 3\sigma(I))$	2.98%	4.24%
$R_w(F, I > 3\sigma(I))$	3.93%	4.50%
GooF	0.9809	0.9455

Table B.5: Selected geometrical parameters relative to the environment of the copper(II) ions in structures 4.3 and 4.4. Distances are given in Å and angles in °. Addison parameter τ is dimensionless.

	Polymer 4.3	Polymer 4.4
d(Cu-O_2)	1.990(2)	1.977(3)
d(Cu-$O_{3'}$)	1.996(2)	1.982(3)
d(Cu-O_1)	1.896(3)	1.888(3)
d(Cu-N)	1.921(3)	1.908(3)
d(Cu-$O_{3''}$)	2.512(3)	2.564(3)
$\widehat{\mathrm{NCuO}_1}$	95.2(1)	95.1(2)
$\widehat{\mathrm{NCuO}_2}$	83.5(1)	83.7(2)
$\widehat{\mathrm{NCuO}_{2'}}$	170.8(1)	168.2(2)
$\widehat{\mathrm{O}_{2'}\mathrm{CuO}_2}$	83.5(1)	83.7(2)
$\widehat{\mathrm{CuO}_2\mathrm{Cu}}$	128.4(1)	128.4(1)
τ	0.10	0.06
Geometry	SBP	SBP

B.4 [$LnTp_2NO_3$] crystal structures

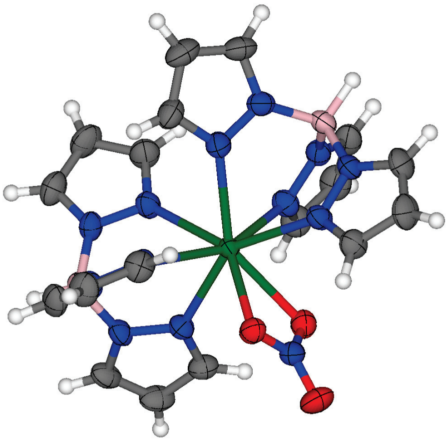

FIGURE B.4.1: ORTEP drawing of the [$LnTp_2NO_3$] complexes 5.1 to 5.5, ellipsoids drawn at 50% probability. Example: [$YbTp_2NO_3$] (5.4).

TABLE B.6: Geometrical parameters related to the the first coordination sphere of lanthanide ions for the [$LnTp_2NO_3$] complexes.

Parameter	[$DyTp_2NO_3$]	[$HoTp_2NO_3$]	[$ErTp_2NO_3$]	[$YbTp_2NO_3$]	[YTp_2NO_3]
Ln-N_{pyr} (Å)	2.448(4)	2.394(2)	2.383(2)	2.353(2)	2.399(2)
	2.472(4)	2.470(2)	2.465(2)	2.437(2)	2.475(2)
	2.404(4)	2.429(2)	2.411(2)	2.408(2)	2.456(2)
	2.460(4)	2.442(2)	2.442(2)	2.391(2)	2.436(2)
	2.445(4)	2.442(2)	2.452(2)	2.414(2)	2.449(2)
	2.496(4)	2.483(2)	2.479(2)	2.452(2)	2.488(2)
Ln-O (Å)	2.399(3)	2.393(2)	2.394(2)	2.355(2)	2.386(2)
	2.460(3)	2.446(2)	2.428(2)	2.421(2)	2.446(2)
$\widehat{\text{NLnN}}$ (°)	70.9(1)	70.7(3)	71.25(9)	71.22(7)	70.86(7)
	71.0(1)	70.8(3)	71.92(8)	71.44(7)	70.89(8)
	76.4(1)	77.7(3)	77.20(9)	77.40(7)	76.98(7)
	77.7(1)	77.4(3)	78.21(8)	78.70(8)	77.75(8)
	80.0(1)	80.5(3)	80.59(9)	81.11(7)	80.34(7)
	80.3(1)	80.8(3)	81.10(8)	81.39(8)	80.54(8)
$\widehat{\text{OLnO}}$ (°)	52.5(1)	52.83(7)	52.9(3)	53.34(7)	52.85(7)

TABLE B.7: Cell and refinement parameters for the single crystal X-Ray diffraction study of the [$LnTp_2NO_3$] complexes 5.1 to 5.5. $N_{IR}/N_{R.R}$: number of independent reflections versus number of refined reflections.

Complex	5.1	5.2	5.3	5.4	5.5
Formula	$C_{18}H_{20}B_2Dy_1N_{13}O_3$	$C_{18}H_{20}B_2Ho_1N_{13}O_3$	$C_{18}H_{20}B_2Er_1N_{13}O_3$	$C_{18}H_{20}B_2Yb_1N_{13}O_3$	$C_{18}H_{20}B_2Y_1N_{13}O_3$
FW (g.mol^{-1})	650.56	652.99	655.32	661.10	576.97
a (Å)	15.7332(5)	15.7363(4)	15.7592(7)	15.7662(4)	15.7452(7)
b (Å)	9.1641(2)	9.1408(2)	9.1332(3)	9.1066(2)	9.1536(3)
c (Å)	17.6410(5)	17.5834(5)	17.5481(7)	17.4455(5)	17.5988(7)
α, γ (°)	90	90	90	90	90
β (°)	104.811(3)	104.864(3)	104.815(4)	104.876(3)	104.785(4)
V (Å^3)	2459.0(2)	2444.6(2)	2441.8(2)	2420.8(2)	2452.4(2)
Z	4	4	4	4	4
Space group	$P2_1/c$	$P2_1/c$	$P2_1/c$	$P2_1/c$	$P2_1/c$
μ (cm^{-1})	3.088	3.288	3.487	3.914	2.428
F_{000}	1276	1280	1284	1292	1168
$N_{I.R}$ / $N_{R.R}$	5699/4124	5717/4299	5700/4263	5924/5046	5722/3972
N. parameters	334	334	334	334	334
R (F, $I > 3\sigma(I)$)	2.90%	2.50%	3.65%	2.21%	3.27%
Rw (F, $I > 3\sigma(I)$)	3.75%	1.95%	0.97%	2.57%	3.94 %
GooF	0.9518	1.2088	0.9132	1.0746	1.0864

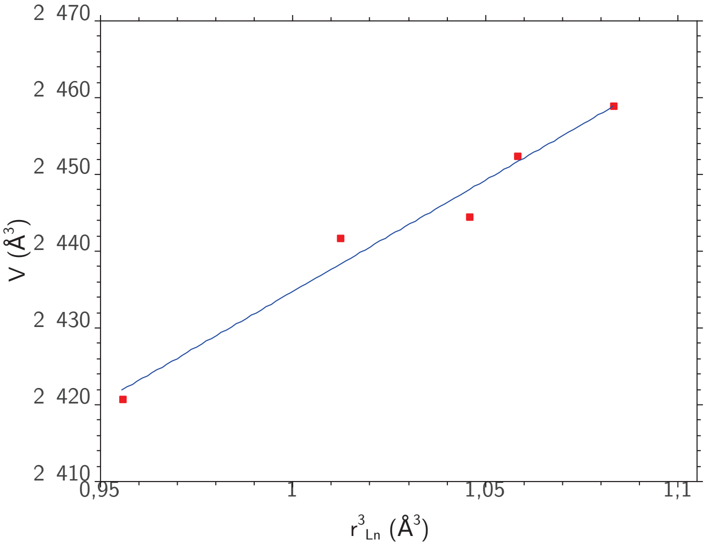

FIGURE B.4.2: Correlation diagram between the volume of the lattice cell of complexes 5.1 to 5.5 and the cube of the ionic radii of the corresponding lanthanides (from[182]). The blue line is the best linear fit ($R^2 = 0.969$).

TABLE B.8: Cell and refinement parameters for the single crystal X-Ray diffraction study of [TbTp$_2$NO$_3$] and the [LnTp$_2$(NO$_3$)(H$_2$O)] complexes (Ln = Tb, Gd, La). N$_{IR}$/N$_{R.R}$: number of independent reflections versus number of refined reflections.

Complex	[TbTp$_2$NO$_3$]	[TbTp$_2$NO$_3$(H$_2$O)]	[GdTp$_2$NO$_3$(H$_2$O)]	[LaTp$_2$NO$_3$(H$_2$O)]
Formula	$C_{18}H_{20}B_2N_{13}O_3Tb_1$	$C_{18}H_{22}B_2N_{13}O_4Tb_1$	$C_{18}H_{22}B_2N_{13}O_4Gd_1$	$C_{18}H_{22}B_2N_{13}O_4La_1$
FW (g.mol^{-1})	649.99	665.00	663.33	649.99
a (Å)	15.7188(4)	9.5445(2)	9.5256(5)	9.6079(2)
b (Å)	9.17912(18)	10.8289(3)	10.7902(6)	10.8615(2)
c (Å)	17.6930(4)	13.6140(4)	13.5149(8)	13.5233(3)
α (°)	90	82.789(2)	82.173(5)	83.038(2)
β (°)	104.789(2)	74.425(2)	75.005(5)	75.745(2)
γ (°)	90	76.153(2)	75.597(5)	73.308(2)
V (Å^3)	2468.27(10)	1313.22(6)	1295.79(14)	1325.95(5)
Z	4	2	2	2
Space group	$P2_1/c$	$P\bar{1}$	$P\bar{1}$	$P\bar{1}$
μ (cm^{-1})	2.915	2.744	2.611	1.662
F$_{000}$	1272	656	654	640
N$_{I.R}$ / N$_{R.R}$	6272/4896	6346/5266	5984/4807	6771/5949
N. parameters	334	343	343	343
R (F, I $> 3\sigma$(I))	2.79 %	3.04%	3.75%	2.43%
Rw (F, I $> 3\sigma$(I))	4.71 %	3.60%	4.40%	3.00%
GooF	0.9615	1.0560	1.1024	1.0113

B.5 [$\mathrm{LnTp_2Acac}$] crystal structures

B.5.1 Monoclinic structures

Without solvent

TABLE B.9: Cell and refinement parameters for the single crystal X-Ray diffraction study of the monoclinic [$\mathrm{LnTp_2Acac}$] structures 5.6 to 5.12. $\mathrm{N}_{IR}/\mathrm{N}_{R.R}$: number of independent reflections versus number of refined reflections.

Complex	5.6	5.7	5.8	5.9	5.10	5.11	5.12
Formula	[$\mathrm{CeTp_2Acac}$]	[$\mathrm{PrTp_2Acac}$]	[$\mathrm{NdTp_2Acac}$]	[$\mathrm{SmTp_2Acac}$]	[$\mathrm{GdTp_2Acac}$]	[$\mathrm{TbTp_2Acac}$]	[$\mathrm{DyTp_2Acac}$]
FW ($\mathrm{g.mol^{-1}}$)	665.29	665.27	669.41	675.57	682.42	684.09	687.67
a (*Å*)	15.2122(4)	15.2225(5)	15.2069(5)	15.213(5)	15.2308(6)	15.2241(6)	15.2071(5)
b (*Å*)	12.9770(3)	12.9576(5)	12.9203(3)	12.883(5)	12.8653(4)	12.8245(4)	12.8077(4)
c (*Å*)	14.9591(3)	14.9516(5)	14.9381(4)	14.917(5)	14.8994(5)	14.8889(5)	14.8944(5)
α, γ (°)	90	90	90	90	90	90	90
β (°)	102.044(2)	102.040(3)	102.065(3)	102.037(5)	102.084(3)	102.026(4)	102.117(3)
V ($Å^3$)	2888.1(1)	2884.3(1)	2870.19(8)	2859.3(2)	2854.8(2)	2843.1(2)	2836.3(2)
Z	4	4	4	4	4	4	4
Space group	$P2_1/c$	$P2_1/c$	$P2_1/c$	$P2_1/c$	$P2_1/c$	$P2_1/c$	$P2_1/c$
μ ($\mathrm{cm^{-1}}$)	1.620	1.733	1.853	2.098	2.367	2.532	2.679
$\mathrm{F_{000}}$	1332	1336	1340	1348	1356	1360	1364
$\mathrm{N}_{I.R}$ / $\mathrm{N}_{R.R}$	7515/5635	6795/4988	6848/5245	7412/5602	6817/5175	6653/4528	7034/5007
N. parameters	361	361	361	361	361	361	361
R (F, $\mathrm{I} > 3\sigma(\mathrm{I})$)	2.80%	2.73%	2.74%	2.53%	3.49%	3.11%	5.09%
Rw (F, $\mathrm{I} > 3\sigma(\mathrm{I})$)	4.01%	3.35%	3.97%	2.94 %	4.24%	4.11%	4.73%
GooF	1.0176	1.0597	1.0534	1.0628	1.1037	1.0871	1.1815

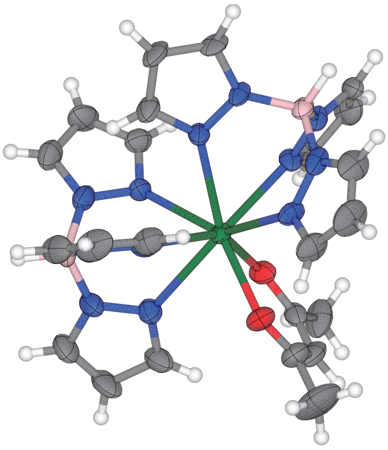

FIGURE B.5.1: ORTEP drawing of the [LnTp$_2$Acac] complexes 5.6 to 5.12 (ellipsoids drawn at 50% probability). Example of [DyTp$_2$Acac] (5.12).

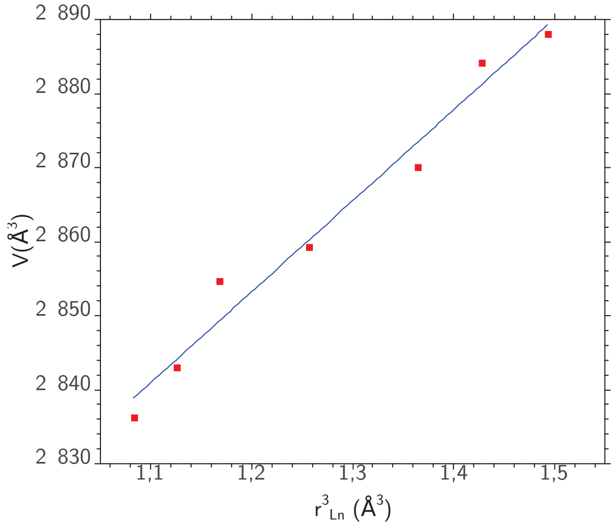

FIGURE B.5.2: Correlation diagram between the volume of the lattice cell of complexes 5.6 to 5.12 and the cube of the ionic radii of the corresponding lanthanides (from[182]). The blue line is the best linear fit ($R^2 = 0.974$).

With solvent

Table B.10: Cell and refinement parameters for the single crystal X-Ray diffraction study of the monoclinic [LnTp$_2$Acac] · solvent structures 5.13 to 5.16. N$_{IR}$/N$_{R.R}$: number of independent reflections versus number of refined reflections.

Complex	5.13	5.14	5.15	5.16
Formula	[PrTp$_2$Acac] · CHCl$_3$	[EuTp$_2$Acac] · CHCl$_3$	[DyTp$_2$Acac] · CHCl$_3$	[DyTp$_2$Acac] · CH$_2$Cl$_2$
FW (g.mol^{-1})	784.64	796.51	807.05	772.60
a (Å)	17.1592(5)	17.148(5)	17.120(5)	8.359(5)
b (Å)	12.8563(4)	12.780(5)	12.738(5)	30.327(5)
c (Å)	15.0007(4)	14.949(5)	14.893(5)	12.734(5)
α, γ (°)	90	90	90	90
β (°)	91.486(2)	91.433(5)	91.224(5)	96.578(5)
V (Å^3)	3308.10(9)	3275(2)	3247(2)	3207(2)
Z	4	4	4	4
Space group	P2$_1$/c	P2$_1$/c	P2$_1$/c	P2$_1$/n
μ (cm^{-1})	1.758	2.203	2.592	2.540
F$_{000}$	1568	1584	1596	1532
N$_{I.R}$ / N$_{R.R}$	7830/5818	7766/5760	7752/5683	7907/6014
N. parameters	397	397	397	388
R (F, I > 3σ(I))	3.06%	3.72%	3.00%	2.92%
Rw (F, I > 3σ(I))	3.63%	4.47%	3.71%	3.30%
GooF	1.0750	1.0811	1.1176	1.1048

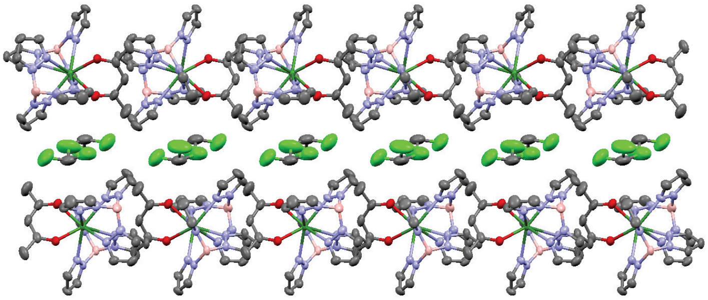

FIGURE B.5.3: 2D-lamellar structure of complexes (5.13) to (5.15).

B.5.2 Triclinic structures

TABLE B.11: Cell and refinement parameters for the single crystal X-Ray diffraction study of the monoclinic [LnTp$_2$Acac] · solvent structures 5.17 to 5.19. N$_{IR}$/N$_{R.R}$: number of independent reflections versus number of refined reflections.

Complex	5.17	5.18	5.19
Formula	[HoTp$_2$Acac]$_2$	[YbTp$_2$Acac]$_2$	[YbTp$_2$Acac] · CHCl$_3$
FW (g.mol^{-1})	1380.20	1396.42	1507.77
a (Å)	11.791(5)	12.7547(3)	11.9386(9)
b (Å)	15.927(5)	14.8810(3)	15.900(2)
c (Å)	18.436(5)	16.1033(4)	18.462(2)
α (°)	68.046(5)	99.060(2)	112.053(7)
β (°)	74.238(5)	104.945(2)	105.816(6)
γ (°)	89.952(5)	92.950(2)	90.315(1)
V (Å^3)	3071(2)	2902.6(1)	3102.1(4)
Z	2	2	2
Space group	P$\bar{1}$	P$\bar{1}$	P$\bar{1}$
μ (cm^{-1})	2.618	3.265	3.149
F$_{000}$	1368	1380	1484
N$_{I.R}$ / N$_{R.R}$	15743/10857	14126/10785	14266/8082
N. parameters	721	721	337
R (F, I > 3σ(I))	3.90%	2.48%	6.49%
Rw (F, I > 3σ(I))	4.03%	3.29%	7.10%
GooF	1.1162	1.0310	1.0730

Note: Due to the low number of reflections, thermal displacements for complex 5.19 were only refined isotropically.

Appendix C

Powder X-Ray diffractogramms

C.1 [$LnTp_2NO_3$] complexes

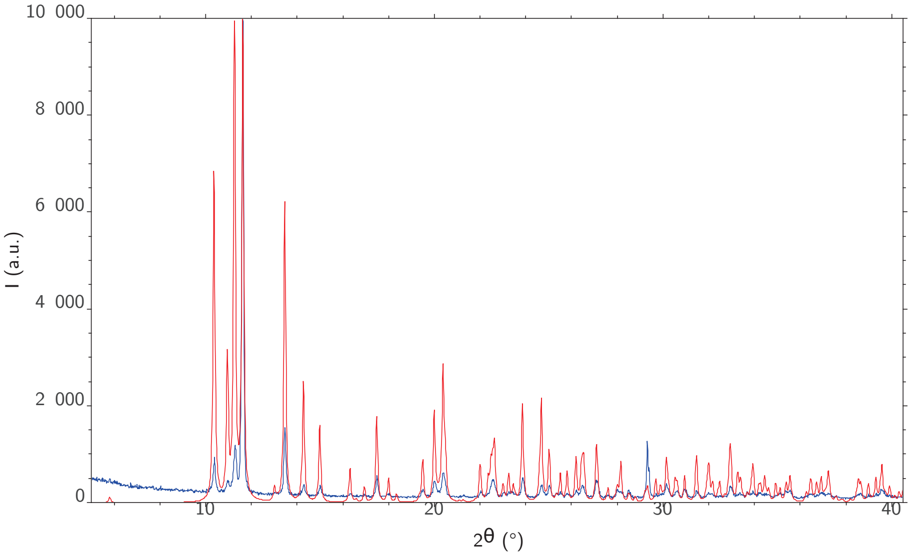

FIGURE C.1.1: Powder X-Ray diffractogramm of complex 5.1 under a Cu Kα radiation (blue line). The red line is the expected pattern from the single-crystal X-Ray diffraction experiment.

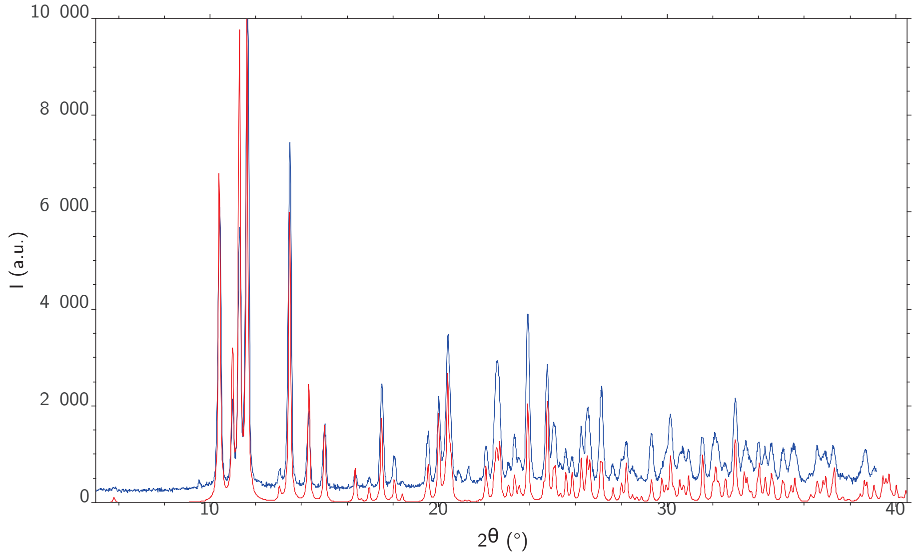

FIGURE C.1.2: Powder X-Ray diffractogramm of complex 5.2 under a Cu Kα radiation (blue line). The red line is the expected pattern from the single-crystal X-Ray diffraction experiment.

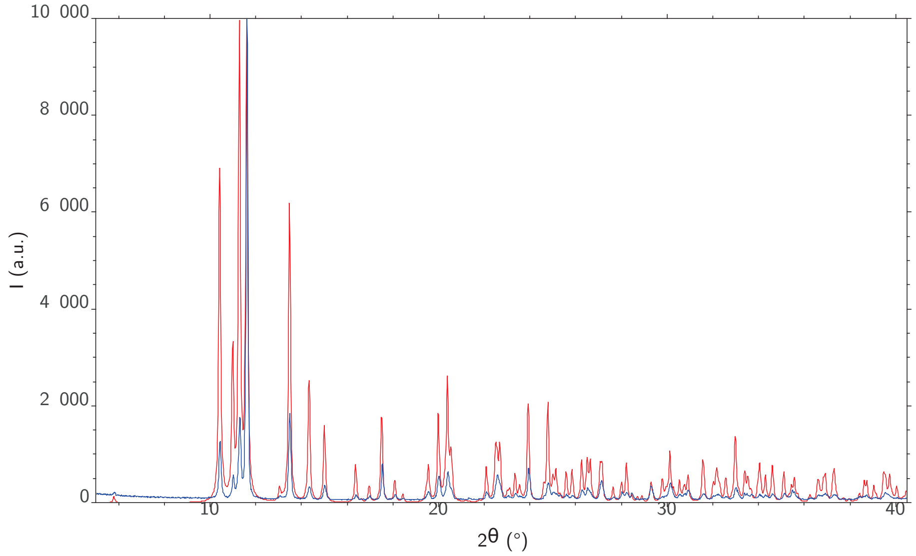

FIGURE C.1.3: Powder X-Ray diffractogramm of complex 5.3 under a Cu Kα radiation (blue line). The red line is the expected pattern from the single-crystal X-Ray diffraction experiment.

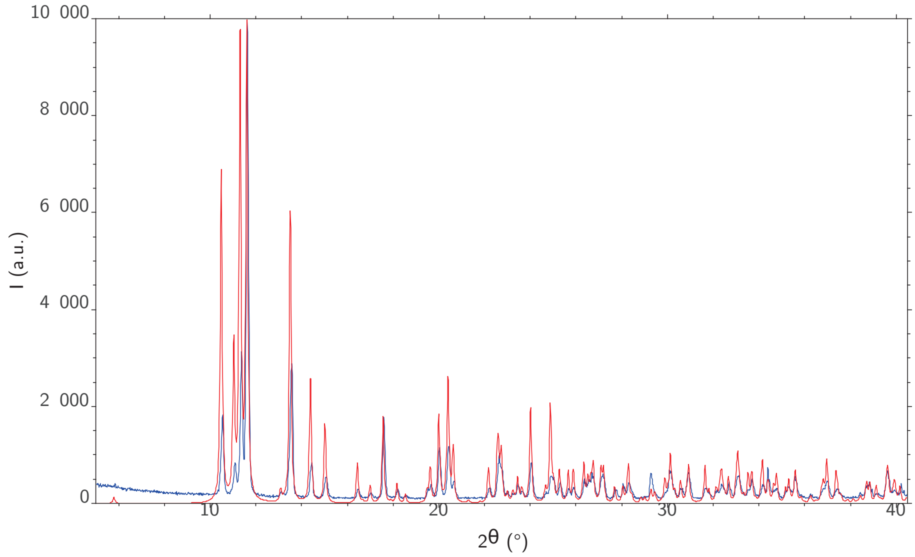

FIGURE C.1.4: Powder X-Ray diffractogramm of complex 5.4 under a Cu Kα radiation (blue line). The red line is the expected pattern from the single-crystal X-Ray diffraction experiment.

C.2 [LnTp$_2$Acac] complexes

C.2.1 Monoclinic structures

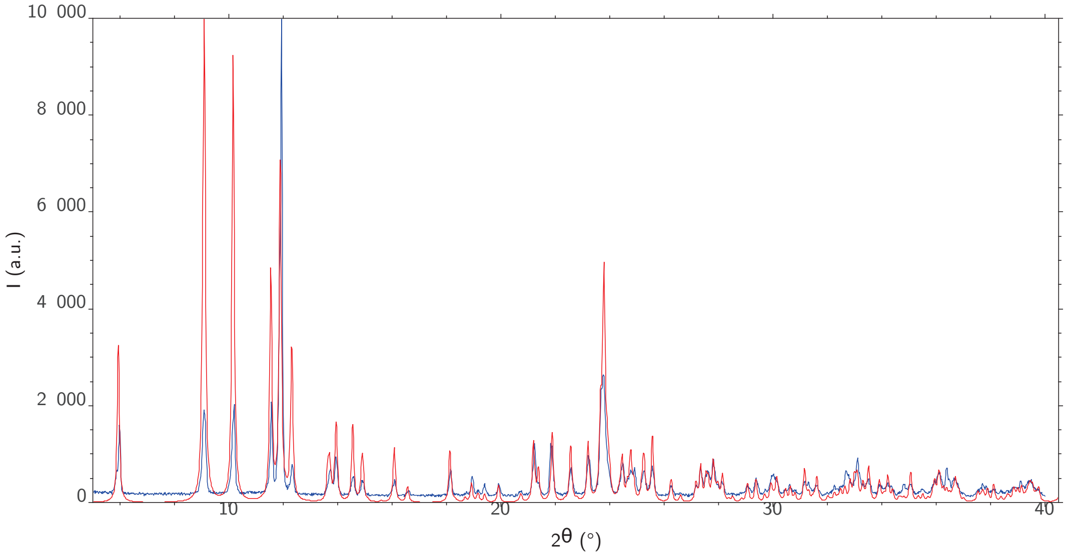

FIGURE C.2.1: Powder X-Ray diffractogramm of complex 5.6 under a Cu Kα radiation (blue line). The red line is the expected pattern from the single-crystal X-Ray diffraction experiment.

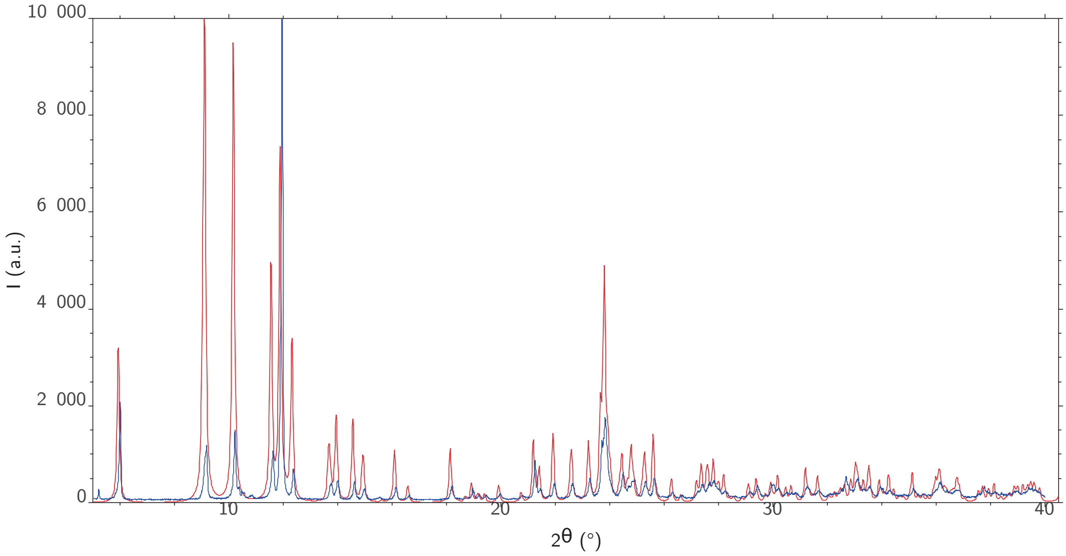

FIGURE C.2.2: Powder X-Ray diffractogramm of complex 5.7 under a Cu Kα radiation (blue line). The red line is the expected pattern from the single-crystal X-Ray diffraction experiment.

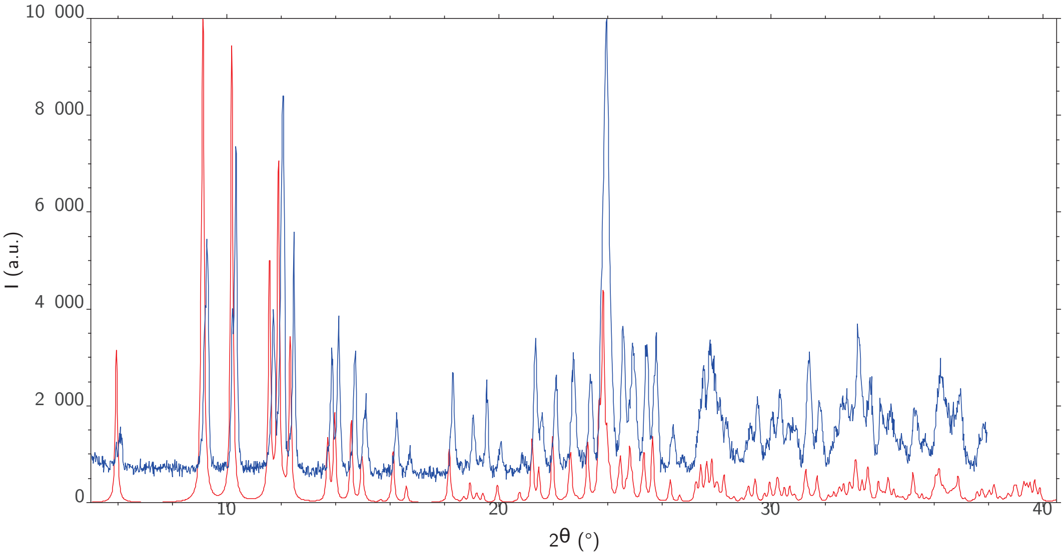

FIGURE C.2.3: Powder X-Ray diffractogramm of complex 5.8 under a Cu Kα radiation (blue line). The red line is the expected pattern from the single-crystal X-Ray diffraction experiment.

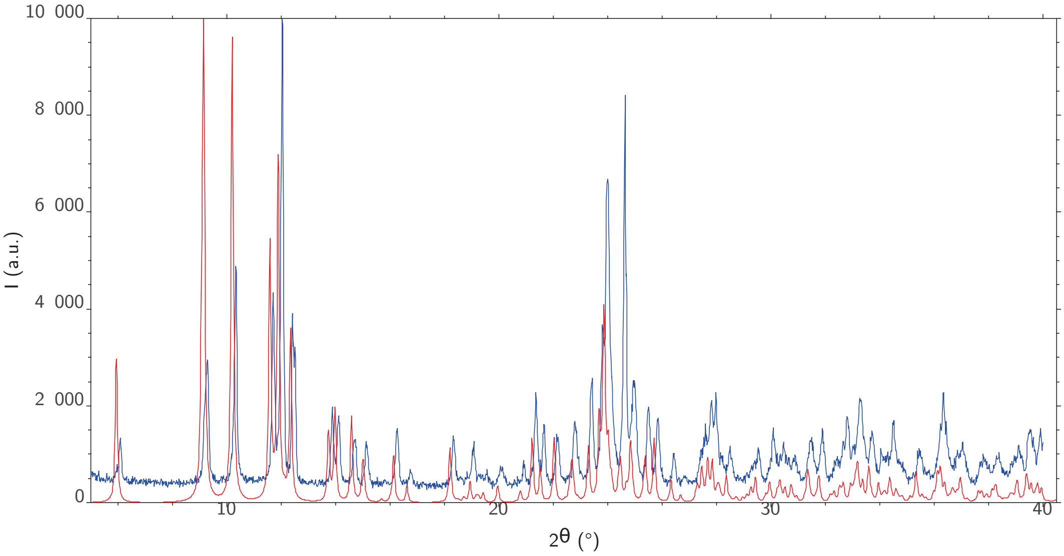

FIGURE C.2.4: Powder X-Ray diffractogramm of complex 5.9 under a Cu Kα radiation (blue line). The red line is the expected pattern from the single-crystal X-Ray diffraction experiment.

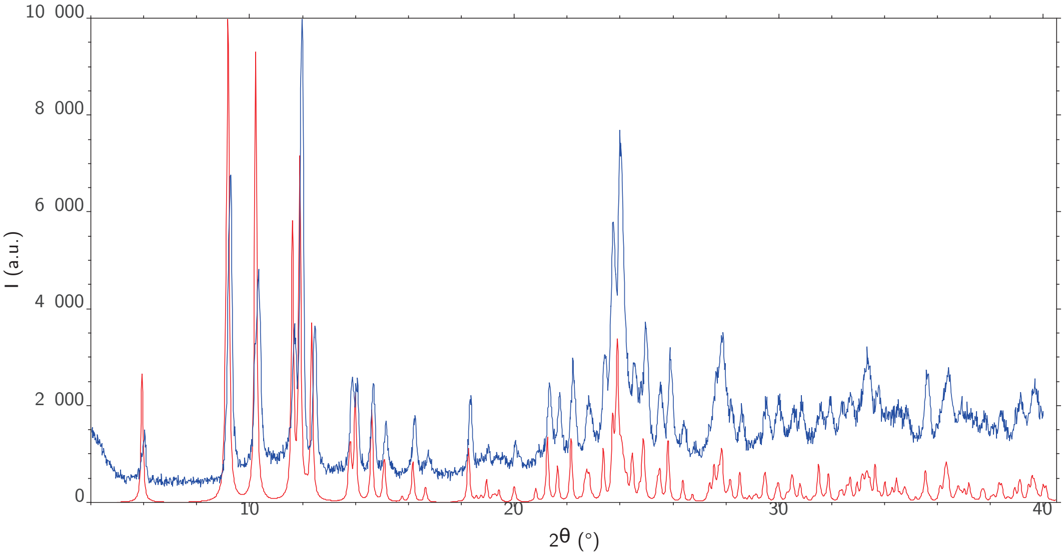

FIGURE C.2.5: Powder X-Ray diffractogramm of complex 5.12 under a Cu Kα radiation (blue line). The red line is the expected pattern from the single-crystal X-Ray diffraction experiment.

Appendix D

Complementary magnetic data

D.1 AC magnetometry of the [LnTp$_2$NO$_3$] complexes

D.1.1 Field dependence of the AC susceptibility

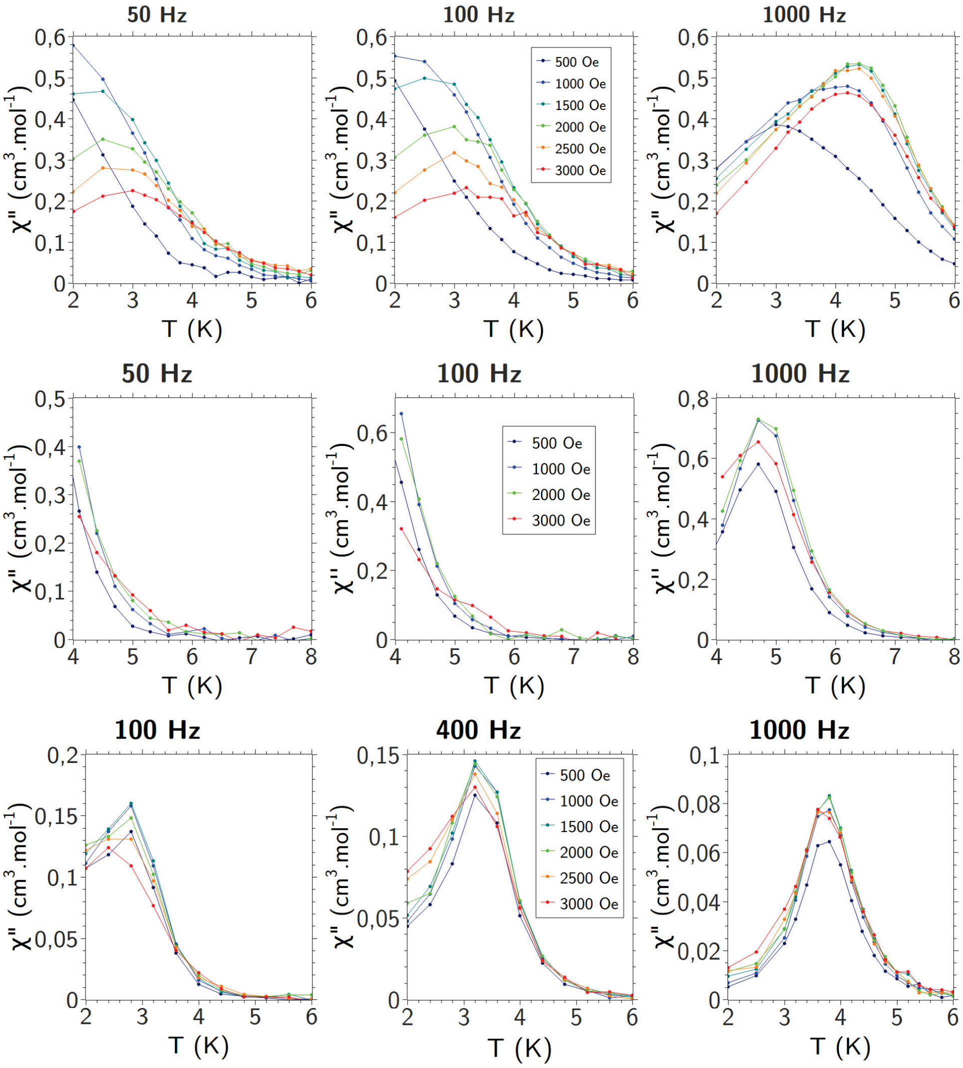

FIGURE D.1.1: $\chi''_m = f(B;T))$ plots for complexes (5.1) (top), (5.3) (middle) and (5.4) (bottom), at three different frequencies.

D.1.2 Cole-Cole plots

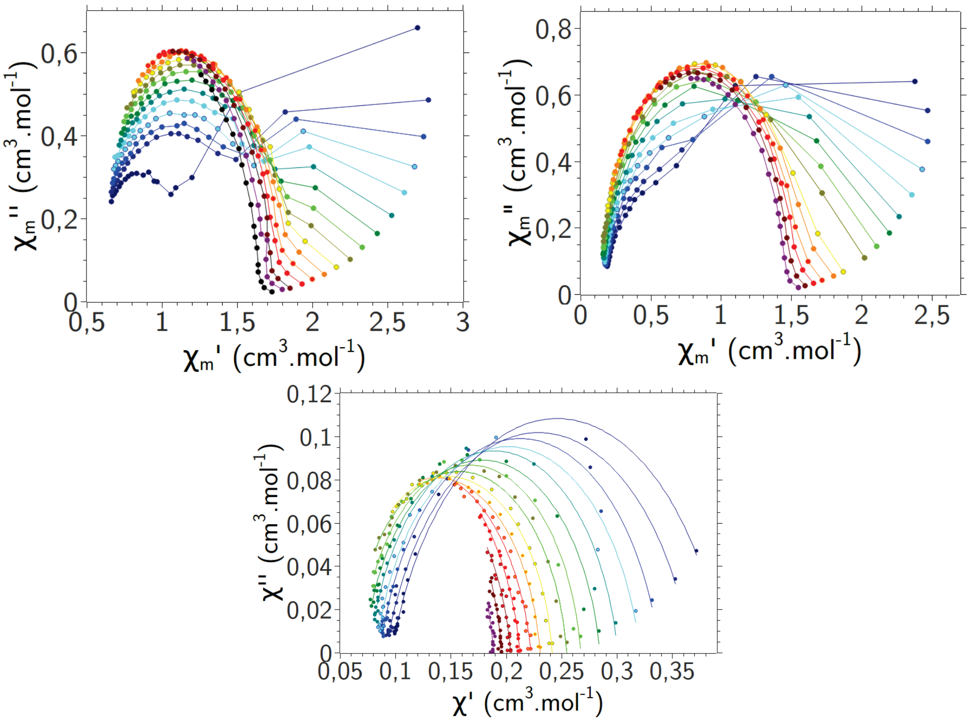

FIGURE D.1.2: Cole-Cole ($\chi''_m = \chi'_m$) plots for complexes (5.1) (top left), (5.3) (top right) and (5.4) (bottom), under a static field of 2000 Oe and between 2K and 6K.

D.2 AC magnetometry of the [LnTp$_2$Acac] complexes

D.2.1 Arrhenius plot for (5.6)

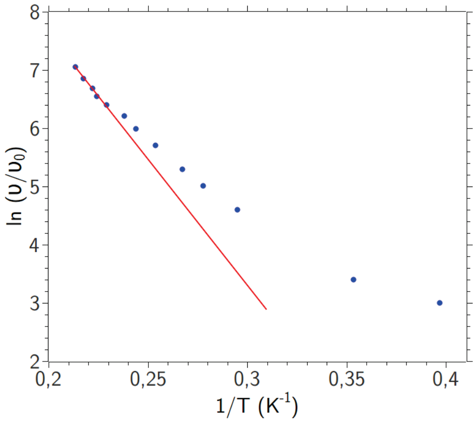

FIGURE D.2.1: Arrhenius plot $ln\nu = f(1/T)$, for complex (5.6), under a static field of 500Oe. The solid line is a guide for the eye.

D.2.2 Cole-Cole plots

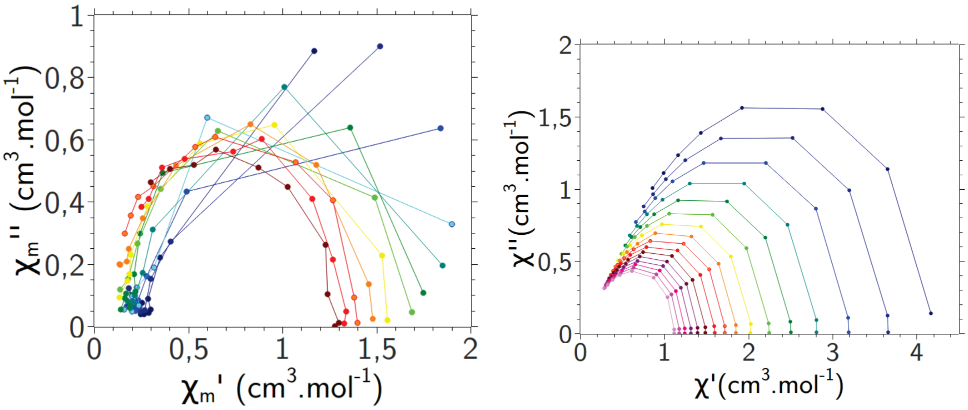

FIGURE D.2.2: Cole-Cole ($\chi''_m = \chi'_m$) plots for complexes (5.8) (left) and (5.12) (right), under static fields of respectively 2000 Oe and 0 Oe.

Appendix E

Programs

E.1 Uncertainties

```fortran
Program Uncertainties
implicit none

double precision, dimension(3,3)              :: chi, chitodiag, chidiag, minchi
double precision, dimension(3,3)              :: delta, tmp, step
double precision, dimension(3)                :: eigen,supeigen,mineigen,vartmp1,var
integer                                       :: num, a, b, c, d, e, f
integer,dimension(3,3)                        :: inc
double precision                              :: time1,time2,yoy
integer                                       :: i,j,k,l,m,n,o
double precision, dimension(:), allocatable   :: eigenval1,eigenval2,eigenval3
character(LEN=80)                             :: entree, filename

write(6,*) 'File␣containing␣the␣tensor␣?␣(format␣:␣)'
write(6,*) 'x11,␣Dx11,␣step11'
write(6,*) 'x12,␣Dx12,␣step12'
write(6,*) 'x13,␣Dx13,␣step13'
write(6,*) 'x22,␣Dx22,␣step22'
write(6,*) 'x23,␣Dx23,␣step23'
write(6,*) 'x33,␣Dx33,␣step33'
write(6,*) '␣without␣.dat␣extension'
read(5,*) entree

CALL CPU_TIME(time1)
! First we get the data
filename = TRIM(entree)//'.dat'
OPEN(unit=12,file=TRIM(filename),action='read')

read(unit=12,fmt=*) chi(1,1), delta(1,1), inc(1,1)
read(unit=12,fmt=*) chi(1,2), delta(1,2), inc(1,2)
read(unit=12,fmt=*) chi(1,3), delta(1,3), inc(1,3)
read(unit=12,fmt=*) chi(2,2), delta(2,2), inc(2,2)
read(unit=12,fmt=*) chi(2,3), delta(2,3), inc(2,3)
read(unit=12,fmt=*) chi(3,3), delta(3,3), inc(3,3)

! we set the matrices (real, symmetric)

 inc(2,1)=inc(1,2)
 inc(3,1)=inc(1,3)
 inc(3,2)=inc(2,3)

 delta(2,1)=delta(1,2)
 delta(3,1)=delta(1,3)
 delta(3,2)=delta(2,3)

 chi(2,1)=chi(1,2)
 chi(3,1)=chi(1,3)
 chi(3,2)=chi(2,3)

! then we compute the step in chi for the computation of the eigenvalues
```

```
do i=1,3
        do j=1,3
                step(i,j)=delta(i,j)/inc(i,j)
        end do
end do

! we then compute the tensor for each component set to its minimum value
do i=1,3
        do j=1,3
                minchi(i,j)=chi(i,j)-delta(i,j)
        end do
end do

! The following 3 lines be commented if the calculation is huge (scales as increment^6),
! since the arrays eigenvalK will contain all the computed eigenvalues
num=(inc(1,1)+1)*(inc(1,2)+1)*(inc(1,3)+1)*(inc(2,2)+1)*(inc(2,3)+1)*(inc(3,3)+1)
allocate(eigenval1(num),eigenval2(num),eigenval3(num))
k=1

! we set the testing values first as the eigenvalues of the starting tensor
do i=1,3
        do j=1,3
        tmp(i,j)=chi(i,j)
        end do
end do

call DSYEVC3(tmp,eigen)
do i=1,3
        mineigen(i)=eigen(i)
        supeigen(i)=eigen(i)
end do

! and we start the loop scanning the 6 components
do a=0,inc(1,1)
        do b=0,inc(1,2)
                do c=0,inc(1,3)
                        do d=0,inc(2,2)
                                do e=0,inc(2,3)
                                        do f=0,inc(3,3)
                                        tmp(1,1)=minchi(1,1)+step(1,1)*a
                                        tmp(1,2)=minchi(1,2)+step(1,2)*b
                                        tmp(1,3)=minchi(1,3)+step(1,3)*c
                                        tmp(2,2)=minchi(2,2)+step(2,2)*d
                                        tmp(2,3)=minchi(2,3)+step(2,3)*e
                                        tmp(3,3)=minchi(3,3)+step(3,3)*f
                                        tmp(2,1)=tmp(1,2)
                                        tmp(3,1)=tmp(1,3)
                                        tmp(3,2)=tmp(2,3)
! we just build the working matrix, that will be diagonalised
                                        call DSYEVC3(tmp,eigen)
                                        do i=1,3
                                                if(eigen(i).GT.supeigen(i)) then
                                                        supeigen(i)=eigen(i)
                                                else if(eigen(i).LT.mineigen(i)) then
                                                        mineigen(i)=eigen(i)
                                                end if
                                        end do
! and we tested the components, to check whether they are smaller
! or bigger than the previous min or max
! if so, we store them as new extrema. That way, we do not
! actually have to store the data
! The next 4 lines actually store the data (debugging option),
! and they may be commented for big calculations
                                        eigenval1(k)=eigen(1)
                                        eigenval2(k)=eigen(2)
                                        eigenval3(k)=eigen(3)
                                        k=k+1
                                        end do
                                end do
                        end do
                end do
        end do
end do
```

```
write(6,*) 'Maximum␣value␣for␣each␣component␣'
write(6,*) supeigen(1),supeigen(2),supeigen(3)
write(6,*) 'Minimum␣value␣for␣each␣component'
write(6,*) mineigen(1),mineigen(2),mineigen(3)
write(6,*) 'Starting␣eigenvalues'
call DSYEVC3(chi,eigen)
write(6,*) eigen(1),eigen(2),eigen(3)

! Same thing as before: if there is a huge number of
! points to compute, these lines may be commented
write(6,*) '␣'
write(6,*) 'Maximal␣values␣read␣from␣the␣whole␣data␣set'
write(6,*) MAXVAL(eigenval1),MAXVAL(eigenval2),MAXVAL(eigenval3)
write(6,*) 'Minimal␣values␣read␣from␣the␣whole␣data␣set'
write(6,*) MINVAL(eigenval1),MINVAL(eigenval2),MINVAL(eigenval3)
filename = TRIM(entree)//'.out'
OPEN(unit=13,file=TRIM(filename),action='write')
do j=1,3
        vartmp1(j)=0
        var(j)=0
end do
do i=1,num
        write(13,*) eigenval1(i),eigenval2(i),eigenval3(i)
        vartmp1(1)=(eigenval1(i)-eigen(1))*(eigenval1(i)-eigen(1))
        vartmp1(2)=(eigenval2(i)-eigen(2))*(eigenval2(i)-eigen(2))
        vartmp1(3)=(eigenval3(i)-eigen(3))*(eigenval3(i)-eigen(3))
        do j=1,3
                var(j)=var(j)+(1.0/(num*1.0))*vartmp1(j)
        end do
end do
Close(13)

write(6,*) 'Variance'
write(6,"(ES12.5E3)") var(1),var(2),var(3)

CALL CPU_TIME(time2)
yoy=time2-time1
write(6,*) 'Calculation␣completed␣in␣',yoy,'s'
end program Uncertainties
```

The `DSYEVC3` subroutine (diagonalisation of matrices) can be found in "J. Kopp, *Int. J. Mod. Phys. C* 19 (**2008**), 523-548".

E.2 Conversion

```
PROGRAM CalcM
implicit none

character(LEN=80)                       :: choice,input,orient,output,filename
character(LEN=80)                       :: sortie1,sortie2,sym
real(8),  parameter                     :: pi=3.14159265358979d0
character(len=80)                       :: formdat
integer                                 :: N,M,P
real(8), dimension(:,:),allocatable     :: fields
real(8), dimension(3,3)                 :: chi,Mccslcri,Mmolcal,Mcrimol
real(8), dimension(3,3)                 :: Mcriccsl,Mcalmol, Mmolcri
real(8), dimension(:,:),allocatable     :: moments,symop
real(8),dimension(:),allocatable        :: meanmom
real(8), dimension(3)                   :: fieldi,momveci,fieldcry,mat1,mat2
real(8)                                 :: momi
real(8)                                 :: time1,time2,time3,tottime
integer                                 :: i,j
CHARACTER(LEN=80)                       :: at0cry,at1cry,at2cry,at3cry,at0cal,at1cal,
CHARACTER(LEN=80)                       :: at2cal,at3cal ! atoms labels in the .inp file
real(8), dimension(3)                   :: Ybcry, X1cry, X2cry, X3cry
! central and other atoms positions in the lattice cell
real(8), dimension(3)                   :: Ybcal, X1cal, X2cal, X3cal
! same, in the calculation frame
real(8), dimension(3,3)                 :: chical ! susceptibility tensor
real(8), dimension(3)                   :: v1ccsl,v2ccsl,v3ccsl ! CCSL basis vectors

write(6,*) ’**********************************************************************’
write(6,*) ’CalcM’
write(6,*) ’Frederic␣Guegan’
write(6,*) ’march␣2016’
write(6,*) ’␣’
write(6,*) ’Program␣for␣the␣calculation␣of␣single␣crystal␣magnetisation␣from␣PND’
write(6,*) ’or␣ab␣initio␣data’
write(6,*) ’␣’
write(6,*) ’**********************************************************************’

write(6,*) ’␣’
write(6,*) ’␣Which␣kind␣of␣data␣would␣you␣like␣to␣use␣:␣PND(p)␣or␣Ab␣Initio(a)␣?’
read(5,*) choice
write(6,*) ’␣Name␣of␣the␣input␣file␣(without␣.inp␣extension)␣?␣’
read(5,*) input
write(6,*) ’␣Name␣of␣orientations␣file␣(without␣.dat␣extension)␣?␣’
read(5,*) orient
write(6,*) ’␣Name␣of␣the␣output␣file␣(without␣.out␣extension)␣?␣’
read(5,*) output
write(6,*) ’␣Name␣of␣the␣symmetry␣file␣(without␣extension␣.sym)␣?␣’
read(5,*) sym

CALL CPU_TIME(time1)
! Now we read the symmetry file

filename = TRIM(sym)//’.sym’
open(unit=10,file=TRIM(filename),action=’read’)
read(unit=10,fmt=*) M
allocate(symop(M,9)) ! we set the size of the array containing the symmetry operations
do i=1,M
                read(unit=10,fmt=*) symop(i,1),symop(i,2),symop(i,3),symop(i,4)&
                &,symop(i,5),symop(i,6),symop(i,7),symop(i,8),symop(i,9)
end do ! we read the symmetry matrices
close(10)
The \texttt{DSYEVC3} subroutine (diagonalisation of matrices) can be found in "J.␣Kopp,␣\textit{Int.␣J.
! We get the orientation data

filename = TRIM(orient)//’.dat’
open(unit=12,file=TRIM(filename),action=’read’)
read(unit=12,fmt=*) N
allocate(fields(N,4)) ! we define the number of orientations to consider
P=N*M
allocate(moments(P,3)) ! and the total number of computed values
allocate(meanmom(N)) ! and the number of mean magnetisation (for the whole symmetries)
```

```
do i=1,N
        read(unit=12,fmt=*) fields(i,1),fields(i,2),fields(i,3),fields(i,4)
end do
! Here we read the orientations of fields and stocked them in the array 'fields'
close(12)

! Now we get the information contained within the input file.

filename = TRIM(input)//'.inp'
open(unit=11,file=TRIM(filename),action='read')
read(unit=11,fmt=*) at0cry,Ybcry(1),Ybcry(2),Ybcry(3)
read(unit=11,fmt=*) at1cry,X1cry(1),X1cry(2),X1cry(3)
read(unit=11,fmt=*) at2cry,X2cry(1),X2cry(2),X2cry(3)
read(unit=11,fmt=*) at3cry,X3cry(1),X3cry(2),X3cry(3) ! Atoms positions in the lattice

read(unit=11,fmt=*) at0cal,Ybcal(1),Ybcal(2),Ybcal(3)
read(unit=11,fmt=*) at1cal,X1cal(1),X1cal(2),X1cal(3)
read(unit=11,fmt=*) at2cal,X2cal(1),X2cal(2),X2cal(3)
read(unit=11,fmt=*) at3cal,X3cal(1),X3cal(2),X3cal(3) ! Same in the calculation frame

read(unit=11,fmt=*) chical(1,1),chical(1,2),chical(1,3),chical(2,1)&
        &,chical(2,2),chical(2,3),chical(3,1),chical(3,2),chical(3,3)
! susceptibility tensor

read(unit=11,fmt=*) v1ccsl(1),v1ccsl(2),v1ccsl(3)
read(unit=11,fmt=*) v2ccsl(1),v2ccsl(2),v2ccsl(3)
read(unit=11,fmt=*) v3ccsl(1),v3ccsl(2),v3ccsl(3) ! CCSL vectors in the lattice cell
CLOSE(11)

! We prepare the matrices

do i=1,3
        Mcriccsl(i,1)=v1ccsl(i)
        Mcriccsl(i,2)=v2ccsl(i)
        Mcriccsl(i,3)=v3ccsl(i)
end do ! Mcriccsl is OK

do i=1,3
        Mcrimol(i,1)=X1cry(i)-Ybcry(i)
        Mcrimol(i,2)=X2cry(i)-Ybcry(i)
        Mcrimol(i,3)=X3cry(i)-Ybcry(i)
end do ! Mcrimol is OK

do i=1,3
        Mcalmol(i,1)=X1cal(i)-Ybcal(i)
        Mcalmol(i,2)=X2cal(i)-Ybcal(i)
        Mcalmol(i,3)=X3cal(i)-Ybcal(i)
end do ! Mcalmol is OK

call inverse(Mcalmol,Mmolcal,3)
call inverse(Mcrimol,Mmolcri,3)
call inverse(Mcriccsl,Mccslcri,3)

! and we inversed the three previous matrices
! Nota: they may not be all used, but we may assume their computation
! is not a tremendously demanding task

if(choice.EQ.'p') then
        call PND(P,N,M,fields,chical,Mcriccsl,moments,symop,meanmom)
else if(choice.EQ.'a') then
        call Abinit(P,N,M,fields,chical,Mccslcri,Mcrimol,Mmolcal,moments,symop,meanmom)
else
        write(6,*) 'Unrecognised␣data␣label.␣Please␣check.'
end if

sortie1 = TRIM(output)//'1.out'
OPEN(unit=13,file=TRIM(sortie1),action='write',status='new')
write(13,*) '*********************************************************************'
write(13,*) 'CalcM'
write(13,*) 'Frederic␣Guegan␣'
write(13,*) 'march␣2016'
write(13,*) '␣'
write(13,*) '␣Program␣for␣the␣calculation␣of␣single␣crystal␣magnetisation␣from␣PND'
```

```
write(13,*) '␣or␣ab␣initio␣data␣'
write(13,*) '␣'
write(13,*) '******************************************************************'
write(13,*) '␣Implemented␣by␣:'
write(13,*) '␣'
write(13,*) '␣Frederic␣Guegan,␣University␣of␣Lyon␣1␣'
write(13,*) '␣frederic.guegan(at)univ-lyon1.fr'
write(13,*) '␣'
write(13,*) '␣␣Team␣Crystallography␣and␣Molecular␣Engineering␣(Prof.␣D.␣Luneau)␣'
write(13,*) '␣␣Multimaterials␣and␣Interfaces␣Laboratory␣(LMI,␣UMR␣CNRS-UCBL␣5615)'
write(13,*) '␣'
write(13,*) '␣␣Team␣Chemometrics␣and␣Theoretical␣Chemistry␣(Prof.␣C.␣Morell)␣'
write(13,*) '␣␣Lyon␣Institute␣for␣Analytical␣Sciences␣(ISA,␣UMR␣CNRS-UCBL-ENS␣5280)'
write(13,*) '␣'
write(13,*) '******************************************************************'
write(13,*) '␣This␣program␣is␣freely␣distributed␣and␣modifiable␣by␣anyone.'
write(13,*) '␣I␣do␣not␣guarantee␣the␣exactitude␣of␣the␣calculations␣(though'
write(13,*) '␣I␣did␣my␣best).␣Please␣feel␣free␣to␣contact␣me␣if␣you␣find␣any'
write(13,*) '␣error␣in␣the␣code␣!'
write(13,*) '******************************************************************'
write(13,*) '␣'
write(13,*) '␣'
write(13,*) 'Type␣of␣data:␣'
if(choice.EQ.'p') then
        write(13,*) '␣␣␣␣PND␣experiment␣'
else if(choice.EQ.'a') then
        write(13,*) '␣␣␣␣Ab␣initio␣data␣'
end if
write(13,*) '␣'

write(13,*) 'Printing␣the␣matrices␣used␣for␣the␣transformation:'

write(13,*) 'Mcalmol␣:'
do i=1,3
        write(13,*) Mcalmol(i,1),Mcalmol(i,2),Mcalmol(i,3)
end do
write(13,*) '␣'

write(13,*) 'Mmolcal␣:'
do i=1,3
        write(13,*) Mmolcal(i,1),Mmolcal(i,2),Mmolcal(i,3)
end do
write(13,*) '␣'

write(13,*) 'Mcriccsl␣:'
do i=1,3
        write(13,*) Mcriccsl(i,1),Mcriccsl(i,2),Mcriccsl(i,3)
end do
write(13,*) '␣'

write(13,*) 'Mccslcri␣:'
do i=1,3
        write(13,*) Mccslcri(i,1),Mccslcri(i,2),Mccslcri(i,3)
end do
write(13,*) '␣'

write(13,*) 'Mcrimol␣:'
do i=1,3
        write(13,*) Mcrimol(i,1),Mcrimol(i,2),Mcrimol(i,3)
end do
write(13,*) '␣'

write(13,*) 'Mmolcri'
do i=1,3
        write(13,*) Mmolcri(i,1),Mmolcri(i,2),Mmolcri(i,3)
end do
write(13,*) '␣'
write(13,*) '␣'
write(13,*) '␣Results␣for␣all␣symmetries'
write(13,*) '␣'

write(13,*) '␣Theta␣␣␣␣␣␣␣␣␣␣␣␣␣␣␣␣␣␣␣␣Mcalc␣␣␣␣␣␣␣␣␣␣␣␣␣␣␣␣␣␣␣␣␣␣H␣norm'
do i=1,P
```

```
        write(13,*) '␣',moments(i,1),'␣',moments(i,2),'␣',moments(i,3)
end do

call CPU_TIME(time2)

tottime=time2-time1

write(13,*) '␣'
write(13,*) 'Total␣time␣of␣execution␣(s):',tottime
close(13)

sortie2 = TRIM(output)//'2.out'
OPEN(unit=14,file=TRIM(sortie2),action='write',status='new')
write(14,*) '******************************************************************'
write(14,*) 'CalcM'
write(14,*) 'Frederic␣Guegan␣'
write(14,*) 'march␣2016'
write(14,*) '␣'
write(14,*) '␣Program␣for␣the␣calculation␣of␣single␣crystal␣magnetisation␣from␣PND'
write(14,*) '␣or␣ab␣initio␣data␣'
write(14,*) '␣'
write(14,*) '******************************************************************'
write(14,*) '␣Implemented␣by␣:'
write(14,*) '␣'
write(14,*) '␣Frederic␣Guegan,␣University␣of␣Lyon␣1␣'
write(14,*) '␣frederic.guegan(at)univ-lyon1.fr'
write(14,*) '␣'
write(14,*) '␣␣Team␣Crystallography␣and␣Molecular␣Engineering␣(Prof.␣D.␣Luneau)␣'
write(14,*) '␣␣Multimaterials␣and␣Interfaces␣Laboratory␣(LMI,␣UMR␣CNRS-UCBL␣5615)'
write(14,*) '␣'
write(14,*) '␣␣Team␣Chemometrics␣and␣Theoretical␣Chemistry␣(Prof.␣C.␣Morell)␣'
write(14,*) '␣␣Lyon␣Institute␣for␣Analytical␣Sciences␣(ISA,␣UMR␣CNRS-UCBL-ENS␣5280)'
write(14,*) '␣'
write(14,*) '******************************************************************'
write(14,*) '␣This␣program␣is␣freely␣distributed␣and␣modifiable␣by␣anyone.'
write(14,*) '␣I␣do␣not␣guarantee␣the␣exactitude␣of␣the␣calculations␣(though'
write(14,*) '␣I␣did␣my␣best).␣Please␣feel␣free␣to␣contact␣me␣if␣you␣find␣any'
write(14,*) '␣error␣in␣the␣code␣!'
write(14,*) '******************************************************************'
write(14,*) '␣'
write(14,*) '␣'
write(14,*) 'Type␣of␣data:␣'
if(choice.EQ.'p') then
        write(14,*) '␣␣␣␣PND␣experiment␣'
else if(choice.EQ.'a') then
        write(14,*) '␣␣␣␣Ab␣initio␣data␣'
end if
write(14,*) '␣'

write(14,*) 'Printing␣the␣matrices␣used␣for␣the␣transformation:'

write(14,*) 'Mcalmol␣:'
do i=1,3
        write(14,*) Mcalmol(i,1),Mcalmol(i,2),Mcalmol(i,3)
end do
write(14,*) '␣'

write(14,*) 'Mmolcal␣:'
do i=1,3
        write(14,*) Mmolcal(i,1),Mmolcal(i,2),Mmolcal(i,3)
end do
write(14,*) '␣'

write(14,*) 'Mcriccsl␣:'
do i=1,3
        write(14,*) Mcriccsl(i,1),Mcriccsl(i,2),Mcriccsl(i,3)
end do
write(14,*) '␣'

write(14,*) 'Mccslcri␣:'
do i=1,3
        write(14,*) Mccslcri(i,1),Mccslcri(i,2),Mccslcri(i,3)
end do
```

```
write(14,*) '␣'

write(14,*) 'Mcrimol␣:'
do i=1,3
        write(14,*) Mcrimol(i,1),Mcrimol(i,2),Mcrimol(i,3)
end do
write(14,*) '␣'

write(14,*) 'Mmolcri'
do i=1,3
        write(14,*) Mmolcri(i,1),Mmolcri(i,2),Mmolcri(i,3)
end do
write(14,*) '␣'
write(14,*) '␣'
write(14,*) '␣Results␣for␣all␣symmetries'
write(14,*) '␣'

write(14,*) '␣Theta␣␣␣␣␣␣␣␣␣␣␣␣␣␣␣␣␣␣␣␣Mcalc␣␣␣␣␣␣␣␣␣␣␣␣␣␣␣␣␣␣␣␣␣␣H␣norm'
do i=1,N
        write(14,*) '␣',moments(i,1),'␣',meanmom(i),'␣',moments(i,3)
end do

call CPU_TIME(time3)

tottime=time3-time1

write(14,*) '␣'
write(14,*) 'Total␣time␣of␣execution␣(s):',tottime
close(14)

end program CalcM

subroutine PND(P,N,M,fields,chi,Mcriccsl,moments,symop,meanmom)
! Subroutine for the calculation of the magnetisation induced by a field applied
! along a given direction, from the local susceptibility tensor (deduced from
! PND experiments) and in the linear approximation : m = XH.
! Arguments: N, number of field orientations ; fields, array of the field orientations;
! chi, susceptibility tensor ; Mcriccsl, matrix of the CCSL vectors in the lattice basis.
! Output of subroutine : array of calculated moments versus theta, and norm of the
! magnetic field (control, should be 1).
implicit none

character(len=80)                       :: formdat,sym
integer                                 :: N,M,P
real(8), dimension(N,4)                 :: fields
real(8), dimension(3,3)                 :: chi,Mcriccsl,Opsym,chisym,tOpsym,tmp
real(8), dimension(P,3)                 :: moments
real(8), dimension(N)                   :: meanmom
real(8), dimension(M,9)                 :: symop
real(8), dimension(3)                   :: fieldi,momveci,fieldcry
real(8)                                 :: momi
integer                                 :: i,j,k,l,t


write(6,*) '******************************************************************'
write(6,*) 'PND'
write(6,*) 'Frederic␣Guegan'
write(6,*) 'march␣2016'
write(6,*) '␣'
write(6,*) '␣Evaluation␣of␣the␣single␣crystal␣magnetisation␣from␣PND␣experiments␣'
write(6,*) '␣'
write(6,*) '******************************************************************'

write(6,*) '␣Format␣of␣the␣orient.dat␣file␣(CCSL:yes,␣crystal:no)'
read(5,*) formdat
if(formdat.EQ.'yes') then
        do i=1,N
                meanmom(i)=0
        end do
        do j=1,M
                do i=1,N
                        fieldi(1)=fields(i,2)
                        fieldi(2)=fields(i,3)
```

```
                        fieldi(3)=fields(i,4)
! we first assign to fieldi the direction of the field at point i
                        do k=1,3
                                l=k+3
                                t=k+6
                                Opsym(1,k) = symop(j,k)
                                Opsym(2,k) = symop(j,l)
                                Opsym(3,k) = symop(j,t)
! we built the matrix for each symm operation (loop in j)
                        end do
                        do l=1,3
                                do t=1,3
                                        tOpsym(l,t)=Opsym(t,l)
! we transpose the symmetry matrix
                                end do
                        end do
                        write(6,*) tOpsym(1,1),tOpsym(1,2),tOpsym(1,3)
                        write(6,*) tOpsym(2,1),tOpsym(2,2),tOpsym(2,3)
                        write(6,*) tOpsym(3,1),tOpsym(3,2),tOpsym(3,3)
                        tmp=MATMUl(chi,Opsym)
! we begin the symmetry transformation of chi

                        chisym=MATMUL(tOpsym,tmp)
                        momveci=MATMUL(chisym,fieldi)
                        momi=momveci(1)*fieldi(1)+momveci(2)*fieldi(2)+momveci(3)*fieldi(3)
! scalar product of vec(m) and vec(H)
                        k=i+(j-1)*N
                        moments(k,1)=fields(i,1)
                        moments(k,2)=momi
                        moments(k,3)=sqrt(fieldi(1)*fieldi(1)+fieldi(2)*fieldi(2)+&
                        &fieldi(3)*fieldi(3))
                        meanmom(i)=meanmom(i)+momi/(M*1.0)
                end do
        end do
else if(formdat.EQ.'no') then
        do j=1,M
                do i=1,N
                        fieldcry(1)=fields(i,2)
                        fieldcry(2)=fields(i,3)
                        fieldcry(3)=fields(i,4)

                        fieldi=MATMUL(Mcriccsl,fieldcry)

                        do k=1,3
                                l=k+3
                                m=k+6
                                Opsym(1,k) = symop(j,k)
                                Opsym(2,k) = symop(j,l)
                                Opsym(3,k) = symop(j,m)
                        end do
                        do l=1,3
                                do m=1,3
                                        tOpsym(l,m)=Opsym(m,l)
! we transpose the symmetry matrix
                                end do
                        end do
                        tmp=MATMUl(chi,Opsym)
! we begin the symmetry transformation of chi
                        chisym=MATMUL(tOpsym,tmp)
                        momveci=MATMUL(chisym,fieldi)
                        momi=momveci(1)*fieldi(1)+momveci(2)*fieldi(2)+momveci(3)*fieldi(3)
! scalar product of vec(m) and vec(H)
                        k=i+(j-1)*N
                        moments(k,1)=fields(i,1)
                        moments(k,2)=momi
                        moments(k,3)=sqrt(fieldi(1)*fieldi(1)+fieldi(2)*fieldi(2)+&
                        &fieldi(3)*fieldi(3))
                        meanmom(i)=meanmom(i)+momi/(M*1.0)
                end do
        end do
else
        write(6,*) 'Unrecognised␣format␣identifier,␣please␣check.'
end if
```

```
end subroutine PND

subroutine Abinit(P,N,M,fields,chi,Mmolcri,Mcalmol,Mcriccsl,moments,symop,meanmom)
! Subroutine for the calculation of the magnetisation induced by a field applied along
! a given direction, from ab initio calculated susceptibility tensor and in the linear
! approximation : m = XH.
! Arguments: N, number of field orientations ; fields, array of the field orientations;
! chi, susceptibility tensor ; Mcriccsl, matrix of the CCSL vectors in the lattice basis;
! Mmolcri, inverse of the matrix of three vectors (based on 4 non collinear atoms) in the
! lattice cell ;
! Mcalmol, inverse of the same matrix but in the basis of the calculation (orthonormal frame).
! Output of subroutine : array of calculated moments versus theta, and norm of the
! magnetic field (control, should be 1).

implicit none
character(len=80)                       :: formdat
integer                                 :: N,P,M
real(8), dimension(N,4)                 :: fields
real(8), dimension(3,3)                 :: chi,Mcriccsl,tMcriccsl,Mcalmol,Mmolcri
real(8), dimension(3,3)                 :: mat1,mat2,mat3,mat4
real(8), dimension(3,3)                 :: chiccsl,Opsym,tOpsym,chisym,tmp
real(8), dimension(p,3)                 :: moments
real(8), dimension(N)                   :: meanmom
real(8), dimension(M,9)                 :: symop
real(8), dimension(3)                   :: fieldi,momveci,fieldcry
real(8)                                 :: momi,norm
integer                                 :: i,j,l,t,k

write(6,*) '*******************************************************************************'
write(6,*) 'Abinit'
write(6,*) 'Frederic␣Guegan'
write(6,*) 'march␣2016'
write(6,*) '␣'
write(6,*) '␣Evaluation␣of␣the␣single␣crystal␣magnetisation␣from␣Ab␣initio␣calculations␣'
write(6,*) '␣'
write(6,*) '*******************************************************************************'

write(6,*) '␣Format␣of␣the␣orient.dat␣file␣(CCSL:yes,␣crystal:no)'
read(5,*) formdat
if(formdat.EQ.'yes') then
        do i=1,N
                meanmom(i)=0
        end do
        mat1=MATMUL(Mcalmol,Mmolcri)
! matrix from the calculated frame to the crystal one
                do i=1,3
                        do j=1,3
                                mat2(i,j)=mat1(j,i)
                        end do
                end do ! mat2 = t(mat1)
                do i=1,3
                        do j=1,3
                                tMcriccsl(i,j)=Mcriccsl(j,i)
                        end do
                end do ! we transpose Mccslcri
        mat3=MATMUL(mat2,chi)
        mat4=MATMUL(mat3,mat1)
        mat1=MATMUL(mat4,Mcriccsl)
        chiccsl=MATMUL(tMcriccsl,mat1)
        norm=chiccsl(1,1)*(chiccsl(2,2)*chiccsl(3,3)-chiccsl(3,2)*chiccsl(2,3))-&
             chiccsl(1,2)*(chiccsl(2,1)*chiccsl(3,3)-chiccsl(3,1)*chiccsl(2,3))+&
             chiccsl(1,3)*(chiccsl(2,1)*chiccsl(3,2)-chiccsl(3,1)*chiccsl(2,2))
        write(6,*) norm
        do j=1,M
                do i=1,N
                        fieldi(1)=fields(i,2)
                        fieldi(2)=fields(i,3)
                        fieldi(3)=fields(i,4)
! we first assign to fieldi the direction of the field at point i
                        do k=1,3
                                l=k+3
                                t=k+6
```

```
                                Opsym(1,k) = symop(j,k)
                                Opsym(2,k) = symop(j,l)
                                Opsym(3,k) = symop(j,t)
! we built the matrix for each symm operation (loop in j)
                        end do
                        do l=1,3
                                do t=1,3
                                        tOpsym(l,t)=Opsym(t,l)
! we transpose the symmetry matrix
                                end do
                        end do
                        tmp=MATMUl(chiccsl,Opsym)
! we begin the symmetry transformation of chi
                        chisym=MATMUL(tOpsym,tmp)
                        momveci=MATMUL(chisym,fieldi)
! evaluation of the magnetisation in the CCSL lattice
                        momi=momveci(1)*fieldi(1)+momveci(2)*fieldi(2)+momveci(3)*fieldi(3)
! scalar product of vec(m) and vec(H) : magnetisation along the field direction
                        k=i+(j-1)*N
                        moments(k,1)=fields(i,1)
                        moments(k,2)=momi
                        moments(k,3)=sqrt(fieldi(1)*fieldi(1)+fieldi(2)*fieldi(2)+&
                        &fieldi(3)*fieldi(3))
                        meanmom(i)=meanmom(i)+momi/(M*1.0)
                end do
        end do
else if(formdat.EQ.'no') then
do i=1,N
! we do the same thing as previously, but we also change the frame for the field (cry -> CCSL)
        meanmom(i)=0
end do
        mat1=MATMUL(Mcalmol,Mmolcri)
! matrix from the calculated frame to the crystal one
                do i=1,3
                        do j=1,3
                                mat2(i,j)=mat1(j,i)
                        end do
                end do ! mat2 = t(mat1)
                do i=1,3
                        do j=1,3
                                tMcriccsl(i,j)=Mcriccsl(j,i)
                        end do
                end do ! we transpose Mccslcri
        mat3=MATMUL(mat2,chi)
        mat4=MATMUL(mat3,mat1)
        mat1=MATMUL(mat4,Mcriccsl)
        chiccsl=MATMUL(tMcriccsl,mat1)
        norm=chiccsl(1,1)*(chiccsl(2,2)*chiccsl(3,3)-chiccsl(3,2)*chiccsl(2,3))-&
             chiccsl(1,2)*(chiccsl(2,1)*chiccsl(3,3)-chiccsl(3,1)*chiccsl(2,3))+&
             chiccsl(1,3)*(chiccsl(2,1)*chiccsl(3,2)-chiccsl(3,1)*chiccsl(2,2))
        write(6,*) norm
        do j=1,M
                do i=1,N
                        fieldcry(1)=fields(i,2)
                        fieldcry(2)=fields(i,3)
                        fieldcry(3)=fields(i,4)
! we first assign to fieldi the direction of the field at point i
                        fieldi=MATMUL(Mcriccsl,fieldcry)
                        do k=1,3
                                l=k+3
                                m=k+6
                                Opsym(1,k) = symop(j,k)
                                Opsym(2,k) = symop(j,l)
                                Opsym(3,k) = symop(j,m)
                        end do
                        do l=1,3
                                do m=1,3
                                        tOpsym(l,m)=Opsym(m,l)
! we transpose the symmetry matrix
                                end do
                        end do
                        tmp=MATMUl(chiccsl,Opsym)
! we begin the symmetry transformation of chi
```

```
                        chisym=MATMUL(tOpsym,tmp)
                        momveci=MATMUL(chisym,fieldi)
! evaluation of the magnetisation in the CCSL lattice
                        momi=momveci(1)*fieldi(1)+momveci(2)*fieldi(2)+momveci(3)*fieldi(3)
! scalar product of vec(m) and vec(H) : magnetisation along the field directio
                        k=i+(j-1)*N
                        moments(k,1)=fields(i,1)
                        moments(k,2)=momi
                        moments(k,3)=sqrt(fieldi(1)*fieldi(1)+fieldi(2)*fieldi(2)+&
                        &fieldi(3)*fieldi(3))
                        meanmom(i)=meanmom(i)+momi/(M*1.0)
                end do
        end do
else
        write(6,*) 'Unrecognised␣format␣identifier,␣please␣check.'
end if
end subroutine Abinit
```

The `inverse` subroutine (inversion of matrices) was implemented by Alexander Godunov (Old Dominion University, USA), and can be found on his webpage (http://ww2.odu.edu/∼agodunov/computing.html).

Appendix F

Publications

PCCP

PAPER

View Article Online
View Journal | View Issue

Cite this: *Phys. Chem. Chem. Phys.*, 2014, **16**, 15558

Dual descriptor and molecular electrostatic potential: complementary tools for the study of the coordination chemistry of ambiphilic ligands

Frédéric Guégan,*[a] Pierre Mignon,[a] Vincent Tognetti,[b] Laurent Joubert[b] and Christophe Morell*[a]

Received 14th April 2014,
Accepted 30th May 2014

DOI: 10.1039/c4cp01613k

www.rsc.org/pccp

In this paper, we show that the ambiphilic properties of some organic ligands in organometallic complexes may be retrieved readily from simple calculations in the framework of conceptual density functional theory (C-DFT): namely, the dual descriptor (DD) and the molecular electrostatic potential (MEP) of the ligands afford a rather straightforward interpretation of experimental trends such as the bonding geometry and the electronic properties of complexes in terms of σ-, π- and back-bonding. The studied ligands were chosen to be representative of the wide variety organometallic chemistry offers, ranging from neutral to charged systems and from diatomic to polyatomic molecules. The present approach is general since all relevant parameters are retrieved from the electron density, obtained either from a DFT or post-Hartree–Fock calculation. It is believed to be helpful for organometallic chemists, since it allows a deep understanding and may be used as a predictive tool of the coordinating properties of ligands.

1 Introduction

The interplay between metallic cation(s) and organic ligand(s) is the cornerstone of organometallic chemistry.[1] According to the simplest scheme, the metallic cations are perfect Lewis acids and the ligands, perfect Lewis bases.[2] However, these ideal cases are certainly not the most interesting from the theoretical and practical point of view. Indeed, most of the time, ligands can also be electrophilic and metals may display a nucleophilic character. This results in non-obvious situations where electron transfers may occur either from ligands to metals and the other way around (as involved for instance in the Dewar–Chatt–Duncanson model[3]). As a consequence, charge transfers are likely to occur, and, in the end, coordination bonds are intermediate between purely ionic and purely covalent. The limits of the so-called Klopman–Salem model,[4,5] stating that reactions usually imply either a charge or an orbital control, are in these cases reached. Hence, to get a complete picture of the chemical behaviour of organometallic compounds one has to rely upon two descriptors, one of them characterizing the charge transfer while the other should describe the electrostatic interactions.

Within the canonical ensemble, such descriptors can be deduced from a survey of the variations of the total energy when the molecule reacts with another compound. To do so, we can perform a second order Taylor expansion of the variations of the total molecular energy with respect to the variation of the external potential $\delta v(\mathbf{r})$ and the number of electrons $\mathrm{d}N$:

$$\begin{aligned}\mathrm{d}E[v(\mathbf{r});N] &= \mu\mathrm{d}N + \frac{\eta}{2}\mathrm{d}N^2 + \mathrm{d}E_{\mathrm{NN}} + \int\rho(\mathbf{r})\delta v(\mathbf{r})\mathrm{d}^3\mathbf{r} \\ &\quad + \mathrm{d}N\int f(\mathbf{r})\delta v(\mathbf{r})\mathrm{d}^3\mathbf{r} + \frac{1}{2}\iint\chi(\mathbf{r},\mathbf{r}')\delta v(\mathbf{r})\delta v(\mathbf{r}')\mathrm{d}^3\mathbf{r}\,\mathrm{d}^3\mathbf{r}'\end{aligned} \tag{1}$$

with E_{NN} the nuclei–nuclei repulsion energy, μ the electronic chemical potential, η the molecular hardness, $f(\mathbf{r})$ the Fukui function and $\chi(\mathbf{r}, \mathbf{r}')$ the non-local linear response kernel (whose evaluation is rather cumbersome and will not be considered in this study). The two first contributions on the right-hand side of eqn (1) are global properties which describe the general response of the molecule as a whole. Conversely, the other terms are essentially local and bear information on the possible regioselectivity of the process, which is the main target of our study. These local terms can be merged into two groups, the first contribution being

$$\mathrm{d}E_1 = \mathrm{d}E_{\mathrm{NN}} + \int\rho(\mathbf{r})\delta v(\mathbf{r})\mathrm{d}^3\mathbf{r} \tag{2}$$

$$= \int\left(-\sum_{\mathrm{M}} Z_{\mathrm{M}}\delta_{\mathrm{D}}(\mathbf{r}-\mathbf{R}_{\mathbf{M}}) + \rho(\mathbf{r})\right)\delta v(\mathbf{r})\mathrm{d}^3\mathbf{r} \tag{3}$$

---

[a] *Laboratoire des Sciences Analytiques, UMR CNRS 5280, Université Claude Bernard Lyon, 1 69622 Villeurbanne Cedex, France. E-mail: frederic.guegan@ens-lyon.org, christophe.morell@univ-lyon1.fr*

[b] *Normandy University, COBRA UMR 6014 & FR 3038, Université de Rouen, INSA Rouen, CNRS, 1 rue Tesnière 76821 Mont St Aignan, Cedex, France*

for a system composed of M atoms of atomic charge Z_M, located at $\mathbf{R_M}$ positions (and δ_D being the Dirac distribution). It is plain to see that this term will essentially contain the electrostatic contributions to the energy variation, plus an exchange and correlation contribution. However, knowing that electrostatic effects are usually more long-ranged than exchange and correlation effects for a charged species, if we assume that our reaction implies ions which are quite remote from each other (early stages of the reaction) the incoming reactant can be treated to a first approximation as a point charge, placed at $\mathbf{R_{pc}}$. The variations of the external potential will thus be approximated by

$$\delta v(\mathbf{r}) = -\frac{\delta q}{|\mathbf{r} - \mathbf{R}_{\text{pc}}|} \tag{4}$$

Putting eqn (4) in eqn (3) yields

$$\mathrm{d}E_1 = \delta q\left(\sum_{\mathrm{M}} Z_{\mathrm{M}} \int \frac{\delta_{\mathrm{D}}(\mathbf{r} - \mathbf{R}_{\mathrm{M}})}{|\mathbf{r} - \mathbf{R}_{\text{pc}}|}\mathrm{d}^3\mathbf{r} - \int \frac{\rho(\mathbf{r})}{|\mathbf{r} - \mathbf{R}_{\text{pc}}|}\mathrm{d}^3\mathbf{r}\right) \tag{5}$$

$$= \delta q\left(\sum_{\mathrm{M}} \frac{Z_{\mathrm{M}}}{|\mathbf{R}_{\mathrm{M}} - \mathbf{R}_{\text{pc}}|} - \int \frac{\rho(\mathbf{r})}{|\mathbf{r} - \mathbf{R}_{\text{pc}}|}\mathrm{d}^3\mathbf{r}\right) = \delta q \cdot \mathrm{MEP}(\mathbf{R}_{\text{pc}}) \tag{6}$$

where MEP is the molecular electrostatic potential. As a result, this first local term seems to be fit for the description of chemical properties driven by charge interactions.

On the other hand, the second term of eqn (1)

$$\mathrm{d}E_2 = \mathrm{d}N\int f(\mathbf{r})\delta v(\mathbf{r})\mathrm{d}^3\mathbf{r} \tag{7}$$

involves the Fukui function, which is defined as

$$f(\mathbf{r}) = \left(\frac{\partial \rho(\mathbf{r})}{\partial N}\right)_{v(\mathbf{r})} \tag{8}$$

Actually, because of the discontinuity of the energy derivatives with respect to the number of electrons, one should rather consider the left ($\mathrm{d}N < 0$) and right ($\mathrm{d}N > 0$) derivatives, respectively corresponding to the $f^-(\mathbf{r})$ and $f^+(\mathbf{r})$ Fukui functions. From their definitions, it is obvious that $f^+(\mathbf{r})$ allows one to find the electrophilic regions, which are likely to gain electrons ($\mathrm{d}N > 0$), and $f^-(\mathbf{r})$ is more fit for looking for the nucleophilic regions (which are prone to lose electron density). This suggests that $\mathrm{d}E_2$ would be rather adapted to describe chemical properties that are driven by "orbital" interactions or more properly by charge density interactions (between nucleophilic and electrophilic regions). As a result, the two local contributions $\mathrm{d}E_1$ and $\mathrm{d}E_2$ should be complementary to study ambiphilic ligands, in the spirit of an extended Klopman–Salem model (where one considers both electrostatic and "orbital" contribution). A further step can be taken by replacing the two Fukui functions by a single descriptor, the dual descriptor (DD):[6,7]

$$\Delta f(\mathbf{r}) = \left(\frac{\partial^2 \rho(\mathbf{r})}{\partial N^2}\right)_{v(\mathbf{r})} \tag{9}$$

It has indeed been shown that this descriptor also conveys information about the charge density interaction. More specifically, one has $\Delta f(\mathbf{r}) > 0$ wherever the molecule is likely to receive electron density (electrophilic regions) and $\Delta f(\mathbf{r}) < 0$ wherever the density is likely to escape (nucleophilic regions).

As a consequence, the combination of the MEP and the DD seems to be adapted to study the coordination chemistry of organometallic complexes. A further simplification of the problem can still be made, considering that usually experimentalists focus on the ligand properties rather than on the metal properties. This is likely due to the fact that changing the metal results in dramatic changes in chemical behaviour, while the synthetic variations of the ligand, such as pendant arms or donor–acceptor substituent, lead to more subtle adjustments. The problem at hand is therefore reduced to a proper description of the ligand properties. They must be characterized at both a global and a local level, that is to say being able to ascertain whether the ligand is rather nucleophilic, electrophilic or both, and its regioselectivity or regiospecificity.

So, in line with recently published studies,[8–10] we propose to use a combination of the DD and the MEP to explain the coordination abilities of ambiphilic or potentially ambiphilic ligands towards metallic cations. To do so, the needed equations are recalled in Section 2, where the details of the computation of the two descriptors are also given. An emphasis is made on the decomposition of the dual descriptor, which allows one to quantify and to build a scale of electrophilicity/nucleophilicity for the studied ligands. In Section 3, different examples are shown and analysed, with a special emphasis on the rationalisation of the experimental trends. Noticeably, ambiphilic behaviours are explicitly rationalised in terms of electron density ("orbital") and charge interactions. Finally, the paper ends with some concluding remarks.

2 Theoretical and computational details

State specific and usual dual descriptor

As discussed in the introduction, calculation of both the MEP and the DD for different ligands should allow us to map quite efficiently their reactivity. Most of computational software now include direct calculations of molecular electrostatic properties (up to the hexapole moment). However it is not necessarily the case for the dual descriptor. Furthermore, eqn (9) is not readily applicable and thus needs to be developed. Usually, two layers of approximations are used:[11]

- Finite difference approximation: one usually approximates the derivative in eqn (9) by the finite variations of the density upon addition or subtraction of electron. This yields

$$\begin{aligned}\Delta f(\mathbf{r}) &\approx \left(\frac{\rho_{N+1}(\mathbf{r}) - \rho_N(\mathbf{r})}{(N+1) - (N)} - \frac{\rho_N(\mathbf{r}) - \rho_{N-1}(\mathbf{r})}{(N) - (N-1)}\right) \\ &= \rho_{N+1}(\mathbf{r}) + \rho_{N-1}(\mathbf{r}) - 2\rho_N(\mathbf{r})\end{aligned} \tag{10}$$

where $\rho_{N\pm i}(\mathbf{r})$ represents the electron density of the system under addition or subtraction of one electron, at constant geometry.

- Frozen orbital hypothesis: if the orbitals remain unchanged upon addition and subtraction of one electron, the only non-zero contribution in the previous difference arises from the frontier orbitals. By identification of the two fractions in eqn (10), one gets

$$\Delta f(\mathbf{r}) \approx \rho_{\mathrm{LU}}(\mathbf{r}) - \rho_{\mathrm{HO}}(\mathbf{r}) \tag{11}$$

with $\rho_{\mathrm{LU}}(\mathbf{r})$ and $\rho_{\mathrm{HO}}(\mathbf{r})$ being the densities of the LUMO and HOMO obtained in a SCF calculation on the system with N electrons.

Some problems arise with these formulations. First, regardless of the frozen orbital hypothesis, eqn (11) suffers from severe limitations: when considering a highly correlated system, canonical orbitals do not convey any relevant information, or when either the LUMO or HOMO shows some degeneracy, this equation becomes quite meaningless. Moreover, when the studied compounds are already negatively charged, the addition of one electron (as done in eqn (10)) might also not be plain. The possible self-ionisation would be missed because of the restricted size of the basis set (the additional electron being localised on an unphysical state). These formulations are also not well formulated for open-shell systems, where the resulting spin state after addition or subtraction of one electron is not obvious. A powerful formulation was recently proposed by some of the authors, and seems well suited for this kind of study: the state specific dual descriptor.[12] In this formulation, the dual descriptor is calculated as the variations in electron density between the excited states and the ground state:

$$\Delta f_{(i)}(\mathbf{r}) = \rho_{(i)}(\mathbf{r}) - \rho_{(0)}(\mathbf{r}) \tag{12}$$

with $\rho_{(i)}(\mathbf{r})$ the density of the excited state i ($i = 0$ meaning ground state). The physical meaning of this development is quite simple: as two reagents approach one another, they exert a mutual perturbation on their densities, through a variation of the external potential. As a result, the perturbed density of a molecule in this reacting configuration is markedly different from the ground state density of the isolated molecule. Assuming that no geometric relaxation occurs – *i.e.*, the variation of the external potential is only due to the approach of the other reagent – this perturbation can be developed on the basis of all the excited states of the isolated molecule. In other words, the approach of a reagent changes the external potential in such a way that excited states can be stabilised, hence yielding a more accurate representation of the properties of the reacting molecule than what the isolated ground state configuration would.

Ideally one should sum up the $\Delta f_{(i)}$ contributions of all the excited states into the so-called extended DD, with a weighting as all the states will not contribute in the same way to the reactivity. The fact is that this weighting remains unknown, but one can assume reasonably that the higher in energy a state is, the less it will contribute to the reactivity in the ground state, as exemplified by the sum-over-states formula giving the molecular polarisability.[13] As a rule of thumb, one might quite often rely upon the very first excited states (first or second) and resume the extended DD to the corresponding state-specific DD.[14]

Description by domains and quantification

Since the DD sums to 0 over the molecule (by construction of the DD), both electrophilic and nucleophilic sites should be present on a given reagent, and there is no reason for an atom to show only one of the two behaviours. In fact, it will be shown hereafter that atoms quite generally exhibit both contributions. However, caution must be taken if one wants to compare the electrophilic and nucleophilic contributions between different ligands. The ''crude'' numerical values can indeed only be compared between systems with the same number of electrons. One can relieve this condition by moving from the canonical to the grand canonical ensemble;[15] upon the Legendre transform $E \to \Omega = E - \mu N$ (with μ the electronic chemical potential) one can define a grand-canonical dual descriptor:

$$\left(\frac{\partial^2 \rho(\mathbf{r})}{\partial \mu^2}\right)_{v(\mathbf{r})} = \frac{\Delta f(\mathbf{r})}{\eta^2} - \frac{\gamma}{\eta^3} f(\mathbf{r}) \tag{13}$$

with η and γ being respectively the chemical hardness and hyperhardness, and $f(\mathbf{r})$ being the Fukui function. The last term of eqn (13) can quite reasonably be neglected, since the ratio γ/η^3 is generally quite small, even though hyperhardness is not necessarily close to zero, unlike what is generally assumed.[16] Hence, in the following we will restrict to the computation of the first term $\Delta f(r)/\eta^2$, $\Delta f(r)$ being computed through the first state specific (canonical) dual descriptor.

Another step must be taken if one wants to compare the chemical properties of different ligands. The grand canonical DD is indeed a local function. Yet, usually reactivity in chemistry is discussed in terms of reactive sites, thus using a ''coarse-grained'' description of the reaction. One must then translate local properties into atomic or fragment contributions. This approach is called condensation, the most widespread being the one developed by Yang and Mortier,[17] based on atomic charges $q(A)$ (whatever their definition). For instance, the condensed values of the Fukui functions are

$$f^{\pm}(A) = \mp[q_N(A) - q_{N\pm1}(A)] \tag{14}$$

with $q_{N\pm1}(A)$ the charge of an atom A when an electron is added to or withdrawn from the molecule through a vertical process (no geometrical rearrangement). The extension to the state-specific dual descriptor is quite straightforward:

$$\Delta f_i(A) = q_{\mathrm{GS}}(A) - q_{\mathrm{ES}i}(A) \tag{15}$$

where $q_{\mathrm{GS}}(A)$ is the charge of A in the ground state and $q_{\mathrm{ES}i}(A)$ the charge in the ith excited-state. Albeit very useful, such a scheme presents some severe drawbacks. Consider for instance a neutral diatomic molecule A_2. By symmetry, $q_{N\pm1}(A) = \mp\frac{1}{2}$, which yields

$$\forall A \quad f^{\pm}(A) = \tfrac{1}{2}, \quad \Delta f(A) = 0. \tag{16}$$

In other words, such a scheme is unable to distinguish between H_2, O_2, N_2 and F_2 for instance, whereas their reactivity strongly differs as it will be shown in the next section.

We recently devised a new approach that is able to discriminate between such molecules. The real space is divided into non-overlapping domains D_i of constant sign for the DD. In practice, from a DD Cartesian grid (cube file), a given grid point is said to belong to the interior of one and only one domain if the DD takes the same sign at every neighbouring point. Refinements were also implemented in order to assure the robustness of this assignment and the stability of such a grid-based algorithm. Once these domains are obtained, the corresponding condensed values are defined by

$$\Delta f(D_i) = \int_{D_i} \Delta f(\mathbf{r})\mathrm{d}^3\mathbf{r} \tag{17}$$

These integrals are computed numerically on the Cartesian grid. In order to assess the accuracy of such a procedure, one should monitor that

$$\sum_i \Delta f(D_i) \approx 0 \tag{18}$$

As an even more coarse-grained representation, the following descriptors can also be evaluated:

$$\Delta f_{\mathrm{D}}{}^{+} = \sum_{i/\Delta f(D_i) > 0} \Delta f(D_i) \tag{19}$$

$$\Delta f_{\mathrm{D}}{}^{-} = \sum_{i/\Delta f(D_i) < 0} \Delta f(D_i) \tag{20}$$

which measure the overall predominant electrophilic and nucleophilic propensities. Note that the DD normalisation implies that $\Delta f_{\mathrm{D}}{}^{+} = -\Delta f_{\mathrm{D}}{}^{-}$. It is also worth adding that from this partition, other domain properties could be evaluated such as populations, barycentres, and moments. Their computation and their use will be described in a forthcoming paper.

Computational details

All ligand structures presented in Table 1 were fully optimised without symmetry restriction at the DFT level of theory. All calculations were carried out using the hybrid B3LYP functional and the 6-31G* gaussian basis set except for the thiocyanate anion and the dihalogens. The SCN^- anion was optimised using the 6-31+G* basis set, as previous studies stressed the need to use diffuse functions to properly model sulfur atoms.[18,19] Dihalogens were optimised using the full-electron, double-zeta with polarisation functions DGDZVP basis set,[20] to ensure consistency of the results and since iodine is unavailable in the 6-31G* basis set. Frequency calculations were performed at the same level of theory to check for no imaginary value. Then, the first ten excited states were computed in the framework of time dependent DFT (TD-B3LYP). Subsequently, the DD was computed according to eqn (12), using the density of the first excited states.

Table 1 Series of studied ligands

Series number	Ligands
1	H_2, CH_2CH_2
2	F_2, Cl_2, Br_2, I_2
3	O_2, $O_2{}^-$, $O_2{}^{2-}$
4	NO^+, CO, CN^-
5	$NO^\bullet$
6	SCN^-
7	Acetylacetonate, hexafluoro-acetylacetonate 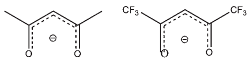

Grand canonical DDs (approximated by their first state-specific components) were represented as isosurfaces, and MEP obtained from the ground state calculations were mapped on density isosurfaces (1×10^{-3} a.u.), using GaussView 5.[21] Chemical hardness was simply computed as the energy difference $\eta \approx E_{\mathrm{LUMO}} - E_{\mathrm{HOMO}}$. When relevant, condensations of the DD were computed according to the former scheme (eqn (19) and (20)) in order to relieve ambiguities or add a supplementary level of explanation to the discussion.

All calculations were carried out using the Gaussian09 code and utilities.[22] Condensations were made using a home made program.

3 Discussion

Various systems were studied here, merged as shown in the series listed in Table 1. The groups were assembled according to the similarities of the ligand reactivity – as H_2 and ethene for instance – or according to the number of electrons – as for series (4). Results are discussed hereafter.

Series (1): H_2 and ethene

Ethene and dihydrogen usually show a similar reactivity as ligands, since they both interact by their main bond, coordinating in a η^2 mode[1] (*cf.* Scheme 1(a)). Therefore, it seemed rather logical to compare their features at the DD and MEP level, represented in Fig. 1. As formerly said, one can see that both nucleophilic and electrophilic parts are observed on the same atoms. The nucleophilic area is indeed located on both sides of the bond (H–H or C=C), indicating a coordination promoted by these bonds. MEP surfaces indicate the same coordination mode, since negative potential surfaces (stabilising for a cation) are found on the sides of the main bonds. In the case of H_2, the minimal value is small (*ca.* -3×10^{-3} a.u.) and the attractive domain quite narrow, which suggests quite a weak bonding. In the case of ethene, the minimal value for the potential is one order of magnitude larger (*ca.* 3×10^{-2} a.u.) and the attractive domains are larger in space, hence implying a stronger bonding capability for ethene as compared to H_2. This is consistent with the known geometries and relative stability of hydrogen and ethene complexes, for instance $[W(P^iPr)_2(CO)_3(H_2)]$ and Zeise's salt[1] $[PtCl_3(C_2H_4)]^-$. Furthermore, electrophilic systems are found, pointing outward from the molecule, essentially π* or σ*-like (in the framework of MO theory[23]). They develop in the neighbourhood of the coordinating site, suggesting quite an efficient backbonding. This is in perfect line with experimental results on ethylene-based complexes, such as tris-ethylene nickel(0)[24] where quite an efficient back-bonding is seen. The reactivity of H_2 is also well reproduced, as seen for instance in the oxidative addition of H_2 on Vaska's complex[25] $[IrCl(CO)(PPH_3)_2]$, or the relative difficulty to ascertain the

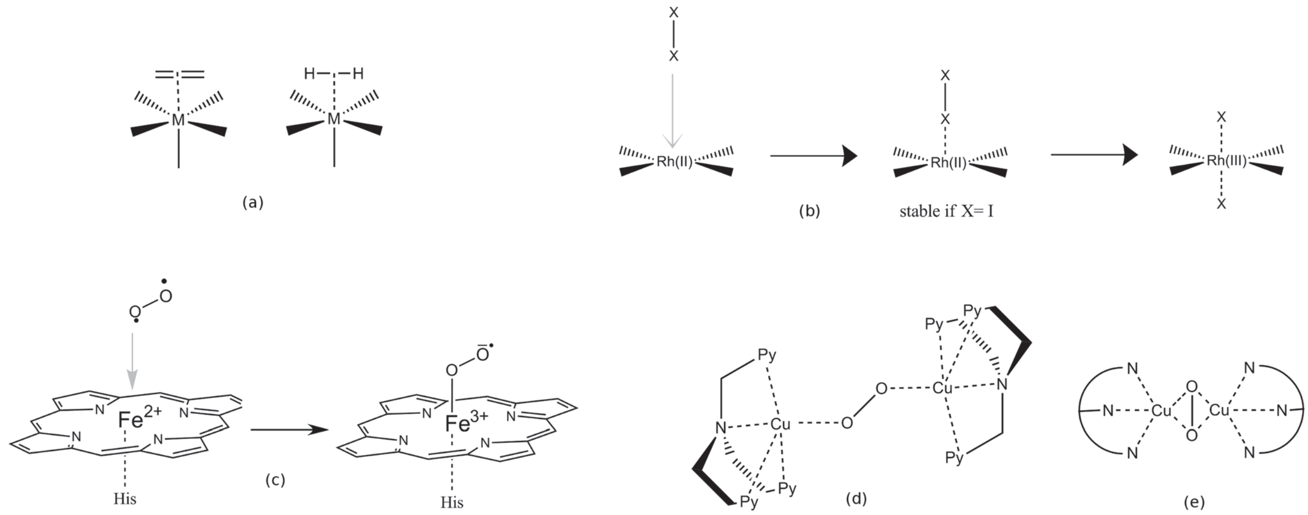

Scheme 1 Schematic representation of (a) the η^2 coordination mode of ethene (left) and H_2 (right); (b) the reaction of [(dpp-nacnac^{CH_3})Rh(phdi)] with iodine; (c) the reaction of dioxo with the haem moiety in haemoglobin; (d) coordination of peroxo in the $[(Cu(TMPA))_2(O_2)]^{2+}$; (e) coordination of peroxo in the catechol oxidase complex.

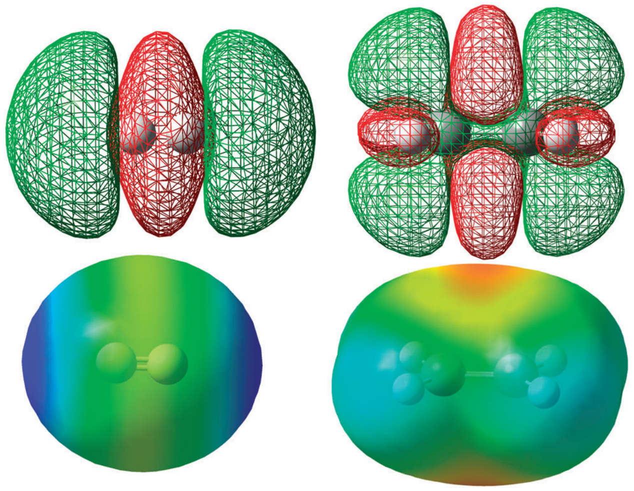

Fig. 1 Up: DD isosurfaces for H_2 and ethylene (from left to right). Isovalues: $\pm 4 \times 10^{-3}$ a.u., green: $\Delta f > 0$, red: $\Delta f < 0$. Down: MEP maps on density isosurfaces, same order. Isodensity: 1×10^{-3} a.u., values ranging from 3.00×10^{-2} (blue) to -3.00×10^{-2} a.u. (red) in the case of ethene, 1.00×10^{-3} to -1.00×10^{-3} for H_2.

oxidation state of the hydrogens in H_2 based complexes, between di-hydrido and neutral dihydrogen.[26]

Series (2): dihalogens

Isosurfaces in the case of the dihalogens from F_2 to I_2 are represented in Fig. 2. Here, caution must be taken when using the term ligand. Indeed, as Rogachev and Hoffmann already stressed previously[27] (and references therein), despite the lone pairs that should turn dihalogens into very good ligands, only a few transition metal complexes involving iodine are known,[28–31] and to the best of our knowledge, none involving other halogens.

Nevertheless, it seemed rather logical to investigate not only iodine, but also lighter parent compounds, and to check if any disparity could be found. The general trends are globally the same for the first two excited states (they are degenerated, and give the same results). All compounds show electrophilicity along the molecular axis, essentially σ*-like (in the framework of MO theory), while nucleophilic areas point on both sides of the bond where one would expect to find lone pairs. These features are consistent with the aforementioned study, where iodine is considered to be essentially electrophilic while coordinating in a linear fashion, and nucleophilic when coordinating on a "bent-side on" mode. The MEP is also in quite a good agreement, developing negative contribution on the sides of the molecules where the nucleophilic lobes are located, and positive (repulsive) contributions along the molecular axes. These electrophilic and positive MEP areas represent general features of halogen compounds, the so-called σ-holes.[32] The bent-side on coordination seems therefore plausible, and is more probable for the heavier halogens since both the minimal values and extents of the attractive MEP domains are larger (from *ca.* -3×10^{-3} a.u. for F_2 to -7×10^{-3} a.u. for I_2 and Br_2). The larger proclivity of the heaviest halogens towards coordination is also stressed by the increase in the spatial extent of the nucleophilic parts of the DD as one moves from fluorine to iodine. It is likewise found in the condensed values of the DD, as shown in Table 2. As a remark, it is worth noticing that the condensation scheme respects the condition of a zero integral of the DD (eqn (18)).

It is plain to see that nucleophilic contributions are increasing when moving from fluorine to iodine, suggesting a more efficient coordination for heavier dihalogens. Both this tendency and the topological features of the DD account for the coordination geometry of iodine[31] in $[Rh(CF_3CO_2)_4(I_2)]$, and two more factors might play a role in the non-existence of other donor dihalogen complexes. First, the weak electrostatic stabilisation (for chlorine and fluorine) can be insufficient to allow a cation approach. Furthermore, dihalogens are quite strong

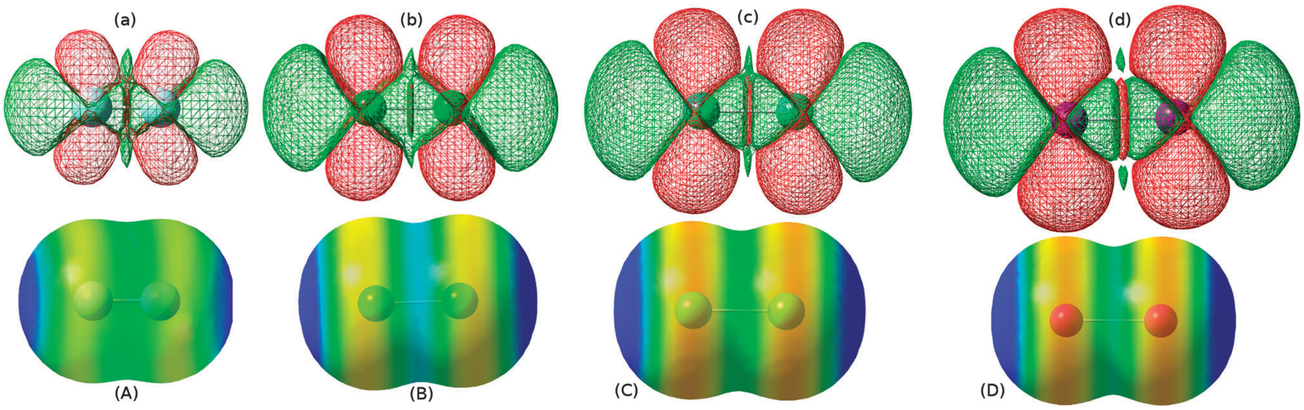

Fig. 2 DD isosurfaces (up) and MEP maps on density isosurfaces (down) for the dihalogens from F_2 (indices A, B and C) to I_2 (index D). DD isovalues: $\pm 4 \times 10^{-3}$ a.u., MEP ranges: $[-1.00 \times 10^{-2}; 1.00 \times 10^{-2}]$ a.u.; same color scheme as Fig. 1.

Table 2 Condensed grand canonical dual descriptor for the dihalogens, sorted by positive or negative contribution

Molecule	$\Delta f_D^{+}/\eta^2$ (a.u.)	$\Delta f_D^{-}/\eta^2$ (a.u.)
F_2	9.17	−9.17
Cl_2	21.27	−21.32
Br_2	31.39	−31.49
I_2	48.06	−48.12

oxidants, hence suggesting that the complexes they might form would not be stable and would undergo oxidative addition with the cleavage of the halogen–halogen bond. This tendency would be exacerbated for the first dihalogens, which show the highest redox potentials (we recall here the standard potentials: $E^0(F_2/F^-) = 2.866$ V/ECS, $E^0(Cl_2/Cl^-) = 1.358$ V/ECS, $E^0(Br_2/Br^-) = 1.087$ V/ECS *versus* $E^0(I_2/I^-) = 0.536$ V/ECS).[33] This hypothesis is supported by the reactivity of [(dpp-nacnac^{CH_3})Rh(phdi)] towards dihalogens.[29] Indeed, addition of chlorine or bromine to this complex leads to an oxidation of the metal center and a cleavage of the halogen–halogen bond, while addition of iodine does not. In this case, a linear-acceptor iodine ligand is found, which is consistent with the description obtained by the DD. The supposed mechanism is depicted in Scheme 1(b). Actually, two other linear-acceptor iodine based complexes are known:[28,30] $[Pt(dmpe)_2(I_2)]$ and $[PtI(C_6H_3(CH_2NMe_2)_2)(I_2)]$. This small number of examples seems to agree well with the previous discussion about the redox activity and both the smaller developments of the DD for lighter halogens, and another feature may explain the relative rarity of complexes based on acceptor iodine. It is indeed plain to see that the linear coordination is electrostatically disfavoured, since the MEP displays along the molecular axis of the dihalogens its largest value, *ca.* 0.022, 0.038, 0.049, and 0.052 a.u. from F_2 to I_2.

As a result, one can see that coordination abilities of dihalogens are quite similar according to the DD and the MEP analyses. Both show a tendency towards donation in a bent-side on geometry, which is expected to be favoured only for the heavier dihalogens. An acceptor ability in a linear coordination geometry is also found, which is expected to be also quite effective for the heavier halogens since they display a smaller gap between their HOMO and LUMO than the lighter ones (*ca.* $\eta = 6.98$ eV for fluorine, 3.05 eV for iodine) with both higher values of the electrophilic grand canonical dual descriptor. Still, these calculations seem to fail to reproduce the rarity of dihalogen-based complexes. In fact, the question is whether this rarity comes from poor coordination abilities or from other causes. As already discussed, the oxidative potential of dihalogens is quite a likely cause of the very few occurrences of dihalogen based complexes. This is the subject of a reactivity study; yet an implicit assumption is that we only consider coordination properties, meaning small perturbations of the electron densities, and not reactivity. With respect to this, our description is correct, and in fact the missing trends can be quite easily found since reactivity can be attained through a proper (yet slightly different) interpretation of the DD. For instance, the positive regions of the DD indicate acceptor regions in terms of coordination, but also the regions that would induce an electrophilic attack. The difference between the two approaches lies in the considered phenomenon: a slight electron delocalisation (from the metal to the ligand here) or a complete electron transfer (oxidative addition).

Series (3): from dioxo to peroxo

Isosurfaces for dioxo, superoxo and peroxo ions are represented in Fig. 3. These ligands are not supposed to show the same reactivity, but they form an electrochemical series that intervenes quite often in bioinorganic chemistry[34] (cell respiration, oxidation cycles).

The differences between all these ligands are striking. The nucleophilicity of dioxo (Fig. 3(a),(A)) is essentially located along two orthogonal directions, either along the molecular axis or perpendicular to it. The main development is found in the interatomic plane, which would suggest a chelate mode of coordination, but since the MEP value in this area is positive – it corresponds to the maximum value of *ca.* 9×10^{-3} a.u. – this coordination mode is rather disfavoured. In fact, slightly negative values of the MEP are found on the sides of each oxygen atom (*ca.* -2×10^{-3} a.u.), forming circular potential domains

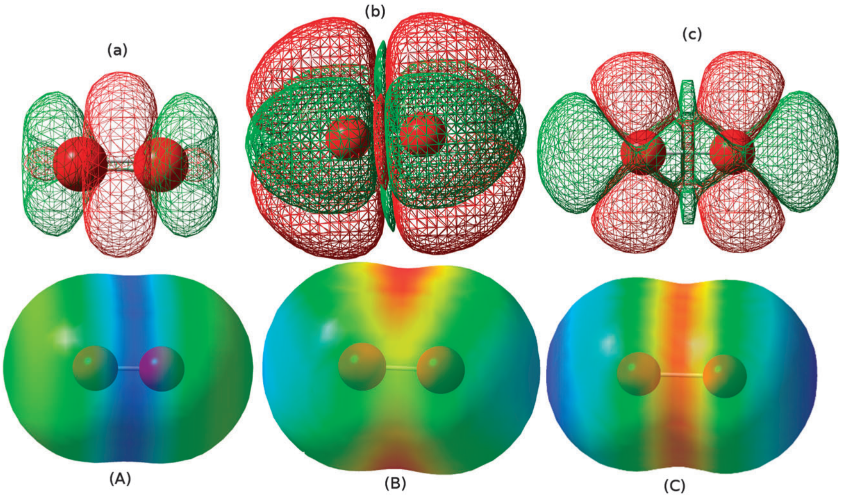

Fig. 3 DD isosurfaces (up) and MEP maps on density isosurfaces (down) for O_2, O_2^- and O_2^{2-} (indices A, B and C). DD isovalues: $\pm 4 \times 10^{-3}$ a.u., MEP ranges: $[-1.00 \times 10^{-2}; 1.00 \times 10^{-2}]$ a.u., $[-2.80 \times 10^{-1}; -2.30 \times 10^{-1}]$ a.u. and $[-5.50 \times 10^{-1}; -4.50 \times 10^{-1}]$ a.u. respectively; same color scheme as Fig. 1.

at the same places one finds electrophilic parts of the DD. This suggests that dioxygen would essentially bind in a bent side-on way, acting as an acceptor ligand, as depicted on the left side of Scheme 1(c). Still, coordination by the central nucleophilic area could be encountered when covalent interactions are stronger than electrostatic interactions. In such a case dioxo is also expected to be quite a good acceptor ligand. It develops indeed large electrophilic lobes in the vicinity of the coordination area. Eventually, in these two geometries the acceptor tendency could lead to a certain reactivity, as what was formerly discussed for dihalogens. These results seem to be in a rather good agreement with the known reactivity of dioxo towards complexes: to the best of our knowledge, no dioxygen complex has been yet unambiguously characterised. Indeed, O_2 undergoes in all cases one or several electron back-transfer, *e.g.* in the haemoglobin complex[35] where a side-on superoxo is found as sketched in Scheme 1(c), or in the oxidative addition of O_2 to iridium complexes[36] where usually a chelate peroxo is finally formed. These results are also quite easily understandable in the framework of MO theory. The nucleophilic parts on the molecular axis arise from σ* contributions, while the central one stems from the bonding π system, which would be stabilised by the approach of an electron-acceptor species. The electrophilic parts are due to the anti-bonding π* system, which in contrast would be stabilised by an interaction with an electron-giving species.

Superoxo (Fig. 3(b),(B)) shows also a balanced trend since both nucleophilic and electrophilic sites show similar developments. In terms of MO theory, they seem to arise essentially from orthogonal π* contributions. This suggests that superoxo would be a fairly good donor ligand, with a possibility to show chelation, and some slight ability for back-bonding due to the development of electrophilic areas in the vicinity of the bonding region. MEP in this case shows only negative values, due to the negative charge of the ligand. Hence, electrostatic interaction is in any case stabilising, but it still makes sense to check for the local minima in order to have a better idea of the regioselectivity of a cation approach. The MEP surface in this case was then represented between its minimal and maximal values. It is plain to see that two potential wells are defined above and below the O–O bond, but not in a circular shape (*ca.* −0.28 a.u.). It is worth noticing that the nucleophilic parts of the DD are also located below and above the O–O bond. Both descriptors thus strongly support the hypothesis of a chelating, donor superoxo. Little back-bonding is expected in this geometry, as the only reachable electrophilic parts are the ones located in the middle of the O–O bond. Yet, as formerly said the electrostatic interaction is stabilising at any point on the isodensity surface. Situations where stabilisation due to orbital interaction would take precedence over electrostatic interaction are therefore possible. For instance, the displacement of a ligand could increase the back-bonding or the σ-bonding while decreasing the electrostatic stabilisation. Depending on the balance between both effects, this displacement will be favoured or not. As a result, geometries involving a cation not exactly located in the potential well, but rather on one of its sides could be encountered. This is also in good agreement with the known reactivity of superoxo; for instance, as already discussed in the haemoglobin complex O_2^- binds in a bent-side on form to Fe(III) (yielding a strong σ-donation).

In the case of peroxo (Fig. 3(c),(C)) finally, the DD representation is very close to what was seen for fluorine. This was expected since they are isoelectronic. The same kind of reactivity is therefore expected at the DD level: chelate or bent donor, or linear and acceptor ligand. Since peroxo is a dianion, here also one expects to observe only negative values of the potential, hence suggesting one to use the same representation (between min and max values). Again, the minimal values are found within the bond area, but this time the potential domain is circular (continuum of minimal values, *ca.* −0.54 a.u.). The chelate mode of coordination is then strongly supported, even if any cation approach is favoured with respect to the MEP (negative values). In this bonding mode, little back-bonding might occur thanks to the central electrophilic developments of the DD, in the middle of the O–O bond. In that case indeed, the O–O bond length is quite long (*ca.* 1.62 Å) and the MEP is strongly negative, hence permitting a close approach of a cation and a subsequent strong interaction with this electrophilic part.

All these tendencies are also in good agreement with the known reactivity of peroxo as a ligand. For instance, in the catechol–oxidase complex, dioxo first binds to two copper(I) ions and then undergoes two electron back-transfer, yielding peroxo bound to two copper(II) in a chelate way as shown in Scheme 1(d) and (e). This complex can then oxidise organic molecules such as phenols,[34] hence exploiting the relative electrophilicity of peroxo (middle-bond developments). As previously said for peroxo, here also other geometries are possible since the MEP is attracting towards cations anywhere on the surface. This allows one to understand the geometry of the $[(Cu(TMPA))2(O2)]^{2+}$ complex, where a peroxo bridges to copper(II) in a end-to-end, bent fashion (*cf.* Scheme 1).[37] In this case indeed, the chelate binding mode seems disfavoured due to steric hindrance generated by the pyridine coordinating groups. Another possible way to bind the metallic cations through the donor parts of peroxo is to bridge by a bis-monohapto mode ($\eta^1 - \eta^1$), as experimentally observed. In these cases also, the combination of both the DD and the MEP allows one to retrieve the coordination chemistry and also the reactivity of O_2 based complexes.

Series (4): nitrosyl, carbonyl, cyanide

As previously stated, the ligands in series (4) are isoelectronic and it is well established that they show similar coordination abilities. For instance, carbonyl, cyanide and nitrosyl are known to yield roughly the same kind of crystal field energy splitting, meaning that they show the same kind of donor and acceptor abilities.[1] DD and MEP isosurfaces are represented in Fig. 4. DD displays similar features: nucleophilic domains are found along the molecular axes, pointing outwards from the molecule. They are more developed on the most electropositive atom, which is known to be the coordinating one (C in CO, N in NO^+, C in CN^-), and can be understood in the framework of the MO theory as arising from σ orbitals. These nucleophilic contributions point in the direction of the minima of MEP (-2×10^{-2} a.u. for C in CO, −0.24 a.u. for C in CN^-, 0.24 a.u. for N in NO^+), strongly supporting linear coordination mode (with a donor ligand). The development of electrophilic domains in the vicinity of this coordination area (essentially π* like) indicates a strong tendency towards back-bonding. This is consistent with the fact that these ligands are known to be strong field ligands, with the following order within the spectrochemical series:[2] $NO^+ < CO \approx CN^-$. The order within this series is furthermore retrieved from the spatial extent of the DD, being larger for carbonyl and cyanide as compared to nitrosyl. This is also plain from the condensed values of the grand canonical DD, as reported in Table 3: NO^+ shows lower contributions (*ca.* ± 3.2 a.u.) than CO (*ca.* ± 4.4 a.u.) and cyanide (*ca.* ± 5.1 a.u.).

In the case of cyanide and carbonyl, the minimal values of the MEP found on the coordinating atom correspond to genuine potential wells; the interplay between charge and covalent interaction therefore suggests that the coordination will essentially imply a linear donor ligand, with a large back-bonding, as observed. In the case of cyanide, since the MEP is negative everywhere, coordination by the N atom is also plausible, even though coordination by the C atom is preferred. This accounts quite well for the observed coordination trends of cyanide, noticeably the possibility to form C,N (end-to-end) bridges like in the prussian blue analogues.[38] In these compounds, the large back-bonding manifests itself in the generally

Table 3 Condensed grand canonical dual descriptor for CO, NO^+ and CN^-, sorted by positive or negative contribution

Molecule	$\Delta f_D^+/\eta^2$ (a.u.)	$\Delta f_D^-/\eta^2$ (a.u.)
CN^-	5.06	−5.07
CO	4.37	−4.38
NO^+	3.17	−3.18

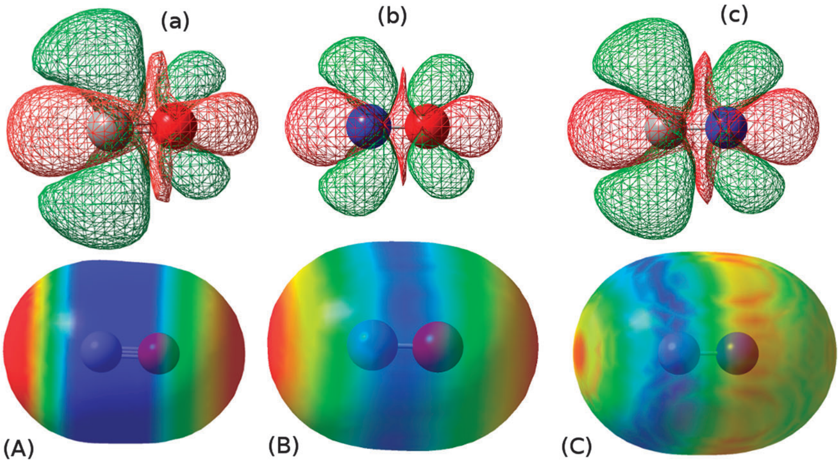

Fig. 4 DD isosurfaces (up) and MEP maps on density isosurfaces (down) for CO, NO^+ and CN^- (indices from A to C). DD isovalues: $\pm 4 \times 10^{-3}$ a.u., MEP ranges: $[-2.00 \times 10^{-2}; 2.00 \times 10^{-2}]$ a.u. (CO), $[2.48 \times 10^{-1}; 3.10 \times 10^{-1}]$ a.u. (NO^+), $[-2.40 \times 10^{-1}; -2.30 \times 10^{-1}]$ a.u. (CN^-); same color scheme as Fig. 1.

large magnetic coupling between the cations. In the case of carbonyl, the relative strength of charge interaction is expected to be lower than what is observed in cyanide, hence suggesting that the restriction to the linear coordination might be weaker, accounting for the possibility to obtain the bent-carbonyl complex carboxyhaemoglobin.[39] This last example is further explained if one remembers that iron in the haem complex is rather nucleophilic (as illustrated by the back-transfer in oxy-haemoglobin between Fe(II) and dioxo), hence trying to increase its interaction with the electrophilic parts of the DD and therefore coordinating in a bent fashion. Finally, in the case of nitrosyl, since no negative MEP value is found, the minimal value corresponds to a repulsive potential (towards cations). As a result, charge control alone limits any coordination (effect of the positive charge). No real interplay between charge and orbital control can be found, and the reactivity must then be controlled solely by orbital interactions. This accounts quite well for the variety of behaviours that nitrosyl can show: when reacting with quite a nucleophilic metal, it will essentially behave like an acceptor in a bent "side-on" geometry,[2] as in $[\mathrm{Ir(PPh_3)_2(CO)(NO)Cl}]^+$. In contrast, when reacting with an electrophilic metal, it would behave like a linear donor,[40] as in $[\mathrm{Fe(CN)_5NO}]^-$, with a large tendency to back-bonding.

Nitrosyl

In the previous series, we discussed a few results for NO^+, which is one of the limit forms that one usually writes to describe the behaviour of a one-electron donor nitrosyl ligand. NO is indeed a non-innocent ligand, and its electronic state is almost never plain:[41] it always balances between NO^+ and NO^-. The cationic form might not be the best form to describe NO, especially when aiming to describe its reactivity. Indeed, the positive charge results in an electrostatic repulsion that might forbid complexation. Let us now focus on the neutral, radicalar form $NO^\bullet$. Computations of the DD and the MEP are shown in Fig. 5. Again, both electrophilic and nucleophilic contributions to the dual descriptor are spatially developed, and might be of similar importance for the reactivity. Yet, the differences with the cationic form are marked: instead of planar electrophilic and nucleophilic parts, orthogonal π*-like contributions are observed. They are mainly located on the N, suggesting a coordination by the nitrogen. This is supported by MEP analysis, showing two local minima on the sides of the N atom (*ca.* -12×10^{-3} a.u.), to be compared with the local minima on the sides of the O (*ca.* -8×10^{-3} a.u.). These features are localised on the same places as the nucleophilic parts of the DD, hence suggesting two possible coordination geometries: either bent and donor, with a slight tendency towards back bonding owing to electrophilic areas not far from the coordination area, or linear and strongly donor (π-donation) with a larger tendency towards back-bonding. This linear form is possible since along the molecular axis the MEP values are negative, hence stabilising for a cation (balance between the full electrostatic stabilisation and the back-bonding). The bent geometry is therefore expected when NO binds to quite a nucleophilic metal, which is consistent with the known data on nitrosyl: the bent form is associated with a 1e donor character while the linear form is associated with a 3e donor character.[41] This is also seen in the Feltham–Enemark model:[42] the more the {MNO} entity contains electrons, the more bent the nitrosyl would be.

Yet, something might seem odd to the reader, since this analysis is in a partial contradiction with the former one on the cationic form: here, the bent geometry is associated with a donor character, while for the cationic form it is related to an acceptor ability. This is actually consistent with the known "non-innocent" character of nitrosyl as a ligand and the fundamental ambiguity that stems from the arbitrary assignment of an electronic state to it. Indeed, instead of considering an acceptor nitrosyl and a donor iridium(I) ion in $[\mathrm{Ir(PPh_3)_2(CO)(NO)Cl}]^+$, one might have thought of a donor nitrosyl bound to an acceptor iridium(II); the apparent problem is only a matter of electron localisation, which should not be encountered while considering entire complexes in which the electronic state of nitrosyl is not relevant (but the total number of electrons is).

Thiocyanate

Thiocyanate is another example of ambidentate ligands, characterised by the so-called geometry signatures:[41] thiocyanate coordinates by the N atom to hard metals, in a linear geometry, or by the S atom to soft metals, in a rather bent-side on geometry.[43] The MEP and DD maps are displayed in Fig. 6. One must bear in mind that a proper quantum calculation of sulfur-containing compound supposes the inclusion of diffuse and polarisation functions, thus suggesting the use of the 6-31+G* basis set in this case. From the DD analysis, it seems that the N atom is essentially nucleophilic, while the sulfur

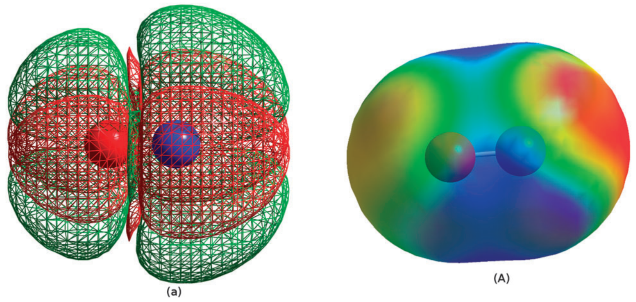

Fig. 5 DD isosurface (left) and MEP maps on density isosurfaces (right) for $NO^\bullet$. DD isovalues: $\pm 4 \times 10^{-2}$ a.u., MEP range: $[-1.20 \times 10^{-2}; 1.20 \times 10^{-2}]$ a.u.; same color scheme as Fig. 1.

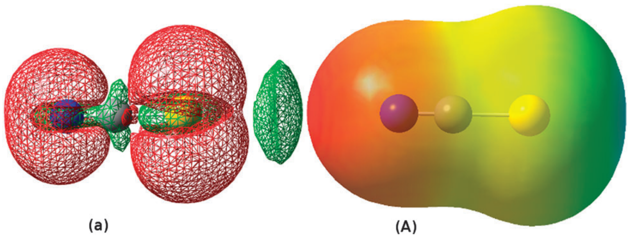

Fig. 6 DD isosurface (left) and MEP maps on density isosurfaces (right) for SCN^-. DD isovalues: $\pm 2 \times 10^{-2}$ a.u., MEP range: $[-1.99 \times 10^{-1}; -1.50 \times 10^{-1}]$ a.u.; same color scheme as Fig. 1.

atom shows both components. The nucleophilic parts can be viewed as arising from essentially π*-like orbitals (in the framework of MO theory), with a hint of σ character for the nitrogen atom, and the largest component is found on the sulfur. This suggests that both atoms are able to act as donor ligands, with essentially no back-bonding while coordinating by the nitrogen, and in contrast a possible back-bonding when coordinating by the sulfur in a bent fashion. MEP also shows that any coordination is possible, since at the chosen isodensity all the values are negative. Yet, the minimal value is found along the SCN bond on the nitrogen (*ca.* −0.20 a.u.), and the maximal value is found along the bond but on the S atom (*ca.* −0.15 a.u.).

As a result, one expects hard metals to coordinate by the N atom since they are most likely to undergo charge control, while in contrast soft metals, likely to undergo covalent control, would rather bind to the sulfur since it shows the largest nucleophilic contribution and also the possibility to yield back-bonding. In the case of N-bonding, the geometry is expected to be linear (orientation along the minimal MEP value, along the bond). The S-bonded complexes are expected to be bent because of the better back-bonding (with respect to a linear situation) and at the same time a larger electrostatic interaction. The coordination properties of thiocyanate are here very well reproduced.

Acetylacetonate and hexafluoroacetylacetonate

Acetylacetonate (acac) is widely used in coordination chemistry, acting as a donor but also quite efficient in enhancing the Lewis acidity of metallic cations, which supposes quite a good attractor behaviour; its hexafluorinated counterpart (hfac) shows the same reactivity, with a larger Lewis acidity enhancement.[44] The computed MEP and DD surfaces are represented in Fig. 7. It is plain to see that both descriptors indicate a coordination by the two oxygen atoms, preferentially in the molecular plane: the nucleophilic parts of the DD consist essentially of the p-type lone pairs of the oxygens, lying in the molecular plane. On the other hand, a (negative) electrostatic potential well is located between the two oxygens, in the same position (*ca.* −0.23 a.u. for hfac, −0.28 a.u. for acac), while other parts of the molecules show positive values of the MEP (which suggests that the charge is quite localised within the two oxygens). One would then expect quite a strong donor character for these ligands, as it is generally observed experimentally. But one can also see that the electrophilic part of the DD, though mostly located on the carbonyl carbons, also develops on the oxygens, perpendicular to the molecular plane. These electrophilic areas are in an appropriate place to allow quite an efficient back-bonding from metal orbitals, thus enhancing its Lewis acidity. This is also experimentally observed. The difference between the protonated and fluorinated form is not really obvious, except that hfac is expected to be a weaker ligand, since MEP minimum is smaller and the spatial extent of the DD is smaller. The MEP feature is quite easily explained if one remembers that trifluoromethyl groups are electron withdrawing, hence delocalising the anionic density over the whole molecule and not only between oxygens. A more careful look at the DD reveals that the electrophilic and nucleophilic parts are rather comparable for hfac, in contrast to the situation of acac where the nucleophilicity is preponderant. This is likely due to the trifluoromethyl groups, which by lowering the density lead to lower the local nucleophilicity and also the local electrophilicity. As a result, hfac is expected to be a stronger electron-withdrawing ligand as compared to acac, which is consistent with its higher "lewis acidity enhancement" properties.[44]

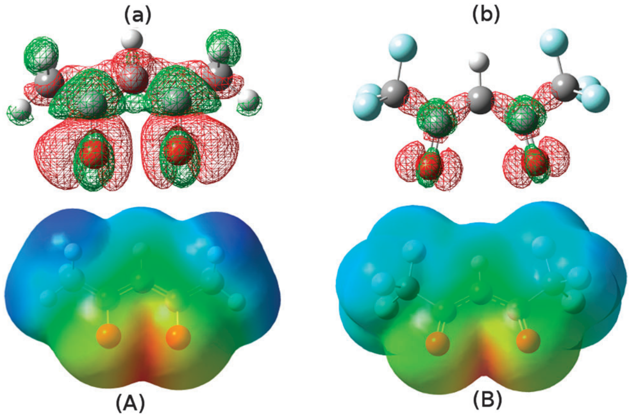

Fig. 7 DD isosurface (up) and MEP maps on density isosurfaces (down) for acetylacetonate and hexafluoro-acetylacetonate (indices A and B). DD isovalues: $\pm 4 \times 10^{-2}$ a.u., MEP ranges: $[-2.80 \times 10^{-1}; -1.00 \times 10^{-1}]$ a.u. (acac), $[-2.30 \times 10^{-1}; -1.00 \times 10^{-1}]$ a.u. (hfac); same color scheme as Fig. 1.

4 Conclusion

In this article, we have shown that the computation of the dual descriptor and the molecular electrostatic potential allows one to interpret the coordination chemistry of ligands in terms of acceptor/donor abilities balanced by electrostatic interactions. The variety of the chosen examples (ranging from neutral diatomic to charged polyatomic ligands) supports the generality of the proposed method, not only for geometry interpretation but also its prediction. In many cases, both descriptors provide similar information, but in some cases ambiguities could only be relieved by the combination of the two descriptions. For instance, in the case of dioxygen (coordination by the electrophilic part of the ligand thanks to the molecular potential) or thiocyanate (coordination possible on every position according to the MEP, limitation to two possibilities thanks to the DD). This tool might be useful for the community of coordination chemists, since it allows one to map unambiguously and at the price of rather simple DFT calculations the relative local nucleophilicity or electrophilicity of a ligand, hence permitting to predict the preferential coordination geometries of a given ligand. Furthermore, the effectiveness of the proposed method suggests that it could be worth checking if any complementary information would not be obtained by considering the dual potential[45,46] instead of the dual descriptor. Yet, the combination of both DD and MEP already allowed us to get an insight into the electronic properties of a ligand, enabling for instance to ascertain which geometries would allow back-bonding and which ones would not. Furthermore, the scope is not limited to these points. Previous studies indeed showed that charge-transfer excitations could be easily computed and explained based on the variations of the density upon a vertical excitation,[47] which are precisely what one computes when looking for the state-specific DD.[48] This means that one can access, in a single and unified framework, both reactivity and optical properties of a molecule, and at a relatively low computational cost.

Acknowledgements

The authors would like to thank Roald Hoffmann for his precious advice and discussions. F.G. is grateful to the Ecole Normale Superieure de Lyon for the financial support. This work has been partially supported by INSA Rouen, Rouen University, CNRS, Labex SynOrg (ANR-11-LABX-0029) and region Haute-Normandie (CRUNCh network). L. J. and V. T. thank the Centre National de la Recherche Scientifique (CNRS) for a ‘‘chaire d'excellence'' at the University of Rouen, and the Centre de Ressources Informatiques de Haute-Normandie (CRIHAN) for computational resources. The research benefited from the support of Aviesan ITMO Cancer within the ‘‘Cancer Plan 2009–2013'' and the application of Action 3.3. A.

References

1 D. F. Shriver and P. W. Atkins, *Inorg. Chem.*, Oxford University Press, 3rd edn, 1999.
2 J. E. Huheey, *Inorganic Chemistry: Principles of Structure and Reactivity*, Harper International Edition, 1972.
3 J. Chatt, L. A. Duncanson and L. M. Venanzi, *J. Chem. Soc.*, 1955, 4456–4460.
4 G. Klopman, *J. Am. Chem. Soc.*, 1968, **90**, 223–234.
5 L. Salem, *J. Am. Chem. Soc.*, 1968, **90**, 543–552.
6 C. Morell, A. Grand and A. Toro-Labbé, *J. Phys. Chem. A*, 2005, **109**, 205–212.
7 C. Morell, A. Grand and A. Toro-Labbé, *Chem. Phys. Lett.*, 2006, **425**, 342–346.
8 J. Martinez-Araya, *J. Mol. Model.*, 2013, **19**, 2715–2722.
9 B. Pinter, N. Nagels, W. A. Herrebout and F. De Proft, *Chem. – Eur. J.*, 2013, **19**, 519–530.
10 C. Cárdenas, N. Rabi, P. W. Ayers, C. Morell, P. Jaramillo and P. Fuentealba, *J. Phys. Chem. A*, 2009, **113**, 8660–8667.
11 C. Morell, P. W. Ayers, A. Grand, S. Gutierrez-Oliva and A. Toro-Labbé, *Phys. Chem. Chem. Phys.*, 2008, **10**, 7239–7246.
12 V. Tognetti, C. Morell, P. W. Ayers, L. Joubert and H. Chermette, *Phys. Chem. Chem. Phys.*, 2013, **15**, 14465–14475.
13 R. R. Zope, T. Baruah, M. R. Pederson and B. I. Dunlap, *Int. J. Quantum Chem.*, 2008, **108**, 307–317.
14 L.-A. Jouanno, V. Di Mascio, V. Tognetti, L. Joubert, C. Sabot and P.-Y. Renard, *J. Org. Chem.*, 2014, **79**, 1303–1319.
15 P. Geerlings, F. De Proft and W. Langenaeker, *Chem. Rev.*, 2003, **103**, 1793–1874.
16 C. Morell, A. Grand, A. Toro-Labbé and H. Chermette, *J. Mol. Model.*, 2013, **19**, 2893–2900.
17 W. Yang and W. J. Mortier, *J. Am. Chem. Soc.*, 1986, **108**, 5708–5711.
18 W. M. Wah, *Quantum Chemical Calculations of Sulfur-Rich Compounds in Elemental Sulfur and Sulfur-Rich Compounds II; Elemental Sulfur and Sulfur-Rich Compounds*, Springer, 2003.
19 I. Hillier and V. Saunders, *Chem. Phys. Lett.*, 1969, **4**, 163–164.
20 A. Yurieva, O. Poleshchuk and V. Filimonov, *J. Struct. Chem.*, 2008, **49**, 548–552.
21 R. Dennington, T. Keith and J. Millam, *GaussView Version 5*, Semichem Inc., Shawnee Mission, KS, 2009.
22 M. J. Frisch, *et al.* Gaussian 09 Revision D.01., Gaussian Inc., Wallingford, CT, 2009.
23 R. Hoffmann, *Acc. Chem. Res.*, 1971, **4**, 1–9.
24 N. Rosch and R. Hoffmann, *Inorg. Chem.*, 1974, **13**, 2656–2666.
25 L. Vaska and J. W. DiLuzio, *J. Am. Chem. Soc.*, 1962, **84**, 679–680.
26 G. J. Kubas, *Metal Dihydrogen and σ-Bond Complexes*, Kluwer Academic Publishers, 2002, pp. 33–51.
27 A. Y. Rogachev and R. Hoffmann, *J. Am. Chem. Soc.*, 2013, **135**, 3262–3275.
28 R. A. Gossage, A. D. Ryabov, A. L. Spek, D. J. Stufkens, J. A. M. van Beek, R. van Eldik and G. van Koten, *J. Am. Chem. Soc.*, 1999, **121**, 2488–2497.
29 D. W. Shaffer, S. A. Ryken, R. A. Zarkesh and A. F. Heyduk, *Inorg. Chem.*, 2012, **51**, 12122–12131.
30 R. Makiura, I. Nagasawa, N. Kimura, S. Ishimaru, H. Kitagawa and R. Ikeda, *Chem. Commun.*, 2001, 1642–1643.
31 F. A. Cotton, E. V. Dikarev and M. A. Petrukhina, *Angew. Chem., Int. Ed.*, 2000, **39**, 2362–2364.
32 T. Clark, M. Hennemann, J. Murray and P. Politzer, *J. Mol. Model.*, 2007, **13**, 291–296.
33 P. Vanýsek, *Handbook of Chemistry and Physics*, Taylor and Francis Group, 92nd edn, 2011, pp. 5-80–5-89.
34 N. Kitajima and Y. Moro-oka, *Chem. Rev.*, 1994, **94**, 737–757.
35 S. Pin, B. Alpert and A. Michalowicz, *FEBS Lett.*, 1982, **147**, 106–110.
36 E. V. Rybak-Akimova, *Physical Inorganic Chemistry: Reactions, Processes, and Applications*, Wiley, 2010, pp. 109–188.
37 Y. Moro-oka, K. Fujisawa and N. Kitajima, *Pure Appl. Chem.*, 1995, **67**, 241–248.
38 M. Verdaguer and G. S. Girolami, *Magnetism: Molecules to Materials V*, Wiley-VCH Verlag, 2005, pp. 283–346.
39 G. B. Vasquez, X. Ji, C. Fronticelli and G. L. Gilliland, *Acta Crystallogr., Sect. D: Biol. Crystallogr.*, 1998, **54**, 355–366.
40 A. Navaza, G. Chevrier, P. M. Alzari and P. J. Aymonino, *Acta Crystallogr., Sect. C: Cryst. Struct. Commun.*, 1989, **45**, 839–841.
41 D. P. Mingos, *J. Organomet. Chem.*, 2014, **751**, 153–173.
42 J. H. Enermark and R. D. Feltham, *Coord. Chem. Rev.*, 1974, **13**, 339–406.

43 M. Kabesova and J. Gazo, *Chem. Zvesti*, 1980, **6**, 800–841.

44 N. A. Bailey, D. E. Fenton, M. V. Franklin and M. Hall, *J. Chem. Soc., Dalton Trans.*, 1980, 984–990, and references therein.

45 C. Morell, P. W. Ayers, A. Grand and H. Chermette, *Phys. Chem. Chem. Phys.*, 2011, **13**, 9601–9608.

46 C. Morell, V. Labet, P. W. Ayers, L. Genovese, A. Grand and H. Chermette, *J. Phys. Chem. A*, 2011, **115**, 8032–8040.

47 T. Le Bahers, C. Adamo and I. Ciofini, *J. Chem. Theory Comput.*, 2011, **7**, 2498–2506.

48 O. A. Syzgantseva, V. Tognetti, A. Boulangé, P. A. Peixoto, S. Leleu, X. Franck and L. Joubert, *J. Phys. Chem. A*, 2014, **118**, 757–764.

PCCP

PAPER

View Article Online
View Journal | View Issue

Cite this: *Phys. Chem. Chem. Phys.*, 2016, **18**, 982

Received 21st August 2015,
Accepted 16th November 2015

DOI: 10.1039/c5cp04982b

www.rsc.org/pccp

Towards the first theoretical scale of the *trans* effect in octahedral complexes†

Frédéric Guégan,*[ab] Vincent Tognetti,[c] Laurent Joubert,[c] Henry Chermette,[a] Dominique Luneau[b] and Christophe Morell*[a]

In this paper, we show that *trans* effects in octahedral complexes can primarily be related to differences in the ability, for a given ligand, to cede electron density to the metal cation under the influence of the ligand at the *trans* position. Using tools from conceptual DFT or from related paradigms, we highlight these effects on a set of representative examples and further provide the basis for a computational *trans* effect scale. This quantification notably retrieves the experimental *trans* orienting series.

1. Introduction

The Kinetic *Trans* Effect (KTE), sometimes simply called the "*trans* effect", is a well-known phenomenon in coordination chemistry since its discovery in 1926.[1] It is characterised by the increase in the substitution kinetics of a ligand in a complex, under the influence of the ligand at the opposite coordination position (whence the label "*trans*").[2,3] A static analogue to this effect is also known: the Structural *Trans* Effect (STE), sometimes called "*trans* influence".[4] It is characterised by an increase of a metal–ligand bond length, under the influence of the ligand at the opposite coordination position.

Both STE and KTE are frequently epitomised by square planar complexes, with a d^8 electronic configuration of the metal cation,[5] and octahedral complexes, with either a d^6 or d^0 metal electronic configuration.[6] More rarely, they can be observed for lanthanide,[7] actinide[8,9] or even iodine[10,11] complexes. These two effects are known to be a likely cause of several chemical properties, ranging from catalytic activity and selectivity[12–14] to metalloprotein reactivity[15–18] and anti-tumoral activity.[19–21]

As such, understanding the origin and mechanisms beneath both the STE and the KTE seems to be necessary. Many experimental and theoretical studies have been dedicated to this task and, to our best knowledge, have not been fully conclusive yet. All these efforts can be traced back to the 1930s when an electrostatic model[22–25] was proposed, based on polarisation effects between the central metal and the ligands. However, its conclusions are generally in contradiction with the outcome of a later model by Chatt, Dewar and Duncanson (CDD).[26,27] The CDD model, even though elegant, only works for the KTE observed with π-acceptor ligands and is unable to account for the generality of the *trans* effects.

Eventually, some other authors tried to correlate metal–ligand σ or π bond strength with the *trans* effects using experimental evidences, such as direct measurements of UV charge transfer bands.[28,29] Lately, many different theoretical studies have confirmed that both electron donations and back-donations[30,31] are acting beneath the KTE of square planar complexes, the former by destabilising the complex, and the latter by stabilising the transition states of metathesis.[32] Yet, such confirmations are still needed in the case of octahedral complexes.

There is no apparent reason why the same line of argument might not be applied. Furthermore, it is plain to see that there is a common ground for all these approaches. In all cases indeed, *trans* effects can be understood in terms of electron density deformations. For instance, within the CDD model, *trans* effects are investigated by monitoring the electron transfers from the metal to the ligands. Similarly, in the electrostatic approach, the dipole moment arises from electron density distortion due to charge accumulation or depletion at given sites. In the case of the donation/back-donation scheme, the extent of electron density shared between the ligand and the metal, as compared to the case of isolated species, could be the relevant parameter to follow.

Conceptual DFT[33–35] (C-DFT) is an elegant framework for characterizing such effects. It expresses the chemical properties of a given system through a set of quantum descriptors. These are based on the response of either the energy or the electron

---

[a] Université de Lyon, Institut des Sciences Analytiques, UMR 5280, CNRS, Université Claude Bernard Lyon 1, 5 rue de la Doua, 69100 Villeurbanne, France. E-mail: frederic.guegan@univ-lyon1.fr, christophe.morell@univ-lyon1.fr

[b] Université de Lyon, Laboratoire des Multimatériaux et Interfaces, UMR 5615, CNRS, Université Claude Bernard Lyon 1, 22 avenue Gaston Berger, 69622 Villeurbanne, France

[c] Normandy University, COBRA UMR 6014 & FR 3038, Université de Rouen, INSA Rouen, CNRS, 1 rue Tesniére, 76821 Mont St Aignan, Cedex, France

† Electronic supplementary information (ESI) available: Theoretical details (dual descriptor formulations, derivation in the grand-canonical ensemble), molecular structures (*xyz* files), supplementary data (complexes 3, S3). See DOI: 10.1039/c5cp04982b

density to external perturbations.[36] Obviously, such a framework is adapted for an in-depth investigation of the physical roots of the *trans* effects in octahedral complexes. Two tools are particularly well fitted to monitor the variations of the electron density, namely the Dual Descriptor (DD)[37–39] and the Extended Transition State–Natural Orbitals for Chemical Valence[40–42] (ETS–NOCV). The latter does not strictly belong to C-DFT, still it uses a density deformation matrix and therefore its theoretical framework is quite close to C-DFT. These two indexes combined together have proved to be very efficient to characterise, understand and rationalise the electron density evolution during a chemical process.[43,44]

In this work, the results of a combined DD/ETS-NOCV survey are reported. In the first part, the physical bases for both descriptors are briefly recalled (see the ESI† for more details). In the second part the methodology to unravel the STE and the KTE is presented. It is then applied on a set of representative examples. The third part is dedicated to the elaboration of a semi-quantitative scale of *trans* orienting groups. The paper ends with some concluding remarks.

2. Theoretical background

2.1 State specific grand canonical dual descriptor

The usual dual descriptor $\Delta f_{\text{usual}}(\mathbf{r})$[45] is defined as the second derivative of the electron density $\rho(\mathbf{r})$ with respect to the number of electrons N, in a frozen geometry (the external potential $v(\mathbf{r})$ remaining constant).

$$\Delta f_{\text{usual}}(\mathbf{r}) = \left(\frac{\partial^2 \rho(\mathbf{r})}{\partial N^2}\right)_{v(\mathbf{r})} \tag{1}$$

It allows the characterisation, in a single representation, of regions within a molecule that are prone to cede ($\Delta f(\mathbf{r}) < 0$) or receive ($\Delta f(\mathbf{r}) > 0$) electron density, the so-called nucleophilic and electrophilic regions in organic chemistry,[38,46] and their use to understand the reactivity of organometallic complexes[47,48] has recently been advocated.

Several approximations of the DD are found in the literature, and are developed in the ESI.† Here, we use a recently devised formulation, the so-called "state-specific" approach,[49–51] where the DD is identified as a sum of electron density differences between the nth excited and the ground states – the so-called nth state specific DDs. Indeed, most of the limitations of the usual approximations are avoided in this formalism; noticeably, the eventual orbital degeneracy is no longer a problem, nor the spin states of the molecules and their associated $N + 1/N - 1$ forms (see the ESI† for more details). Furthermore, the DD within this approach is expected to take into account polarisation effects,[52] and as such to represent reactivity more accurately. More specifically, we focus on the first state specific DD $\Delta f_1(\mathbf{r})$, which usually provides the major contribution to reactivity:

$$\Delta f_1(\mathbf{r}) = \rho_1(\mathbf{r}) - \rho_0(\mathbf{r}) \approx \Delta f_{\text{usual}}(\mathbf{r}) \tag{2}$$

Here, we are interested in comparing chemical systems with different numbers of electrons N. Eqn (1) and (2) hold only for a fixed N value (canonical ensemble), and the Legendre transformation to the grand-canonical ensemble is needed if one wants to set N as a free parameter. The result of such a transformation has already been reported[50] (and the details are recapped in the ESI†), and it can be shown that one simply needs to divide the canonical DD by the square of the molecular hardness η in order to obtain the Grand-Canonical Dual Descriptor (SS-GCDD) $\Delta s(\mathbf{r})$:

$$\Delta s(\mathbf{r}) \approx \frac{\Delta f_{\text{usual}}(\mathbf{r})}{\eta^2} \approx \frac{\rho_1(\mathbf{r}) - \rho_0(\mathbf{r})}{\eta^2}. \tag{3}$$

For the sake of simplicity and concision, we will refer to the SS-GCDD as the DD in the following.

2.2 DD partition into reactive domains

In order to extract the meaningful chemical information contained within the DD, it is relevant to partition it into domains of constant sign $D_i^{\pm}$, associated with a univocal and specific reactivity. More precisely, all points belonging to a given D_i^{+} (respectively D_i^{-}) feature a positive (resp. negative) DD value and are surrounded by neighbours exhibiting the same DD sign that corresponds to a predominant electrophilic (resp. nucleophilic) behaviour.

Such a real space partition can be achieved using DOMAINS, a recently developed code.[53] In the latest version of the program, two thresholds are implemented in order to get a clearer picture of the domains. The first threshold, τ_{r}, excludes from the domains any point in space that would be closer than τ_{r} to any nucleus. This allows us to withdraw the contribution of core regions, which are not expected to contribute significantly to the reactivity, or which may not be accurately described (with the use of pseudo-potentials). The second threshold, τ_{DD}, allows a better separation of the domains by excluding any point in space associated with a norm of the DD that is inferior to τ_{DD} (lower boundary). This permits an efficient delimitation of the reactive sites.

It is possible to integrate the DD within these domains, and thus to gain a deeper insight into the reactivity of the corresponding sites. More precisely, it is possible for each domain $D_i^{\pm}$ to compute its volume, $V_{D_i^{\pm}}$, the integrated value of the DD within this volume, $\Delta s(D_i^{\pm})$, and the average value of the DD in the domain, $\overline{\Delta s(D_i^{\pm})}$. This last value is expected to yield the most valuable information on the domain reactivity, since it shares the same unit as the DD. As we will show in the last part, those average values will actually be the basis for a quantification of the *trans* effect.

2.3 Extended transition state–natural orbitals for chemical valence (ETS–NOCV)

The NOCV Ψ_i are the eigenvectors that diagonalise the deformation density $\Delta\rho(\mathbf{r})$ of two isolated fragments when they are allowed to interact. Mathematically this can be translated by

$$\Delta\rho(\mathbf{r}) = \sum_m \nu_m \left[-\Psi_{-m}(\mathbf{r})^2 + \Psi_m(\mathbf{r})^2\right]. \tag{4}$$

Practically, the NOCVs permit the decomposition of the electron density deformation on the basis of the orbitals of each isolated fragment. It therefore helps in monitoring the evolution of the electron density during a chemical process. For instance, it is possible to distinguish between σ and π bonding, and also to separate donation and back- donation effects;[54] physics beneath the interactions is thus unveiled. In addition to this decomposition of the electron density transfers, an assessment of the associated energetic stabilisation is possible, through the framework of the extended transition state.[55]

2.4 Computational details

All the structures of complexes presented in this work have been fully optimized without symmetry restrictions at the B3LYP level of theory using the Gaussian09 package.[56] Pople basis sets are used for all the coordinating atoms: 6-311+G(d) for S and P atoms, 6-311G(d) for the other ones. Metal cations are modelled with the Stuttgart–Dresden Electron Core Potentials (ECP) and the corresponding basis set (keywords SDD in Gaussian09).[57] Frequency calculations have been performed at the same level of theory to ensure that the obtained geometries correspond to genuine minima of the potential energy hypersurface (the coordinates are reported in the ESI†). To evaluate the DDs, the first ten excited states have been computed using the Time Dependant DFT framework (TD-B3LYP), and the DD has been subsequently evaluated using eqn (2) and (3).[49] Chemical hardness has been approximated as $\eta = E_{\mathrm{LUMO}} - E_{\mathrm{HOMO}}$. Condensation was performed using DOMAINS,[53] and the same threshold values were used for all complexes: τ_{DD} = 0.2 a.u. and τ_{r} = 0.5 a.u.

To ensure that computed DD are reliable, they have also been calculated using two other exchange–correlation functionals (PBE0 and M06-2X) for a few complexes. As expected the results are very similar and make the DD a trustable descriptor. In the same spirit, the adequacy of the basis sets and ECP has been confirmed by additional calculations on the cobalt complexes, at the B3LYP/6-311++G(2d,2p) (C, H, N, O)/Wachters+f (Co) level.[58,59] Apart from computation time, which increases a lot, the tendency remains the same (though the figures change, naturally), hence giving confidence in the adequacy of the computational model. The NOCV calculations have been performed using the Amsterdam Density Functional program (ADF2013),[60] at the B3LYP/TZP-small core level of theory. Both the DD and NOCV density deformations have been represented using GaussView 5.[61]

3. *Trans* effect in octahedral complexes

Note: in the following, the labels *trans* and *cis* will refer to the corresponding position in a complex with respect to the strongest *trans* orienting ligand.

3.1 Methodology

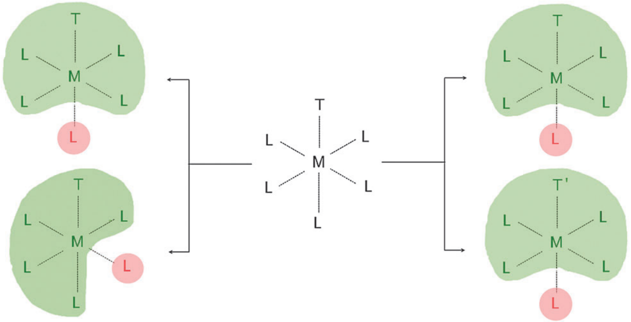

Scheme 1 Schematic representation of the applied methodology; left side, highlight of the differentiation between *trans* and *cis* ligands. Right side, comparison between two trans orienting groups T and T′.

The aim of this study is to characterise and rationalize the *trans* effects in octahedral complexes. As pictured in Scheme 1, two approaches have been unfolded. First, the differences in the electronic demand between the *cis* and the *trans* positions in a given complex are compared, highlighting the *trans* effect induced by a specific ligand T (left side of the figure). To do so, the geometries of the full complexes are optimised, and afterwards either the *cis* or *trans* ligand L is removed. The DDs of the corresponding incomplete [ML_4T] complexes are computed, as well as the NOCVs associated with the coordination of the removed ligands. As exemplified in the following, this approach permits the characterisation of the STE, where one often compares two bond lengths in the same complex (inner reference).

Second, we compare the electronic demand at the *trans* positions in two similar [ML_5T] and [ML_5T'] complexes, differing only by the *trans* orienting ligands T and T′. A similar approach to the previous was used: the first optimisation of the structure, followed by the removal of *trans* ligands. The DDs of the corresponding fragment complexes [ML_4T] and [ML_4T'] are calculated, as well as the NOCVs associated with the coordination of the removed *trans* ligands. This approach likely allows the characterisation of the KTE, where one usually compares two complexes only differing by the *trans* orienting ligand.

The validity of these approaches is supported by the fact that ligand substitution in octahedral complexes generally proceeds *via* dissociative mechanisms. [ML_5] moieties therefore bear some chemical meaning as potential intermediates.[2] In the following discussion, the two approaches are developed in order to assess the efficiency of both tools (DD and NOCV) to retrieve and rationalise the *trans* effects. The complexes listed in Table 1 have been chosen to be representative of the variety both *trans* effects offer, either in electronic configuration (d^0 and d^6 for the STE, d^6 for the KTE), period of the metal (4 and 5) or ligand nature (σ or π donor, π acceptor).

Table 1 List of the studied complexes. Complex S3 is given in ESI

Label	Formula	Specificity
1	$[Co(NH_3)_2(NO_2)_3(CH_3)]^-$	STE, d^6, σ donors
2	$[NbO(SCN)_5]^{2-}$	STE, d^0, σ, π donors
3-H$_2$O	$[Rh(NH_3)_4(H_2O)_2]^{3+}$	KTE, d^6, σ donors
3-Cl	$[Rh(NH_3)_4(H_2O)Cl]^{2+}$	KTE, d^6, σ, π donors
4-OH	$[Co(en)_2(H_2O)OH]^{2+}$	KTE, d^6, σ, π donors
4-SO$_3$	$[Co(en)_2(H_2O)SO_3]^+$	KTE, d^6, π acceptor
S3[a]	$[RhL(PMe_3)_2Cl_3]$	STE, d^6, σ, π donors

[a] L = dimethylaminocarbene.

3.2 Comparing *cis* and *trans* positions

3.2.1 The first example of a d^6 STE complex: [Co(NH$_3$)$_2$(NO$_2$)$_3$(CH$_3$)]$^-$. The first chosen example, [Co(NH$_3$)$_2$(NO$_2$)$_3$(CH$_3$)]$^-$ (**1**), is known to show a marked STE[62] due to the methyl ligand. Indeed, the Co(III)–NO$_2^-$ bond length is 0.10 Å longer *trans* to CH$_3^-$ than *cis*. Two [ML$_5$] fragments have been built by removing either the *trans* or a *cis* nitrito ligand. The DDs computed for the fragments are presented in Fig. 1. The similarity between the metal contributions to the DD in both fragments is striking. They comprise a nucleophilic part reminiscent of a non-bonding metal d orbital, and an electrophilic part developing towards the coordination vacancy. The latter feature could be expected: removing a ligand, *i.e.* a nucleophile, will logically exacerbate the electrophilicity of the remaining [ML$_5$] species.

This electrophilic basin looks noticeably larger in **1-*cis*** than in **1-*trans***, even using an isovalue that is twice higher. The results of the condensation on these domains are summarised in Table 2. In the case of **1-*trans***, the integrated value is about 7 times smaller than that of **1-*cis***. The volume of the domain is also smaller for **1-*trans***, but in a much weaker proportion (roughly 30%). In the end, the mean value of the DD $\overline{\Delta s(D^{+}_{\rm Co})}$ is much higher for **1-*cis*** than for **1-*trans***. The *trans* position, being much less electrophilic than the *cis* one, is then expected to stabilise ligands less efficiently: the associated metal–ligand bond is expected to be longer.

This is in total compliance with the experimental results. This could also be retrieved using NOCVs for the coordination of nitrite to the [ML$_5$] fragments. The deformation density associated with the first (and main) NOCV pair is represented in Fig. 2. In both cases the incoming ligand (NO$_2^-$) loses electron density, which relocates between the ligand and the cobalt atom: a cobalt–nitrite bond is formed. Furthermore, some internal relocations are observed on the [ML$_5$] moiety.

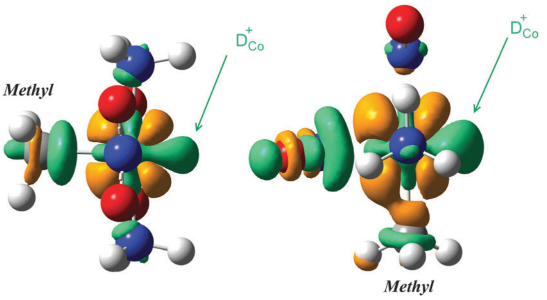

Fig. 1 DD isosurfaces for the [ML$_5$] fragments derived from complex **1**. Left: **1-*trans***, deprived of the *trans* nitrito group with respect to methyl, $-0.4 \le \Delta s(\mathbf{r}) \le 0.4$ a.u. Right: **1-*cis***, deprived of the *cis* nitrito with respect to methyl, $-0.2 \le \Delta s(\mathbf{r}) \le 0.2$ a.u. Surfaces colours: orange, $\Delta s(\mathbf{r}) < 0$; green, $\Delta s(\mathbf{r}) > 0$. Colour scheme: red, O atoms; blue, N atoms; grey, C atoms; white, H atoms: lavender, Co atoms. Coordination vacancies are directed on the right side of each [ML$_5$] fragment, and green arrows point towards the $D^{+}_{\rm Co}$ domains. Methyl ligands are highlighted.

Table 2 DD condensation for [ML$_5$] fragments deriving from complex **1**. All values in atomic units

	1-*cis*	1-*trans*
$\Delta s(D^{+}_{\rm Co})$	145.6	21.4
$V(D^{+}_{\rm Co})$	24.1	17.6
$\overline{\Delta s(D^{+}_{\rm Co})}$	6.04	1.22

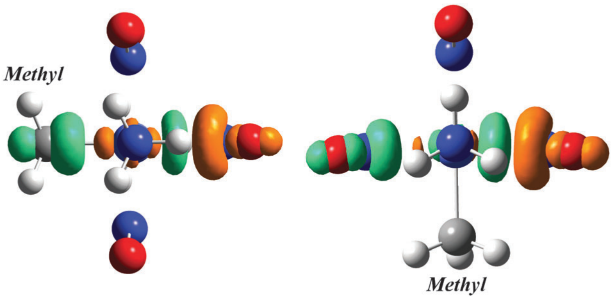

Fig. 2 Deformation density for the first NOCV pair, associated with the coordination of a nitrito ligand to **1-*trans*** (left) and **1-*cis*** (right). Isovalue: $\Delta\rho(\mathbf{r}) = \pm 4 \times 10^{-3}$ a.u. Colour scheme: orange, $\rho(\mathbf{r})$ depletion; green, $\rho(\mathbf{r})$ accumulation. Atom colours and orientations of the fragments were chosen as in Fig. 1. The incoming ligand is located on the right side of each complex, and methyl ligands are highlighted.

Those can be seen as the withdrawal of an excess of electron density that was transferred from the ligands to the metal cation to counteract the coordination vacancy. The coordination of the *cis* nitrito is associated with a NOCV (±1) energetic stabilisation of 40.1 kcal mol^{-1} and a transfer of 0.66 electrons. On the other hand, the coordination of the *trans* nitrito is associated with an energetic stabilisation of 31.3 kcal mol^{-1} and a transfer of 0.57 electrons. The metal–ligand bond is then weaker at the *trans* position, and as such we retrieve the expected STE.

3.2.2 An example of a d^0 STE complex: [NbO(SCN)$_5$]$^{2-}$. The second example, [NbO(SCN)$_5$]$^{2-}$ (**2**), is known to exhibit a marked STE due to the oxide ligand:[63] the Nb(V)–SCN$^-$ bond length is 0.18 Å longer *trans* to the oxido as compared to the *cis* position. One can notice formally the d^0 electronic configuration of the metal cation. Similarly to complex **1**, two [ML$_5$] fragments have been built by removing the *trans* thiocyanate (**2-*trans***) or the *cis* one (**2-*cis***), and the DD has been computed. The results are displayed in Fig. 3.

The DD contributions on the metal cation are again similar. Noticeably, the electrophilic part recalls a non-bonding metal d orbital, in perfect line with the previous example. Indeed, in the framework of MO theory, these non-bonding orbitals are empty in the d^0 case, thus likely associated with electrophilicity, and fully occupied in the d^6 case, and associated with nucleophilicity. In the case of **2-*cis***, these electrophilic domains are adapted to fit a π-donor ligand, and thus may efficiently stabilise a N-bonding thiocyanate.

2-*trans* will not offer such a stabilisation: the electrophilic domains develop perpendicularly to the eventual thiocyanate–niobium bond. The *trans* thiocyanate is then expected to be much less stabilised than the *cis* one. Furthermore, the DD lobes on the *trans* thiocyanate in **2-*cis*** are much more developed than on any other one. The aspect is indeed very typical of an isolated SCN$^-$ ligand, thus suggesting that this ligand in the complex

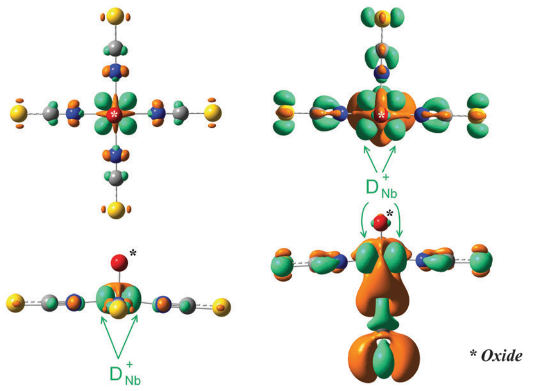

Fig. 3 DD isosurfaces for the [ML_5] fragments derived from complex **2**, **2-*trans*** (left) and **2-*cis*** (right). Isovalues: $-0.2 \leq \Delta s(\mathbf{r}) \leq 0.2$ a.u. Same colour scheme as in Fig. 1, the S atoms are depicted in yellow. Top, view along the O–Nb(V) bond; bottom, side view. Green arrows highlight the D^+_{Nb} domains, and an asterisk highlights the oxide position.

behaves more like a free ligand than a coordinated one, not to say like a leaving group. Unfortunately, the same partition as previously could not be applied: only negligible values of the DD at the *trans* position could be obtained, since no development of the DD is observed at that position. Actually, this is not a pitfall: if no quantification is possible in that case, one is still able to characterise a *trans* effect.

More insight is gained from the ETS-NOCV study of the coordination of thiocyanate to the [$Nb(SCN)_4O$]$^-$ fragments. The results are recapped in Fig. 4. In the case of the *cis* SCN^-, the main energetic stabilisation is associated with the formation of a σ bond (NOCV ±2, −30.4 kcal mol^{-1}, 0.47 electrons transferred), but the highest number of transferred electrons is associated with the formation of a π bond (NOCV ±1, −12.7 kcal mol^{-1}, 0.49 electrons). A different tendency is observed for the *trans* SCN^-: an energetic stabilisation of −18.0 kcal mol^{-1} for the σ bond formation (NOCV ±1), and 0.34 electrons transferred, −8.1 kcal mol^{-1} and 0.52 electrons for the π bond formation (NOCV ±2).

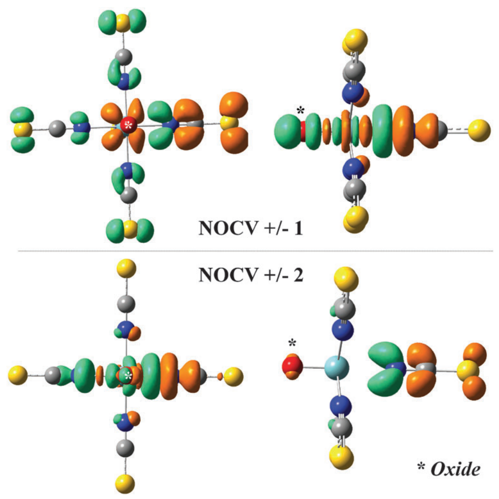

Fig. 4 Deformation density associated with the first (upper side) and second (lower side) NOCV pairs, for the coordination of a thiocyanate to **2-*cis*** (left) and **2-*trans*** (right). The same colour scheme as in Fig. 2, the incoming ligand being located on the right side. Isovalue: $\Delta\rho(\mathbf{r}) = \pm 4 \times 10^{-3}$ a.u. Oxide ligand positions are highlighted by asterisks.

Roughly the same number of electrons is transferred during the formation of the π bonds, but the associated energetic stabilisation is much higher for *cis* SCN^-. Regarding the σ bond formation, both the number of transferred electrons and the energetic stabilisation are higher in the case of *cis* SCN^-. Thus one expects *trans* thiocyanate to be much less stabilised in the complex than the *cis* ones, and as such to be more weakly coordinated: a STE is retrieved.

3.3 Comparing *trans* orienting ligands

3.3.1 An example of a KTE complex: [$Rh(NH_3)_4(H_2O)X$]$^{n+}$.

The two previous examples, in addition to the 3 other examples provided in the ESI,† confirmed that it is possible to highlight differences between the *trans* and *cis* positions in given complexes, and to relate these differences to a possible STE or a KTE. A further step can be taken if one compares two different *trans* orienting ligands, with the remains of the complex being conserved.

Let us consider [$Rh(NH_3)_4(H_2O)X$]$^{n+}$, with X = H_2O, $n = 3$ (**3-H$_2$O**) and X = Cl^-, $n = 2$ (**3-Cl**). It was shown experimentally that water substitution proceeds 5000 times faster for **3-Cl** than for **3-H$_2$O**.[64] In agreement with our methodology, we built two [ML_5] fragments based on these two complexes by removing the coordinated water molecule (**ML5-3-H$_2$O** and **ML5-3-Cl**), and computed the corresponding DD, as represented in Fig. 5. The DD features are very similar to those observed for complex **1**. Noticeably, we retrieve the d AO-type nucleophilic contribution on the metal, and the electrophilic development towards the vacancy. It is not plain whether **ML5-3-H$_2$O** or **ML5-3-Cl** bears the largest contribution at first sight.

Results of the condensation are gathered in Table 3, and help us to answer this question. The integrated value of the DD for **ML5-3-H$_2$O** is approximately twice the value for **ML5-3-Cl**, while the volume of the basins remains rather similar. As a consequence, the mean value of the DD is higher for **ML5-3-H$_2$O**: the associated vacancy exhibits a higher electrophilicity than **ML5-3-Cl**. The water molecule should then be more stabilised in

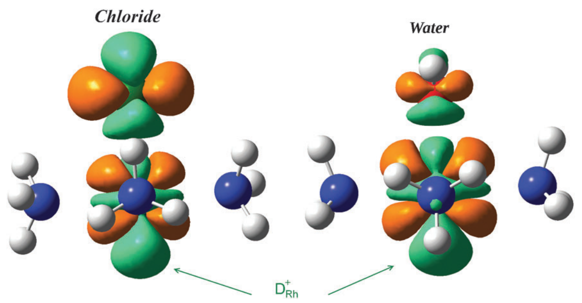

Fig. 5 DD isosurfaces for the [ML_5] fragments built from **3-Cl** (left) and **3-H$_2$O** (right). The same colour scheme and isovalues as in Fig. 3. Cl atoms are represented in olive, and green arrows point towards the D^+_{Rh} domains.

Table 3 DD condensation for [ML_5] fragments deriving from complex **3**. All values in atomic units

	ML5-3-H$_2$O	**ML5-3-Cl**
$\Delta s(D^+_{Rh})$	43.9	21.9
$V(D^+_{Rh})$	25.2	19.2
$\overline{\Delta s}(D^+_{Rh})$	1.74	1.14

3-H$_2$O than in **3-Cl**, and as such to be less easily replaced: we retrieve a KTE.

This is also confirmed at the NOCV level, as sketched in Fig. 6. In both cases, a basin of electron density relocation is observed between the incoming water and the rhodium cation, indicating the formation of a σ bond. Further reorganisation of electron density is observed on the remaining of the ligand. It can be assigned here also to a withdrawal of excess electron density that was transferred from the ligands to the metal cation, in order to counteract the coordination vacancy. The coordination of water to **ML5-3-H$_2$O** is associated with a transfer of 0.48 electrons, and an energetic stabilisation of 31.0 kcal mol^{-1}.

On the other hand, coordination to **ML5-3-Cl** leads only to the transfer of 0.36 electrons and a stabilisation of 16.7 kcal mol^{-1}. The incoming water molecule is then much less stabilised in **3-Cl** and one expects its replacement to proceed much quickly: the KTE is retrieved.

3.3.2 Another KTE complex: [Co(en)$_2$(H$_2$O)X]$^{n+}$.

Let us now consider the case of [Co(en)$_2$(H$_2$O)X]$^{n+}$, with X = OH$^-$, n = 2 (**4-OH**) and X = SO$_3$$^{2-}$, n = 1 (**4-SO$_3$**) (en = ethylenediamine). This complex involves a π-acceptor ligand, and thus differences in the aspect of the DD with respect to the previous cases might be expected. It was shown experimentally that water substitution is 2000 times faster in **4-SO$_3$** than in **4-OH.**[65,66] In the same spirit as previously, we built two [ML$_5$] fragments by removing the coordinated water molecule of **4-SO$_3$** (**ML5-4-SO$_3$**) and **4-OH** (**ML5-4-OH**), and computed the DD.

The results are presented in Fig. 7. The metal cation here also bears a nucleophilic domain with a shape reminiscent of a d-type metal AO, and an electrophilic domain developing towards the vacancy. In the case of **4-SO$_3$** the domains look quite distorted, and the electrophilic one is very small as compared to **4-OH.** This apparent lower electrophilicity is retrieved in numerical values from the condensation, recapped in Table 4.

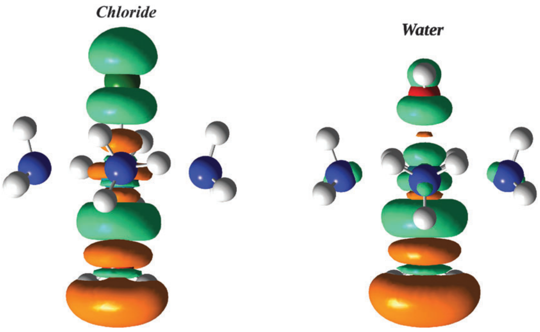

Fig. 6 Deformation density associated with the first NOCV pair for the coordination of H$_2$O to **ML5-3-Cl** (left) and **ML5-3-H$_2$O** (right). The same colour scheme and isovalues as Fig. 4, the incoming ligands being located on the lower side (same orientation as in Fig. 5).

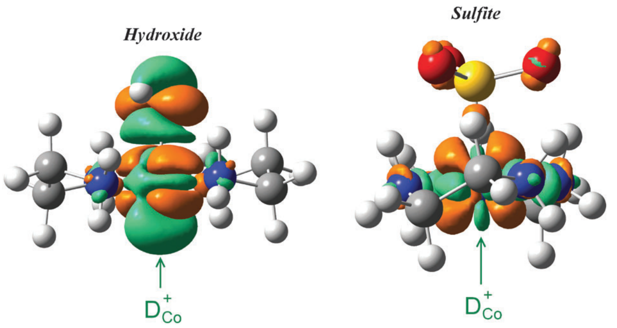

Fig. 7 DD isosurfaces for the [ML$_5$] fragments built from **4-OH** (left) and **4-SO$_3$** (right). The same colour scheme and isovalues as in Fig. 3. Green arrows point towards the D^+_{Co} domains, hydroxide and sulfite being highlighted.

The integrated value is indeed between 3 to 4 times larger for **ML5-4-OH** than for **ML5-4-SO$_3$**, and the mean value is also much larger. More electrophilicity is then seen on the vacancy when the *trans* ligand is hydroxo, thus suggesting the coordinated water would be much more stabilised in **4-OH** than in **4-SO$_3$.**

This is also completely retrieved at the NOCV level, as represented in Fig. 8. During coordination of water to the [ML$_5$] fragments, a basin of electron density relocation is observed between H$_2$O and the cobalt atom, indicating as previously the formation of a σ bond. From the graphical point of view, this relocation of electron density is much larger for **4-OH** than for **4-SO$_3$.**

This is retrieved in the numerical values: coordination of water to **4-OH** involves the relocation of 0.33 electrons and a stabilisation of 15.6 kcal mol^{-1}. On the other hand, only 0.22 electrons are transferred during coordination to **4-SO$_3$**,

Table 4 DD condensation for [ML$_5$] fragments deriving from complex **4**. All values in atomic units

	4-OH	**4-SO$_3$**
$\Delta s(D^+_{Co})$	73.7	20.0
$V(D^+_{Co})$	33.6	13.4
$\overline{\Delta s}(D^+_{Co})$	2.19	1.49

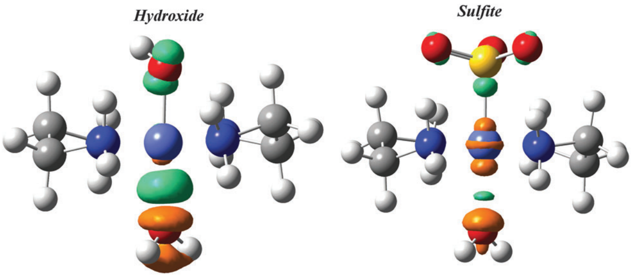

Fig. 8 Deformation density associated with the first NOCV pair for the coordination of H$_2$O to **ML5-4-OH** (left) and **ML5-4-SO$_3$** (right). The same colour scheme, orientations and isovalues as Fig. 2. The incoming water molecule is located on the lower side.

with a stabilisation of 6.3 kcal mol^{-1}. As a result, coordination of water is much weaker when *trans* to a sulfito ligand, as compared to hydroxo. One would then expect an easier substitution in that case, as observed experimentally.

4. A quantitative scale

From the previous examples, it appears that our methodology permits us to highlight the *trans* effects by either differentiating the *cis* and *trans* positions in a given complex, or by comparing two different *trans* orienting ligands. Furthermore, using our recently devised topological partition of the DD we have been able to relate these effects to differences in electrophilicity at given sites around the metal cation: systematically, lower values were observed at the position where either a STE or a KTE is expected. This is in perfect line with the conclusions of both Chval and De Proft (and co-workers).[31,32] The former interpreted the *trans* effects as a "competition between the ligands [...] for the opportunity to donate their electron density to the central" metal cation. On the other hand, the latter proposed that a very efficient donation from the *trans* orienting ligand would translate in an electron density accumulation at the *trans* position, which in turn would induce a strong Pauli repulsion with the *trans* ligand, hence destabilising it. It is obvious that both effects would translate in a smaller electrophilicity at the *trans* position with respect to the strongest donor, as observed.

We intend to show in this last part that this electrophilicity can be used to draw a quantitative scale of the *trans* orienting ligands. This scale resembles the experimental one, which is roughly as follows (ranking from high STE to low):[2,3,6]

$$\mathrm{CH_3}^- \approx \mathrm{CO} \approx \mathrm{NO_2}^- > \mathrm{Cl}^- > \mathrm{Pyridine} > \mathrm{NH_3} > \mathrm{H_2O}$$

Let us then consider complex **3** derivatives $[\mathrm{Rh(NH_3)_4(H_2O)X}]^{n+}$ with X belonging to the previous series. If we apply the same methodology as in part 3.3, for every fragment $[\mathrm{Rh(NH_3)_4X}]^{n+}$ an electrophilic domain is observed on the metal cation, pointing towards the vacancy. Because the shapes of the DD are always the same, in the following we will only discuss the condensed values. They are all summed up in Table 5.

As previously, the ranges of both the integrated DD values and the volume of the electrophilic domains are large. On the other hand, the mean values are rather close to unity (ranging from 0.36 to 1.74 a.u.), with a smaller dispersion. Furthermore, as we discussed in the "Theoretical backgrounds" part, these mean values are also more readily understandable than mere integrated values, having the same units as the DD. In our context, they are the best index to build a quantitative scale.

Ranking the ligands from the lowest to the highest mean values $\overline{\Delta s(D^+_{\mathrm{Rh}})}$, one obtains:

$$\mathrm{NO_2}^- < \mathrm{CH_3}^- \approx \mathrm{CO} < \mathrm{NH_3} < \mathrm{Cl}^- < \mathrm{Pyridine} < \mathrm{H_2O}$$

which is close to the experimental series. Noticeably, one retrieves that the high field ligands are associated with the lowest electrophilicity, and as such to stronger *trans* effects. On the other hand the order of the weak *trans* orienting ligands seems to be less correctly reproduced.

Table 5 DD condensation for [ML$_5$] fragments deriving from complex **3**. All values in atomic units

X	$\Delta s(D^+_{\mathrm{Rh}})$	$V(D^+_{\mathrm{Rh}})$	$\overline{\Delta s(D^+_{\mathrm{Rh}})}$
$\mathrm{CH_3}^-$	9.5	10.7	0.88
CO	14.1	15.8	0.89
$\mathrm{NO_2}^-$	1.6	4.5	0.36
Pyridine	36.4	24.9	1.47
$\mathrm{NH_3}$	18.5	17.9	1.03
Cl^-	21.9	19.2	1.14
$\mathrm{H_2O}$	43.9	25.2	1.74

Table 6 DD condensation for [ML$_5$] fragments deriving from complex **5**. All values in atomic units

X	$\Delta s(D^+_{\mathrm{Ru}})$	$V(D^+_{\mathrm{Ru}})$	$\overline{\Delta s(D^+_{\mathrm{Ru}})}$
$\mathrm{CH_3}^-$	22.4	28.9	0.77
CO	18.3	21.5	0.85
$\mathrm{NO_2}^-$	21.0	35.2	0.60
Pyridine	29.4	26.1	1.13
Cl^-	36.3	26.4	1.37
$\mathrm{H_2O}$	43.2	30.6	1.41

This was rather expected, since the experimental series is averaged over large sets of complexes, studied under rather different conditions (temperature, solvents). This experimental series provides a rough trend, rather than a precise order, and many exceptions are known.[6] As such, our computed ranking might actually bear much meaning than the experimental series. Noticeably, it should be possible to isolate the contribution of each experimental parameter – temperature, pressure, solvent – to the overall *trans* effect, using a purely computational framework. Such a study goes beyond the scope of this paper, and may be the subject of a following survey.

In order to confirm our calculated scale, at least in the strong-field part of the series, we decided to study another series of complexes,[67] $[\mathrm{Ru(NH_3)_5X}]^{n+}$ (**5**) with the same X – to the exception of NH$_3$, which would be meaningless, since no differentiation would be seen due to the octahedral symmetry. The shape of the DD is also very similar to the previous examples, and we will only discuss the numerical values summarised in Table 6. The order of the ligands ranked from the lowest to the highest $\overline{\Delta s(D^+_{\mathrm{Ru}})}$ is:

$$\mathrm{NO_2}^- < \mathrm{CH_3}^- < \mathrm{CO} < \mathrm{Pyridine} < \mathrm{Cl}^- < \mathrm{H_2O}$$

As one can remark, the same order as the previous is obtained for the lowest contributions, with NO$_2^-$, CH$_3^-$ and CO being strong *trans* orienting ligands in both cases. On the other hand, the order of the weak *trans* orienting ligands is different, being closer to the experimental trends.

5. Conclusions

In conclusion, we showed that it is possible to retrieve the *trans* effects for some octahedral complexes, using tools from conceptual DFT or close paradigms. It seems that both effects are due to differences in the way electron density is likely to reorganise in the complex, under the influence of a specific ligand. This ligand, by decreasing the need for electron density at the *trans* position, weakens the associated metal–ligand bond and as such leads to an increase in the bond length or kinetics. Monitoring the electrophilicity then allows the characterisation and quantification of the *trans* effects, and permitted us to build a quantitative scale of the *trans* orienting ligands following a systematic approach. This scale, although not perfect, follows rather closely the experimental trends. This suggests that *trans* effects are primarily controlled by the electron density donation properties of the ligands at the *trans* position. The rather large diversity of the studied cases, either in transition metal series and ligand types, suggests that these findings are quite general.

Both *trans* effects are often encountered in coordination chemistry, but failed to be precisely understood. We hope our results will help us to change this fact, and may for instance allow us to rationally design molecular devices for specific drug delivery or catalysis, based on the KTE. For a wider scope, we hope our combined DD/NOCV study will stimulate further research effort, in order to enlighten the physics beneath metal–ligand interaction in coordination complexes.

References

1 I. I. Chernayev, *Ann. Inst. Platine.*, 1926, **4**, 243–275.
2 J. E. Huheey, E. A. Keiter and R. L. Keiter, *Inorganic Chemistry*, DeBoeck Université, French Edition, 1993.
3 D. F. Shriver, P. W. Atkins and C. H. Langford, *Inorganic Chemistry*, Oxford University Press, 2nd edn, 1994.
4 J. K. Burdett and T. A. Albright, *Inorg. Chem.*, 1979, **18**, 2112–2120.
5 J. V. Quagliano and L. Schubert, *Chem. Rev.*, 1952, **50**, 201–266.
6 B. J. Coe and S. J. Glenwright, *Coord. Chem. Rev.*, 2000, **203**, 5–80.
7 K. Krogh-Jespersen, M. D. Romanelli, J. H. Melman, T. J. Emge and J. G. Brennan, *Inorg. Chem.*, 2010, **49**, 552–560.
8 H. Chermette, K. Rachedi and F. Volatron, *THEOCHEM*, 2006, **762**, 109–121.
9 A. J. Lewis, K. C. Mullane, E. Nakamaru-Ogiso, P. J. Carroll and J. E. Schelter, *Inorg. Chem.*, 2014, **53**, 6944–6953.
10 V. Tognetti, A. Boulangé, P. A. Peixoto, X. Franck and L. Joubert, *J. Mol. Model.*, 2014, **20**, 2342.
11 P. K. Sajith and C. H. Suresh, *Inorg. Chem.*, 2012, **51**, 967–977.
12 Y.-X. Jia, B.-B. Li, Y. Li, S. A. Pullarkat, H. Hirao and P.-H. Leung, *Organometallics*, 2014, **53**, 6053–6058.
13 G. Zhang, K. Chen, H. Chen, J. Yao and S. Shaik, *Inorg. Chem.*, 2013, **52**, 5088–5096.
14 J. Kwak, Y. Ohk, Y. Jung and S. Chang, *J. Am. Chem. Soc.*, 2012, **134**, 17778–17788.
15 A. P. Hunt and N. Lehnert, *Acc. Chem. Res.*, 2015, **48**, 2117–2125.
16 D. Lieb, F. C. Friedel, M. Yawer, A. Zahl, M. M. Khusniyarov, F. W. Heinemann and I. Ivanovic-Burmazovic, *Inorg. Chem.*, 2012, **52**, 222–236.
17 N. Dolker, F. Maseras and A. Lledos, *J. Phys. Chem. B*, 2003, **107**, 306–315.
18 K. Czarnecki, S. Nimri, Z. Gross, L. M. Proniewicz and J. R. Kincald, *J. Am. Chem. Soc.*, 1996, **118**, 2929–2935.
19 Y. Zhang, Z. Guo and X.-Z. You, *J. Am. Chem. Soc.*, 2001, **123**, 9378–9387.
20 M.-H. Baik, R. A. Friesner and S. J. Lippard, *J. Am. Chem. Soc.*, 2003, **125**, 14082–14092.
21 J. Raber, C. Zhu and L. A. Eriksson, *J. Phys. Chem. B*, 2005, **109**, 11006–11015.
22 I. I. Chernayev, *Ann. Inst. Platine.*, 1927, **5**, 109.
23 A. A. Grinberg, *Ann. Inst. Platine.*, 1932, **10**, 58.
24 A. A. Grinberg, *Acta Phys. Chim.*, 1935, **3**, 573.
25 H. S. La Pierre, M. Rosenzweig, B. Kosog, C. Hauser, F. W. Heinemann, S. T. Liddle and K. Meyer, *Chem. Commun.*, 2015, **51**, 16671–16674.
26 J. Chatt and L. A. Duncanson, *J. Chem. Soc.*, 1953, 2939–2947.
27 M. J. S. Dewar, *Bull. Soc. Chim. Fr.*, 1951, **18**, C71.
28 B. A. Bovykin, *Teor. Eksp. Khim.*, 1974, **10**, 238–240.
29 A. Pidcock, R. E. Richards and L. M. Venanzi, *J. Chem. Soc. A*, 1968, 1970–1973.
30 M. P. Mitoraj, H. Zhu, A. Michalak and T. Ziegler, *Int. J. Quantum Chem.*, 2009, **109**, 3379–3386.
31 Z. Chval, M. Sip and J. V. Burda, *J. Comput. Chem.*, 2008, **29**, 2370–2381.
32 B. Pinter, V. Van Speybroeck, M. Waroquier, P. Geerlings and F. De Proft, *Phys. Chem. Chem. Phys.*, 2013, **15**, 17354–17365.
33 P. Geerlings, F. De Proft and W. Langenaeker, *Chem. Rev.*, 2003, **103**, 1793–1873.
34 H. Chermette, *J. Comput. Chem.*, 1999, **20**, 129–154.
35 J. L. Gazquez, *J. Mex. Chem. Soc.*, 2008, **52**, 3–10.
36 R. G. Parr and W. Yang, *J. Am. Chem. Soc.*, 1984, **106**, 4049–4050.
37 C. Morell, A. Grand and A. Toro-Labbé, *J. Phys. Chem. A*, 2005, **109**, 205–212.
38 P. Geerlings and F. De Proft, *Phys. Chem. Chem. Phys.*, 2008, **10**, 3028–3042.
39 J. I. Martinez-Arraya, *J. Math. Chem.*, 2015, **53**, 451–465.
40 M. Mitoraj and A. Michalak, *J. Mol. Model.*, 2007, **13**, 347–355.
41 A. Michalak, M. Mitoraj and T. Ziegler, *J. Phys. Chem. A*, 2008, **112**, 1933–1939.
42 M. P. Mitoraj, M. Parafiniuk, M. Srebro, M. Handzlik, A. Buczek and A. Michalak, *J. Mol. Model.*, 2011, **17**, 2337–2352.
43 F. De Proft, V. Forquet, B. Ourri, H. Chermette, P. Geerlings and C. Morell, *Phys. Chem. Chem. Phys.*, 2015, **17**, 9359–9368.
44 B. Pinter, N. Nagels, W. A. Herrebout and F. De Proft, *Chem. – Eur. J.*, 2013, **19**, 519–530.
45 C. Morell, A. Grand and A. Toro-Labbé, *Chem. Phys. Lett.*, 2006, **425**, 342–346.

46 P. Geerlings, P. W. Ayers, A. Toro-Labbé, P. K. Chattaraj and F. De Proft, *Acc. Chem. Res.*, 2012, **53**, 683–695.

47 J. M. del Campo and J. I. Martinez-Arraya, *Propellants, Explos., Pyrotech.*, 2014, **39**, 890–896.

48 J. I. Martinez-Arraya, *J. Mol. Model.*, 2013, **19**, 2715–2722.

49 V. Tognetti, C. Morell, P. W. Ayers, L. Joubert and H. Chermette, *Phys. Chem. Chem. Phys.*, 2013, **15**, 14465–14475.

50 F. Guégan, P. Mignon, V. Tognetti, L. Joubert and C. Morell, *Phys. Chem. Chem. Phys.*, 2014, **16**, 15558–15569.

51 L.-J. Jouanno, V. Di Mascio, V. Tognetti, L. Joubert, C. Sabot and P.-Y. Renard, *J. Org. Chem.*, 2014, **19**, 1303–1319.

52 E. Falkowska, V. Tognetti, L. Joubert, P. Jubault, J.-P. Bouillon and X. Pannecoucke, *RSC Adv.*, 2015, **5**, 6864–6868.

53 V. Tognetti, C. Morell and L. Joubert, *J. Comput. Chem.*, 2015, **36**, 648–659.

54 M. Mitoraj and A. Michalak, *Organometallics*, 2007, **26**, 6576–6580.

55 M. P. Mitoraj, A. Michalak and T. Ziegler, *J. Chem. Theory Comput.*, 2009, **5**, 962–975.

56 M. J. Frisch, G. W. Trucks, H. B. Schlegel, G. E. Scuseria, M. A. Robb, J. R. Cheeseman, G. Scalmani, V. Barone, B. Mennucci, G. A. Petersson, H. Nakatsuji, M. Caricato, X. Li, H. P. Hratchian, A. F. Izmaylov, J. Bloino, G. Zheng, J. L. Sonnenberg, M. Hada, M. Ehara, K. Toyota, R. Fukuda, J. Hasegawa, M. Ishida, T. Nakajima, Y. Honda, O. Kitao, H. Nakai, T. Vreven, J. A. Montgomery, Jr., J. E. Peralta, F. Ogliaro, M. Bearpark, J. J. Heyd, E. Brothers, K. N. Kudin, V. N. Staroverov, R. Kobayashi, J. Normand, K. Raghavachari, A. Rendell, J. C. Burant, S. S. Iyengar, J. Tomasi, M. Cossi, N. Rega, J. M. Millam, M. Klene, J. E. Knox, J. B. Cross, V. Bakken, C. Adamo, J. Jaramillo, R. Gomperts, R. E. Stratmann, O. Yazyev, A. J. Austin, R. Cammi, C. Pomelli, J. W. Ochterski, R. L. Martin, K. Morokuma, V. G. Zakrzewski, G. A. Voth, P. Salvador, J. J. Dannenberg, S. Dapprich, A. D. Daniels, Ã. Farkas, J. B. Foresman, J. V. Ortiz, J. Cioslowski and D. J. Fox, *Gaussian 09 Revision D.01*, Gaussian Inc., Wallingford, CT, 2009.

57 U. Wedig, M. Dolg, H. Stoll and H. Preuss, *Quantum chemistry: the challenge of transition metals and coordination chemistry*, Reidel, Dordrecht, 1986.

58 A. J. H. Wachters, *J. Chem. Phys.*, 1970, **52**, 1033–1036.

59 C. W. Bauschlicher, S. R. Langhoff, L. A. Partridge and H. Barnes, *J. Chem. Phys.*, 1989, **91**, 2399–2411.

60 E. J. Baerends, *et al.*, *ADF 2013*, SCM, Theoretical Chemistry, Vrije Universiteit, Amsterdam, The Netherlands.

61 R. Dennington, T. Keith and J. Millam, *GaussView version 5*, Semichem Inc., Shawnee Mission, KS.

62 P. Kofod, P. Harris and S. Larsen, *Inorg. Chem.*, 1997, **5**, 2258–2266.

63 B. Kamenar and C. K. Prout, *J. Chem. Soc.*, 1970, **9**, 2379–2384.

64 L. Monsted and O. Monsted, *Acta Chem. Scand.*, 1984, **A38**, 67–71.

65 D. R. Stranks and J. K. Yandell, *Inorg. Chem.*, 1970, **9**, 751–757.

66 E. N. Maslen and J. K. Yandell, *J. Chem. Soc., Dalton Trans.*, 1975, 327–329.

67 F. Bottomley, *J. Chem. Soc., Dalton Trans.*, 1972, 2148–2152.

Bibliography

[1] C. Cohen-Tannoudji, B. Diu and F. Laloë, *Mécanique Quantique, vol. I*.

[2] J.-L. Basdevant and J. Dalibard, *Mécanique Quantique*, Editions de l'École Polytechnique, 2002.

[3] C. Leforestier, *Introduction à la chimie quantique*, Dunod, 2005.

[4] C. Cohen-Tannoudji, B. Diu and F. Laloë, *Mécanique Quantique, vol. II*, Hermann, 1996.

[5] P. Fleurat-Lessard, *M1 Lectures on "Ab initio quantum chemistry"*, 2012, ENS Lyon.

[6] P. Mignon, *M2 RFCT Label Lectures on "Hartree Fock and post-Hartree Fock methods"*, 2012, ENS Lyon.

[7] A. Szabo and N. S. Ostlund, *Modern Quantum Chemistry*, Dover Publications, 1996.

[8] C. J. Cramer, *Essentials of Computational Chemistry, 2nd Edition*, John Wiley & Sons, 2004.

[9] J. B. Foresman and A. Frisch, *Exploring chemistry with electronic structure methods, 2nd. edition*, Gaussian Inc., 1996.

[10] C. D. Sherrill and H. F. S. III., Academic Press, 1999, vol. 34, pp. 143 – 269.

[11] J. Cizek, *J. Chem. Phys.*, 1966, **45**, 4256–4266.

[12] J. A. Pople, *Rev. Mod. Phys.*, 1999, **71**, 1267–1274.

[13] C. Møller and M. S. Plesset, *Phys. Rev.*, 1934, **46**, 618–622.

[14] B. O. Roos, P. R. Taylor and P. E. M. Siegbahn, *Chem. Phys.*, 1980, **48**, 157–173.

[15] B. O. Roos, *Adv. Chem. Phys.*, 1987, **69**, 399–445.

[16] F. Neese, *ORCA manual*, 2013, version 3.0.

[17] R. C. Gibbs, D. T. Wilber and H. E. White, *Phys. Rev.*, 1927, **29**, 790–793.

[18] K. Andersson, P. A. Malmqvist, B. O. Roos, A. J. Sadlej and K. Wolinski, *J. Phys. Chem.*, 1990, **94**, 5483–5488.

[19] G. Ghigo, B. O. Roos and P. Åke Malmqvist, *Chem. Phys. Lett.*, 2004, **396**, 142 – 149.

[20] J. Jung, *Ph.D. thesis*, Université Rennes 1, 2015.

[21] S. Cotton, *Lanthanide and Actinide Chemistry*, John Wiley & Sons, 2006.

[22] K. G. Dyall, *The Journal of chemical physics*, 1995, **102**, 4909–4918.

[23] C. Camacho, H. A. Witek and S. Yamamoto, *J. Comput. Chem.*, 2009, **30**, 468–478.

[24] J. Miralles, O. Castell, R. Caballol and J.-P. Malrieu, *Chem. Phys.*, 1993, **172**, 33 – 43.

[25] C. J. Calzado, J. Cabrero, J. P. Malrieu and R. Caballol, *The Journal of chemical physics*, 2002, **116**, 2728–2747.

[26] J. Miralles, J.-P. Daudey and R. Caballol, *Chem. Phys. Lett.*, 1992, **198**, 555 – 562.

[27] H. Chermette, *M2 RFCT Label Lectures on "Density Functional Theory"*, 2015, Université Lyon 1.

[28] D. Schwarzenbach and G. Chapuis, *Cristallographie*, Presses Polytechniques et Universitaires Romandes, 2006.

[29] P. Hohenberg and W. Kohn, *Phys. Rev.*, 1964, **136**, B864–B871.

[30] R. G. Parr and W. Yang, *Density Functional Theory of atoms and molecules*, Oxford University Press, 1989.

[31] W. Koch and M. C. Holthausen, *A chemist's guide to Density Functional Theory*, John Wiley & Sons, 2001.

[32] W. Kohn and L. J. Sham, *Phys. Rev.*, 1965, **140**, A1133–A1138.

[33] J. P. Perdew and K. Schmidt, *AIP Conference Proceedings*, 2001, **577**, year.

[34] A. J. Cohen, P. Mori-Sanchez and W. Yang, *Chem. Rev.*, 2012, **112**, 289–320.

[35] ed. M. A. L. Marques, C. Ulrich, F. Nogueira, A. Rubio, K. Burke and E. K. U. Gross, Springer, 2006, vol. 706.

[36] H. Chermette, *J. Comp. Chem.*, 1999, **20**, 129–154.

[37] P. Geerlings, F. De Proft and W. Langenaeker, *Chem. Rev.*, 2003, **103**, 1793–1874.

[38] R. P. Iczkowski and J. L. Margrave, *J. Am. Chem. Soc.*, 1961, **83**, 3547–3551.

[39] R. G. Parr and R. G. Pearson, *J. Am. Chem. Soc.*, 1983, **105**, 7512–7516.

[40] R. G. Parr and W. Yang, *J. Am. Chem. Soc.*, 1984, **106**, 4049–4050.

[41] C. Morell, A. Grand and A. Toro-Labbé, *J. Phys. Chem. A.*, 2005, **109**, 205–212.

[42] M. Reiher, *Wiley Interdisciplinary Reviews: Computational Molecular Science*, 2012, **2**, 139–149.

[43] C. Chang, M. Pelissier and P. Durand, *Phys. Scripta*, 1986, **34**, 394.

[44] T. Nakajima and K. Hirao, *Chem. Rev.*, 2012, **112**, 385–402.

[45] N. Sablon, R. Mastalerz, F. Proft, P. Geerlings and M. Reiher, *Theor. Chem. Acc.*, 2010, **127**, 195–202.

[46] L. Landau and L. Lifchitz, *Quantum mechanics*, Editions MIR, 1967.

[47] P. Åke Malmqvist and B. O. Roos, *Chem. Phys. Lett.*, 1989, **155**, 189 – 194.

[48] P. Åke Malmqvist, B. O. Roos and B. Schimmelpfennig, *Chem. Phys. Lett.*, 2002, **357**, 230 – 240.

[49] A. D. McNaught and A. Wilkinson, *IUPAC. Compendium of Chemical Terminology*, 2014.

[50] P. C. Vollhardt and N. E. Schore, *Organic Chemistry*, De Boeck Université, French edn., 1995.

[51] J. E. Huheey, E. A. Keiter and R. L. Keiter, *Inorg. Chem.*, DeBoeck Université, French Edition edn., 1993.

[52] A. Werner, *Nobel Lecture*, 1913.

[53] J. H. Van Vleck, *Phys. Rev.*, 1932, **41**, 208–215.

[54] D. F. Shriver, P. W. Atkins and C. H. Langford, *Inorg. Chem.*, Oxford University Press, 2nd edn., 1994.

[55] P. H. Walton, *Chimie et théorie des groupes*, De Boeck Université, French edn., 2001.

[56] S. F. A. Kettle and A. J. Smith, *J. Chem. Soc. A*, 1967, 688–692.

[57] P. Curie, *J. Phys. Theor. Appl.*, 1894, **3**, 393–415.

[58] J. S. Griffith and L. E. Orgel, *Q. Rev. Chem. Soc.*, 1957, **11**, 381–393.

[59] J. Hollas, *Modern Spectroscopy*, Wiley, 2004.

[60] J.-L. Rivail, *Éléments de chimie quantique à l'usage des chimistes*, EDP Sciences/C-NRS éditions, 1999.

[61] G. Klopman, *J. Am. Chem. Soc.*, 1968, **90**, 223.

[62] L. Salem, *J. Am. Chem. Soc.*, 1968, **90**, 543.

[63] P. W. Atkins, *Physical Chemistry*, Oxford University Press, Sixth Edition edn., 1998.

[64] O. Kahn, *Molecular Magnetism*, VCH Publishers, 1993.

[65] G. A. Bain and J. F. Berry, *J. Chem. Ed.*, 2008, **85**, 532–536.

[66] B. Diu, C. Guthmann, D. Lederer and B. Roulet, *Physique Statistique*, Hermann, 2001.

[67] J. C. Slater, *Quantum Theory of Atomic Structure*, 1960, vol. II.

[68] J. H. Van Vleck, *The theory of electric and magnetic susceptibilities*, Oxford University Press, 1932.

[69] B. Albela, *M1 Lectures on "Molecular Magnetism"*, 2012, ENS Lyon.

[70] K. Ridier, *Ph.D. thesis*, Université Paris-Sud, 2014.

[71] R. Sessoli, H. L. Tsai, A. R. Schake, S. Wang, J. B. Vincent, K. Folting, D. Gatteschi, G. Christou and D. N. Hendrickson, *J. Am. Chem. Soc.*, 1993, **115**, 1804–1816.

[72] R. Sessoli, D. Gatteschi, A. Caneschi and M. A. Novak, *Nature*, 1993, **365**, 141–143.

[73] A. M. Ako, I. J. Hewitt, V. Mereacre, R. Clérac, W. Wernsdorfer, C. E. Anson and A. K. Powell, *Angew. Chem. Int. Ed.*, 2006, **45**, 4926–4929.

[74] F. Neese and D. A. Pantazis, *Faraday Discuss.*, 2011, **148**, 229–238.

[75] Y. Journaux, *Engineering Single Molecule Magnet: Design, Constraints and Compromises*, 2015.

[76] N. Ishikawa, M. Sugita, T. Ishikawa, S. Koshihara and Y. Kaizu, *J. Am. Chem. Soc.*, 2003, 8694–8695.

[77] D. N. Woodruff, R. E. P. Winpenny and R. A. Layfield, *Chem. Rev.*, 2013, 5110–5148.

[78] J. Luzon and R. Sessoli, *Dalton Trans.*, 2012, **41**, 13556–13567.

[79] J. D. Rinehart and J. R. Long, *Chem. Sci.*, 2011, **2**, 2078–2085.

[80] A. Abragam and B. Bleaney, *Electron Paramagnetic Resonance of Transition Ions*, Oxford University Press, 2012.

[81] K. W. H. Stevens, *Rep. Progr. Phys.*, 1967, 189–226.

[82] J. Schnack, *Molecular Magnetism Web: a gate to molecular magnetism*, http://www.molmag.de.

[83] M.-E. Boulon, G. Cucinotta, S.-S. Liu, S.-D. Jiang, L. Ungur, L. F. Chibotaru, S. Gao and R. Sessoli, *Chemistry–A European Journal*, 2013, **19**, 13726–13731.

[84] I. J. Hewitt, J. Tang, N. Madhu, C. E. Anson, Y. Lan, J. Luzon, M. Etienne, R. Sessoli and A. K. Powell, *Angewandte Chemie International Edition*, 2010, **49**, 6352–6356.

[85] N. W. Ashcroft and N. D. Mermin, *Physique des solides*, EDP sciences, 2012.

[86] J. Schweizer, in *Structures magnétiques, densités d'aimantation et facteurs de forme magnétiques mesurés par diffraction de neutrons polarisés*, 2008, p. 87.

[87] A. Gukasov and P. J. Brown, *J. Phys. Condens. Matter*, 2002, 8831–8839.

[88] K. Ridier, B. Gillon, A. Gukasov, G. Chaboussant, A. Cousson, D. Luneau, A. Borta, J.-F. Jacquot, R. Checa, Y. Chiba, H. Sakiyama and M. Mikuriya, *Chem. Eur. J.*, 2016, **22**, 724–735.

[89] V. Tognetti, C. Morell, P. W. Ayers, L. Joubert and H. Chermette, *Phys. Chem. Chem. Phys.*, 2013, **15**, 14465–14475.

[90] M. S. Richard P. Feynman, Robert B. Leighton, *Le Cours de physique de Feynman*, Dunod, 1999.

[91] R. G. Pearson, *J. Am. Chem. Soc.*, 1988, **110**, 2092–2097.

[92] Z. Boisdenghien, S. Fias, F. Da Pieve, F. De Proft and P. Geerlings, *Mol. Phys.*, 2015, **113**, 2–9.

[93] J. Chatt, L. A. Duncanson and L. M. Venanzi, *J. Chem. Soc.*, 1955, 4456–4460.

[94] G. Naray-Szabo and G. G. Ferenczy, *Chem. Rev.*, 1995, **95**, 829–847.

[95] J. I. Martínez-Araya, *J. Mol. Model.*, 2013, **19**, 2715–2722.

[96] V. Tognetti, C. Morell and L. Joubert, *J. of Comput. Chem.*, 2015, **36**, 649–659.

[97] M. J. Frisch, G. W. Trucks, H. B. Schlegel, G. E. Scuseria, M. A. Robb, J. R. Cheeseman, G. Scalmani, V. Barone, B. Mennucci, G. A. Petersson, H. Nakatsuji, M. Caricato, X. Li, H. P. Hratchian, A. F. Izmaylov, J. Bloino, G. Zheng, J. L. Sonnenberg, M. Hada, M. Ehara, K. Toyota, R. Fukuda, J. Hasegawa, M. Ishida, T. Nakajima, Y. Honda, O. Kitao, H. Nakai, T. Vreven, J. A. Montgomery, Jr., J. E. Peralta, F. Ogliaro, M. Bearpark, J. J. Heyd, E. Brothers, K. N. Kudin, V. N. Staroverov, R. Kobayashi, J. Normand, K. Raghavachari, A. Rendell, J. C. Burant, S. S. Iyengar, J. Tomasi, M. Cossi, N. Rega, J. M. Millam, M. Klene, J. E. Knox, J. B. Cross, V. Bakken, C. Adamo, J. Jaramillo, R. Gomperts, R. E. Stratmann, O. Yazyev, A. J. Austin, R. Cammi, C. Pomelli, J. W. Ochterski, R. L. Martin, K. Morokuma, V. G. Zakrzewski, G. A. Voth, P. Salvador, J. J. Dannenberg, S. Dapprich, A. D. Daniels, O. Farkas, J. B. Foresman, J. V. Ortiz, J. Cioslowski and D. J. Fox, *Gaussian 09 Revision E.01*, Gaussian Inc. Wallingford CT 2009.

[98] N. Rosch and R. Hoffmann, *Inorg. Chem.*, 1974, **13**, 2656–2666.

[99] G. J. Kubas, *Metal Dihydrogen and σ-Bond Complexes*, Springer US, 2001.

[100] L. Vaska and J. W. Di Luzio, *J. Am. Chem. Soc.*, 1962, **84**, 679–680.

[101] A. Y. Rogachev and R. Hoffmann, *J. Am. Chem. Soc.*, 2013, **135**, 3262–3275.

[102] R. A. Gossage, A. D. Ryabov, A. L. Spek, D. J. Stufkens, J. A. M. van Beek, R. van Eldik and G. van Koten, *J. Am. Chem. Soc.*, 1999, **121**, 2488–2497.

[103] D. W. Shaffer, S. A. Ryken, R. A. Zarkes and A. F. Heyduk, *Inorg. Chem.*, 2012, **51**, 12122–12131.

[104] R. Makiura, I. Nagasawa, N. Kimura, S. Ishimaru, H. Kitagawa and R. Ikeda, *Chem. Commun.*, 2001, 1642–1643.

[105] F. A. Cotton, E. V. Dikarev and M. A. Petrukhina, *Angew. Chem. Int. Ed.*, 2000, **39**, 2362–2364.

[106] T. Clark, M. Hennemann, J. S. Murray and P. Politzer, *J. Mol. Model.*, 2007, **13**, 291–296.

[107] P. Vanysek, *Handbook of Chemistry and Physics*.

[108] N. Kitajima and Y. Moro-oka, *Chem. Rev.*, 1994, **94**, 737–757.

[109] Y. Moro-oka, K. Fujisawa and N. Kitajima, *Pure Appl. Chem.*, 1995, **67**, 241–248.

[110] S. Pin, B. Alpert and A. Michalowicz, *FEBS Lett.*, 1982, **147**, 106–110.

[111] F. Neese, *Wiley Interdisciplinary Reviews: Computational Molecular Science*, 2012, **2**, 73–78.

[112] M. Verdaguer and G. S. Girolami, *Magnetism: Molecules to Materials*, Wiley-VCH Verlad, 2005.

[113] A. Navaza, G. Chevrier, P. M. Alzari and P. J. Aymonino, *Acta Crysta. C*, 1989, **45**, 839–841.

[114] D. P. Mingos, *J. Organomet. Chem.*, 2014, 153–173.

[115] J. H. Enermark and R. D. Feltham, *Coord. Chem. Rev.*, 1974, **13**, 339–406.

[116] M. Kabesova and J. Gazo, *Chem. Zvesti.*, 1980, **6**, 800–841.

[117] N. A. Bailey, D. E. Fenton, M. V. Franklin and M. Hall, *J. Chem. Soc., Dalton Trans.*, 1980, 984–990.

[118] I. I. Chernayev, *Ann. Inst. Platine*, 1926, 243–275.

[119] J. V. Quagliano and L. Schubert, *Chem. Rev.*, 1952, **50**, 201–260.

[120] B. J. Coe and S. J. Glenwright, *Coord. Chem. Rev.*, 2000, **203**, 5 – 80.

[121] Y.-X. Jia, B.-B. Li, Y. Li, S. A. Pullarkat, H. Hirao and P.-H. Leung, *Organomet.*, 2014, **53**, 6053–6058.

[122] G. Zhang, K. Chen, H. Chen, J. Yao and S. Shaik, *Inorg. Chem.*, 2013, **52**, 5088–5096.

[123] J. Kwak, Y. Ohk, Y. Jung and S. Chang, *J. Am. Chem. Soc.*, 2012, **134**, 17778–17788.

[124] A. P. Hunt and N. Lehnert, *Acc. Chem. Res.*, 2015, **48**, 2117–2125.

[125] D. Lieb, F. C. Friedel, M. Yawer, A. Zahl, M. M. Khusniyarov, F. W. Heinemann and I. Ivanovic-Burmazovic, *Inorg. Chem.*, 2012, **52**, 222–236.

[126] N. DOlker, F. Maseras and A. Lledos, *J. Phys. Chem. B*, 2003, **107**, 306–315.

[127] Y. Zhang, Z. Guo and X.-Z. You, *J. Am. Chem. Soc.*, 2001, **123**, 9378–9387.

[128] M.-H. Baik, R. A. Friesner and S. J. Lippard, *J. Am. Chem. Soc.*, 2003, **125**, 14082–14092.

[129] J. Raber, C. Zhu and L. A. Eriksson, *J. Phys. Chem. B.*, 2005, **109**, 11006–11015.

[130] I. I. Chernayev, *Ann. Inst. Platine*, 1927, **5**, 109.

[131] A. A. Grinberg, *Ann. Inst. Platine*, 1932, **10**, 58.

[132] A. A. Grinberg, *Acta Phys. Chim.*, 1935, **3**, 573.

[133] H. S. La Pierre, M. Rosenzweig, B. Kosog, C. Hauser, F. W. Heinemann, S. T. Liddle and K. Meyer, *Chem. Commun.*, 2015, **51**, 16671–16674.

[134] J. Chatt and L. A. Duncanson, *J. Chem. Soc.*, 1953, 2939–2947.

[135] M. J. S. Dewar, *Bull. Soc. Chim. Fr.*, 1951, **18**, C71.

[136] B. A. Bovykin, *Teor. Eksp. Khim.*, 1974, **10**, 238–240.

[137] A. Pidcock, R. E. Richards and L. M. Venanzi, *J. Chem. Soc. A*, 1968, 1970–1973.

[138] M. P. Mitoraj, H. Zhu, A. Michalak and T. Ziegler, *Int. J. Quantum Chem.*, 2009, **109**, 3379–3386.

[139] Z. Chval, M. Sip and J. V. Burda, *J. Comput. Chem.*, 2008, **29**, 2370–2381.

[140] B. Pinter, V. Van Speybroeck, M. Waroquier, P. Geerlings and F. de Proft, *Phys. Chem. Chem. Phys.*, 2013, **15**, 17354–17365.

[141] M. Mitoraj and A. Michalak, *J. Mol. Model.*, 2007, **13**, 347–355.

[142] A. Michalak, M. Mitoraj and T. Ziegler, *J. Phys. Chem. A*, 2008, **112**, 1933–1939.

[143] M. Mitoraj, M. Parafiniuk, M. Srebro, M. Handzlik, A. Buczek and A. Michalak, *J. Mol. Model.*, 2011, **17**, 2337–2352.

[144] M. Mitoraj and A. Michalak, *Organomet.*, 2007, **26**, 6576–6580.

[145] M. Mitoraj, A. Michalak and T. Ziegler, *J. Chem. Theory Comput.*, 2009, **5**, 962–975.

[146] E. J. Baerends, T. Ziegler, A. J. Atkins, J. Autschbach, D. Bashford, A. Bérces, F. M. Bickelhaupt, C. Bo, P. M. Boerritger, L. Cavallo, D. P. Chong, D. V. Chulhai, L. Deng, R. M. Dickson, J. M. Dieterich, D. E. Ellis, M. van Faassen, A. Ghysels, A. Giammona, S. J. A. van Gisbergen, A. W. Götz, S. Gusarov, F. E. Harris, P. van den Hoek, C. R. Jacob, H. Jacobsen, L. Jensen, J. W. Kaminski, G. van Kessel, F. Kootstra, A. Kovalenko, M. Krykunov, E. van Lenthe, D. A. McCormack, A. Michalak, M. Mitoraj, S. M. Morton, J. Neugebauer, V. P. Nicu, L. Noodleman, V. P. Osinga, S. Patchkovskii, M. Pavanello, C. A. Peeples, P. H. T. Philipsen, D. Post, C. C. Pye, W. Ravenek, J. I. Rodríguez, P. Ros, R. Rüger, P. R. T. Schipper, H. van Schoot, G. Schreckenbach, J. S. Seldenthuis, M. Seth, J. G. Snijders, M. Solà, M. Swart, D. Swerhone, G. te Velde, P. Vernooijs, L. Versluis, L. Visscher, O. Visser, F. Wang, T. A. Wesolowski, E. M. van Wezenbeek, G. Wiesenekker, S. K. Wolff, T. K. Woo and A. L. Yakovlev, *ADF2013*.

[147] P. Kofod, P. Harris and S. Larsen, *Inorg. Chem.*, 1997, **5**, 2258–2266.

[148] B. Kamenar and C. K. Prout, *J. Chem. Soc.*, 1970, **9**, 2379–2384.

[149] L. Monsted and O. Monsted, *Acta Chem. Scand.*, 1984, **A38**, 67–71.

[150] D. R. Stranks and J. K. Yandell, *Inorg. Chem.*, 1970, **9**, 751–757.

[151] E. N. Maslen and J. K. Yandell, *J. Chem. Soc., Dalton Trans.*, 1975, 327–329.

[152] F. Bottomley, *J. Chem. Soc., Dalton Trans.*, 1972, 2148–2152.

[153] T. issue: Biomimetic Inorganic Chemistry, *Chem. Rev.*, 2004, **104**, 347–1200.

[154] E. I. Solomon, U. M. Sundaram, and T. E. Machonkin, *Chemical Reviews*, 1996, **96**, 2563–2606.

[155] O. Kahn, *Chemical Physics Letters*, 1997, **265**, 109 – 114.

[156] J. Yoon and E. I. Solomon, *Coordination Chemistry Reviews*, 2007, **251**, 379 – 400.

[157] D. Loss and D. P. DiVincenzo, *Phys. Rev. A*, 1998, **57**, 120–126.

[158] B. L. Guennic, S. Petit, G. Chastanet, G. Pilet, D. Luneau, N. B. Amor, and V. Robert, *Inorganic Chemistry*, 2008, **47**, 572–577.

[159] S. Petit, *Ph.D. thesis*, Université Lyon 1, 2007.

[160] A. Messai, *Ph.D. thesis*, Université Mentouri de Constantine, 2010.

[161] A. D. Becke, *The Journal of Chemical Physics*, 1993, **98**, year.

[162] R. Ditchfield, W. J. Hehre and J. A. Pople, *The Journal of Chemical Physics*, 1971, **54**, year.

[163] A. W. Addison, T. N. Rao, J. Reedijk, J. van Rijn and G. C. Verschoor, *J. Chem. Soc., Dalton Trans.*, 1984, 1349–1356.

[164] T. H. Dunning Jr. and P. J. Hay, in *Methods of Electronic Structure Theory*, ed. H. F. S. III., Springer, 1997, vol. 3, pp. 1–27.

[165] D. A. Pantazis, X.-Y. Chen, C. R. Landis and F. Neese, *Journal of chemical theory and computation*, 2008, **4**, 908–919.

[166] S. Sinnecker, A. Rajendran, A. Klamt, M. Diedenhofen and F. Neese, *The Journal of Physical Chemistry A*, 2006, **110**, 2235–2245.

[167] J.-D. Chai and M. Head-Gordon, *Phys. Chem. Chem. Phys.*, 2008, **10**, 6615–6620.

[168] D. Figgen, G. Rauhut, M. Dolg and H. Stoll, *Chem. Phys.*, 2005, **311**, 227–244.

[169] F. M. Floris, J. Tomasi and J. L. P. Ahuir, *Journal of Computational Chemistry*, 1991, **12**, 784–791.

[170] K. Fukui, *Accounts of chemical research*, 1981, **14**, 363–368.

[171] J. Girerd, O. Kahn and M. Verdaguer, *Inorganic Chemistry*, 1980, **19**, 274–276.

[172] L. Noodleman, *The Journal of Chemical Physics*, 1981, **74**, 5737–5743.

[173] L. Noodleman and E. R. Davidson, *Chemical physics*, 1986, **109**, 131–143.

[174] F. Neese, *Journal of Physics and Chemistry of Solids*, 2004, **65**, 781–785.

[175] I. N. Shcherbakov, T. M. Ivanova, M. A. Kiskin, S. V. Kolotilov, V. M. Novotortsev, I. L. Eremenko and V. A. Kogan, *Inorganica Chimica Acta*, 2014, **421**, 507–512.

[176] L.-L. Wang, Y.-M. Sun, Z.-Y. Yu, Z.-N. Qi and C.-B. Liu, *The Journal of Physical Chemistry A*, 2009, **113**, 10534–10539.

[177] Y. Yu, C. Li, B. Yin, J.-L. Li, Y.-H. Huang, Z.-Y. Wen and Z.-Y. Jiang, *The Journal of chemical physics*, 2013, **139**, 054305.

[178] N. Onofrio, *Ph.D. thesis*, Université de Grenoble, 2011.

[179] C. J. Calzado, C. Angeli, C. de Graaf and R. Caballol, *Theoretical Chemistry Accounts*, 2011, **128**, 505–519.

[180] N. Queralt, D. Taratiel, C. de Graaf, R. Caballol, R. Cimiraglia and C. Angeli, *J. Comput. Chem.*, 2008, **29**, 994–1003.

[181] S. Trofimenko, *J. Am. Chem. Soc.*, 1967, **89**, 3170–3177.

[182] R. D. Shannon, *Acta Cryst. A*, 1976, **32**, 751–767.

[183] J. Mink, M. Y. Skripkin, L. Hajba, C. Németh, A. Abbasi and M. Sandström, *Spectrochim. Acta A*, 2005, **61**, 1639 – 1645.

[184] H. Tanak, K. Pawlus and M. Marchewka, *J. Mol. Struct.*, 2016, **1121**, 142 – 155.

[185] H. M. Badawi and W. Förner, *J. Mol. Struct.*, 2013, **1037**, 218 – 224.

[186] C. Kuhnt, S. Tschierlei, M. Karnahl, S. Rau, B. Dietzek, M. Schmitt and J. Popp, *J. Raman Spec.*, **41**, 922–932.

[187] S. P. Sinha, *Z. Anorg. Allg. Chem.*, 1977, **434**, 277–292.

[188] W. W. Rudolph and G. Irmer, *Dalton Trans.*, 2015, **44**, 295–305.

[189] M. Niemeyer, *Z. Anorg. Allg. Chem.*, 2006, **632**, 1449–1456.

[190] Q.-W. Li, J.-L. Liu, J.-H. Jia, Y.-C. Chen, J. Liu, L.-F. Wang and M.-L. Tong, *Chem. Commun.*, 2015, **51**, 10291–10294.

[191] K. S. Pedersen, J. Dreiser, H. Weihe, R. Sibille, H. V. Johannesen, M. A. Sørensen, B. E. Nielsen, M. Sigrist, H. Mutka, S. Rols, J. Bendix and S. Piligkos, *Inorg. Chem.*, 2015, **54**, 7600–7606.

[192] X. Yi, K. Bernot, V. Le Corre, G. Calvez, F. Pointillart, O. Cador, B. Le Guennic, J. Jung, O. Maury, V. Placide, Y. Guyot, T. Roisnel, C. Daiguebonne and O. Guillou, *Chem. Eur. J.*, 2014, **20**, 1569–1576.

[193] R. F. Ziessel, G. Ulrich, L. Charbonnière, D. Imbert, R. Scopelliti and J.-C. G. Bünzli, *Chem. Eur. J.*, 2006, **12**, 5060–5067.

[194] F. Pointillart, B. Le Guennic, S. Golhen, O. Cador, O. Maury and L. Ouahab, *Chem. Commun.*, 2013, **49**, 615–617.

[195] G. Cucinotta, M. Perfetti, J. Luzon, M. Etienne, P.-E. Car, A. Caneschi, G. Calvez, K. Bernot and R. Sessoli, *Angew. Chem. Int. Ed.*, 2012, **51**, 1606–1610.

[196] J. Long, J. Rouquette, J.-M. Thibaud, R. A. S. Ferreira, L. D. Carlos, B. Donnadieu, V. Vieru, L. F. Chibotaru, L. Konczewicz, J. Haines, Y. Guari and J. Larionova, *Angew. Chem. Int. Ed.*, 2015, **54**, 2236–2240.

[197] G. Cosquer, F. Pointillart, J. Jung, B. Le Guennic, S. Golhen, O. Cador, Y. Guyot, A. Brenier, O. Maury and L. Ouahab, *Eur. J. Inorg. Chem.*, 2014, 69–82.

[198] F. Pointillart, J. Jung, R. Berraud-Pache, B. Le Guennic, V. Dorcet, S. Golhen, O. Cador, O. Maury, Y. Guyot, S. Decurtins, S.-X. Liu and L. Ouahab, *Inorg. Chem.*, 2015, **54**, 5384–5397.

[199] J.-C. Bünzli and S. Eliseeva, in *Comprehensive Inorg. Chem. {II} (Second Edition)*, ed. J. Reedijk and K. Poeppelmeier, Elsevier, Amsterdam, Second Edition edn., 2013, pp. 339 – 398.

[200] M. Kasha, *Discuss. Faraday Soc.*, 1950, **9**, 14–19.

[201] H. Lueken, *Lectures on magnetism of lanthanide ions under varying ligand and magnetic fields*, http://www.molmag.de.

[202] P. J. Brown, *The Cambridge Crystallographic Subroutine Library*, https://www.ill.eu/sites/ccsl/html/ccsldoc.html.

[203] E. Lucaccini, L. Sorace, M. Perfetti, J.-P. Costes and R. Sessoli, *Chem. Commun.*, 2014, **50**, 1648–1651.

[204] J.-D. Leng, J.-L. Liu, Y.-Z. Zheng, L. Ungur, L. F. Chibotaru, F.-S. Guo and M.-L. Tong, *Chem. Commun.*, 2013, **49**, 158–160.

[205] N. F. Chilton, S. K. Langley, B. Moubaraki, A. Soncini, S. R. Batten and K. S. Murray, *Chem. Sci.*, 2013, **4**, 1719–1730.

[206] L. Zhang, P. Zhang, L. Zhao, J. Wu, M. Guo and J. Tang, *Inorg. Chem.*, 2015, **54**, 5571–5578.

[207] D. Gatteschi, R. Sessoli and J. Vilain, *Molecular Nanomagnets*, Oxford University Press, 2006.

[208] R. Sessoli and A. K. Powell, *Coord. Chem. Rev.*, 2009, **253**, 2328 – 2341.

[209] R. C. Gibbs, D. T. Wilber and H. E. White, *Phys. Rev.*, 1927, **29**, 790–793.

[210] F. Aquilante, L. De Vico, N. Ferré, G. Ghigo, P.-A. Malmqvist, P. Neogrady, T. Pedersen, M. Pitonak, M. Reiher, B. O. Roos, L. Serrano-Andrés, M. Urban, V. Veryazov and R. Lindh, *J. Comput. Chem.*, 2010, **31**, 224–247.

[211] L. Chibotaru and L. Ungur, *J. Chem. Phys.*, 2012, **137**, 064112.

[212] D. Gatteschi and R. Sessoli, *Angew. Chem. Int. Ed.*, 2003, **42**, 268–297.

[213] R. G. Lawrence, T. A. Hamor, C. J. Jones, K. Paxton and N. M. Rowley, *J. Chem. Soc., Dalton Trans.*, 2001, 2121–2126.

[214] M. A. J. Moss, C. J. Jones and A. J. Edwards, *J. Chem. Soc., Dalton Trans.*, 1989, 1393–1400.

[215] M. A. J. Moss, C. J. Jones and A. J. Edwards, *Polyhedron*, 1988, **7**, 79–81.

[216] S. Hino, M. Maeda, Y. Kataoka, M. Nakano, T. Yamamura and T. Kajiwara.

[217] C. Takehara, P. L. Then, Y. Kataoka, M. Nakano, T. Yamamura and T. Kajiwara, *Dalton Trans.*, 2015, **44**, 18276–18283.

[218] J. J. Le Roy, I. Korobkov, J. E. Kim, E. J. Schelter and M. Murugesu, *Dalton Trans.*, 2014, **43**, 2737–2740.

[219] Y.-N. Guo, G.-F. Xu, Y. Guo and J. Tang, *Dalton Trans.*, 2011, **40**, 9953–9963.

[220] S. K. Langley, D. P. Wielechowski, N. F. Chilton, B. Moubaraki and K. S. Murray, *Inorganic Chemistry*, 2015, **54**, 10497–10503.

[221] J. J. Baldoví, J. M. Clemente-Juan, E. Coronado, Y. Duan, A. Gaita-Ariño and C. Giménez-Saiz, *Inorganic Chemistry*, 2014, **53**, 9976–9980.

[222] G. Poneti, K. Bernot, L. Bogani, A. Caneschi, R. Sessoli, W. Wernsdorfer and D. Gatteschi, *Chem. Commun.*, 2007, 1807–1809.

[223] K. Shrivastava, *physica status solidi (b)*, 1983, **117**, 437–458.

Joint experimental and theoretical approaches in coordination chemistry:

"from the *trans* effects to Single Molecule Magnets"

Résumé :

Dans ce travail, nous nous sommes principalement intéressé à la description et à la rationalisation de certaines propriétés des complexes de coordination, par des approches mixtes expérience/théorie.

La première de ces études, purement théorique, revisite les propriétés de coordination des ligands par des méthodes de type DFT conceptuelle. Dans un premier temps, les ligands seuls sont étudiés, puis les résultats de cette première approche sont utilisés pour caractériser et rationaliser les effets *trans* dans les complexes octaédriques.

La deuxième étude ci-présentée concerne la synthèse et la caractérisation de complexes polynucléaires de Cu(II) et de ligands de type base de Schiff dérivés d'acides aminés. Dans un premier temps, la réactivité de ces complexes en solution est rationalisée par des mesures spectroscopiques et des calculs de type DFT. Puis, les propriétés magnétiques de deux complexes trinucléaires sont présentées et analysées grâce au support de calculs *ab initio* de haut niveau.

Enfin, dans la troisième étude nous nous intéressons à des complexes mononucléaires d'ion lanthanides présentant une dynamique lente de l'aimantation à basse température. Des mesures magnétiques, mais aussi de luminescence et de diffraction de neutrons polarisés, combinées à des calculs de type SA-CASSCF/RASSI-SO permettent de rationaliser les propriétés magnétiques ainsi observées.

Mots-clés :

Chimie de coordination, chimie théorique, magnétisme moléculaire, cristallographie, luminescence.

Abstract: In this work, we focused on the description and rationalisation of certain properties of coordination complexes through the use of joint experiment/theory approaches.

The first study is purely theoretical, and revisits the coordination properties of ligands using conceptual DFT methods. In a first time, ligands alone are studied, and the results of this study are then employed to characterise and rationaliser the *trans* effects in octahedral complexes.

The second study deals with the syntheses and characterisation of polynuclear Cu(II) complexes deriving from amino-acid based Schiff base-like ligands. In a first time, the reactivity of these complexes in solution is rationalised through the use of spectroscopies and DFT calculations. Then, the magnetic properties of two trinuclear complexes are presented and analysed thanks to high level *ab initio* calculations.

Finally, in the third study we focus on mononuclear lanthanide-based complexes presenting a slow dynamics of magnetisation at low temperature. Magnetic measurements, as well as luminescence and polarised neutron diffraction experiments, combined to SA-CASSCF/RASSI-SO calculation allow the rationalisation of the observed magnetic properties.

Keywords:

Coordination chemistry, theoretical chemistry, molecular magnetism, crystallography, luminescence.

INSTITUT DES
SCIENCES
ANALYTIQUES

LMI
UMR CNRS 5615
Laboratoire
Multimatériaux
Interfaces

UNIVERSITÉ
DE LYON

Lyon 1